



UNIVERSITY OF SHEFFIELD

The Theory of Critical Distance to design 3D printed notched components

Adnan Ali Ahmed

A thesis submitted in partial fulfilment for the degree of
Doctor of Philosophy (PhD)

The Department of Civil and Structural Engineering
University of Sheffield

April 2020

Declaration of Authorship

I hereby declare that the work, which will present in this thesis entitled, (The Theory of Critical Distance to design 3D printed notched components) is my own composition and it is a record of work achieved myself.

Adnan Ali Ahmed

The Theory of Critical Distance to design 3D printed notched components

Abstract

The three-dimensional (3D) printing technology is a manufacturing technique for fabricating a wide range of structures and complex geometries from 3D model data. The fused deposition modelling is a common additive manufacturing (AM) technique in this industry, using filaments of raw material to produce the final product, while Polylactic acid (PLA) is considered to be one of the most convenient polymers for use in this kind of fabrication. The PLA components produced by this technique are usually required to maintain good mechanical properties in several applications, especially when they are manufactured with complex geometries resulting in high stress concentration. Therefore, it is recommended to investigate the strength of AM PLA components under different kinds of loading.

The Theory of Critical Distances (TCD) is the name that has been given to a group of design methodologies that are considered highly precise and reliable tools for predicting the static strength of brittle notched materials. The TCD represents an ideal method for optimising the mechanical properties of 3D printed PLA parts used in sensitive applications like tissue engineering. In this respect, this study used the TCD to predict the strength of a large number of AM PLA components, tested under both tensile and bending loading and containing different geometrical features.

Two groups of specimens were tested in this experimentally based study. The first group was solid AM PLA with an infill ratio of 100%. The influence of several printing parameters on the strength of plain specimens was investigated.

The TCD's validity as a method for determining static strength of notched PLA specimens was checked with different notch shapes and root radii, under tension and bending loading. The TCD was found to be highly accurate in estimating the static strength of notched AM PLA solid specimens, with its use returning estimates falling mainly within an error interval of $\pm 20\%$.

The second group of specimens was for AM PLA plain and notched porous specimens manufactured with variable infill levels. A novel approach combining conventional TCD with the equivalent homogenised material concept was formulated to perform a static assessment of plain/notched objects of PLA when this polymer is additively manufactured with different infill levels. The key idea was that the internal net structure resulting from the 3D-printing process could be modelled by treating the material as a continuum, homogenous and isotropic, thus allowing the internal voids to be considered in terms of the change in their mechanical/strength properties. This idea was initially applied by addressing this problem in a Kitagawa-Takahashi setting via the Theory of Critical Distances, for plain porous specimens. Subsequently, the

approach was extended to the static strength assessment of notched porous components of 3D-printed PLA. The results showed that the TCD applied alongside the equivalent homogenised material concept was able to model successfully the static strength of plain AM PLA materials, as well as notched materials, fabricated with variable infill levels. Again, predictions fell mainly within an error interval of $\pm 20\%$.

Publications

The work of this theses has produced the following published papers:

1. Adnan A. Ahmed, Luca Susmel, On the use of length scale parameters to assess the static strength of notched 3D-printed PLA, *Frattura ed Integrità Strutturale*, 41 (2017) 252-259.
2. A. A. Ahmed, L. Susmel, Additively Manufactured PLA under static loading: strength/cracking behaviours vs deposition angle, *Procedia Structural Integrity* 3 (2017) 498–507.
3. A. A. Ahmed, L. Susmel, A material length scale- based methodology to assess static strength of notched additively manufactured polylactide (PLA), *Fatigue & Fracture of Engineering Materials & Structures* 2018;1–28, Wiley Publishing Ltd.
4. Ahmed, A. A., Susmel, L., Additively manufactured PLA: strength and fracture behaviour under static loading. In: *Proceedings of The BSSM's 12th International Conference on Advances in Experimental Mechanics*, Sheffield, UK, 29-31 August 2017 (available on-line at <http://www.bssm.org/2017papers>).
5. Adnan A. Ahmed, Luca Susmel, Static assessment of plain/notched polylactide (PLA) 3D-printed with different in-fill levels: equivalent homogenised material concept and Theory of Critical Distances, *Fatigue and Fracture of Engineering Materials and Structures*. 2018; 1–22. Wiley Publishing Ltd.
6. Adnan A. Ahmed and Luca Susmel, Crack paths in plain and notched specimens of additively manufactured PLA under static loading, 6th International Conference on Crack Paths (CP 2018), Verona, Italy, 19-21 September 2018.
7. Ahmed, A. and Susmel, L A (2019) Estimating static strength of plain/notched PLA additively manufactured with different in-fill levels. *Proceedings of the Fifth IJ Fatigue & FFEMS Workshop: Characterisation of Crack Tip Fields* (pp 30-31). Heidelberg, Germany, 8 April 2019 - 10 April 2019

Acknowledgements

I would like to present my gratitude to my supervisors Professor Luca Susmel and Professor Matthew Gilbert in the Department of Civil and Structural Engineering.

Particularly, I am grateful to Professor Luca for his crucial guidance and encouragement through the events of this thesis. Many problems, throughout the research, have not been solved without his precious advice and efforts.

I also would like to admit my very special thanks to the Ministry of Higher Education of Iraq and Kerbela University for their sponsorship of my PhD study.

Needless to mention, experimental barriers might not be able to be tackled without the support of the technical staff in the structural lab. Moreover, and most important, is to thank my family especially my brothers Thamer and Ehsan, for their kindness and endless support to finish my mission.

Finally, I would like to express my sincere appreciation to all my friends in Sheffield university, in particular, my research group for their help and support in solving many problems I have faced through the course of this research.

List of contents

DECLARATION OF AUTHORSHIP	I
ABSTRACT	II
PUBLICATIONS	IV
ACKNOWLEDGEMENTS	V
List of contents	vi
LIST OF FIGURES	IX
LIST OF TABLES	XIV
CHAPTER 1-INTRODUCTION	1
1.1 Background	1
1.1.1 3D printing technology	1
1.1.2 Fracture mechanics and TCD	2
1.2 Scope of research	4
1.3 Aim and Objectives	5
1.4 Structure of the Thesis	6
CHAPTER 2-3D PRINTING REVIEW	8
2.1 Introduction	8
2.2 Cost comparison of AM vs injection moulding parts	8
2.3 3D Printed polymer	9
2.4 Examples of AM techniques using polymer	9
2.5 PLA material	11
2.5.1 Composition of PLA	11
2.5.2 Physical and mechanical properties	12
2.5.3 Disadvantages of PLA	13
2.5.4 Fracture behaviour of PLA	13
2.5.5 3D printed PLA	14
2.6 Applications	16
CHAPTER 3- ANISOTROPIC MATERIALS	17
3.1 Introduction	17
3.2 Woody materials	17
3.3 Fiber-reinforced composite	19
CHAPTER 4-FRACTURE MECHANICS	21
4.1 Introduction	21
4.2 Modes of fracture	21

4.3 Stress Concentration	22
4.4 Fracture criteria	24
4.4.1 Energy criterion	24
4.4.2 Stress intensity criterion	26
4.5 Factors affecting <i>K_{IC}</i>	29
4.6 The Theory of Critical Distance	30
4.6.1 TCD methods	31
4.6.2 Point and Line methods	31
4.6.3 Area method and volume method	34
4.6.4 Imaginary crack method (ICM)	37
4.6.5 Finite Fracture Mechanics (FFM)	38
4.6.6 Estimating the Material Constants values	39
4.6.7 Critical distance L in polymers	40
4.6.8 TCD with polymers	41
4.7 TCD and Kitagawa-Takahashi's diagram under static loading	43
4.8 TCD and other fracture theories	45
4.9 Benefits of TCD	47
CHAPTER 5- METHODOLOGY	49
5.1 Experimental work	49
5.2 Solid PLA specimens, 100% infill ratio	50
5.2.1 Fabricating and testing of specimens	50
5.2.2 Elastic modulus	55
5.2.3 Strength properties	55
5.2.4 Specimens with crack-like notches	56
5.2.5 Notched PLA specimens	57
5.2.6 Plane strain fracture toughness test	60
5.3 Porous PLA specimens with variable infill level	63
5.4 Numerical simulations	64
CHAPTER 6- RESULTS AND DISCUSSION FOR SOLID AM PLA PARTS	69
6.1 Mechanical properties and behaviour of plain AM PLA	69
6.2 Behaviour of AM PLA notched samples under static loading	75
6.3 Cracking behaviour	84
6.4 Fracture toughness	87
6.5 Static strength of notched PLA parts	91
6.6 Conclusion	95

CHAPTER 7-RESULTS AND DISCUSSION OF AM PLA POROUS PARTS	97
7.1 Plain PLA porous components	97
7.2 Notched PLA porous components.....	102
7.3 Mechanical behaviour in terms of the Equivalent Homogenised Material Concept	106
7.4 Static strength modelling of plain porous AM PLA	107
7.5 Static strength of notched porous AM PLA components	112
7.6 Conclusion	119
CHAPTER 8- GENERAL DISCUSSION, CONCLUSION AND FUTURE WORK...	120
8.1 Discussion	120
8.2 Conclusions.....	121
8.3 Recommendations for future work.....	122
REFERENCES.....	124
APPENDIX A. AM PLA SOLID SAMPLES	132
A.1 The pictures of the PLA specimens	132
A.2 The tables of results for the tested solid AM PLA samples	141
A.3 Figures of tested AM PLA solid samples	145
A.4 Microscopic pictures of tested PLA specimens.....	157
A.5 FE modelling scheme and test figures for solid PLA samples	160
A.6 Tables of PLA strength prediction by the TCD	172
APPENDIX B. AM PLA POROUS SAMPLES	177
B.1 The pictures of PLA porous samples	177
B.2 Tables of the test results for AM PLA porous parts.....	180
B.3 Figures of the tested porous AM PLA samples.....	187
B.4 Microscopic pictures of porous plain PLA samples	199
B.5 Tables of the strength prediction for porous PLA samples.....	204

List of figures

Figure 4.1 Three modes of cracks in an object under loading	22
Figure 4.2 Elliptic flaw in an infinite plate.....	24
Figure 4.3 Plane stresses near a crack tip in an elastic material.....	26
Figure 4.4 Additional strain energy release in semi-infinite plate	27
Figure 4.5 Shape factor [77].....	29
Figure 4.6 Point method	33
Figure 4.7 Line method	34
Figure 4.8 Area method.....	35
Figure 4.9 The imaginary crack at the notch root for ICM	37
Figure 4.10 TCD evaluation for ductile material	40
Figure 4. 11 Transition modelling from a short to long-crack regime according to TCD for a material under tension.....	44
Figure 4. 12 Local, non-local and global theories	45
Figure 5.1 Manufacturing layout.....	51
Figure 5.2 Plain specimen. Dimensions in millimetres	53
Figure 5.3 PLA fibres orientation on the applied load.....	54
Figure 5.4 Test set-up for plain specimen	54
Figure 5.5 Hookean region and offset yield strength [102] [115].....	55
Figure 5.6 Specimens with crack-like notches (dimensions in mm (a) $\alpha = 0^\circ$; (b) $\alpha = 30^\circ$).....	57
Figure 5.7 Notched specimens (dimensions in millimetres), the tolerance equal to ± 0.02	58
Figure 5.8 Testing of notched specimen under tension.....	59
Figure 5.9 Failure stress of notched specimen under 3-point bending.....	59
Figure 5.10 Notched specimens under 3-point bending.....	60
Figure 5.11 Compact tension configuration, CT [104]	61
Figure 5.12 CT testing apparatus.....	62
Figure 5.13 Determination of C and PQ for CT test [104].....	62

Figure 5.14 The effective void size, dv	64
Figure 5.15 FE Model set-up and boundary conditions: a) U-notched sample under tension: b) V-notched sample under 3-point bending.....	65
Figure 5.16 Partitioning for PLA specimens model under tension, a) Whole sample, b) At the notch tip.....	66
Figure 5.17 Partitioning for PLA sample model under 3-point bending, a) Whole sample, b) At the notch tip.....	67
Figure 6.1 Plain specimens with ts equal to 0.....	71
Figure 6.2 Stress vs. strain for plain samples under tension for different ts and θP , a) $ts = 0, \theta P = 0^\circ$; b) $ts = 0, \theta P = 30^\circ$; c) $ts = 0.4\text{ mm}, \theta P = 0^\circ$; d) $ts = 0.4\text{ mm}, \theta P = 0^\circ$; e) $ts = 0.8\text{ mm}, \theta P = 0^\circ$; f) $ts = 0.8\text{ mm}, \theta P = 30^\circ$	72
Figure 6.3 Effect of shell thickness on (E) for different θP	74
Figure 6.4 Strength distribution of plain specimens.....	74
Figure 6.5 Distribution of 0.2% proof stress for plain specimens.....	74
Figure 6.6 load vs displacement for notched specimens, a) $\theta P = 45^\circ$; b) $\theta P = 30^\circ$; c) $\theta P = 0^\circ$; d) $\theta P = 0^\circ$; e) $\theta P = 0^\circ$; f) $\theta P = 0^\circ$	77
Figure 6.7 Cracked specimens with microscope picture for the crack tip, $ts = 0\text{ mm}$	78
Figure 6.8 Ultimate strength vs. θP for crack-like specimens.....	79
Figure 6.9 Failure strength for U-notches specimens under tension.....	79
Figure 6.10 Failure stress for U-notched specimens under 3-point bending.....	80
Figure 6.11 Failure strength for open notched specimens under tension.....	80
Figure 6.12 Failure strength for open notched specimens under 3-point bending....	81
Figure 6.13 Crack path of u-notched parts under tension.....	81
Figure 6.14 Contour plot of failure stress vs. ts and θP for U-notches under tension.....	82
Figure 6.15 Contour plot of the ultimate stress vs. θP and rn for U-notches under 3-point bending.....	82
Figure 6.16 Contour plot of ultimate stress vs. θP and rn for U-notches under tension.....	83

Figure 6.17 Contour plot of failure stress vs. t_s and θP for V-notches under 3-point bending	83
Figure 6.18 Microscopic pictures of plain specimens, $t_s=0$ mm	85
Figure 6.19 Microscopic pictures of crack-Like specimens	86
Figure 6.20 Microscopic pictures of U-notches under tension.....	87
Figure 6.21 Distribution of KC for crack-like notched specimens, $t=4$ mm	89
Figure 6.22 CT-20 mm specimens	89
Figure 6.23 Distribution of fracture toughness of CT specimens, $t=20$ mm	90
Figure 6.24 Example of cracking behaviour of CT specimens, $t=20$ mm and $t=30$ mm	90
Figure 6.25 CT-30 mm specimens	90
Figure 6.26 CT specimens test with a thickness of 30 mm and θP equals 45°	91
Figure 6.27 Stress convergence in FE modelling	92
Figure 6.28 Estimating (L) value for solid AM PLA	94
Figure 6.29 PM strength prediction error for notched solid AM PLA	94
Figure 6.30 Area method strength prediction error for notched solid AM PLA	95
Figure 7.1 Measurements of Void's dimensions.....	98
Figure 7.2 Examples of fictitious stress vs. strain for plain porous PLA specimens: a) with 30% infill; b) with 50% infill; and c) with 70% infill.	100
Figure 7.3 Crack propagation in plain porous PLA, a) $\theta p=30^\circ$; b) $\theta p = 45^\circ$	100
Figure 7.4 The relationship of the infill ratio of PLA parts with: a) Elastic modulus, b) Failure stress , and c) Proof yield stress,	101
Figure 7.5 Selection of load vs. displacement curves displayed by notched porous AM PLA samples	104
Figure 7.6 Crack pattern for notched samples	104
Figure 7.7 Facticitious stress vs in-fill density for notched specimens	105
Figure 7.8 The transformation process to estimate the static strength of the plain porous AM PLA parts	108
Figure 7.9 Accuracy of the proposed methodology in modelling static strength of plain porous AM PLA: a) PM, b) LM	111

Figure 7.10 The notched AM PLA samples with manufactured voids, dimensions are in mm	112
Figure 7.11 Notched porous AM PLA components with the suggested process zone and fictitious linear elastic stress	114
Figure 7.12 The accuracy of the proposed approach in evaluating the static strength of notched porous AM PLA, A) PM for U-notched samples, B) LM for U-notched samples, C) Area method for U-notched samples, D) PM for V-notched samples, E) LM for V-notched samples, and F) Area method for V-notched samples.	118
Figure A.1.1 Plain specimens with t_s equal 0 mm.....	132
Figure A.1.2 Plain specimens with t_s equal to 0.4 mm.....	133
Figure A.1.3 plain specimens with t_s equal to 0.8 mm	133
Figure A.1.4 U-notched specimens under tension (a) Sharp notches (b) Medium notches (c) Blunt notches.....	135
Figure A.1.5 Open notched specimens tested under tension (a) Sharp notches ..	136
Figure A.1.6 U-notched specimens tested under 3-point bending (a) Sharp notches (b) Medium notches (c) Blunt notches.....	138
Figure A.1.7 Open-notched specimens tested under 3-point bending, (a) Sharp notches (b) Medium notches (c) Blunt notches	139
Figure A.1.8 Crack-like notched specimens with microscopic picture for the crack tip, (a) $t_s = 0.4$ mm, (b) $t_s = 0.8$ mm	140
Figure A.3.1 Stress vs. strain curves for plain specimens, $t_s = (0, 0.4, 0.8)$ mm...	147
Figure A.3.2 Force vs. displacement for U-notched specimens under tension.....	148
Figure A.3.3 Force vs. displacement for V-notched specimens under tension.....	150
Figure A.3.4 Force vs. displacement for U-Notched specimens under 3-point bending	151
Figure A.3.5 Force vs. displacement for V-notched specimens under 3-point bending	152
Figure A.3.6 Load vs. displacement for crack-like notched specimens, $t_s = (0, 0.4, 0.8)$ mm	154
Figure A.3.7 Evaluating PQ for CT-20 mm specimens	156

Figure A.3.8 Evaluating PQ for CT-30 mm specimens	156
Figure A.4.1 Plain specimens, $t_s=0.4$ mm.....	157
Figure A.4.2 Plain specimens, $t_s=0.8$ mm.....	158
Figure A.4.3 Open notches under tension.....	159
Figure A.4.4 U-notches under 3-point bending.....	159
Figure A.4.5 Open notches under 3-point bending.....	160
Figure A.5.1 Test scheme of U-notches under tension	163
Figure A.5.2 Test scheme of open notches under tension	166
Figure A.5.3 Test scheme of U-notches under 3-point bending	169
Figure A.5.4 Test scheme of V-notches under 3- point bending	172
Figure B.1.1 Plain porous specimens with 0° deposit angle.....	177
Figure B.1.2 Plain porous specimens with 30° deposit angle.....	178
Figure B.1.3 Plain porous specimens with 45° deposit angle.....	178
Figure B.1.4 Notched PLA samples manufactured with different infill levels, a) U-notches, $\theta_P=0^\circ$, b) U-notches, $\theta_P=45^\circ$, c) V-notches, $\theta_P=0^\circ$, d) V-notches, $\theta_P=30^\circ$, e) V-notches, $\theta_P=45^\circ$	180
Figure B.3.1 Fictitious stress vs. strain for plain porous PLA samples	191
Figure B.3.2 Load vs displacement for U-notched porous samples	195
Figure B.3.3 Load vs displacement for V-notched porous samples.....	198
Figure B.4.1 Microscopic images for plain porous samples.....	203

List of tables

Table 5. 1 PLA and 3D printing specification.....	50
Table 5.2 The test matrix of solid AM PLA specimens	52
Table 5.3 The test matrix of porous AM PLA specimens.....	52
Table 6.1 Results of solid plain specimens under tension.....	73
Table 6.2 Results of U-notched specimens under tension	76
Table 7.1 An example for the measurements of the voids' dimensions	98
Table 7.2 The dimension and test results for plain porous specimens	99
Table 7. 3 The test results for the U-notched porous PLA samples	103
Table A.2.1 Results of open notched specimens under tension.....	141
Table A.2.2 Results of U-notched specimens under 3-point bending.....	142
Table A.2.3 Results of V-notched specimens under 3-point bending	143
Table A.2.4 Results of crack-like notched specimens under tension	144
Table A.2.5 Plane strain fracture toughness, t=20 mm and t=30 mm	145
Table A.6.1 PM prediction for U-notches under tension	173
Table A.6.2 PM prediction for V-notches under tension	173
Table A.6.3 AM prediction for U-notches under tension	174
Table A.6.4 AM prediction for V-notches under tension	174
Table A.6.5 AM prediction for U-notches under 3-point bending.....	175
Table A.6.6 AM prediction for V-notches under 3-point bending	175
Table A.6.7 PM prediction for U-notches under 3-point bending.....	176
Table A.6.8 PM prediction for V-notches under 3-point bending	176
Table B.2.1 Results of plain porous PLA samples with $\theta_p= 30^\circ$	181
Table B.2.2 Results of plain porous PLA samples with $\theta_p= 45^\circ$	182

Table B.2.3 Results of U-notched PLA porous samples with $\theta_p = 30^\circ$	183
Table B.2.4 Results of U-notched porous PLA samples with $\theta_p = 45^\circ$	184
Table B.2.5 Results of V-notched porous PLA samples with $\theta_p = 0^\circ$	185
Table B.2.6 Results of V-notched porous PLA samples with $\theta_p = 30^\circ$	186
Table B.2.7 Results of V-notched porous PLA samples with $\theta_p = 45^\circ$	187
Table B.5.1 Strength prediction for plain porous samples, $\theta_p = 0^\circ$	204
Table B.5.2 Strength prediction for plain porous samples, $\theta_p = 30^\circ$	204
Table B.5.3 Strength prediction for plain porous samples, $\theta_p = 45^\circ$	205
Table B.5.4 Strength prediction for U-notched porous samples, $\theta_p = 0^\circ$	205
Table B.5.5 Strength prediction for U-notched porous samples, $\theta_p = 30^\circ$	206
Table B.5.6 Strength prediction for U-notched porous samples, $\theta_p = 45^\circ$	206
Table B.5.7 Strength prediction for V-notched porous samples, $\theta_p = 0^\circ$	207
Table B.5.8 Strength prediction for V-notched porous samples, $\theta_p = 30^\circ$	207
Table B.5.9 Strength prediction for V-notched porous samples, $\theta_p = 45^\circ$	208

Chapter 1-Introduction

1.1 Background

1.1.1 3D printing technology

3D printing is a powerful manufacturing technique which can be used to fabricate a variety of engineering products with a wide range of applications. Nowadays, it is considered to be the fastest improving sector of technology, science and art, with potential uses that are still being explored and extended. The technology involves converting a virtual model, produced by a 3D software, into a physical component. It has come to the foreground due to its low manufacturing costs and high production speed[1].

Additive manufacturing (AM) is one emerging popular 3D printing technique that fabricates objects in a layer by layer manner from a computer-aided design (CAD) model. The ability to produce customised products for the individual has already been demonstrated in several sectors (including the medical, aerospace and automotive industries). In this method, the component is constructed by melting a filament of material through a heated nozzle and filling it on a platform to the requested shape. Fused deposition modelling, FDM is one of the most common techniques in the field of 3D printed manufacturing. It is considered to be an extremely efficient technique that can produce complicated geometries precisely and quickly[2].

Thermoplastics are the traditional materials that have been used in this kind of 3D printing. In this respect, Polylactic acid (PLA) is a common polymer used in FDM industry, with advantages of low thermal expansion and thus less warping during the printing process[3]. It is worth pointing out that several fabrication parameters affect the final mechanical properties of the product, such as deposition angle, layer thickness, printing orientation and shell perimeter thickness. Despite the limited mechanical properties of PLA material, the parts produced by FDM printer using this material can be as strong functionally as those produced by injection moulding, at least in tensile applications. Moreover, it is highly recommended to maintain good mechanical properties for printed PLA parts used in several applications. Another advantage of PLA is that it is both biodegradable and non-toxic, which means that it can be used in medical applications. For example, it is preferable over the metal bone fixations, since it is able to provide sufficient fixing strength during the healing period, without the need to conduct a second operation to remove the implant [4]. In addition, AM PLA components with low infill density are used as scaffolds or grafts inside the human body for bone regeneration [5]. Furthermore, using the AM technique to produce prostheses and orthoses represents another practical application for PLA polymer in the medical field[6].

Additionally, the use of PLA objects, produced by the AM method in aerospace applications, such as manufacturing the structural components of unmanned aerial vehicles, has demonstrated the ability of these components to undergo flexural loads as well [7].

1.1.2 Fracture mechanics and TCD

One of the most crucial improvements in the field of mechanics has been the science of fracture mechanics, which characterises the behaviour of cracked components under different kinds of loading. The prediction of crack propagation using linear elastic stress analysis, under known specific conditions, has led to the discipline of linear elastic fracture mechanics (LEFM) [8]. Three parameters are linked by applying fracture mechanics equations: the existing stress, the fracture toughness of the material, and the crack length [9].

In a situation where there is a non-linear plastic zone in a component, but this is small with regards to the overall component dimensions, LEFM postulates that the stress field in the plastic zone and any subsequent failure of the material under loading are characterised by the behaviour of the linear zone. In order to utilise the LEFM approach successfully, the length of the crack should be sufficiently large compared to the non-linear region. Most brittle materials, such as ceramic and glass, show a linear elastic response under loading and maintain this behaviour until failure, in some conditions. The rapid crack propagation which causes brittle failure may start from a stress riser, like a notch, or defects in the material. Geometrical discontinuities like corners, holes, grooves and bends are also associated with the concentration of stress and are a reason for mechanical fracture in materials[8].

Notches are used by researchers to study the concentration of stress since they are simple to make, test and theoretically analyse to predict the strength of engineering components which may have complex geometrical irregularities [8]. Some notches, with low values of stress concentration, fail like a plain specimen with (σ_{ult}) near the - notch root. Notched components with a higher stress concentration and small root radius, meanwhile, fail like sharp cracks, where k equals K_{IC} . In general, however, the use of notched specimens represents an intermediate case between sharply cracked specimens and plain specimens.

Owing to the limitation on the use of LEFM to materials with large crack before failure with root radius $\rho = 0$, and it doesn't work with notched components with $\rho > 0$, the theory of critical distance (TCD) was suggested to predict the failure strength of all types of geometric irregularities like defects, joints, and notches involving both plain components and those which have sharp cracks. The TCD is considered as a modification of LEFM, taking account of a characteristic material length[8].

Due to the tendency of brittle notched components subjected to a static load to fail suddenly and rapidly, assessing the strength of these components has gained increasing interest in the last decades. TCD is a collection of methods that have been used to evaluate the strength of brittle notched components by utilising a critical

distance from the apex of the stress riser, in the direction perpendicular to the applied load, denoted as L .

The TCD postulates that the material should be linear elastic, where a brittle fracture mechanism is dominant and there is little or no plastic deformation before failure. To evaluate the strength of notched components, TCD utilises not only the finite element analysis FEA, to estimate the linear elastic stress field near the notch's root, but the analytical solution as well. The recent improved availability of FE modelling programs has meant that the use of FE models to apply TCD in linear elastic contexts has become much easier and more practical in a wide range of applications[8].

TCD originated in Neuber's[10] and Peterson's[11] work to evaluate the fatigue-related failure of notched metallic materials. Their contribution was improved in 1958 when the concept of the critical distance was introduced as a way to assess the fatigue of metals [12][13]. Neuber innovated a method similar to what is now called the line method by taking the effective stress as the average stress in front of a notch's root over a distance equal to the structural particle's length, which is known now as $2L$. While evaluating the fatigue fracture of steel, he noticed that the critical distance was likely to be related to the inverse of the ultimate tensile strength of the material. Peterson suggested taking the effective stress at a specific point within a critical distance from the notch tip, which is like what is called now the Point Method (PM).

In 1957, Irwin [14], established the fundamentals of Linear Elastic Fracture Mechanics by defining the concepts of the rate of energy release and stress intensity parameter. He showed that the stress around a sharp crack apex could be evaluated mathematically by using these parameters. On the other hand, Novozhilov and McClintock [15][16], assessed the fracture strength of carbon nanotubes by utilising LM and PM methods and using the spacing between atoms as the critical distance.

Whitney and Nuismer[17], in 1974, estimated the influence of notch length and the size of circular holes on the strength of composite laminates by improved methods similar to LM and PM (then known as average stress and point stress methods). Taylor[8], concluded a final definition of the TCD on the basis that this refers to a collection of methods that all use a specific critical distance with the analysis achieved by the linear elastic approach.

Compared to other strategies, TCD is considered to be a highly precise and reliable tool for predicting the static strength of brittle notched materials, with a variety of root radii and opening angles [18]. By contrast, the application of linear elastic fracture mechanics LEFM, is limited to cracks and notches with zero opening angles and root radii [19]. The benefits of TCD over other approaches are its simplicity and the limited mechanical properties that are needed. It is well established that TCD is a modulation of LEFM with the micro-mechanistic inclusion by the existence of length parameter (L). The point method and line method are the simplest methods among the four strategies used in applying TCD, which will be mentioned later. [18].

The key advantage of the TCD is that it does not require complex non-linear constitutive models[20] [21] [22], with this holding true independently of the level of ductility characterising the material being assessed [23] [24]. Further, since the TCD takes the morphology of the assessed material directly into account via suitable length

scale parameters, it is capable of accurate estimates regardless of the shape and sharpness of the geometrical features being designed [23][25], Lastly, by its nature, the TCD can be applied by making direct use of linear - elastic stress fields determined numerically via commercial FE software packages.

Based on the discussion above and by reviewing the literature work, it can be seen that the fracture strength of notched polymer parts produced by 3D printing technology, has never been studied, especially notched polymer objects printed with variable infill level. Accordingly, this work selected the FDM printing technique to manufacture PLA notched components and to investigate the fracture behaviour and the static strength of the 3D printed product under tensile and bending load, with different types of notches and in-fill density, by using TCD approach.

1.2 Scope of research

The main focus of this study is to investigate the fracture behaviour of additive-manufactured PLA notched components under different printing parameters with notches of various geometries and root radii. Then, verifying the TCD approach in evaluating the static strength of AM PLA notched parts manufactured with different notches sharpness and load configuration. The scope of this research can be summarised as follows:

- a) Evaluation of the tensile strength of plain AM PLA specimens (manufactured with 100% infill level) with different manufacturing parameters.
- b) Characterisation of the stress intensity factor of cracked AM PLA specimens.
- c) Evaluation of the fracture strength of notched AM PLA specimens with different sharpness and deposition angles, under tension.
- d) Estimation of the static strength of AM PLA notched components under 3-point bending with different sharpness, deposition angles and notch's geometries.
- e) Estimation of the static tensile strength of plain AM PLA specimens with different infill levels and deposition angles.
- f) Evaluation of the static strength of AM PLA notched specimens with different infill levels, notches' geometries and deposition angles, under tension.
- g) Evaluation of the stress field near the notch apex using FE modelling for the tested specimens.
- h) Verifying the TCD approach for the tested specimens based on FEM and experimental results.

1.3 Aim and Objectives

AM PLA polymer parts have a lot of practical applications, especially when manufactured with complex geometries resulting in high-stress concentration under loading. Evaluating the strength of these parts under different types of loading is important to have effective functional employment of these components. This work is set out to investigate an efficient methodology suitable for evaluating the static strength of notched AM PLA parts with different levels of stress concentration, manufactured with variable infill levels and under different types of loading. The detailed objectives of this work can be summarised as follows:

1. Understanding the fracture behaviour of AM PLA components, manufactured with 100% infill level, specifically:
 - a) Investigating the effect of the deposition angle θ_p , on the tensile strength of plain specimens.
 - b) Studying the effect of the θ_p on crack initiation and propagation in plain specimens under tension.
 - c) Exploring the relationship between the shell thickness and the ultimate strength of plain specimens under tension.
 - d) Examining the effect of the θ_p on the stress intensity factor for cracked components by testing crack-like notched specimens under tensile loading.
 - e) Estimating the effect of the θ_p on the plane strain fracture toughness of AM PLA components by conducting the CT test according to ASTM D5045-14.
 - f) Estimating the flexural strength of single notched AM PLA parts, manufactured with two kinds of notches and different root radii, by testing them under three-point bending.

2. Utilising the TCD approach to predict the static strength of AM PLA notched components under tension and 3-point loading with the following variables:
 - a) The deposition angle θ_p .
 - b) The type of notch.
 - c) The root radius of the notch.

3. Evaluating the static strength of additively manufactured porous PLA components with different infill levels under tension by using the TCD approach:
 - a) Predicting the static strength of plain porous AM PLA components.
 - b) Estimating the static strength of notched porous AM PLA components with different types of notches' kinds and root radii.
4. Utilising 2D finite element model by using ANSYS software for all AM PLA notched samples to evaluate the linear elastic stress field requested for TCD validation.

1.4 Structure of the Thesis

The work of this thesis is presented in eight main chapters in addition to two appendixes. Each chapter will be concluded in the following:

- The first current chapter has presented the 3D printing technology and the benefits of using PLA material in producing components by additive manufacturing. Also, the historical background for the formulation of the theory of critical distance TCD and its preferable features over other methods used in estimating the strength of objects with different stress risers, have been discussed. Finally, the objectives and outlines of the research have been set.
- Chapter (2): Presents the 3D printing manufacturing methods and their applications. Moreover, The composition and the microstructure of PLA material will be discussed in this chapter in addition to the previous studies which have been implemented on the 3D printed PLA components
- Chapter (3): Shows the fracture behaviour of anisotropic materials, which are considered to be analogous to AM PLA's likely behaviour, namely wood and fiber-reinforced composites.
- Chapter (4): Discusses the fracture mechanics criteria and the evaluation of the stress intensity factor for different kinds of cracks, in addition to the derivation of different TCD methods, the literature work on TCD application to polymeric materials and comparing this theory with other fracture theories.
- Chapter (5): discusses the manufacturing method of the AM PLA parts and the test procedure for plain and notched specimens under tension and bending.

-
- Chapter (6): Discusses the experimental results of the specimen's fabricated with 100% infill level and the TCD verification for these specimens.
 - Chapter (7): Discusses the result of PLA components manufactured with less than 100% infill levels and the strength prediction by using the proposed equivalent homogenised material approach.
 - Chapter (8): Presents comprehensive discussion and conclusions about the results obtained by this research and the validity of the TCD methods in predicting the static strength of AM PLA. In addition, The recommendations of the future work related to this research, is declared in this chapter.
 - Appendix A: Shows the pictures, tables and curves for the experimental tests of the samples manufactured with 100% infill level.
 - Appendix B: Includes the pictures, curves and tables of the PLA specimens manufactured with lower than 100% infill level.

Chapter 2-3D printing review

2.1 Introduction

Additive manufacturing AM, which is also known as Three-Dimensional Printing (3D Printing), is a flexible technology that has been used to produce a wide range of products from different materials, including plastics, concretes, metals and ceramics[26]. AM is a technique in which an object is formed by successive layers of manufacturing. This technique allows functional products with complex geometries to be manufactured very easily and cost-effectively, even when conventional manufacturing processes are not effective [27][28].

First, virtual models are made using specific software packages (such as AutoCAD or Solid Work). Second, a software program is used to convert the model into information that the 3D printing machine can understand. Finally, the program slices the model into thin layers, and the printer receives these sections and combines them as layers to achieve the final physical product[29]. Some AM systems make direct use of digital CAD data to produce polymer parts of the highest quality [28].

AM is particularly important in fields where traditional manufacturing reaches its limits, but the compatibility of 3D printing with modern industry has made this technology more prominent in all industrial fields in recent years. It has the potential to change the way we develop, produce, market and distribute all sorts of products and, in time, to become a replacement for most of the available manufacturing methods[30].

Some companies are working on the development of new 3D printers capable of working up to 500 times quicker and with products ten times bigger than the latest 3D printers. Their plan is to support the industrial manufacture of product needs for applications in robotics, automotive, aerospace, medical, and other applications, utilising cheap and fast manufacturing polymer components[27].

Polymers, with different phases, are increasingly important materials with a range of applications and are suitable for the advanced and robust fabrication of more complex 3D Printed geometries [31]. This research has used Poly lactic acid (PLA), a common polymer in this industry, as its main material.

2.2 Cost comparison of AM vs injection moulding parts

Comparing the AM metal parts with objects produced by conventional manufacturing, the former technique offers lower upfront expense and lower non-recurrent engineering fees. In addition, the injection moulding (IM) is not the most effective method in some manufacturing circumstances [32]. Nowadays, the selective laser sintering SLS, one of the AM techniques, is considered as a competitive manufacturing method comparing to injection moulding process in terms of cost and repeatability, especially in the range of low and medium production volumes. The AM polymer is

more cost-effective than the IM part due to less tooling cost and time. It has been shown that the IM method needs very high production volume to cover the cost of the mould. While AM parts have the same price per part regardless of the production volume [33].

2.3 3D Printed polymer

Acrylonitrile butadiene styrene (ABS) and poly lactide (PLA) are the most common polymers in 3DP technology and are compatible with all printers. Other engineering polymers, like polyamide, polyphenyl sulfone and polycarbonate, require higher-grade printers [31]. PLA is an absorbable and biocompatible polymeric substance, widely used in medical engineering, architectural modelling and numerous other fields. While 3D printing machines use the preformed polymer materials in powder, filament and sheet form, other additive manufacturing processes utilise the active polymerisation of photosensitive resins. Photo curing is particularly attractive as a methodology for 3D printing for several reasons: high levels of build resolution, smooth part surfaces that do not typically require finishing processes, good z-axis strength due to chemical bonding between layers, and the ability to print clear objects and to build products quickly [29].

2.4 Examples of AM techniques using polymer

AM incorporates about 18 different kinds of processing, which can be categorised according to the physical state of the printed matter (i.e. liquid, solid and powder-based processes), or by the method used to fuse materials at a molecular level (thermal, ultraviolet UV-light, laser, or electron beam) [34]. In the following are some of these methods:

(a) Stereo lithography apparatus (SLA)

This method uses laser technology to cure photopolymer materials layer-by-layer (since the polymer is vulnerable to change in its properties due to light exposure). The process is accomplished in a pool of resin. A directed laser beam treats the resin in the pool by tracing the pattern of the model in successive layers. The platform is lowered by the thickness of each layer during every construction cycle until the completion of the model.

(b) Selective laser sintering (SLS)

Unlike the SLA technique, this method employs a semi-crystalline thermoplastic polymer to build the model, fusing the particles of metals, plastic, glass or ceramic with

a high-power laser. The process is supplied with unsintered materials and no supporting substance (as in SLA) is required [35].

(c) Laminated manufacturing object (LMO)

A variety of materials in the foils form is used with successive layer's addition process to implement the final model with this technique. A locative patterning is achieved by laser or blade cutting through every laminated layer [26].

(d) Selective Heat Sintering (SHS)

Instead of a laser head, SHS uses a thermal head to melt the thermoplastic powder surface into the layered object but otherwise follows the same approach as the SLS method [26].

(e) Multi-Jet Modelling (MJM)

This method uses hundreds of jets, incorporated in one head, to add successive thermo-polymer layers in a process that is an analogue to inkjet printing. The head can move in three directions (x, y and z) to extrude the moulded materials on every layer [35].

(f) Fused Deposit Modelling FDM / (FFF)

The FDM technique was invented in 1990 as a new method for using polymer within an AM process. In this method, melt extrusion is applied through a small nozzle to a platform after preheating the filament [26]. This technique has been adopted in this research due to its availability and because it is a straightforward process. FDM is considered to be one of the most convenient techniques for 3D printing, regardless of technical features, due to its simple approach (melting- deposition- solidification). By using multiple platforms and extruders, several studies have tried to compare the mechanical properties, filling speed, roughness and material costs [36].

Melting and extruding standard polymer through a nozzle is recognised as a simple manufacturing method. The movement of the nozzle is controlled in three directions to apply the melted material in layered form. The temperature should be maintained above the melting point of the material during the process and pre-heating of the platform can control the shrinkage of the product [36].

FDM products are affected by various parameters during the fabrication process, such as the thickness of the layers, filling speed, nozzle size, filament spacing, filling angle, and filling pattern [37]. In addition, the designer should know their material properties to take the full advantage of the available technology.

(g) Big area additive manufacturing (BAAM)

This method can produce large-scale models using ABS thermoplastic with a percentage of carbon fibres. The printer uses the FDM technique but across a larger building space of 20 x 8 x 6 ft. The deposition nozzle size is well above the filament diameter. Recently, a Chinese company manufactured one of the largest 3D printers which used concrete as deposition material. The building volume of this printer is (40 x 10 x 6.7) m. They intend to use this technique to print furniture, houses and five-story buildings [38].

2.5 PLA material

2.5.1 Composition of PLA

In 1932 Carothers [39] was the first to produce PLA (poly lactic acid or poly lactide). The molecular weight of his produced PLA was very low, and he noticed that this affected all the thermal and mechanical properties, in addition to crystallisation. Recently, several methods have been used to produce PLA with higher molecular weights, such as ring-opening and poly-condensation polymerisation, in addition to enzymatic and zeotropic dehydration. PLA with high molecular weight is a linear thermoplastic aliphatic polyester, made from industrial fermentation of plant resources, like sugarcane, potatoes, tapioca roots, chips, or corn-starch, in addition to chemical synthesis. The chemical symbol of PLA polymer is $(C_3H_4O_2)_n$.

PLA has the potential to supersede the use of polymers extracted from petroleum resources since it has been mass-produced commercially for various industries [40]. In addition, PLA is considered to be a highly significant plastic material owing to its good mechanical features, biocompatibility and degradation ability. Understanding how to control the manufacture of PLA so as to be able to produce materials with various properties and microstructures is therefore important to ensure that its potential is maximised across a full range of different industrial needs and applications [41].

Crystallisation is the ordered arrangement of molecules during the formation. It is well established that crystallisation is an important parameter in polymer structure since higher crystallinity is related to greater strength and stiffness; as yet, however, no polymer is available that is fully crystalline. Thus, to get the best material properties, semi-crystalline polymers are preferable to amorphous ones [42]. Within polymers, macromolecules are structures of molecules repeated in chain form and bonded together by covalent bonding. In semi-crystalline polymers, these macromolecules are partly organised, while in amorphous polymers the chains remain twisted and disorganised. The repeated units in the semi-crystalline polymers warp in a condense zone called crystallites, which give the polymer high strength and stiffness by acting as crosslinks. After a specific temperature called T_g (glass transition temperature), the polymer behaves as flexible material due to the deformation in the valence bonds. T_g plays a vital role in studying the material's properties [41].

Overall, PLA has many good features like being biocompatible, easy to produce, and good mechanical properties, making it a preferable choice in medical and pharmaceutical applications. Four PLA dimers are available; D-PLA, L-PLA, DL-PLA meso-PLA. L-PLA is considered a convenient semi-crystalline material with high toughness and strength [41].

2.5.2 Physical and mechanical properties

It is noticeable that polymers' molecular weight has a significant influence on the crystallisation process and mechanical properties, although it does not affect thermal characteristics. Crystallinity, in turn, controls several properties of the polymer such as tensile strength, hardness, melting point, creasing and stiffness. The glass transition temperature T_g is another important factor, which specifies the physical properties such as density heat capacity, as well as mechanical properties. This factor is particularly essential for amorphous PLA due to the drastic changes which take place in the main polymer chains after this temperature T_g . It is noteworthy that all polymer characteristics are taken in room temperature, in standard conditions, and they reduce dramatically at higher temperatures, especially after T_g [43][56].

The mechanical properties of PLA vary widely, from elastic and soft plastic to high strength and stiff materials. The approximate values for semi-crystalline PLA are: tensile strength = 50 to 70 MPa, flexural strength = 100 MPa, flexural modulus = 5 GPa and elongation = 4%.

Park [43][56] investigated the effect of crystallinity on the fracture toughness K_c of amorphous and crystalline PLA plates. Mode I loading tests were implemented on components with single-edge notched bending, (SENB). A quasi-static loading rate was used to calculate the K_c , and differential scanning calorimetry DSC, to evaluate the crystallinity X_c . The general trend showed that K_c decreases with higher crystallinity. This occurs due to the reduction in the crazing process with higher crystallinity.

The yield strength σ_y of polymers is taken to occur at the point of zero inclination of their stress-strain curve, or at the point at which nonlinearity starts to be evident, if the peak of the curve is not clear, usually at a strain of 1%. The compression strength of polymer is always about 20% higher than the tensile strength[44].

Zane [45] compared the strength of both thermally treated and normally cast PLA films. The former showed lower strength and greater liability. The modulus of elasticity for the treated film was less by three times and the elongation was 30 times more than cast PLA films.

The modulus of elasticity for PLA materials can be computed from three-point loading tests. A central load is applied to the simply supported specimen, and the load-deflection curve is constructed. The following equation calculates Young modulus:

$$E = \frac{KL^3}{4bd^3} \quad (4.1)$$

Where K , is the slope of the straight part of the curve, L is the spacing between supports, d is the thickness and b is the width of the sample. [46].

2.5.3 Disadvantages of PLA

1. The extruded PLA materials have low crystallinity, even though some PLA grades are semi-crystalline. In addition, the distortion of PLA materials by heat is very limited due to the low temperature of glass transition (60 °C).
2. It is hard to modify the surface of PLA products because the main chain groups are chemically inactive [40].
3. The low gas prevention and high brittleness of PLA products restrict their use.
4. PLA polymers are chemically unstable and degrade easily which may sometimes lead to unexpected performance [59].

2.5.4 Fracture behaviour of PLA

It is generally noticed that the strength of polymer is in inverse correlation to the crystallinity percentage. That is because the local stress concentrates higher levels of stress on the crystallites than the overall applied stress. In addition, due to the passive effect of crystallites on the shear yielding and crazing, the material fails with lower stress than expected. Crystallinity also has a negative influence on impact strength. The thermal and mechanical handling can control the shape and size of spherulites, which affects the temperature that is needed to transform the material from a brittle to a ductile state [47]. It is well established that, at low temperatures, polymer materials behave as a brittle material before fracture and that they present some plastic deformation at the process zone. The behaviour of polymers under loading is different from other materials and considered as a complex behaviour[48] [87]. In addition, polymer fracture behaviour is very sensitive to ambient temperature and loading rate. Whilst increasing the loading rate encourages brittle behaviour, a rise in temperature will suppress brittleness. Compared to other materials, polymers have lower fracture toughness and strength, and because of non-linear deformations, blunt notches and small cracks will not affect the component strength[48].

It is believed that crazing plays a paramount role in increasing the strength of polymeric materials. This mechanism starts in components with notches, voids or other non-homogeneities that behave as stress raisers for the local stress or hydrostatic tension. Craze is formed by micro voids collecting together to develop a crack with small ligaments across its face, which requires high stress to grow into an ordinary crack. A region of plastic microscopic deformation created by the merging of micro-voids and

severely drawn microfibrils in small size of the material. The molecular weight is a guide to the tufts (micro-fibrils) length, which is usually a portion of one μm . Micro-cracks are formed by the coherence of micro-voids produced from stretching tufts when regional stress surpasses the critical stress. Consuming the dominant portion of fracture energy, the crazing mechanism is considered to be the trigger for brittle failure at the microscopic level in several kinds of brittle polymers. In addition to crazing and shear yielding, fracture mechanisms in polymer include de-bonding and cavitation processes[47].

2.5.5 3D printed PLA

The most common plastic materials used in 3D printing-based manufacturing are PLA (Polylactic acid) and ABS (Acrylonitrile butadiene styrene). These are thermoplastic materials that are mouldable in the sense that they soften upon heating and become solid again after cooling. This ability, alongside other features, making them convenient materials in the 3D printing industry, which requires materials with three primary characteristics: the ability to melt into a filament, the ability to bond during the printing process and suitable material properties for the products' end-use [46].

PLA displays less warping than other plastic materials, meaning that it can be printed without using a heated bed. Strong bonding between layers is produced by increasing the flow of melted material, and this gives the resulting product higher strength. PLA also has a high 3D printing speed with low layers' height, meaning that components can be produced with sharp edges. Furthermore, PLA products are considered to have a less environmental impact than other plastic waste [46]. For all these reasons, this work aims to support the use of PLA in the field of load-bearing and mechanical application by using the TCD method to evaluate its fracture behaviour and material strength.

It is well known that several factors affect the PLA parts produced by additive manufacturing, AM, such as layer thickness, infill percentage, nozzle size, filling pattern, filling speed, movement speed and filling temperature. AM products have shown that extruding temperature influences the degree of crystallinity, which affects the material strength. Matter [49], studied three parameters and their influence on PLA properties, produced by Fused Deposition Modelling (FDM): infill percentage, layer thickness and filling pattern. His work tried to find the optimal combination of parameters for the mentioned factors. Although increasing the infill percentage increased the strength, the trend was not linear. He noticed that the ultimate strength increased with layer thickness up to 0.2 millimetres but that with thicknesses above 0.2 mm the strength remained approximately stable. Moreover, filling in the z-direction (vertical direction) gave less strength by about 30% than other directions, with linear filling showing higher strength by 10% than 45° infill [50].

Wittbrodt [51], using FDM according to ASTM F2792-12a, showed that the crystallinity of coloured PLA materials was higher than the natural material (without colour) and PLA with a white colour resulted in five times more crystallinity than with the natural colour. By drawing a temperature-crystallinity curve, he found that there is a critical

extruding temperature which gives higher crystallinity. Another effect of printing temperature is the porosity of the completed product. The scanning electron microscopy images showed 10.8% of the material was made up of triangular gaps between the fused layers when the printing was done at 190 °c, but this could be reduced to 3% with a filling temperature of 210 °c. Thus, the filling temperature significantly influenced the yield strength for PLA printed products. He suggested that there should be an ideal processing temperature for every material.

Rodríguez [52] showed that fused deposited materials are highly affected by manufacturing parameters that influence the meso-structure (properties at the fibre scale) and the bond strength between adjacent fibres. Other processing parameters were considered, such as the gap between fibres (g), fibre width (w) and skewed or aligned translation.

Caterina [3] used the AM technique to fabricate PLA and ABS polymer components, with different deposition angles ranging between 0°, 45° and 90°. The result of specimens with raster angles of 0° and 45°, showed some plastic behaviour, while 90° raster samples acted as a brittle material. In addition, the bond strength of PLA beads was higher than ABS samples.

Lanzotti [53] studied the effect of three manufacturing parameters (layer thickness, raster angle and shell perimeter thickness) on PLA samples fabricated with mono-directional deposition using the AM technique. Increasing the layer thickness showed less influence in terms of increasing the strength than decreasing the raster angles. Moreover, a higher thickness of the shell and a raster angle of 0° showed perfect brittle behaviour, while moving to a 90° deposition angle and a lower shell thickness presented ductile material behaviour. The strength of AM PLA parts was increased with the shell thickness. While the layer thickness showed unclear influence on the material strength. On the other hand, increasing the raster angle presented negative effect on the elastic modulus and the ultimate strength of PLA parts.

Chacón [54] verified the influence of three printing parameters on strength properties of AM PLA components with three kinds of deposit orientation. The best mechanical properties were shown by samples with on-edge and flat orientations, with ductile behaviour. Upright specimens, meanwhile, showed brittle behaviour. Lastly, higher flexural and tensile strength is presented by increasing the layer thickness.

Letcher [55] found that a raster angle of 45° gives optimal mechanical properties when testing AM PLA specimens, with different deposition angles under tension and flexural loading.

The influence of plate temperature and layer thickness on the impact strength of AM PLA parts was examined by Wang [56]. Optical microscopy showed higher crystallinity for samples manufactured with a printing plate temperature of 160° C and a layer thickness of 0.2 mm. In addition, this printing temperature gave PLA parts with an impact factor 114% higher than components fabricated using traditional injection moulding.

Finally, The 3D printing manufacturing of PLA parts can be a replacement of the conventional fabrication due to the same fracture toughness and mechanical properties obtained from AM PLA comparing to the injection moulded parts [57].

2.6 Applications

3D printing technology has a lot of applications within the medical, dental, automotive, sports equipment, architecture, and aerospace fields. Owing to the biodegradable feature of PLA material, several applications for 3D printing PLA components have been adopted in the medical field such as bone implant and repairing, surgery, tissue engineering and organs printing[38].

PLA scaffolds produced by AM are widely used for repairing bones since AM is able to fabricate structures with precise dimensions and is easily controlled. In particular, AM can produce a lattice structure which is useful in reducing the weight and the quantity of material used in any application while maintaining its strength[5].

Another medical application for the AM technique is the fabrication of orthoses, or braces, for the ankle-foot to support patients with biomechanical deficiencies in their feet. The AM-produced braces are considered more practical and comfortable than pre-fabricated braces [58]. AM produced PLA screws are also commonly used for fixation of broken bones.

In addition, a lot of laboratory equipment in the medical field which are sophisticated high-quality devices, produced in small quantities, are manufactured using this technology. AM does not need expensive tools like traditional manufacturing and thus is able to reduce the costs entailed in producing small numbers of high-quality products [28].

Moreover, 3D printing technology has been used in the manufacturing of unmanned aerial vehicle for both commercial and military purposes taking advantage of the method's ability to embed structural elements that can withstand flexural loading and deliver high reliability and survivability [59].

It is worth pointing out that aerospace firms have generally expanded their reliance on 3D printing for future manufacturing strategies. They are using this technology to fabricate turbine and engine components in addition to interior cabin parts [28]. Some companies are working on 3D printing wings of up to 30 metres in length for remote-controlled aircraft. Moreover, AM has been innovated to produce miniaturised components through the Micro Laser-Sintering (MLS) technique. In addition, architecture companies have been able to take advantage of 3D printing to reduce the time needed to produce architectural models by up to 80%, while also achieving models that are more robust and up to 60% lighter than machined products [50]. Finally, NASA launched and operated the first zero-gravity AM printer in 2014 to open a new perspective horizon for this industry in space technology [60].

Chapter 3- Anisotropic materials

3.1 Introduction

The interest of this work, as mentioned in previous chapters, is the plastic components produced by Fused Deposit Modelling (FDM), which have the form of layers of fibres. Since there isn't much literature on the fracture behaviour of AM PLA components, and for the purposes of this literature review, the following sections will examine the work on the fracture behaviour of anisotropic materials that are considered to be analogous to AM PLA's likely behaviour, namely wood and composites.

3.2 Woody materials

Wood is a structural material that is strong, hard and stiff, and with a ratio of strength to weight like steel [61]. Bamboo is an important woody material, which has particularly high strength and toughness comparing to other kinds of wood. The cross-section of the Bamboo shows that it consists of fibres and matrix. Tensile tests have been conducted to evaluate the fracture toughness of bamboo. By studying the fracture behaviour of bamboo specimens under tensile loading, it was noticed that the cracks initiate either in the matrix, as in composite ceramic, or in fibres, as is the case in fibre reinforced plastic [62].

Because of the strong interface between fibres and matrix, failure starts with fibre cracking, which is the nature of fracture in bamboo, accompanied by fibres dropping out on the crack faces. The following formula can be used to calculate the strength of the matrix:

$$\sigma_m \leq \left(\frac{E_m}{E_f} \right) \sigma_f \quad (3.1)$$

Where σ_m is matrix strength, σ_f is fibre strength, E_m and E_f are the moduli of elasticity of matrix and fibre, respectively. The stress-strain curve of the tested specimens showed that fibre breakage occurred after the peak stress, represented by stress drops in the curve. The crack surface of bamboo is like the failure surface of fibre-reinforced materials, with fibres being pulled out from the matrix. The fracture toughness K_{IC} of the bamboo specimens was evaluated by the following:

$$K_{IC} = \sigma \sqrt{\pi a} / F(\xi) \quad (3.2)$$

Where (a) is the crack length, $\xi = (a / w)$, w is specimen width and F (ξ) is the geometry factor which is computed as following:

$$F(\xi) = 1.12 - 0.231 \xi + 10.55 \xi^2 - 21.72 \xi^3 + 30.39 \xi^4 \quad (3.3)$$

Dongsheng [63] studied the uniaxial features of bamboo materials made up of bamboo fibres, bonded at high pressure in a single direction. The bamboo material was considered to be a fibre-reinforced composite with orthogonal properties. It was found that the stress-strain relationship was perfectly linear before brittle failure at the ultimate load. It was noticed that the tensile strength in the direction of the fibers was twice that of the compressive strength, whereas the tensile strength in the direction transverse to the fibers was much lower than the compressive strength [63].

Yanga [64] conducted a failure analysis study of laminated bamboo called Glubam, which is a constructional material with bidirectional fibres. Sheets of Glubam with a 4:1 sheet ratio were subjected to several tensile tests encompassing different angles to the main laminate axis. The angle of loading to the main fibre direction varied from 0 to 90 degrees. It was found that the tensile strength of the tested specimens depended on the loading angle to the main fibre direction. Also, the results showed that the strength in the direction of main fibres (i.e. a loading angle of 0°) was four times that in the transverse direction.

Yanga also noticed that the fibre in the major direction was the most dominant when the loading angle was less than 45°. When the angle was greater than 45°, the secondary fibres played the main role. With the exception of when the loading was at 0°, failure occurred through separation or fracture of fibres in the orthogonal direction. Yanga used the following formulas to calculate the tensile strength for any angle of loading direction:

$$f_{t,\alpha} = \frac{f_{1,t,0} f_{1,t,90}}{f_{1,t,0} \sin^{n_1} \alpha + f_{1,t,90} \cos^{n_2} \alpha} \quad 0 \leq \alpha < \pi/4 \quad (3.4)$$

$$f_{t,\alpha} = \frac{f_{2,t,0} f_{2,t,90}}{f_{2,t,0} \sin^{n_2}(\pi/2 - \alpha) + f_{2,t,90} \cos^{n_2}(\pi/2 - \alpha)} \quad \pi/4 \leq \alpha \leq \pi/2 \quad (3.5)$$

Where $f_{1,t,0}$ and $f_{1,t,90}$ are the tensile strength in the major and minor directions, $f_{2,t,0}$ and $f_{2,t,90}$ are the average tensile stress in the major and minor directions in the secondary fiber layers, while n_1 and n_2 are constants which can be taken from previous work [64].

Vermaa [65] carried out tensile testes for thin laminates composed of bamboo culms bound together using epoxy and cold pressing. This bamboo-composite was comprised of four unidirectional laminate layers. The behaviour of the bamboo

laminates was considered as analogous to a fibrous composite, where the epoxy is assumed to be the matrix and the bamboo fibres the reinforcement. Vermaa proposed a formula for the component strength was:

$$\sigma = \sigma_f V_f + \sigma_m (1 - V_f) \quad (3.6)$$

Where σ_f and σ_m are the strength of fibres and matrix respectively, and V_f is the volume fraction of the fibres. The stress-strain curve of the tested specimens displays a bilinear relationship with brittle fracture, before the ultimate load. The first slope change occurs due to the softening of the matrix, followed by delamination at 90% of the ultimate load before failure.

3.3 Fiber-reinforced composite

Fibre-reinforced composites have complex geometrical properties due to their heterogeneous microstructure and different orientations of reinforcement. Nevertheless, the behaviour of fibres within the matrix under loading, when aligned in a bidirectional way, has a very similar failure mechanism to fibres in plastic parts produced by fused deposition modelling (FDM), which are the components of interest in this work.

The bonds in fiber-reinforced metal, such as bonds between ceramic fibres and metal matrixes can be achieved by chemical adhesives, physical bonding and mechanical keying. On the other hand, five types of cracks are expected in composite materials. Three of these are in fibres: in-plane bending, out of plane bending and stretching. The other two types are in matrix materials: radial cracking and matrix de-cohesion [66].

Matzenmille [67] studied the correlation between the elastic features and the material damage in fibre-composite components. It was established that the formation of micro-cracks and cavities is responsible for the elastic-brittle behaviour in composite materials, with three modes of failure mechanism being observed in these materials:

Mode1: Fibre cracking, which is caused by tensile loads in the fibre direction. This cracking mode shows a linear relationship in the load-displacement curve. The fibres break in the region of maximum stress and debone from the matrix to form cavities before complete failure occurs. The material strength is proportional to the tensile strength of fibres and the volume ratio of fibres in the matrix.

Mode 2: buckling and kinking of fibre due to uniaxial compression load in the main direction of the fibres (in-plain bending).

Mode 3: Matrix rupture accompanied by transverse shearing and tension. The micro-cracks are unstable with increasing load and failure occurs after the formation of a few micro-cracks in the contact area between the fibre and the matrix (coating decohesion).

Ramesh [68] summarised the following damage mechanism in fibre-reinforced composites at a macro level:

a) Interfacial debonding

The properties of the interfacial area between the fibre and the matrix play a paramount role in the fibre-reinforced material's performance. The adhesive forces at the interfacial surface participate significantly in transferring the stresses at the macroscopic level.

b) Interlaminar (matrix) cracking

This is also called transverse cracking and occurs due to tensile, thermal and fatigue loads. It is well known that, in composite materials, the properties of components in transverse orientation are lower than other directions, and that this encourages cracks to originate in this direction. In some cases, the trigger for these cracks is the availability of voids or fabrication defects in addition to the debonding of fibre-matrix bonds.

c) Interlaminar cracking/ delamination

This kind of cracking develops through the thickness of composite laminates when exposed to shear stress or in-plane loading, leading to the separation of two adjoining plies. It can be initiated from cut edges such as holes or exposed surfaces.

Chapter 4-Fracture mechanics

4.1 Introduction

Before 1960, fracture mechanics was restricted to the behavior of loaded materials within the linear elastic range. Since that time, the paramount effort has been made to develop the theories to comprise the plastic and viscoelastic behavior in addition to fatigue problem, which is considered as an extension to the linear elastic fracture mechanics [69]. It has been noticed that the linear elastic fracture mechanics approach (LEFM) does not work when the failure precedes by considerable plastic deformation[70].

The presence of stress risers like holes or corners makes the materials fail with less strength than the expected material's strength, leads to the development of the fracture mechanics science. This science is the important solid mechanic's field which is trying to find the relation between the crack length, material's resistance and the stress which followed by final failure[71].

Fracture mechanics is the methodology used to reduce the opportunity of component's fracture in case of cracks or flaw availability when selecting and designing structural components. So, it is the toughness assessment of materials and their resistance to fracture. In other words, studying any material failure, which happens by the extension of existing cracks, is the speciality of fracture mechanics science. It had got a lot of innovation during the last decades of the 20th century with the aid of the great development of computer technology. For instance, three-dimensional simulation of the cracked component can be easily implemented with any desktop computer [70].

Fracture mechanics approach utilizes solid mechanics analysis to compute the force which drives the crack and evaluate the material strength by experimental methods. By applying the elastic and plastic theories to the microscopic defects, fracture mechanics has predicted different components failure[72].

4.2 Modes of fracture

In general, the crack initiation and propagation in any loaded component depends on various factors, such as material properties, object geometry, loading configuration, rate of loading, microstructure of the material and circumferential condition. To study the crack behaviour and propagation in elastic materials, it is important to consider three modes of loading, Figure 4.1:

- a. Mode I loading, crack opening (the tensile stress normal to crack plane). It is the most common fracture in structural design, which has received a lot of attention in failure analysis.

- b. Mode II loading, crack sliding (in-plane shear stress parallel to crack plane and normal to crack front). This cracking problem is considered as 2-D due to the in-plane action.
- c. Mode III loading, crack tearing (the shear stress parallel to crack plane and crack front). This type of cracking is rarely happen comparing to the other two kinds.

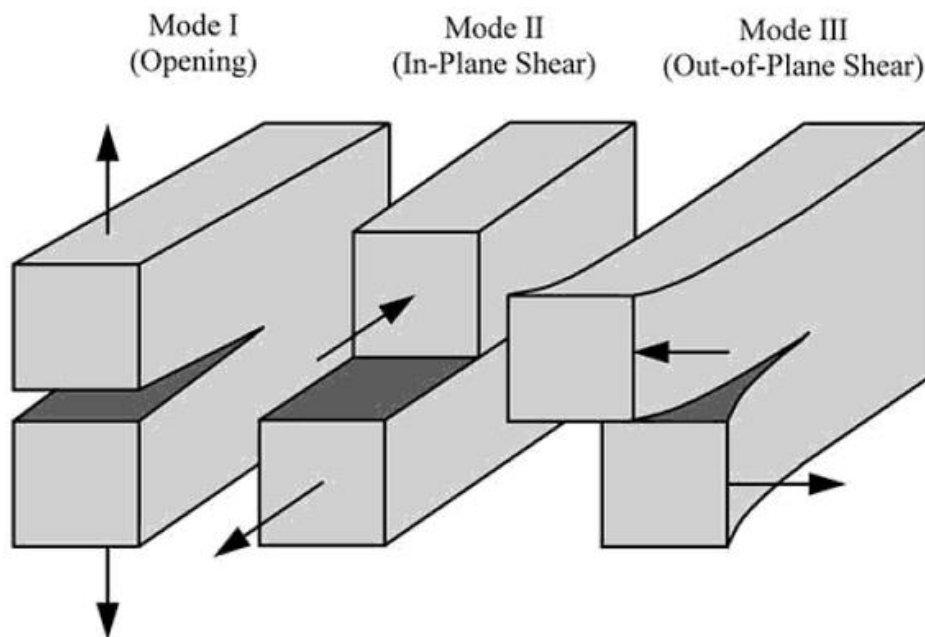


Figure 4.1 Three modes of cracks in an object under loading.

It is worth pointing out that the modes of the cracks are not restricted to the mentioned modes above. Generally, mixed modes crack propagation is responsible for the failure of parts under loading. Due to its responsibility for quick fracture in brittle materials, mode I crack has got a lot of interest in fracture investigation

4.3 Stress Concentration

The dimensionless factor K_t is used to evaluate the concentration of stress in loaded structural components with stress rising discontinuities, like notches, grooves and holes. The value of K_t is equal to the ratio of the maximum stress near the notch tip to the nominally applied stress σ_n .

$$K_t = \frac{\sigma_{max}}{\sigma_n} \quad (4.1)$$

In some polymers and metals, if the value of K_t for a loaded notched component is less than $(\sigma_o / \sigma_{ULT})$, the fracture strength will not be influenced by the existence of the notch [48] [73].

The magnification of the applied stress at a hole in a loaded plate was firstly noticed by Inglis [74]. The increasing of stress depends on the radius of curvature of the hole, as Inglis found using linear elastic analysis. The stress concentration factor K_t is the norm of stress magnification which is the ratio of max stress near the discontinuity to the applied stress on materials' cross-section. The K_t value for an elliptic hole in the uniformly loaded plate, as Inglis proposed, is given by following [69]:

$$K_t = 1 + 2 \sqrt{\frac{c}{\rho}} \quad (4.2)$$

Where c represents the length of major axis of the ellipse and ρ is the radius of curvature. When the value of the length of major axis to minor axis of an ellipse approaches to infinity, the geometry turns to crack-like. The stress at the edge of a crack, in a plate with dimensions too larger than crack size, with a crack length of $2a$ and width of $2b$, $a \gg b$, is given by the following [70]:

$$\sigma_A = \sigma \left(1 + 2 \sqrt{\frac{a}{\rho}} \right) \quad (4.3)$$

Where σ is the applied stress on the remote edge, and ρ is the radius of curvature of the crack tip $\left(\frac{b^2}{a} \right)$ as shown in Figure 4.2. When the crack width ($2b$) is very small compared to the length ($2a$), Equation (4.2) will be as follows [70]:

$$\sigma_A = 2\sigma \sqrt{\frac{a}{\rho}} \quad (4.4)$$

4.4 Fracture criteria

Two methods are available for the analysis by fracture mechanics: energy formula and stress intensity criterion:

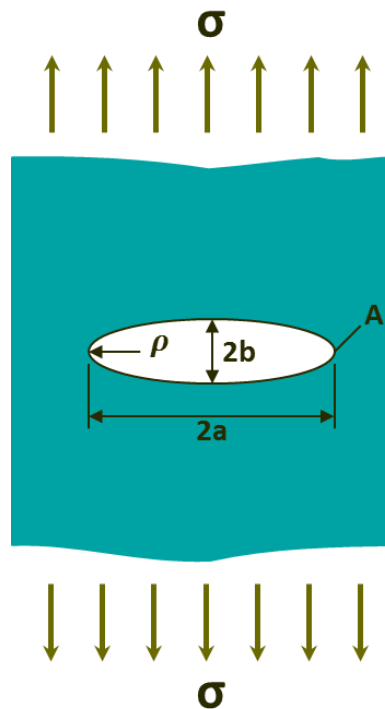


Figure 4.2 Elliptic flaw in an infinite plate

4.4.1 Energy criterion

The first energy formula of fracture was proposed by Griffith [69], in 1920. The fracture toughness for any material is represented by the critical rate of energy release Y_s when the fracture is happening. In linear elastic cracked materials, there is a change in the potential energy Y during crack propagation. According to Griffith, there are two conditions necessary for crack growth[70]:

- The bonds at the crack tip must be stressed to the point of failure. The stress at the crack tip is a function of the stress concentration factor K_t , which depends on the ratio of the length of the crack to the radius of curvature.

- For an increment of crack extension, the amount of strain energy released must be greater than or equal to that required for the surface energy of the two new crack faces.

By testing artificial crack in an experimental brittle specimen, he found that the product of the fracture stress σ_f and the square root of crack length (a), was constant[70].

$$\sigma_f \sqrt{a} = C \quad (4.5)$$

The anticipated failure occurs, as Griffith supposed, when the free energy C , (crack surface energy – elastic energy near crack tip) reaches maximum value with critical crack size.

$$C = \sqrt{\frac{2E Y_s}{\pi}} \quad (4.6)$$

And the remote fracture stress is:

$$\sigma_f = \sqrt{\frac{2E Y_s}{a \pi}} \quad (4.7)$$

The material's surface energy release per unit area is Y_s , and E is young modulus. Irwin[75], proposed additional dissipated energy for crack growth in ductile materials which is the plastic dissipation Y_p , plastic work per unit area, and the energy amount of crack growth g is:

$$g = Y_s + Y_p \quad (4.8)$$

By incorporating g in Equation (4.7) the product is the modified Griffith energy formula for fracture stress in ductile materials[71] [74]:

$$\sigma_f = \sqrt{\frac{2E g}{\pi a}} \quad (4.9)$$

For an infinite plate with a central crack of $2a$ length, Figure 4.2, the failure stress will be[76]:

$$\sigma_f = \sqrt{\frac{E g}{\pi a}} \quad (4.10)$$

It is noticed that the plastic energy dissipation is dominant in ductile materials while in brittle materials the surface energy dissipation is the prevalent [70].

4.4.2 Stress intensity criterion

The application of the energy formula is not practical due to the difficulties in evaluating the fracture work. Moreover, the use of Griffith formula is not adequate to compute the stress for crack propagation. By contrast, investigating of crack growth and evaluating stress state near the crack root, by using stress intensity factor is more practical and easier [70]. In 1957, Irwin [75] proposed mathematical expression for the stress field $\sigma(r, \theta)$ in the proximity of the sharp crack tip shown in Figure 4.3 as follows

$$\sigma_{yy} = \frac{K_I}{\sqrt{2\pi r}} \cos \frac{\theta}{2} \left(1 + \sin \frac{\theta}{2} \sin \frac{3\theta}{2} \right) + \dots \quad (4.11)$$

$$\sigma_{xx} = \frac{K_I}{\sqrt{2\pi r}} \cos \frac{\theta}{2} \left(1 - \sin \frac{\theta}{2} \sin \frac{3\theta}{2} \right) + \dots \quad (4.12)$$

$$\tau_{xy} = \frac{K_I}{\sqrt{2\pi r}} \cos \left(\frac{\theta}{2} \right) \sin \left(\frac{\theta}{2} \right) \cos \left(\frac{3\theta}{2} \right) + \dots \quad (4.13)$$

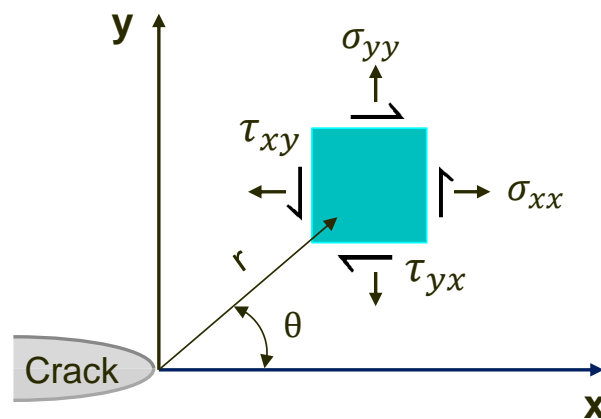


Figure 4.3 Plane stresses near a crack tip in an elastic material

It is worth noting that the higher term represented by dots, in Equations (4.11) to (4.13), can be cancelled when $r \leq 0.1a$, and the equations do not work at a large distance from the crack tip where the crack has no influence on the stress field. The I subscript refers to Mode I loading and the other loading Modes II and III have similar criteria. It can be noticed that the factor $(r^{-\frac{1}{2}})$ controls the stress singularity near the crack tip [72].

Also, noteworthy, every stress component is related to a single constant K_I . This constant is called the stress intensity factor which describes the stress condition at the crack apex in the materials with linear elastic behaviour. The stress condition, at failure, happens at a specific value of K_I called critical stress intensity factor K_{IC} , which is an assessor for fracture toughness in linear elastic materials. For the material shown in Figure 4.2, K_I is computed per the following [70] [71]:

$$K_I = \sigma F \sqrt{\pi a} \quad (4.14)$$

Where F is the geometry factor. For instance, the value of F equals 1.12 for a short crack in the semi-infinite component. The shaded black area in Figure 4.4, represents the additional strain energy-releasing which requires 12% correction to K_I value [70].

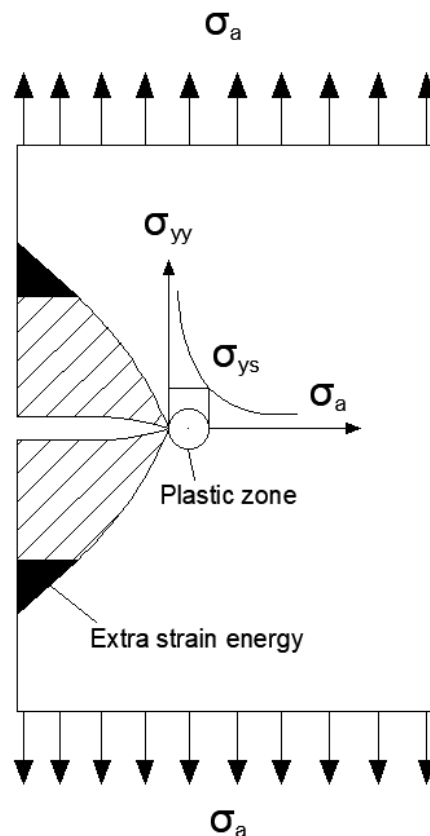


Figure 4.4 Additional strain energy release in semi-infinite plate

The stress intensity factor K_I is considered as driving force for the cracks while K_{IC} , a material property, shows the resistance to fracture and does not depend on components size. It is clear from Equations (4.11) to (4.13) that the distribution of stresses, around the crack tip, is the same for all crack lengths and the magnitude of stress at the crack apex is infinite [70]. However, it is not the case in practical applications due to the yielding of materials at a specific stress level. Hence, there is a region near the crack tip which called a plastic zone, where the linear elastic approach is not more working, Figure 4.4. The magnitude of stress in this region is taken as σ_y instead of the higher value given by Equations (4.11) to (4.13). By substituting $\theta = 0$ in the equations, the radius for this region r_p , can be found as follows [72]:

$$r_p = \frac{K_I^2}{2\pi \sigma_y^2} \quad (4.15)$$

The singularity of stress near crack tip may not be available owing to the non-linear elastic deformation of atomic bond stretching, in brittle materials. Using K_I , the stress singularity near the crack tip can be quantified. It is well known that K_{IC} is always measured in a plane strain condition and has the property to be additive for complicated load system. Despite this, K_{IC} value of different materials should meet the corresponding Griffith energy balance criterion for a crack extension. By relating Equations (4.10) and (4.14), we will get the following expression [71][76]:

$$g = \frac{K_I^2}{E} \quad (4.16)$$

For components with plane strain case, the following expression applies at critical loading state [72]:

$$K_{IC}^2 = E g_c (1 - \nu^2) \quad (4.17)$$

Where ν is Poisson's ratio. Equations (4.16) and (4.17) show that the energy and stress intensity methods, for linear elastic material, are analogous as fracture mechanics approach [71]. On the other hand, the fracture toughness of a cracked component under different stress field condition K_C can be estimated according to Linear Elastic Fracture Mechanics (LEFM), Equation (4.14), by considering the shape factor $F = f(\lambda)$, (a) is the crack-like notch depth and λ equal to (a/c), as shown in Figure 4.5 [77].

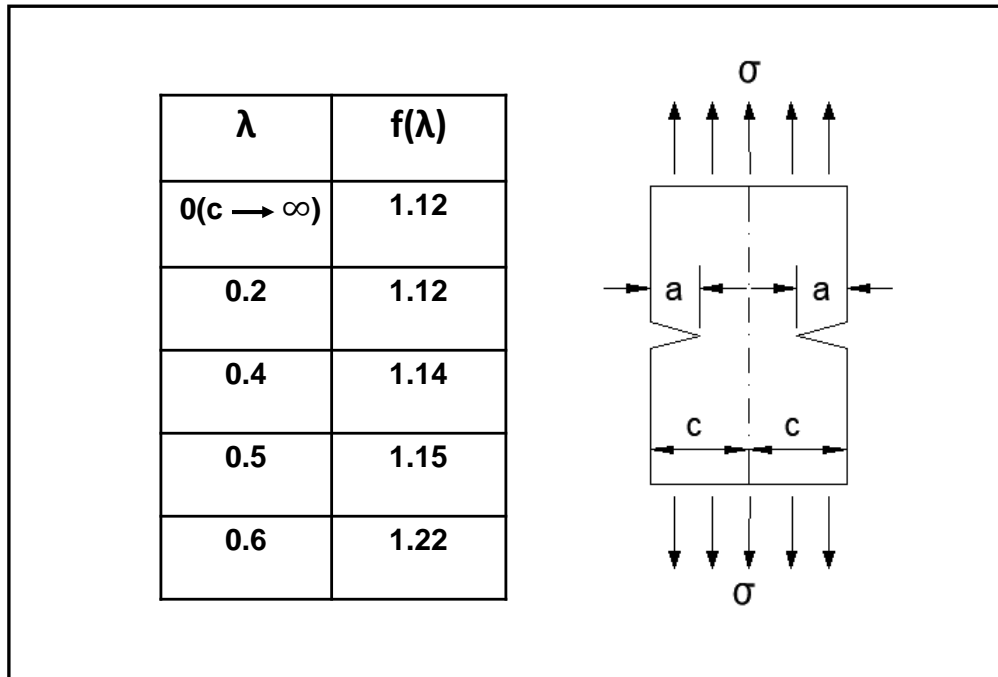


Figure 4.5 Shape factor [77]

4.5 Factors affecting K_{IC}

The fracture toughness K_{IC} is a material property, for specific material condition, which expresses the resistance to fracture, and it is size-independent property. It represents the amount of stress that the material reaches before failure. The following variables are influencing the K_{IC} value[76]:

1. Temperature condition.
2. Loading rate.
3. Chemical synthesis and impurities.
4. Heat treatment.
5. Fabrication history (rolling, injection moulding, etc.).
6. The microstructure and macrostructure of the Material.

The macrostructure of the AM PLA will be studied extensively in this work by investigating the strength and behaviour of the solid and porous AM PLA samples .

4.6 The Theory of Critical Distance

The need for reliable formula to estimate the strength of brittle notched components subjected to static loading originated from the idea that the stress condition becomes critical at a specific point of the geometrical discontinuity. Using finite element analysis (FEA) has been argued to be ineffective in calculating the maximum principal stress for materials with sharp notches or cracks, due to the existence of stress singularity near the tip of the stress raiser [24]. Also, using the stress concentration factor, K_t (which is the ratio of the maximum stress at the notch apex to the nominal stress) underestimates the strength for notched components. On the other hand, the application of linear elastic fracture mechanics (LEFM) is limited to cracks or notches with null root radius and opening angle and produces inaccurate predictions when the length of the crack is very small [19]

The theory of critical distances, TCD, has been considered as a potential solution to estimate the strength of brittle notched components subjected to static loading. TCD comprises a group of methodologies used to evaluate the static and fatigue strength of brittle components with stress concentrators like notches and cracks. All the TCD methods use the material parameter length L to assess fracture strength[8]. The formalisation of TCD depends on the concept that the theory of continuum mechanics does not give the real elastic stress value near the discontinuity [78].

Applying TCD with the linear elastic stress and then post-processing the finite element analysis results can reduce design cost and time[48]. TCD is also considered as a modification of LEFM that can be used to evaluate components with notches even when there is only a small process zone, exhibiting nonlinear behaviour, near the discontinuity [73]. For these reasons, and because of the extensive development and improved affordability of FEA programs, TCD applications have experienced a lot of interest in the context of various kinds of problems in recent decades [24].

TCD presents two parameters: the critical distance L , which is related to the size of a material's microstructure, and inherent strength σ_0 , material strength without defects, that modifying easy and quick performance for this theory. In addition, when there is a change in the load or dimensions of a component, the result could be extracted from linear scaling [24]. This theory has also been applied successfully to several types of materials, such as polymers, metals, ceramics and composites, with both static and fatigue loading. Moreover, linear-elastic and elastoplastic material behaviour is not an obstacle to the effective application of TCD[78].

According to the above, it can be seen that TCD is a powerful engineering tool which is appropriate for evaluating different mechanical assemblies in practical applications, with various materials and different loading types. In addition, owing to its features, it could be a suitable theory for linking different engineering specialities such as mechanical engineering, civil engineering and material science.

4.6.1 TCD methods

TCD includes four main methods, each of which makes use of the critical material length. Two are stress-dependent methods: the point method (PM) and the line method (LM). While the other two are stress-intensity dependent: the imaginary crack method (ICM) and the finite fracture mechanics (FFM) method. The latter approaches utilise energy to deal with finite crack extension. PM and LM methods are convenient to use when FEA results are available, whereas ICM and FFM methods can be expressed in equations and are good for characteristics studies. Some applications of TCD, however, have combined the two approaches, stress and energy. This is computationally more difficult but maybe appropriate when the above methods break down, especially in the case of components which are small compared to the (L) value [19].

To estimate the strength of fibre-reinforced composites, TCD methods were first suggested in 1970 when the LEFM was first established with the definition of L as in Equation (4.22). Ever since these methods have been increasingly used to assess different kinds of materials and the fracture of complex geometries. TCD has also been used to assess components without notches, like vehicle suspension parts and joints with pin loading, in addition to microscopic and nanomaterial objects[8]. Two other approaches also exist, related to the TCD method, but which use the average stress within a specific area, area method, and the average stress over a limited volume, volume method. Although they have a valid prediction, the application of these two methods is difficult and, in some cases, they are not accurate when compared with experimental results [48]. Overall, it is well established that the point method and line method are the most applicable and simple approaches among the various TCD methodologies [8].

4.6.2 Point and Line methods

Neuber[13] was the first to use TCD to assess notched metallic components subjected to fatigue load, by taking the effective stress to be the average linear elastic stress across a line starting from the notch root and vertical to the applied load. This approach has become known as the line method. In 1975, the static evaluation of notched fibre reinforced composite with the use of fracture toughness through LEFM in conjunction with the ultimate tensile strength of the plain component was verified by Whitney and Nuismer[79]. Lately, the application of TCD has been extended to evaluate the behaviour of brittle components with notches, subjected to axial and multiaxial loads. In this context, Peterson[12] suggested taking the effective stress at specific distance from the notch root, which represented the first formulation of the point method.

The point method postulates that a component will break when the computed static stress at a distance $L/2$ from the notch root equals the inherent material strength σ_0 , Figure 4.6, as follows[24]:

$$\sigma_{eff} = \sigma \left(\theta = 0, r = \frac{L}{2} \right) = \sigma_o \quad (4.18)$$

Westergaard equation for the stress at distance r from the apex of a through crack with a length of $2a$, in an infinite body under tensile stress, is shown below[80]:

$$\sigma(r) = \frac{\sigma}{\left[1 - \left(\frac{a}{a+r} \right)^2 \right]^{0.5}} \quad (4.19)$$

When the calculated stress is at a point very near to the crack apex, $r \ll a$, Equation (4.19) can be reduced as follows:

$$\sigma(r) = \sigma \sqrt{\frac{a}{2r}} \quad (4.20)$$

When a component with a sharp crack with zero root radius ($\rho = 0$) is considered, the LEFM technique and TCD will produce the same failure strength prediction. According to LEFM, the fracture of a body takes place when the stress intensity factor K_I reaches the fracture toughness of the material K_{IC} , which in turn relates to the failure stress as follows[71]:

$$\sigma = \frac{K_{IC}}{\sqrt{\pi a}} \quad (4.21)$$

By taking the suggestion from the point method, $r = \frac{L}{2}$, and gathering Equations (4.20) and (4.21), the critical distance L can be produced as follows:

$$L = \frac{1}{\pi} \left(\frac{K_{IC}}{\sigma_o} \right)^2 \quad (4.22)$$

K_{IC} is the fracture toughness of the material evaluated in a plane strain condition. Through the line method, Figure 4.7, the static brittle failure in a notched component is assumed to occur if the stress averaged over a distance d from the notch apex, equals the inherent material strength σ_o as in the following formula[21]:

$$\sigma_{eff} = \frac{1}{d} \int_0^d \sigma(\theta = 0, r) dr = \sigma_o \quad (4.23)$$

σ In the above formula is the linear-elastic stress, which can be estimated using the classical theories such as Tresca, Maximum principal stress and Von Mises criterion, while d is the critical distance. We can find the distance d by linking this assumption with the case of long and sharp cracks in fracture mechanics and substituting Equation (4.20) for $\sigma(r)$ in Equation (4.23), which leads to:

$$d = \frac{2}{\pi} \left(\frac{K_{IC}}{\sigma_o} \right)^2 \quad (4.24)$$

This distance is equal to twice the value of L defined in Eq. (4.22). Thus Eq. (4.23) can be re-written for the line method approach as:

$$\sigma_{eff} = \frac{1}{2L} \int_0^{2L} \sigma(r) dr = \sigma_o \quad (4.25)$$

TCD postulates that σ_o and L are both material characteristics that can be estimated experimentally or by using Equation (4.22) [21] [94]. It is worth pointing out that the above formula was obtained by activating the fracture mechanics hypotheses for the case of sharp and long cracks[8]:

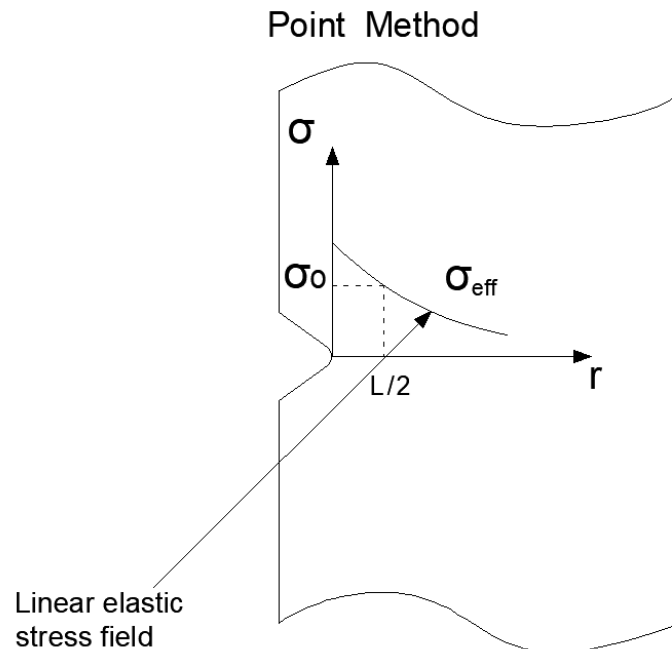


Figure 4.6 Point method

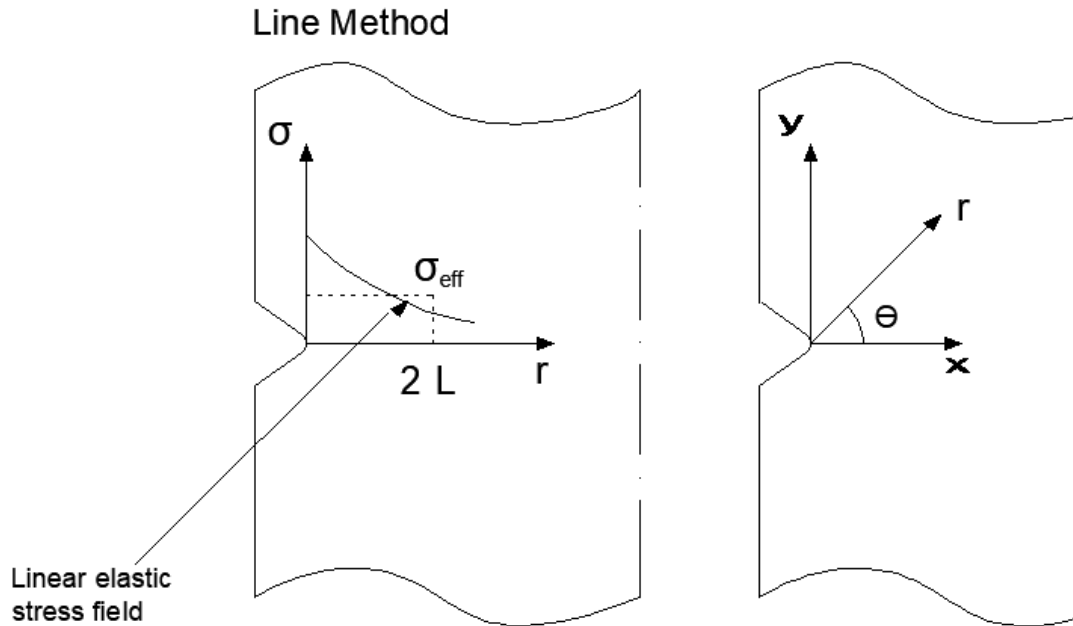


Figure 4.7 Line method

Line method and point method have been verified as offering good predictions for the static strength of metals with uniaxial and multiaxial loading. It was shown that the most accurate prediction for both methods, with ductile materials, when Von Mises criteria was used to compute the stress at the notch root. While the maximum principal stress formula has given acceptable results with uniaxial loading conditions [21]. On the other hand, due to the fact that even brittle materials exhibit small amounts of plastic behaviour, TCD has shown more precise predictions. Due to related features, point method and line method, have mainly been adopted in this work to assess the fracture behaviour of polymer, in addition to area method, which will be presented in the next section.

It is noticeable that TCD could be applied to components with a plane stress condition. In this case, plane stress can be said to dominate when a component with thickness B and yield stress σ_y has higher fracture toughness value than the following[81]:

$$K_C = \sigma_y (\pi B)^{0.5} \quad (4.26)$$

4.6.3 Area method and volume method

In the area method form, the stress is averaged over a semi-circular area centred at the emanating point of the focus line at the notch tip, Figure 4.8. According to this

method, it is postulated that when this stress is equal to the material's inherent stress failure will occur.

$$\sigma_{eff} = \frac{4}{\pi r_c^2} \int_0^{\frac{\pi}{2}} \int_0^{r_c} \sigma_1(\theta, r) \cdot r \cdot dr \cdot d\theta \quad (4.27)$$

The radius of this area, r_c , can be attained by taking the elastic stress surrounding a long crack in 2-D, which can be estimated by the following equations [82]:

$$\sigma_{\theta}(r, \theta) = \frac{K_I}{\sqrt{2\pi r}} \left(\frac{3}{4} \cos \frac{\theta}{2} + \frac{1}{4} \cos \frac{3\theta}{2} \right) \quad (4.28)$$

$$\sigma_r(r, \theta) = \frac{K_I}{\sqrt{2\pi r}} \left(\frac{5}{4} \cos \frac{\theta}{2} + \frac{1}{4} \cos \frac{3\theta}{2} \right) \quad (4.29)$$

$$\tau_r(r, \theta) = \frac{K_I}{\sqrt{2\pi r}} \left(\frac{1}{4} \sin \frac{\theta}{2} + \frac{1}{4} \sin \frac{3\theta}{2} \right) \quad (4.30)$$

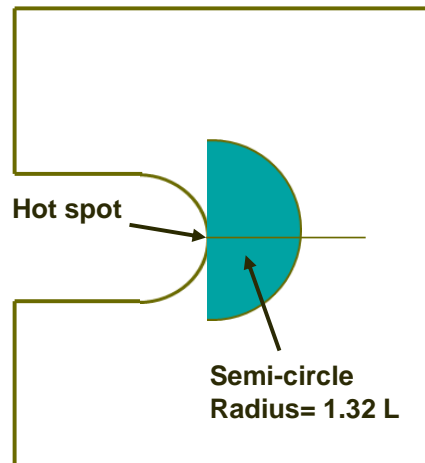


Figure 4.8 Area method

The maximum principal stress at a point in the stress field can be calculated by the equation below:

$$\sigma_1 (r, \theta) = \frac{K_I}{\sqrt{2\pi r}} \left(\cos \frac{\theta}{2} + \sqrt{(\cos \frac{\theta}{2} \sin \frac{\theta}{2})^2} \right) \quad (4.31)$$

According to Eq. (4.27), the product of the integration will be the average stress σ_{ave} over a semi-circle with a radius of r_c from the notch tip:

$$\sigma_{ave} = 0.648 \frac{K_I}{\sqrt{r_c}} \quad (4.32)$$

By taking the postulated failure condition, this stress should be equal to the material inherent stress σ_o , thus, the critical radius will be:

$$r_c = 0.42 \left(\frac{K_C}{\sigma_o} \right)^2 \quad (4.33)$$

In terms of the length scale of the material (L):

$$r_c = 1.32 L \quad (4.34)$$

In this work, this represents the radius of the circle adopted in evaluating the 2-D stress field around the notches using area method.

With regards to the volume method, this approach suggests averaging the stress over a hemisphere as a critical volume influencing the stress field gradient from all directions. The coordinates of the spherical system should be activated to calculate the critical radius of the sphere following the same area method procedure, with triple integration [82]:

$$\sigma_{eff} = \frac{1}{V} \iiint \sigma_1(r, \Phi, \theta) r^2 \sin. \Phi. dr d\Phi d\theta \quad (4.35)$$

$$\sigma_{ave, sph} = 0.699 \frac{K_I}{\sqrt{r_c}} \quad (4.36)$$

When the average stress equal to the material inherent stress, and comparing to Eq. (4.22), the critical radius will be:

$$r_c = 1.54 L \quad (4.37)$$

4.6.4 Imaginary crack method (ICM)

ICM is considered to be a fracture mechanics method which relies on the energy release rates from crack propagation. In this approach, a notched component is analysed by introducing a sharp imaginary crack at the notch root (Figure 4.9), and the extension of this crack obeys LEFM laws. The length of the imaginary crack is assumed to be a material constant. The analysis is accomplished by calculating the stress intensity factor of the notch-root crack to predict component failure [8]. The stress intensity factor, K_c , of a through crack of $2a$ length in an infinite plate was given by the Equation (4.14) [71], and According to the ICM method, the stress intensity factor for the effective length ($a + a_o$) at failure will be [48]:

$$K_c = F \sigma_f \sqrt{\pi(a + a_o)} \quad (4.38)$$

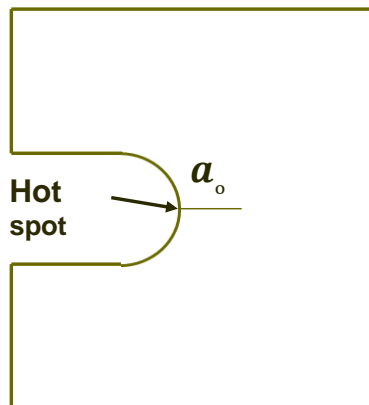


Figure 4.9 The imaginary crack at the notch root for ICM

Where K_c is the critical stress intensity factor, a is the crack or notch length and a_o is the imaginary crack length. For a plain specimen, $a = 0$ and $\sigma_f = \sigma_o$, the imaginary crack length is computed as:

$$a_o = \frac{1}{\pi} \left(\frac{K_c}{F \sigma_o} \right)^2 \quad (4.39)$$

And the corresponding K_c is:

$$K_c = F \sigma_o \sqrt{\pi a_o} \quad (4.40)$$

By comparing Equations (4.38) and (4.40), the failure stress for cracked components can be evaluated by the following[8]:

$$\sigma_f = \sigma_o \sqrt{\frac{a_o}{a_o + a}} \quad (4.41)$$

It is worth pointing out that ICM and LM give the same predictions when $F=1$, i.e., the case of a through crack in an infinite component, and where $a_o = L$. Also, both methods coincide when $a = 0$ (plain specimen), and when $a \gg a_o$ [8].

Taylor[8], mentioned that a_o is not a real material constant because it also changes with the crack shape. El Haddad [83], suggested that, at the notch root, the presumed crack represents the damage zone, which was noticed when assessing the fatigue failure of composite materials, and that a_o changes according to the material's grain size. As a conclusion, ICM has similar predictions to point method and identical predictions to line method in a lot of cases [48].

4.6.5 Finite Fracture Mechanics (FFM)

Finite fracture mechanics has recently been suggested to be capable of predicting the failure condition by presuming a limited amount of crack expansion Δa and relying on energy balance. When the crack propagates by δa , the elastic energy stored in the body will decrease by the amount δW per unit material thickness, and can be expressed as [8]:

$$\delta W = \frac{\sigma^2}{E} \pi a \delta a \quad (4.42)$$

By integration, the difference in the strain energy for a notched body or for an existing crack length a , can be estimated as:

$$\int_a^{a+\Delta a} dW \quad (4.43)$$

If we define the elastic energy release rate for a cracked body by G_c , the amount of energy required for the crack to grow will be $G_c \Delta a$, which is equal to the product of Eq. (4.43):

$$\int_a^{a+\Delta a} G da = G_c \Delta a \quad (4.44)$$

In terms of stress intensity, Eq. (4.43) can be written as:

$$\int_0^{2L} K^2 da = K_c^2 \cdot 2L \quad (4.45)$$

The suitable value of the crack extension Δa for this approach is constant for a given brittle material, and equal to $2L$. Material fracture takes place when the applied stress σ_f reaches a critical value, given by the following [81]:

$$\sigma_f = \frac{K_c}{\sqrt{\pi\left(a + \frac{\Delta a}{2}\right)}} \quad (4.46)$$

The application of this approach to notches and sharp cracks have similar and the same predictions as to the point method and line method [48].

4.6.6 Estimating the Material Constants values

The fracture toughness K_c and the inherent strength σ_o , are both material constants in Equation (4.22). When there is no plastic deformation before failure, as in brittle materials, σ_o can be taken as the ultimate tensile strength σ_{ult} , while in components with a specific amount of plastic deformation, σ_o will be higher than the ultimate tensile strength and can be found by experimental investigations. The method of finding σ_o and L , for material with some ductile behaviour, is simplified as shown in Figure 4.10, by drawing the stress-distance curve for sharp and blunt notched specimens with a linear elastic approach and taking σ_o and $L/2$ from the intersection point of the two lines. This method was proposed by Taylor [19], as an enhancement of the point method and was called the modified point method. In order to get an accurate prediction, however, σ_o and K_c should be evaluated in materials without defects [24]. Voiconi [84] proposed that there is a linear relationship between the ultimate stress σ_{ULT} and the inherent stress σ_o , when applying TCD for materials with a porous

and cellular microstructure. He tested v-notches and circular holes to estimate the L and σ_o values.

Cicero[81] mentioned that σ_o has the same value of σ_{ULT} for materials with linear-elastic behaviour, at both micro and macro level, as in the failure of ceramics and some rocks. It is also noteworthy that the unity ratio of σ_o / σ_{ult} is correlated to the fact that the material is isotropic, homogeneous and linear. While a ratio higher than one refers to plastic deformation and non-linear elastic trends [73]. A cracked specimen can be used to evaluate TCD parameters as one of the two specimens, if $\sigma_o / \sigma_{ult} = 1$, in addition to a plain specimen. This test method is often dispensed with, however, since TCD parameters are already available for many materials. However, For Polymethyl methacrylate PMMA polymer, the intersection of the stress-displacement curve occurs at different points for plain and blunt-notched specimens [19].

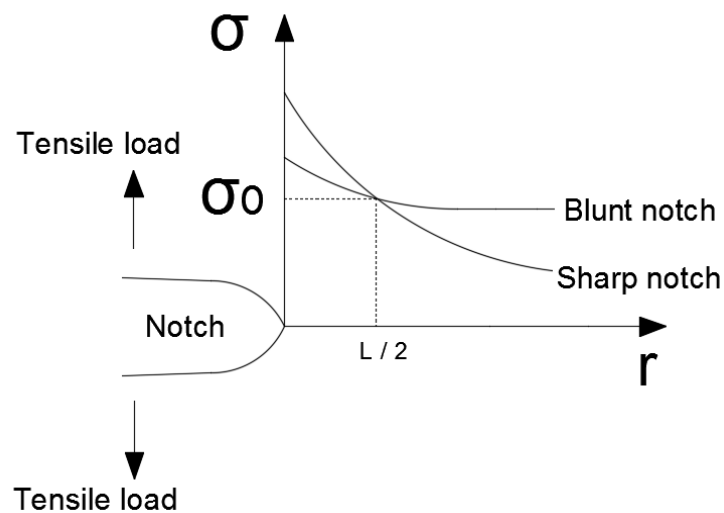


Figure 4.10 TCD evaluation for ductile material

4.6.7 Critical distance L in polymers

Fracture theories have recently realised the importance of incorporating material characteristic length in the formation of theoretical models. For instance, the inclusion of spacing and grain size, which are related to a material's microstructure, has been used in some models as correlative to physical length [8]. Unlike ceramics, however, the critical distance L in polymers is not related to microstructure or grain size because most of them do not have such a microstructure. When testing PMMA, however, Tsuji [85] noticed that L had the same value as the craze length and that the craze tended to have a fixed size. This fact was not true when the material showed a noticeable amount of plastic behaviour, however. In fact, when some plastic deformation exists, the magnitude of L will correspond to the size of the process zone [48].

Voiconi [84] suggested that there was a linear relationship between the material characteristic length L and the size of its cells or pores, when investigating the effect of notches on the fracture properties of polyurethane material (PUR), which has a porous and cellular microstructure. In other materials, such as metals and ceramics, however, the critical distance is equal, or proportional, to the grain size [48] [73].

4.6.8 TCD with polymers

Cicero [81] conducted several tests on notched PMMA to verify the validity of using TCD to analyse the effect of notches on the apparent fracture toughness. This polymer is considered to be an important engineering material because it has a brittle behaviour at the macroscopic level with a linear elastic trend, in addition to non-linear behaviour due to the effect of crazing at the microscale.

It is used widely in the medical field as bone cement, which is vulnerable to undergo some types of stress concentration. Three methodologies of TCD, point method, line method and FFM, were used to calibrate the material parameters related to the application of this theory. The first two methods are considered to be the most practical and important versions of TCD. For notch components, the fracture evaluation used the apparent fracture toughness K_{IN} , instead of the fracture toughness K_C used in cracked specimens, to reduce the analysis to an equivalent state in cracked specimens. In this approach, failure occurs when:

$$K_I = K_{IN} \quad (4.47)$$

K_I is the stress intensity factor for equivalent cracked sample with the same length of the notch. By using the Creager and Paris[86] equation for the stress at the notch tip and regarding the point method, the relationship between the K_{IN} and K_C is as follows[81]:

$$K_{IN} = K_C \frac{(1+\rho/L)^{3/2}}{(1+2\rho/L)} \quad (4.48)$$

Where ρ is the notch radius. The stress ahead of the notch root σ_r was assessed at $r = \rho/2$ from the crack apex as follows [86]:

$$\sigma_r = \frac{2K_I(r+\rho)}{(2r+\rho)^{3/2}\sqrt{\pi}} \quad (4.49)$$

K_I represents the stress intensity factor for Mode I loading. It was seen that the point method and line method have good prediction comparing to the test results. Also, while the notch radius remains below its critical value, the behaviour of material was brittle, and the notch is considered as a crack. If the notch radius reaches the critical value, the failure process becomes non-linear with higher ultimate fracture stress, and the TCD predictions will deviate significantly[81].

Kinloch [87], when studying cracked epoxy materials, found that the growth of crack and toughness measurements is affected by the local plastic zone, which occurs due to material yielding near the crack tip. He suggested a method like point method to compute the fracture toughness for brittle materials. The following equation was used to evaluate the critical stress σ_c at a critical distance c from the crack root:

$$\sigma_c = \frac{\sigma\sqrt{a} \left(1 + \frac{\rho}{c}\right)}{\sqrt{2c} \left(1 + \rho/2c\right)^{3/2}} \quad (4.50)$$

Where σ is the applied stress, a and ρ are the crack length and crack radius, respectively.

Taylor[48] verified the application of TCD on PMMA materials with notches and holes which are small. He found that TCD can give a good prediction for the stress concentration K_t greater than 2, while it could not predict the failure of plane specimens. Additionally, notches less than the critical size will not influence the material strength. For instance, the critical diameter of a hemisphere in PMMA was 0.38 mm. Also, large notches, with K_t factor less than 2, showed no effect on material strength.

Gomez [88] checked the application of several criteria, based on characteristic length for critical stress, on notched PMMA components. The analysis showed that, among seven fracture formulas, the mean stress criterion was the most accurate in terms of predicting failure and also has the simplest form. This approach was suggested by Seweryn [89], which presumed that failure of notched material starts when the average circumferential stress within a specific distance, d_c , from the notch apex, reaches the critical stress σ_c . This approach is like LM and uses two specimens (a smooth specimen, $R = \infty$, and a cracked specimen, $R = 0$) to evaluate the critical parameters, σ_c and d_c . Creager and Paris [86] expression was used in this method to assess the stress at distance x from the notch root:

$$\sigma_{(x,0)} = \frac{2Kc^U(x+R)}{\sqrt{\pi(2x+R^3)^{3/2}}} \quad (4.51)$$

Where R is the radius of the notch and Kc^U is the critical stress intensity factor which is given by the following:

$$Kc^U = K_t \sigma_c \sqrt{\pi \frac{R}{4}} \quad (4.52)$$

K_t is the stress concentration factor and σ_c is the critical nominal stress. On the other hand, Kinloch [87] noticed that σ_o has a higher value than the yield strength, σ_y , for polymers with the ratio of (σ_o / σ_y) reaching as high as 5.5 in some polymers.

Taylor[48] showed that some polymers have no single intersection point when drawing the stress-distance curve, using linear elastic stress analysis, especially for very blunt notches and plane specimens. It is well known that the fracture toughness K_{Ic} , for polymers with notches, depends on the stress condition, which relates to the component thickness [79]. In more detail, if the thickness of the component is large enough, the crack will start from inside the material, where the plane strain condition is active near the notch root, and the brittle failure in polymers mostly arises from this condition. In contrast, a plane stress condition will be dominant if the specimen is just a few millimetres' thick, leading in this case to the formation of a plastic zone spreading throughout the material's thickness.

It is worth pointing out that verification of TCD for polymers manufactured by AM with fused deposit modelling, has not been implemented before, which is the main work of this research.

4.7 TCD and Kitagawa-Takahashi's diagram under static loading

The TCD can be utilised to assess the static strength of components with cracks and different kinds of notches. TCD's key feature is that the evolution of static strength in the existence of geometrical discontinuity can be implemented accurately by processing the effective stress σ_{eff} in the vicinity of crack initiation, that is representing the entire linear elastic stress field acting on the material in a specific finite-size region [8].

This process zone can be thought of as that portion of material controlling the overall static strength of the component being designed. The size of the process zone depends on material microstructural features, local micromechanical properties, and characteristics of the physical mechanisms leading to final breakage [90]. By changing the size and shape of the integration domain used to calculate σ_{eff} , the TCD can be formalised according to the point method, the line method, or the area method, (Equations (4.18), (4.25) and (4.27)). Although these equations can design components containing geometrical features of all kinds, they must be derived solely for an infinite plate containing a through-thickness central crack [91].

Another important aspect is that the TCD can describe the transition from the short-crack to the long-crack regime. [8] [92][93][94]. By using the classic analytical solution

from Westergaard [95], to describe the stress distribution in the vicinity of the crack tip, the PM and the LM can be respectively expressed as: [8].

$$\sigma_f = \sigma_{UTS} \sqrt{1 - \left(\frac{a}{a+\frac{L}{2}}\right)^2} \quad (4.53)$$

$$\sigma_f = \sigma_{UTS} \sqrt{\frac{L}{a+L}} \quad (4.54)$$

Where a is the half-crack length, and σ_f is the failure stress related to the gross area of the cracked plate.

Figure 4.11 displays the Kitagawa-Takahashi diagram, which emphasises the validity of TCD Equations (4.54) and (4.55) in presenting the regime transition from short to long crack. Particularly, the application of the point method and line method give the same results of the farthest cases of material without crack and the long-crack components, represented in the figure by the two asymptotic straight lines. The horizontal line is related to the plain material with σ_{UTS} , and the inclined line is for modelling according to LEFM. Examining the transition zone from short to long-cracks, the application of the line method displays more conservatism than the point method, Figure 4.11.

The theoretical framework summarised in this section will be utilised to form a novel methodology appropriate for evaluating the static strength of plain and notched AM PLA manufactured by setting the infill level less than 100%.

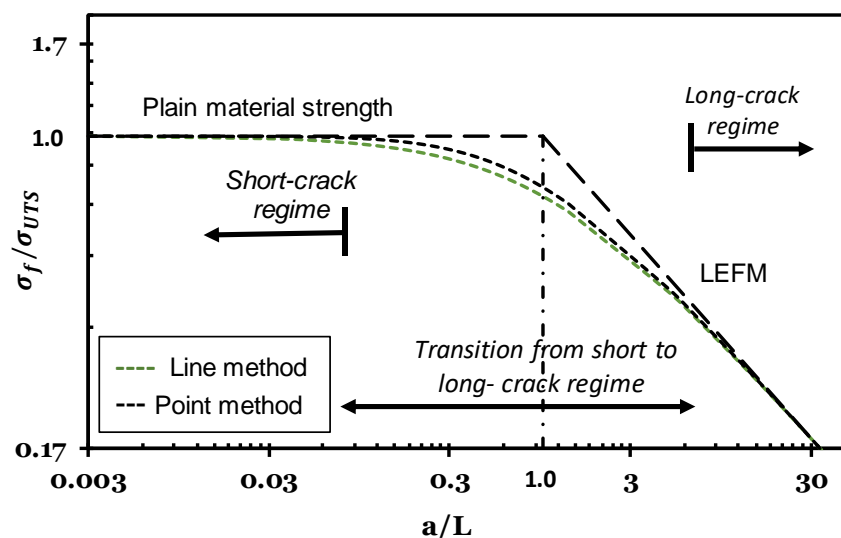


Figure 4.11 Transition modelling from a short to long-crack regime according to TCD for a material under tension

4.8 TCD and other fracture theories

The fracture process of notched materials is very intricate and still only partially understood. Several other theoretical models have been used to estimate the failure in notched materials. The main theories can be classified as follows:

(a) Non-Mechanistic Model

This model represents the continuum mechanics model which has some simplifications for use in the design process. Failure in this model is not related to grain boundaries and takes place when a specific condition is achieved in the continuum mechanics parameters, like strain, stress and energy. Three types of this model are available: global, local and non-local, as shown in Figure 4.12 [8]. The whole component is considered when using the global model, while in the local model the information from each specific point in the material is considered to evaluate the failure. This model is useful in complex geometries and is common in fatigue problems. In addition to the individual point, the non-local model uses data from other points in the material to assess the failure strength. For instance, TCD with the PM approach is classified as a non-local model because the information from other places in the component has a role in computing the critical distance[8].

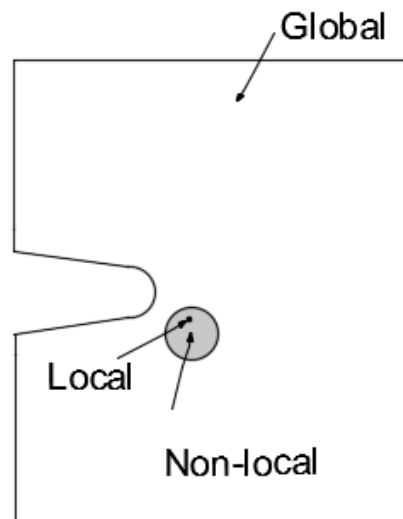


Figure 4. 12 Local, non-local and global theories

(b) Mechanistic Models

The simple model of Ritchie[96] is representative of this kind of model. In this approach, failure is related to grain boundaries, and the model can easily predict different kinds of behaviour. This model can enlighten the actual physical mechanism of fracture. It is like PM in the TCD approach, except it uses the elastic-plastic stress field instead of the elastic stress field.

(c) Statistical Models

The existence of imperfection and manufacturing flaws leads to differences in the properties of the material from place to another. Accordingly, when a component is exposed to uniform stress, failure will occur in the worst place. This is the assumption of Weibull [97], who suggested the equation below for calculating the probability of failure, P_f :

$$P_f = 1 - \exp \left[-\left(\frac{\sigma}{\sigma^*}\right)^b \right] \quad (4.55)$$

Where σ is the applied stress, σ^* is material strength and b is the scattering degree. A low grade of fracture potential is hard to evaluate, however, due to the need for precise modelling of the defect's distribution [8].

(d) Modified Fracture Mechanics

Owing to the limits for the application of LEFM to components with long and sharp cracks, several attempts have been implemented to modify this approach. Three types of LEFM modification will be mentioned below:

Elastic-plastic fracture mechanics, EPFM, is used in problems with considerable plasticity and where the plastic zone is significant in size comparing to the specimen's dimension and crack size. This method has been used with FE modelling to assess materials' failure.

The notch stress intensity factor, NSIF, approach was applied to components with features which are not cracks. This method is specialised in geometries with sharp V-notches. Williams [98] was the first to suggest an equation for estimating the stress field ahead of the V-notched root.

The crack modelling method, CMM, was modified to solve fatigue problems with sharp notches. Smith and Miller [99] used this approach to model sharp notches as a crack with the same length [8].

(e) Process-Zone Theories

Metals experience a toughening mechanism which is related to plastic deformation. While in brittle materials, failure occurs due to micro-cracks or delamination, with no or limited plasticity. In some quasi-brittle materials, such as concrete and fibre composites, plastic behaviour can contribute to a significant increase in toughness. Some methods postulate that failure will occur when the plastic zone (process zone) reaches a specific size. Hillerborg [100] developed a process zone model for predicting the fracture strength of brittle materials. In this method, the process zone is replaced by a line extending from the root of the crack, and the stress-strain curve within this line represents the material behaviour. This approach can be used to evaluate the fracture strength of notches and for plane specimens. The size of the process zone can be calculated from the function $(K_C/\sigma_U)^2$, which is very similar to L in the TCD approach[8]. Nevertheless, the L value in brittle polymers is related to the craze size instead of the plastic zone size.

4.9 Benefits of TCD

Compared to other methods, TCD is considered to be a continuum mechanics approach with the inclusion of the mechanistic theory by adding a length scale, which related to the grain boundaries of the material. The following features can describe the applications of this theory:

1. TCD can evaluate the strength of notched components regardless of their sizes and sharpness and with complex geometries.
2. It can be used to assess cracked materials regardless of the crack length.
3. It can evaluate components with notches despite the existence of a small process zone, with nonlinear behaviour, near the discontinuity [73].
4. The application of TCD needs few materials properties, and these are usually available from the material records or can be supplied by the manufacturer.
5. It could be the appropriate theory to make a transversal linkage amongst different engineering specialities such as mechanical engineering, civil engineering and material science.
6. It does not need to utilise the complex non-linear stress field owing since it depends instead on the elastic stress field near the discontinuity.
7. By post-processing the finite element analysis results, with linear elastic stress, this method will reduce design cost and time[48].

8. When there is a change in load or dimensions of the component, the result could be extracted from linear scaling [19].
9. The use of critical distance, which relates to a material's microstructure, process zone or craze size, gives a proper explanation for the physical mechanism of material failure.

Moreover, several works [19][81] have verified the good prediction of TCD for the strength of notched polymer components, in addition to the works on methods which are like TCD approach [87] [76][101].

For all the above reasons, the current work selected the TCD approach to evaluate the fracture strength of PLA notched components produced by 3D printing technology

Chapter 5- Methodology

5.1 Experimental work

PLA components were produced using an Ultimaker 3D printer (2 Extended+), with a nozzle of 0.4 mm. The specimen was drawn by CAD and saved to a STL file. The Cura program transferred the STL model to the G-code file, which is understood by the 3D printer to manufacture the required parts. The key manufacturing parameters were set as shown in Table 5.1.

The experimental programme was comprised of PLA specimens manufactured by the Fused Deposition Modelling, FDM. The printing process was in the horizontal plane, or in the width and length plane for all specimens with different values of the manufacturing angle θ_p between the reference manufacturing direction (longitudinal axis of the build-plate), and the longitudinal axis of the specimens (see Figure 5.1). The deposition of the fused filament was layer-upon-layer at $\pm 45^\circ$ to the reference manufacturing line. The next infill layer was constructed by moving the build-plate downward by the layer thickness magnitude. The layer thickness, for all specimens, was consistent at 0.1 mm. The average dimensions of all tested specimens were measured using a high-precision calliper and an optical microscope. The thickness of the plain and notched tested specimens was fixed at 4 mm.

Table 5.2 displays the experimental programme of the solid AM PLA specimens, manufactured with 100% infill level, and Table 5.3 presents the tested porous samples printed with less than 100% in-fill density. The printing of every PLA parts started with the deposition of the shell perimeter with thickness varied from (0, 0.4 and 0.8) mm, for plain solid samples and fixed at 0.4 mm for notched solid specimens, plain porous PLA and notched porous PLA parts.

The crack-like AM PLA specimens were manufactured to investigate the influence of the shell thickness on the fracture toughness of these samples. In addition, CT specimens were printed and tested according to ASTM D5045-14, to evaluate the plain fracture toughness of the AM PLA material (see Table 5.2).

Independent of geometry and the type of applied loading, all samples were tested using a Shimadzu universal machine with a displacement rate of 2 mm/s. The local strain in the plain specimens was measured using an extensometer with a gauge length equal to 50 mm. To generate statistically meaningful data, the average results of three repeated samples for every specific geometry and loading configuration, tested up to complete failure, were taken.

Table 5. 1 PLA and 3D printing specification

Description	Value
Material	PLA
Form	Filament
Manufacturer	New Verbatim
Melting temperature	200-220 ° C
Size	2.85 mm
Colour	White
Printing temperature	210 °C
Nozzle size	0.4 mm
Bed temperature	60 °C
Speed of filling in the x-y direction	30 mm/s
Speed of filling in the z-direction	30 mm/s
Shell thickness	0.4 mm

5.2 Solid PLA specimens, 100% infill ratio

5.2.1 Fabricating and testing of specimens

In order to check the validity of the theory of critical distance in evaluating the static strength of notched AM PLA, a large number of samples were fabricated with various geometrical features and printing parameters, as shown in Tables 5.2 and 5.3.

Figure 5.2 displays the technical drawing of the plain specimen, which was manufactured to investigate, experimentally, the ultimate tensile strength of the additively manufactured PLA. Each measured dimension, for the tested specimens, is taken as an average result of three measurements in different places on each sample.

The specimens were printed horizontally by setting the manufacturing angle θ_p , equal to 0°, 30°, 45°, 60° and 90°. Three different specimens were tested for each deposition angle, θ_p . If the specimen's deposition angle is presented in the same way as that used for the fibre-reinforced composite material, the θ_p angle (Fig. 5.1) (equal to 0° and 90°) leading to an equivalent angle of $\pm 45^\circ$; the θ_p of 30° resulting in a configuration of $(-15^\circ/+75^\circ)$, and, lastly, θ_p equal to 45° resulting in an equivalent of $0^\circ/+90^\circ$ angle, as shown in Figure 5.3.

When a 3D-printer manufactures a new layer, the shells are always the first parts to be made, so that a kind of external retaining wall is created before the internal structure of the object is built up. The shell's thickness is typically a multiple of the nozzle diameter, so the nozzle does not need to be changed during the process of printing the PLA parts.

Three groups of specimens were manufactured with different values of shell thickness t_s (0 mm, 0.4 mm, and 0.8 mm). The plain specimen dimensions were measured using the digital callipers. By contrasting the actual dimensions (reported in the tables of the testing results, see Table 6.1) with the nominal dimensions indicated in Figure 5.2, we can conclude that the accuracy of the dimensions was slightly affected by the manufacturing angle θ_p and the shell thickness.

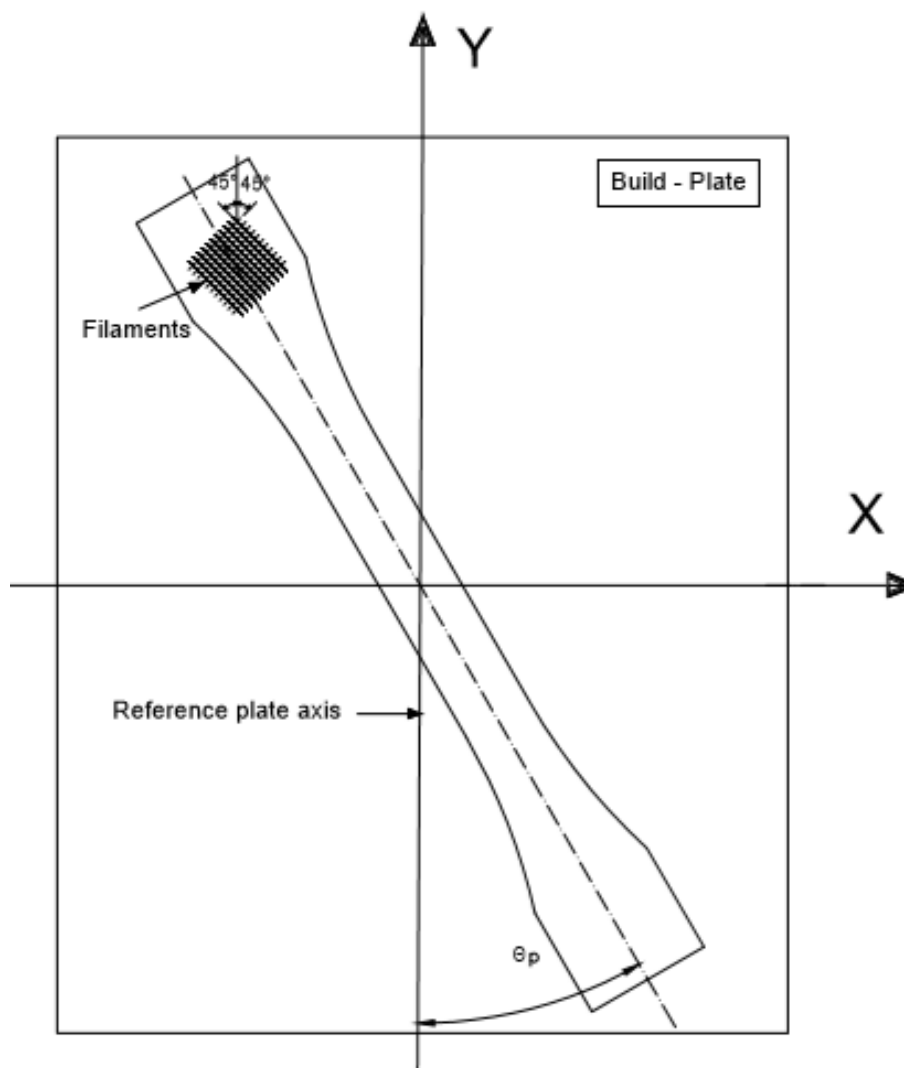


Figure 5.1 Manufacturing layout

Table 5.2 The test matrix of solid AM PLA specimens

Code	Description of AM PLA Specimens	θ_p [°]	r_n [mm]	t_s [mm]	No. of Specimens	The aim of the test is to find:
nsP_ θ_p	Solid plain	0, 30, 45, 60, 90	—	0	15	The mechanical properties
P_ θ_p	Solid plain	0, 30, 45, 60, 90	—	0.4	15	Shell effects on strength
8P_ θ_p	Solid plain	0, 30, 45, 60, 90	—	0.8	15	Shell effects on strength
C_ θ_p	Crack-like notched	0, 30, 45, 60, 90	—	0	15	Shell effects on K_C
Sc_ θ_p	Crack-like notched	0, 30, 45, 60, 90	—	0.4	15	Shell effects on K_C
8C_ θ_p	Crack-like notched	0, 30, 45, 60, 90	—	0.8	15	Shell effects on K_C
CT_ θ_p	CT, t = 20 mm	0, 30, 45	—	0.4	9	K_{IC}
CT30_ θ_p	CT, t = 30 mm	45	—	0.4	3	K_{IC}
S04_ θ_p	U-notched	0, 30, 45	0.5 mm	0.4	9	Strength under tension by TCD
I04_ θ_p	U-notched	0, 30, 45	1.0 mm	0.4	9	Strength under tension by TCD
B04_ θ_p	U-notched	0, 30, 45	3.0 mm	0.4	9	Strength under tension by TCD
OR0_ θ_p	V-notched	0, 30, 45	0.5 mm	0.4	9	Strength under tension by TCD
OR1_ θ_p	V-notched	0, 30, 45	1.0 mm	0.4	9	Strength under tension by TCD
OR3_ θ_p	V-notched	0, 30, 45	3.0 mm	0.4	9	Strength under tension by TCD
BR0_ θ_p	U-notched	0, 30, 45	0.05 mm	0.4	9	Strength under 3-point bending by TCD
BR1_ θ_p	U-notched	0, 30, 45	1.0 mm	0.4	9	Strength under 3-point bending by TCD
BR3_ θ_p	U-notched	0, 30, 45	3.0 mm	0.4	9	Strength under 3-point bending by TCD
OBR0_ θ_p	V-notched	0, 30, 45	0.35 mm	0.4	9	Strength under 3-point bending by TCD
OBR1_ θ_p	V-notched	0, 30, 45	1.0 mm	0.4	9	Strength under 3-point bending by TCD
OBR3_ θ_p	V-notched	0, 30, 45	3.0 mm	0.4	9	Strength under 3-point bending by TCD

Table 5.3 The test matrix of porous AM PLA specimens

Code	Description of AM PLA Specimens	θ_p [°]	Infill [%]	r_n [mm]	t_s [mm]	No. of Specimens	The aim of the test is to find:
P0_infill%	Plain porous	0	10, 20, ..., 90	—	0.4	27	The mechanical properties
P30_infill%	Plain porous	30	10, 20, ..., 90	—	0.4	27	The mechanical properties
P45_infill%	Plain porous	45	10, 20, ..., 90	—	0.4	27	The mechanical properties
S θ_p _infill%	U-notched porous	0, 30, 45	30, 50, 70	0.5 mm	0.4	27	Strength under tension by TCD
I θ_p _infill%	U-notched porous	0, 30, 45	30, 50, 70	1.0 mm	0.4	27	Strength under tension by TCD
B θ_p _infill%	U-notched porous	0, 30, 45	30, 50, 70	3.0 mm	0.4	27	Strength under tension by TCD
OS θ_p _infill%	V-notched porous	0, 30, 45	30, 50, 70	0.5 mm	0.4	27	Strength under tension by TCD
OI θ_p _infill%	V-notched porous	0, 30, 45	30, 50, 70	1.0 mm	0.4	27	Strength under tension by TCD
OB θ_p _infill%	V-notched porous	0, 30, 45	30, 50, 70	3.0 mm	0.4	27	Strength under tension by TCD

The plain specimens were tested to verify the influence of the fibre deposition angle and the shell thickness on the tensile strength, yield strength and elastic modulus of the material. The tensile tests were conducted with Quasi-static loading, according to ASTM D638-14, using the Shimadzu universal testing machine with a load capacity of 10 KN, and a crosshead speed of 2 mm/min, (Figure 5.4) which was controlled via a computer running the Trapezium software. In addition, a 50 mm long extensometer was used to measure the deformation in the central part of the specimen at different loading stages. The thickness and width of each plain specimen was measured at the centre and within 5 mm from the ends of the gauge length.

The first step in preparing for the test was to fix the grips of the testing machine at 25 mm from the end of each side of the specimen, aligning the longitudinal specimen axis with an imaginary centre line of the machine crossheads. To prevent the specimen from slipping during the test, the grips were tightened firmly and evenly. The next step was to check the load on the specimens and move the crosshead until zero or near zero loads were achieved, while setting the displacement to the zero position. Then, the extensometer was fixed in the central part of the sample. Finally, the load was applied with the specific jog rate until the specimen failed. It is worth noting that the testing machine works with auto-save test data, and the load vs displacement can be taken from the saved information on the computer.

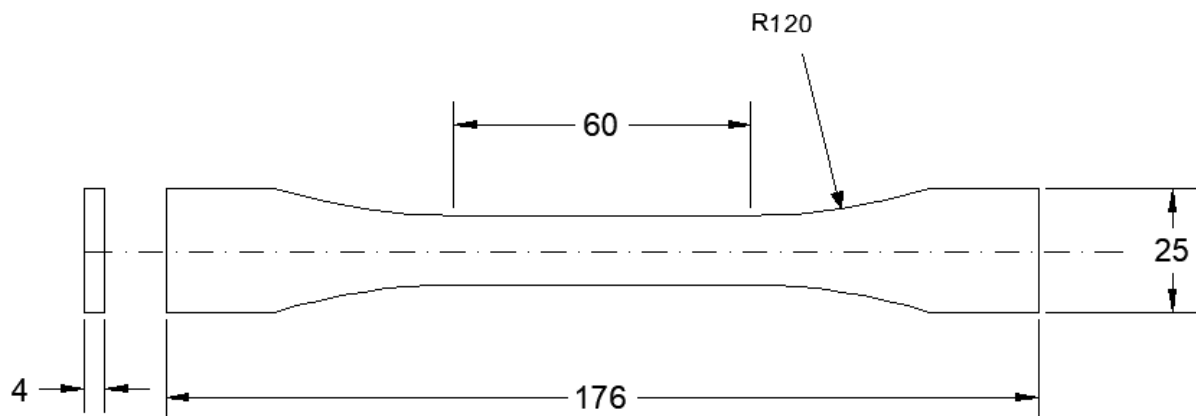


Figure 5.2 Plain specimen. Dimensions in millimetres

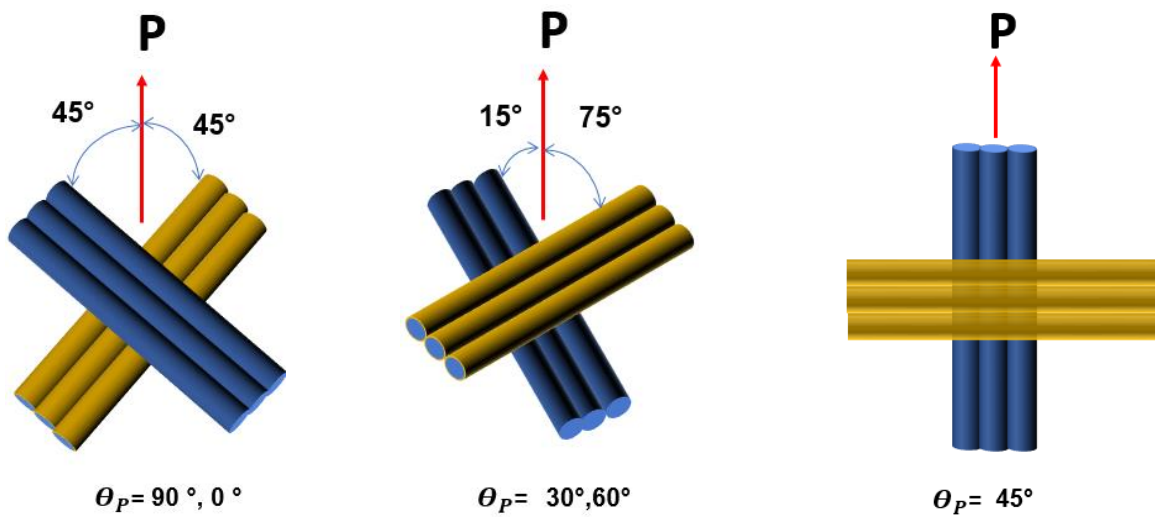


Figure 5.3 PLA fibres orientation on the applied load



Figure 5.4 Test set-up for plain specimen

5.2.2 Elastic modulus

The elastic modulus E of the PLA material, i.e., the ratio of nominal stress to corresponding strain below the proportional limit, is determined from the slope of the linear portion of the stress-strain curve (see Figure 5.5). For most plastic materials, this linear portion is very small, occurs very rapidly, and must be recorded automatically. To get the right values of material properties, the toe region in the stress vs strain curve, which exists due to slack and the seating of specimens at the beginning of the loading process, was recovered as shown in Figure 5.5. The intersection point of the straight portion (CD) of the curve with the x-axis, was selected as the zero-strain point. As a result, the elastic modulus is the ratio of the stress at any point on CD, to the strain at this point measured from point B. Young's Modulus is computed from the net cross-sectional area of the sample within the gauge length portion, and evaluating E value for PLA plain specimens was conducted according to ASTM D-638-14 [95] specification.

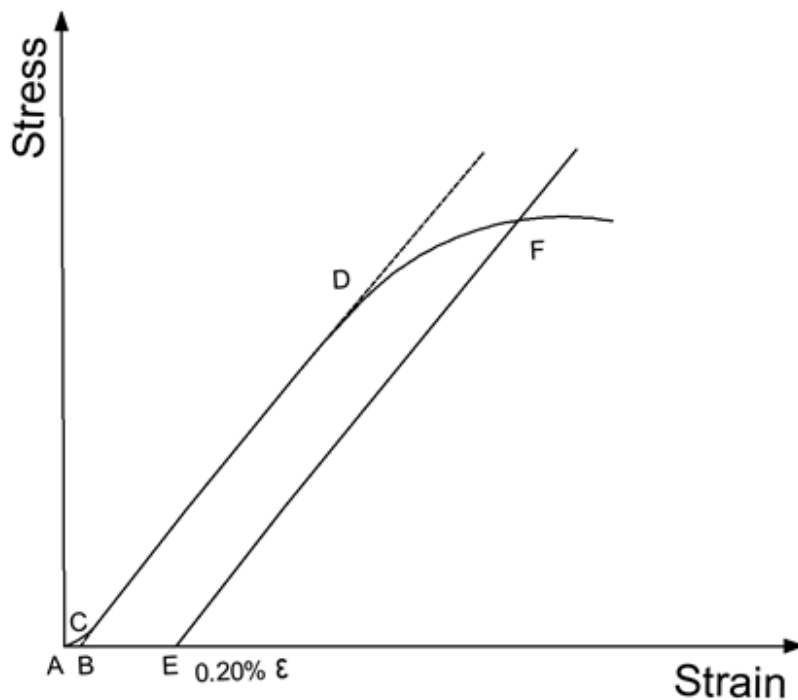


Figure 5.5 Hookean region and offset yield strength [102]

5.2.3 Strength properties

Most plastic materials evidence gradual curvature in the yield range of the stress vs strain curve. To signify the yield stress for the PLA material, therefore, the 0.2% offset yield strength, was used to evaluate the yield point on the curve. Referring to Figure

5.5, and by drawing the line, EF, at a strain offset of 0.2% on the strain axis, parallel to the linear part of the stress-strain curve, BD, we get the proof yield strength from the intersection of line, EF, with the stress-strain curve, point F. The ultimate tensile strength was computed by dividing the maximum sustained load, which represents the highest point in the specimen's stress-strain curve, over the net cross-sectional area within the extensometer length.

5.2.4 Specimens with crack-like notches

The crack-like sample groups were manufactured by the same printing parameters used for plain specimens with a specimen thickness of 4 mm. Three groups of specimens with different shell perimeter thicknesses were made. The shell thickness varied from 0 mm, 0.4 mm, to 0.8 mm; and the deposition angle changed between 0°, 30°, 45°, 60° and 90°. It should be noted that the crack-like notches, with 0° crack opening angle α , were fabricated by cutting the specimens from both sides via a sharp, thin knife (Figure 5.6a). By contrast, the specimens with shell thickness 0.4 mm and 0.8 mm, (Figure 5.6b) were fabricated directly by the 3D printer with an opening angle α of 30°, due to the adhesion of the shell perimeter on both sides of the flanks of the crack when making $\alpha = 0^\circ$. These specimens were tested to estimate the fracture behaviour of PLA AM material under investigation. The dimensions of the specimens were measured with a high- precision calliper and an optical microscope. The tests were conducted up to the complete breakage of the specimens. Three different specimens were tested for each geometry/manufacturing configuration investigated.

It was not possible to use an extensometer to measure the displacement when testing the sample under tension due to the sudden and rapid failure of the specimens. The deformations of the axial tensile test were therefore recorded from the crosshead movement, which was available on the computer records. The testing machine's grips were fixed at 25 mm from both edges of the specimen. The load vs displacement curves were sketched according to the information saved on the computer.

A quasi-static tensile loading test was conducted using a Shimadzu universal machine, under a constant displacement rate of 2 mm/min. A total of 45 specimens was tested, with a different deposition angle and shell perimeter thickness, to estimate the influence of these parameters on the fracture toughness K_{IC} of AM PLA components. The values for K_{IC} were estimated according to the Linear Elastic Fracture Mechanics (LEFM) [77].

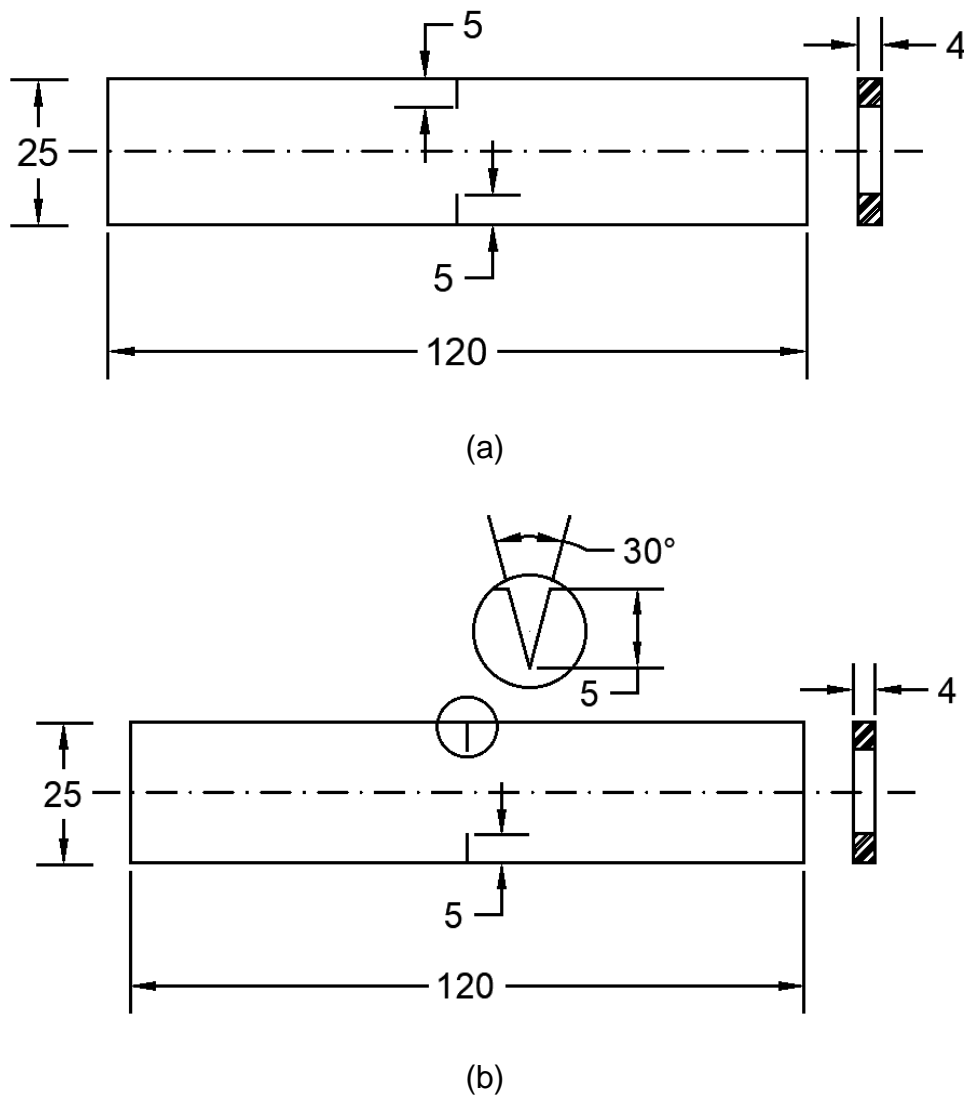


Figure 5.6 Specimens with crack-like notches (dimensions in mm (a) $\alpha = 0^\circ$; (b) $\alpha = 30^\circ$)

5.2.5 Notched PLA specimens

Experimental tensile tests were performed on PLA notched specimens with a 4 mm thickness. Figure 5.7 presents the details of specimens with different variables. The test included several notches with different stress concentration factors. The notches were selected to represent a wide variety of sizes and different stress riser shapes. The fracture strength and behaviour, under tension and 3-point bending, were analysed, and the TCD was verified per the test results and the FE analysis for different parameters.

To investigate the strength and behaviour of the notched AM PLA under static loading, U-notched and open notched samples were manufactured with deposition angle θ_p varying in the range of 0, 30, and 45 degrees. All samples had a thickness equal to 4 mm. Three types of notches were used: sharp ($r_n=0.5$ mm), medium ($r_n=1.0$ mm), and blunt ($r_n=3$ mm), to obtain different values of the stress concentration factor. Doing this allowed the influence of various stress field distributions near the notch tip to be investigated. Figure 5.7 displays the dimensions sent by the STL file to the printer for the U-notched and V-notched samples.

Regarding the loading type (Figures 5.7a- 5.7f) display the U-notched and V-notched specimens tested under tensile loading; while Figures 5.7g-5.7m present the U-notched and V-notched samples tested under 3-point bending. Quasi-static tensile and 3-point bending tests were run using a Shimadzu universal machine, with a constant displacement rate of 2 mm/min. The tests were conducted up to the complete breakage of the specimens. Three different specimens were tested for each notch root radius and deposition angle investigated.

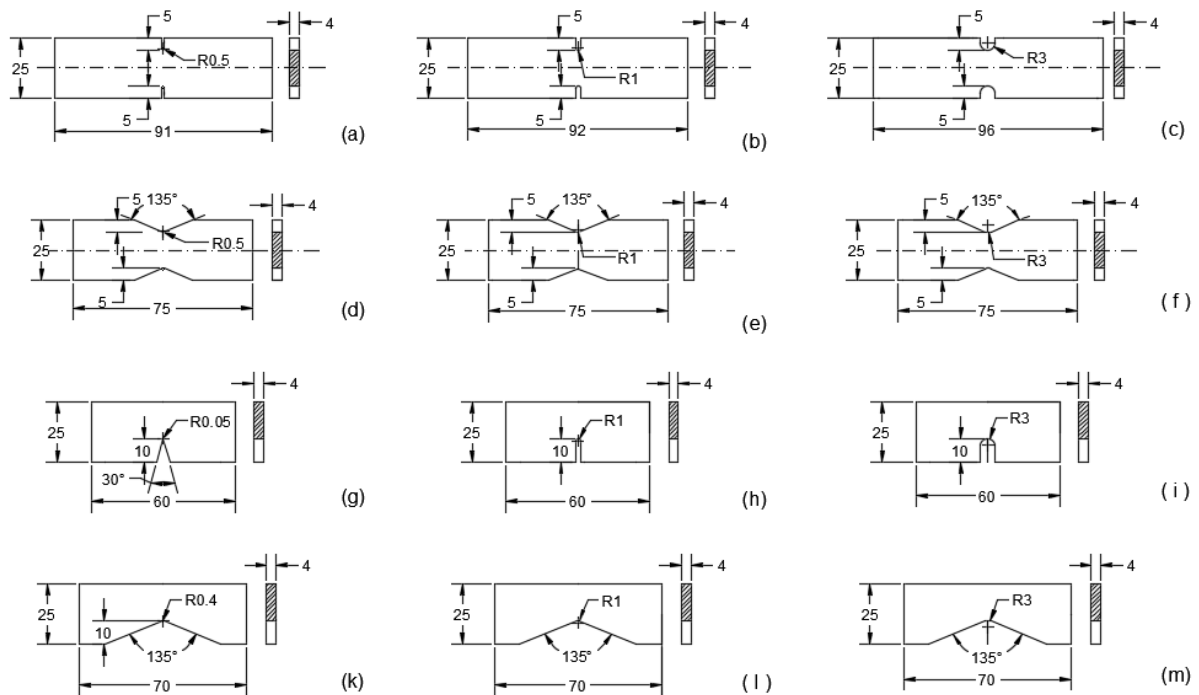


Figure 5.7 Notched specimens (dimensions in millimetres), the tolerance equal to ± 0.02

The influence of the notch radius and the deposition angle on the fracture behaviour and strength of every specimen kind was investigated. In addition, the load-displacement relation for every tested specimen was constructed based on the test results. The main objective when testing these specimens was to evaluate the static strength of the notched PLA AM components by utilising the PM, LM and area method strategies of TCD.

Regarding open notched specimens, it is well known that the notch opening angle, α , affects the distribution of the local linear–elastic stress fields. The effect of the opening angle can be neglected with little loss of accuracy, however, as long as α is lower than 90° . In contrast, for α values greater than 90° , the opening angle influences the overall strength of the notched component, in addition to the profile and magnitude of the local linear elastic stress field. Accordingly, the manufacturing of the open notched specimens was achieved with an α value equalling 135° [103].

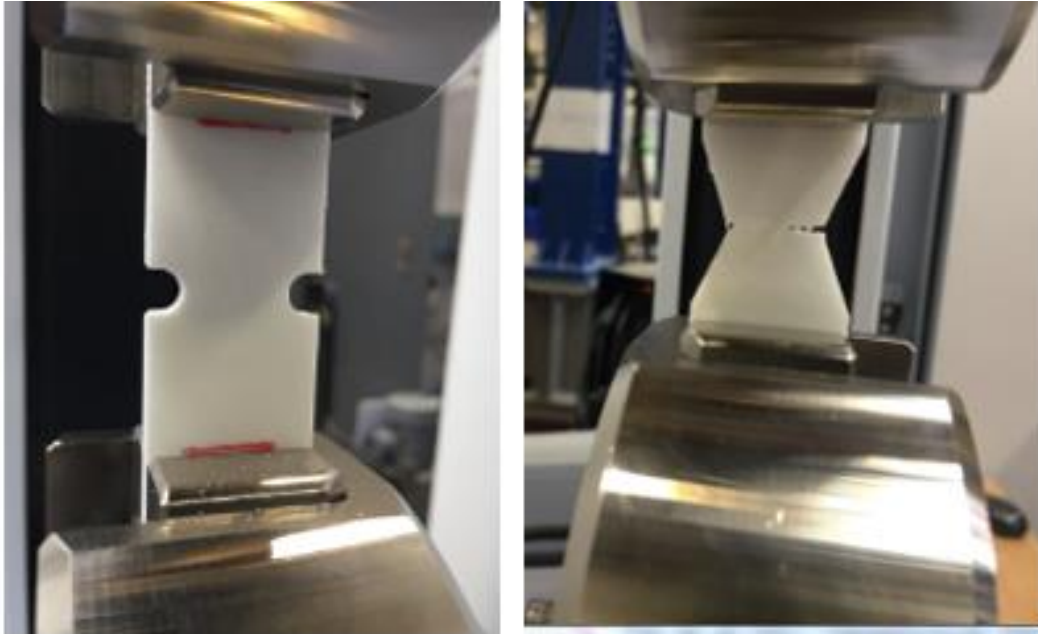


Figure 5.8 Testing of notched specimen under tension

The failure stress σ_f for specimens under tensile loading is computed by dividing the ultimate applied load F_f , on the net cross-sectional area between the notches. Figure 5.8 presents the testing apparatus for notched AM PLA samples under tension. For notched specimens under 3-point bending, the failure stress (σ_f), is calculated as the maximum stress before the failure, from the FE modelling, Figure 5.9.

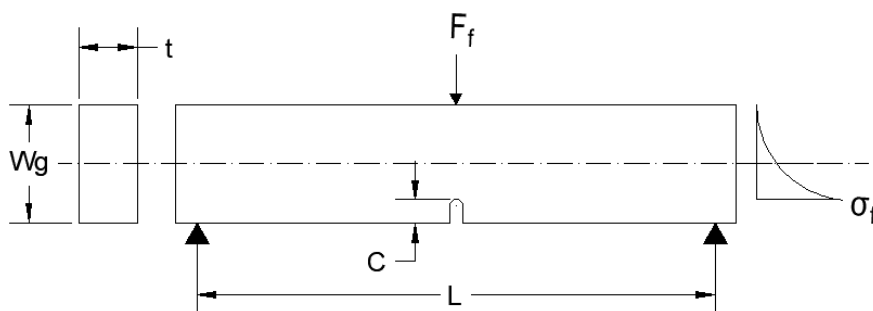


Figure 5.9 Failure stress of notched specimen under 3-point bending

The samples with single edge U and V notches (Figures 5.7g to 5.7m) were tested with 3-point bending. For U-notched samples, the span between the two lower supports was set to 50 mm (Figure 5.7g - 5.7i), and to 60 mm for the samples containing single open notches (Figures 5.7k - 5.7m). Bending tests were conducted on U-notched and V-notched specimens to evaluate the fracture strength and the fracture behaviour under this kind of loading. Figure 5.10 displays a sample picture of PLA specimens, loaded under 3-point bending. The effect of different manufacturing parameters on the strength and fracture behaviour was investigated. Each specimen's configuration had its own FE model to assess the stress field near the notch root.

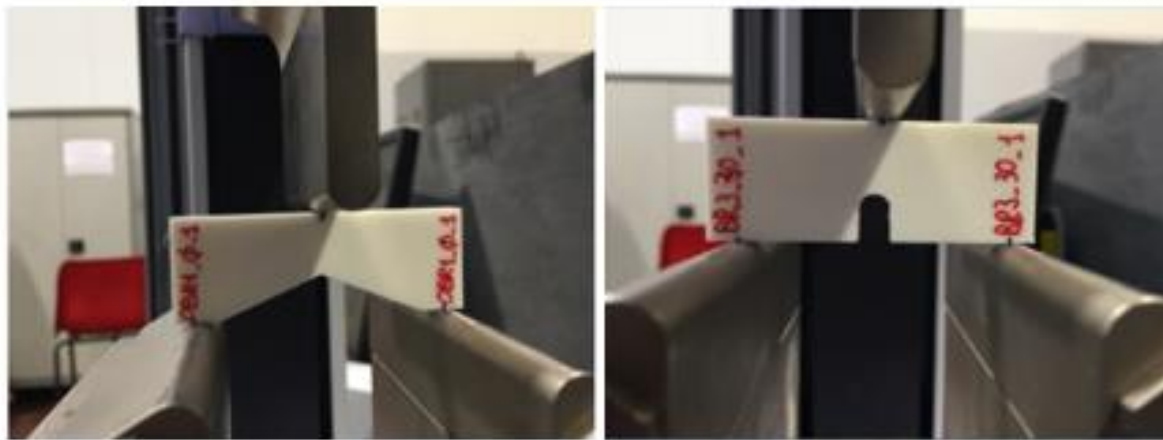


Figure 5.10 Notched specimens under 3-point bending

5.2.6 Plane strain fracture toughness test

The Compact Tension (CT) test was implemented according to ASTM, D5045-14 [104] to estimate the plane strain fracture toughness K_{IC} (Figure 5.11). The thickness of the tested specimens was set to 20 mm, and the shell thickness, t_s , to 0.4 mm. The manufacturing angle, θ_p , alternated between 0° , 30° and 45° , and the test was repeated three times for every value of θ_p . Contrary to the ASTM D5045-14 recommendation, no pre-crack was involved in CT specimens in order to estimate the influence of shell thickness on the fracture toughness of AM PLA components.

The CT testing apparatus is shown in Figure 5.12. Before the start of the test, the sample was fixed with screws so that the specimen aligned with the crosshead centre of the testing machine. The test was conducted at a temperature of 23°C , and the crosshead movement's rate was 2 mm/min. The machine recorded the load-displacement for every step of the test until complete failure occurred. To find the value of the applied load P_Q , which is used in estimating the fracture toughness (Equation

5.1) the inverse slope of load vs. displacement is needed to draw the line AB*, as shown in Figure 5.13. If the value of $(P_{max}/P_Q) \leq 1.1$, P_Q (extracted for the intersection of AB* with the load vs. displacement curve), will be substituted in Equation (5.1); otherwise, the test is invalid. The fracture toughness was calculated according to the following equations [104],

$$K_Q = \left(\frac{P_Q}{BW^2} \right) f(x) \quad (5.1)$$

Where $(0.2 < x < 0.8)$

$$f(x) = \frac{(2+x)(0.886+4.64x-13.32x^2+14.72x^3-5.6x^4)}{(1-x)^{3/2}} \quad (5.2)$$

Where:

P_Q = load (KN)

B =specimen thickness (cm)

W = specimen width (cm)

a = crack length (cm)

$x = (a / w)$

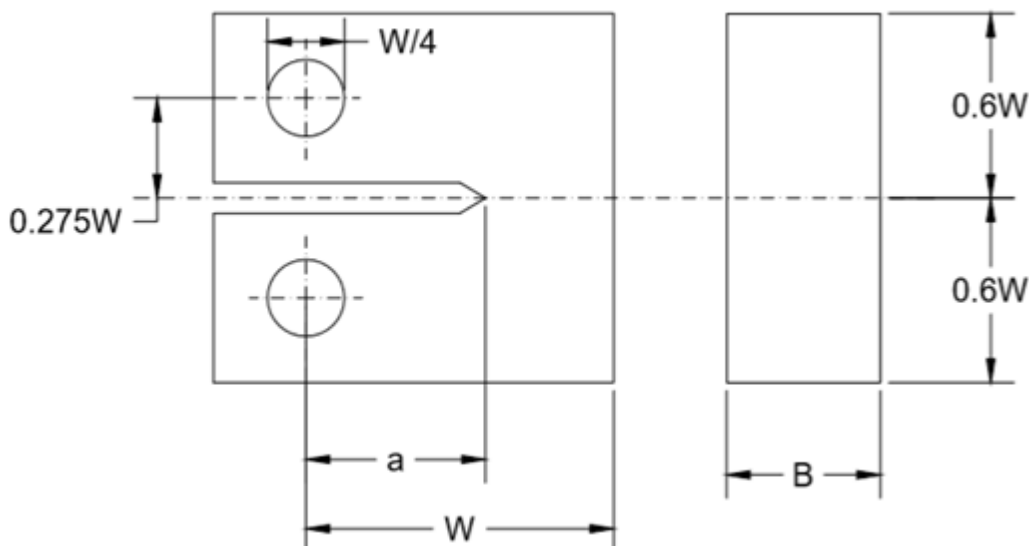


Figure 5.11 Compact tension configuration, CT [104]

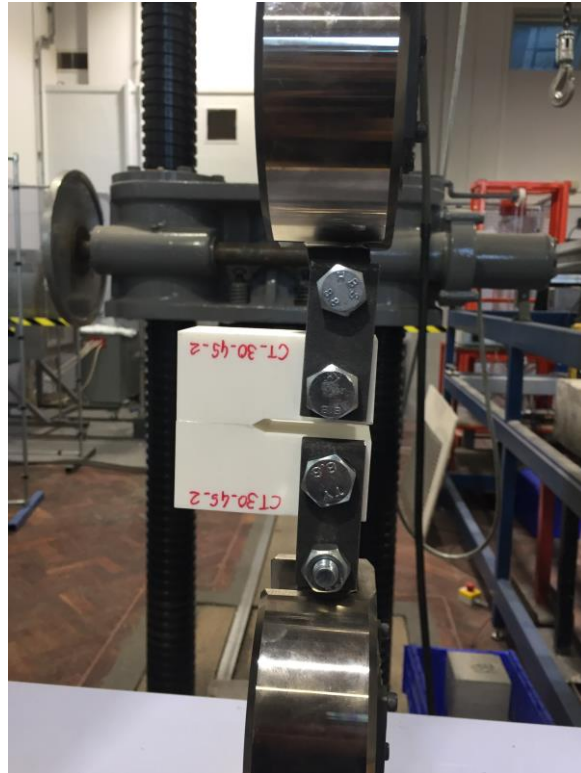
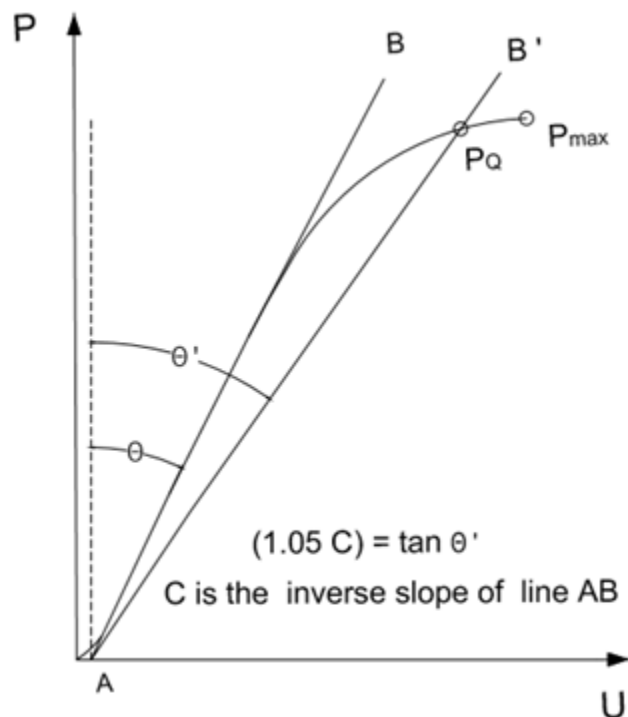


Figure 5.12 CT testing apparatus

Figure 5.13 Determination of C and P_Q for CT test [104]

It is important to check the validity of K_Q , which is obtained from Equation (5.1) as follows:

$$\text{If: } 2.5 \left(\frac{K_Q}{\sigma_y} \right)^2 < B, a, (w-a) \quad (5.3)$$

Then: $K_Q = K_{IC}$

Otherwise, the thickness of the specimen should be increased because the test does not give a valid K_{IC} value [6]. The symbol σ_y in Equation (5.3) is the material's yield stress. Consequently, and to get a valid plane strain fracture toughness K_{IC} , the thickness of the CT specimen was increased to 30 mm.

5.3 Porous PLA specimens with variable infill level

The manufacturing parameters and testing procedure, implemented in PLA porous parts with less than the 100% infill ratio, were the same as for solid specimens (100% infill level). Investigating the influence of the infill ratio on the mechanical performance of the plain PLA samples was achieved by alternating the ratio within the range of 10% to 90%, while the deposition angle θ_p alternated between 0°, 30° and 45°. The dimensions of the plain specimens are the same as for the solid samples (Figure 5.2). Every specimen's configuration was repeated three times to obtain statistical reliability for the test results. The thickness and the width of specimens were measured in three places within the middle of the part, which is the place for the extensometer measurements. The shell thickness of all porous samples was 0.4 mm, and the tensile test was achieved under 2 mm/min displacement.

Figures 5.7a -- 5.7f display the dimensions of notched porous specimens. The deposition density is set to 30%, 50%, and 70%, while θ_p was varied between 0°, 30°, and 45°. All porous PLA specimens were tested under tension, whereas testing the porous PLA notched parts under 3-point bending was not done as part of this work because of time limits. The effective size of the manufactured voids d_v were measured for both plain and notched specimens by an optical microscope, as defined in Figure 5.14.

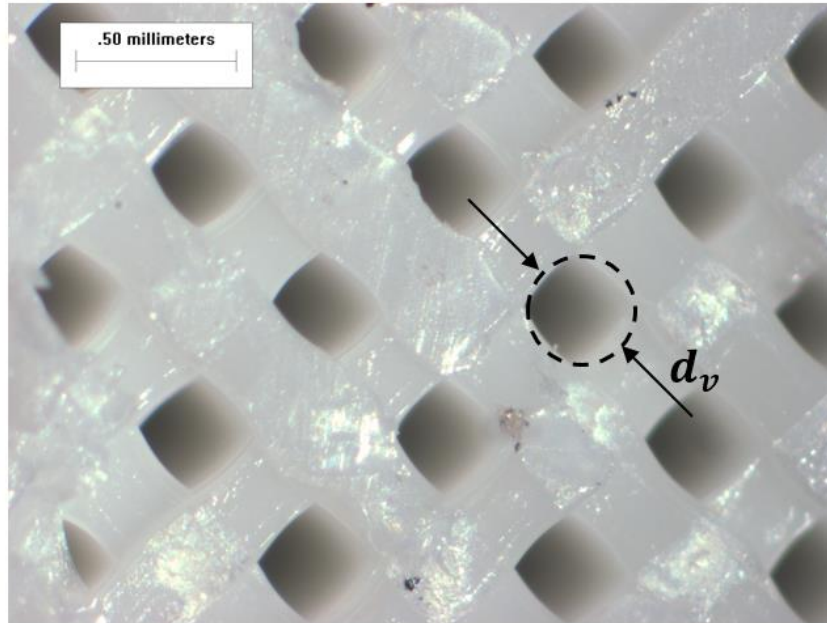


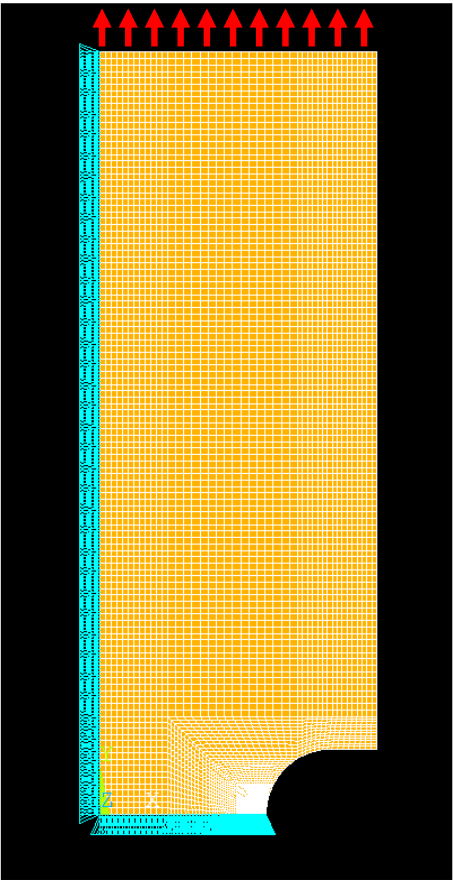
Figure 5.14 The effective void size, d_v

5.4 Numerical simulations

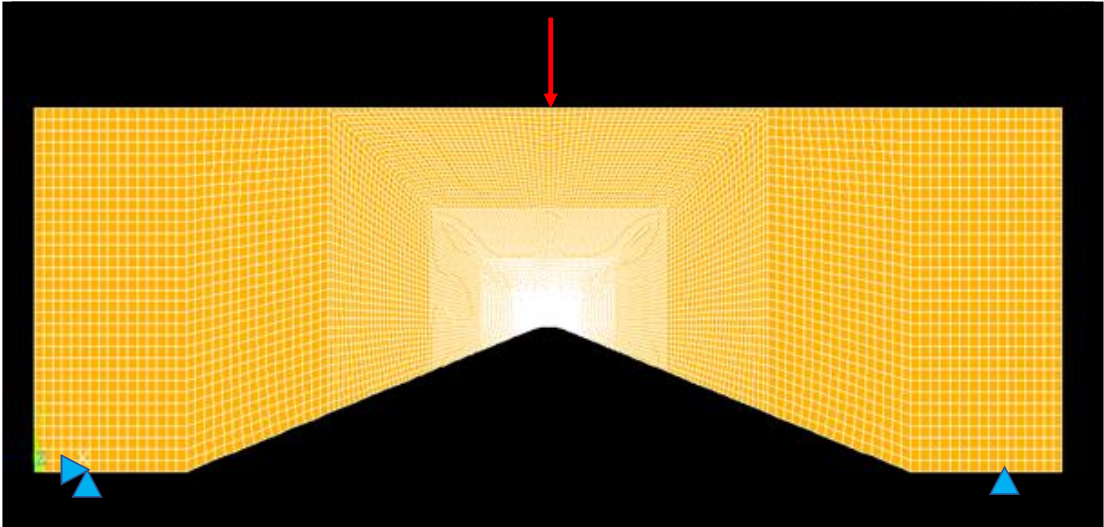
To assess the stress field around the notch's apex in the incipient fracture, it is necessary to use FE modelling. Bi-dimensional FE models, with plane stress, for all notched specimens were conducted using Ansys software by setting the material as homogeneous and isotropic. The material is processed as linear elastic; and the modelling was accomplished with a specific Poisson ratio 0.33[105]; an average elastic modulus 3550 MPa; and a yield stress of 41.8 MPa, as computed from the plain specimens' results.

Regarding the specimen's symmetry, the model was expressed as a quarter of the sample for tensile loading. On the contrary, for 3-point bending, the whole geometry was modelled to simulate the full supporting condition. Figure 5.15 displays the loading and boundary conditions for the FE models under tension and 3-point bending.

The final stress field was taken after the process of the mapped mesh refining will not considerably affect the magnitude of the maximum stress at notch tip, and the convergence of the stress field will occur for every model. When the aspect ratios of the boundaries and the edges are too large and the geometry is complex, it is important to simplify the mesh operation by using the geometric partitioning concept. Different algorithms of partitioning can be used, and the most appropriate option is problem dependent. In order to maintain the map meshing technique, the partitioning in this work followed the diagonal line emanating from the critical zone as shown in Figures 5.16 and 5.17.

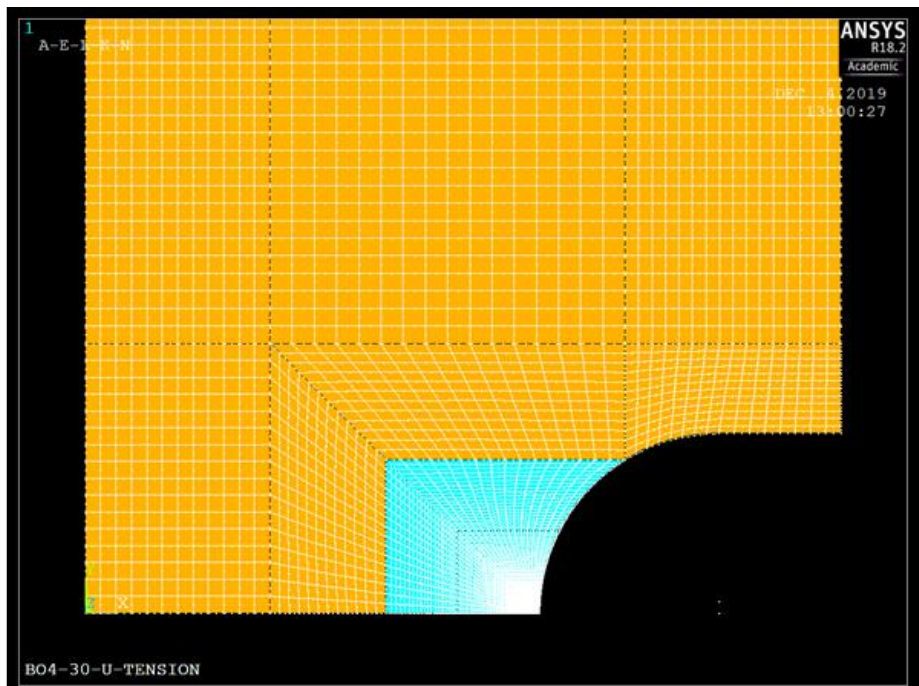


(a)

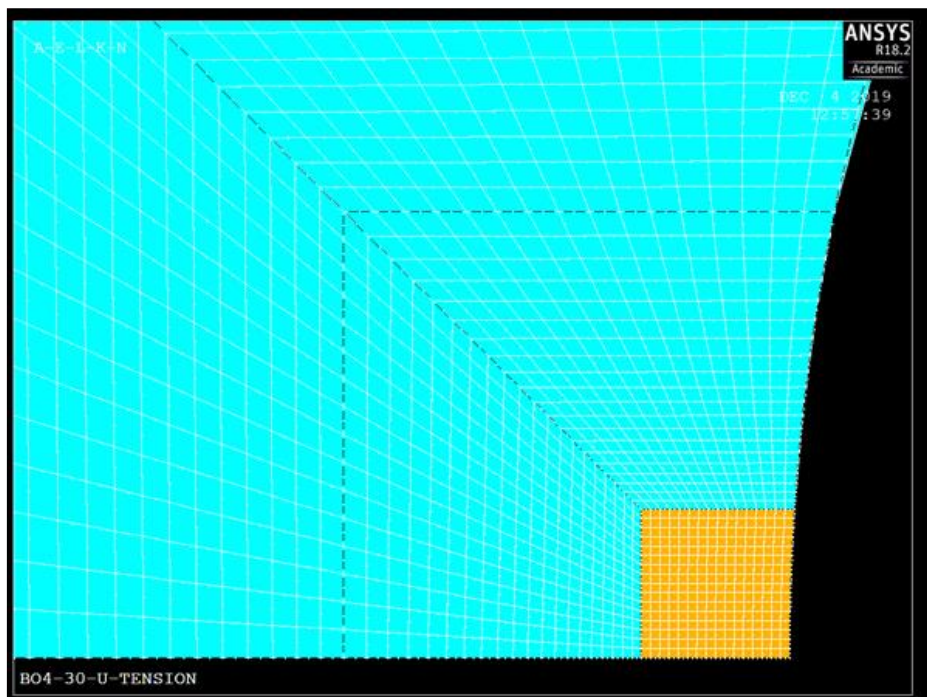


(b)

Figure 5.15 FE Model set-up and boundary conditions: a) U-notched sample under tension: b) V-notched sample under 3-point bending



(a)

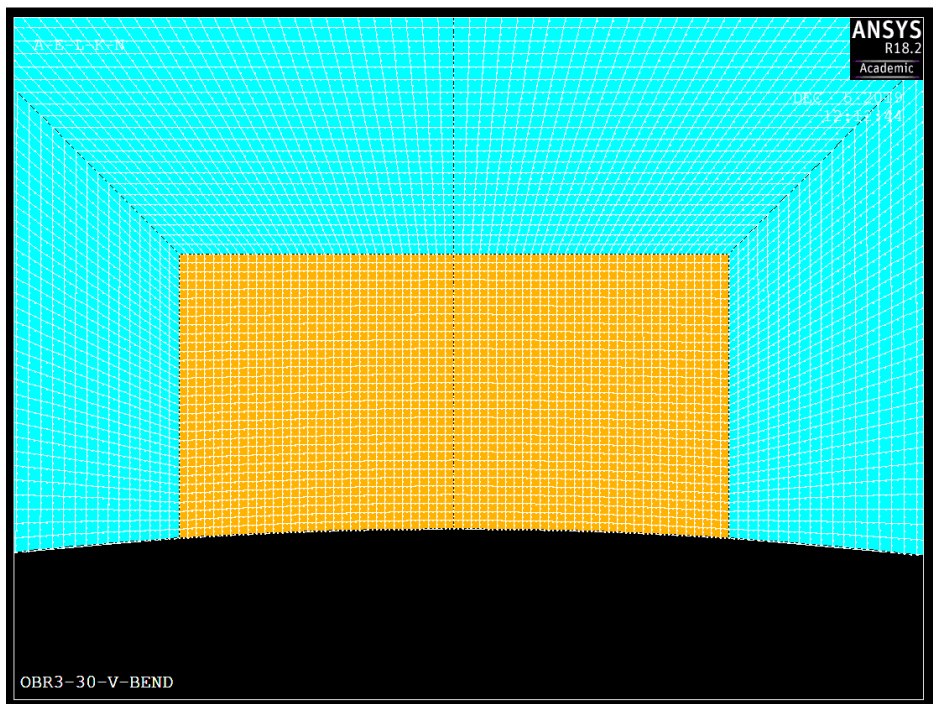


(b)

Figure 5.16 Partitioning for PLA specimens model under tension, a) Whole sample, b) At the notch tip



(a)



(b)

Figure 5.17 Partitioning for PLA sample model under 3-point bending, a) Whole sample, b) At the notch tip

The analysis was conducted by employing the two-dimensional element, eight-nodes type Plane 183. The used element was quadratic with plane stress type. This element has eight nodes and is suitable for modelling various kinds of meshing produced by different CAD/CAM programs. The element behaves with two kinds of nodal displacement: in the y and x direction. It is able to be used for modelling problems with a large strain and large deflection [106].

It is worth noting that the implemented meshing was fine at the notch tip, while coarse at the far end, in order to reduce program processing time. TCD can give reasonable predictions when evaluating the stress field in the critical region by FE modelling when the element size is less than the critical distance L [8]. Nevertheless, the finer meshing can give an accurate picture for the stress field, which was done according to the common FEA procedure by refining the mesh until convergence occurs. The element shape in the process zone was square (see Figures 5.16b and 5.17b), while the element size in this zone after convergences ranged between 0.001 mm to 0.015 mm.

The stress values were taken from FE simulation, on a line representing the expected crack propagation path, and used to validate the accuracy of a TCD approach regarding experimental results. The stress-displacement curves were plotted for every model by considering the stress values perpendicular to the process line, with a symmetry around the line. The process line starts from the notch root and proceeds with the normal of load direction in specimens under tension, parallel to load direction in notched specimens under 3-points bending. Eventually, the average stress over a semi-circular area near the notch root was computed by activation of macros using ANSYS software.

Chapter 6- Results and discussion for solid AM PLA parts

6.1 Mechanical properties and behaviour of plain AM PLA

This chapter will discuss the test results, and behaviour of different specimens of AM PLA, under tension and 3-point bending, manufactured with variable printing parameters and 100% infill density. In addition, the strength prediction of different geometries and load configuration will be presented according to the TCD approach.

Figure 6.1 displays a sample of plain PLA specimens printed with different deposition angles and zero shell thickness. It is clear that the PLA parts with a deposition angle θ_p equal to 0° and 90° showed a higher length than other samples due to the plastic deformation evidenced by these parts before failure (see also Figures A.1.1-A.1.3). To evaluate the mechanical properties of PLA with a 100% infill ratio, these parts were tested under tensile loading according to the specifications available in the test matrix, (see Table 5.2). Figure 6.2 displays an example of the stress-strain curves for the plain PLA specimens tested under tension, manufactured with different values of shell thickness and infill angles. The curves showed that the behaviour of the tested PLA before the maximum stress, almost linear, independently of the deposition angle and shell thickness.

In other words, according to Figures 6.2 and A.4, whose validity is fully supported by the experimental findings of Song et al. [107], the stress vs. strain behaviour of the tested AM material could be modelled as purely linear elastic up to the *UTS*, resulting in just a slight loss of accuracy. Regarding the material's behaviour after the ultimate strength, within the nonlinear portion of the curve, components with a manufacturing angle θ_p equal to 0° and 90° showed a high degree of plastic behaviour. On the contrary, samples with θ_p equal to 30° , 45° and 60° , almost failed after the maximum stress with no noticeable elongation. This attributes to the cracking mechanism resulting in the failure of every specimen.

The fracture mechanism in the AM PLA plain specimens is comprised of two components: rectilinear cracking of the fibres and the de-bonding between the fused filaments. The first component depends on the raw materials and the ultimate tensile strength of the filament as manufactured, whereby the deposited filament fails under tensile stress. This component plays a crucial role in the elastic range of the stress vs strain curve of the material in addition to the ductile behaviour and the plastic elongation after the specimens reach the ultimate load. The second component is the weaker mechanism, always resulting in brittle failure of the material. This component depends on several printing parameters: deposition temperature, flow rate, deposition's speed, nozzle size, layer thickness, and the platform's temperature.

Referring to Figure 5.3, the failure of PLA parts manufactured with θ_p equal to 0° and 90° is controlled by rectilinear cracking of filament in every fused layer; and the weaker de-bonding mechanism contributes little to failure, which leads to noticeable ductile behaviour before final breakage. On the contrary, the crack path followed the direct tension failure of the filaments in one layer and the de-bonding between adjacent

filaments in the next layer, for AM PLA specimens fabricated with θ_p equal to 30° , 45° and 60° . This reveals the higher contribution of the weaker failure mechanism (de-bonding) in these parts leading to brittle failure after the maximum load (see Fig. A.4). This confirms the finding of Song et al. [99], when comparing the 3D printed PLA parts by testing them in the out-of-plane direction leading to brittle failure, and the in-plane test direction resulting in ductile failure.

The values of ultimate strength σ_{UTS} , elastic modulus E , and proof stress $\sigma_{0.2\%}$ were computed from the stress-strain curves, according to ASTM D638-14 [95]. Table 6.1 lists the values of mechanical properties for different deposition angles and shell thicknesses. According to this table, the ultimate strength ranged from (37 to 50) MPa, and the elastic modulus ranged between (3215-3800) MPa.

The distribution of these mechanical properties (E , σ_{UTS} and $\sigma_{0.2\%}$), vs deposition angle, θ_p , and for different values of shell thickness, are shown in Figures 6.3 to 6.5. The figures indicate a slight increase in the mechanical properties with the shell thickness. This is because the shell strengthens the direct tension mechanism and delays the crack initiation. In general, the distribution of the three mechanical properties has no trend, falling within $\pm 20\% S_D$. So, the deposition angle and shell thickness had effect on the values of the three mechanical properties measured for AM PLA components.

From an engineering viewpoint, it can be assumed that the influence of both θ_p and t_s is negligible, and the average mechanical properties values, for the 45 plain specimens being tested, are: $\sigma_{UTS} = 42.9$ MPa; $E = 3501$ MPa; and $\sigma_{0.2\%} = 41.8$ MPa, as shown in Figures 6.3-6.5. Also, given a 2% slight difference between $\sigma_{0.2\%}$ and σ_{UTS} , it is evident that the investigated stress vs strain relation for AM PLA can be modelled as linear up to its ultimate strength. Within this framework, and regarding the static assessment of the AM PLA components, it can be seen that the mechanical behaviour can be estimated without the use of non-linear stress vs strain relationships.

It is important to highlight that from the material science viewpoint, both the deposition angle θ_p and the shell perimeter thickness, influence the overall mechanical properties of the printed PLA parts.

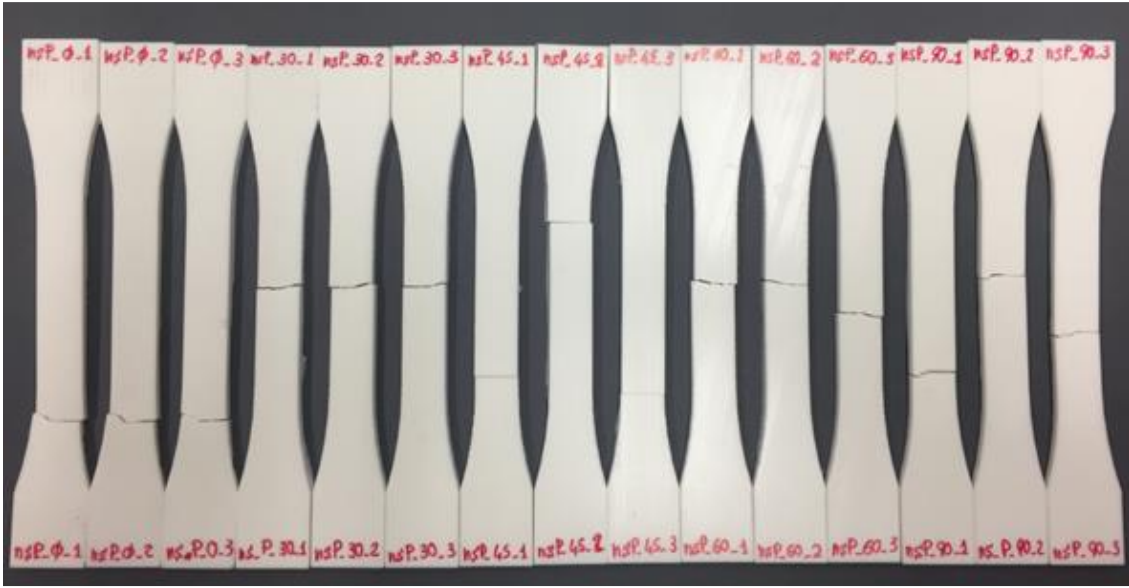
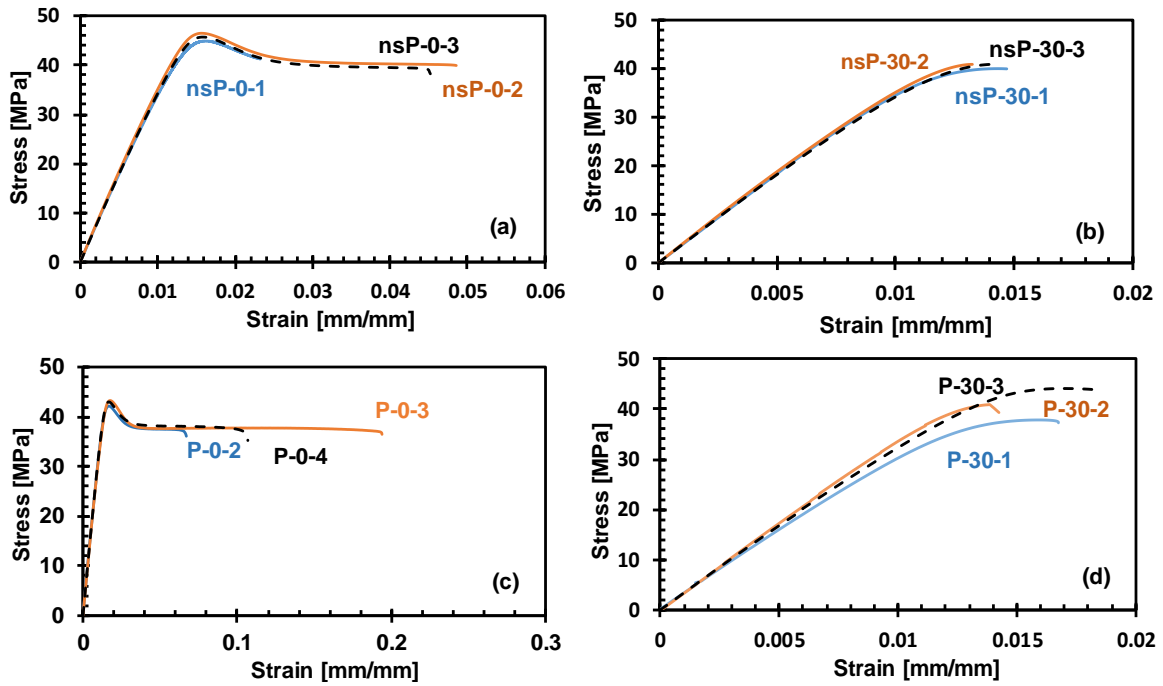


Figure 6.1 Plain specimens with t_s equal to 0



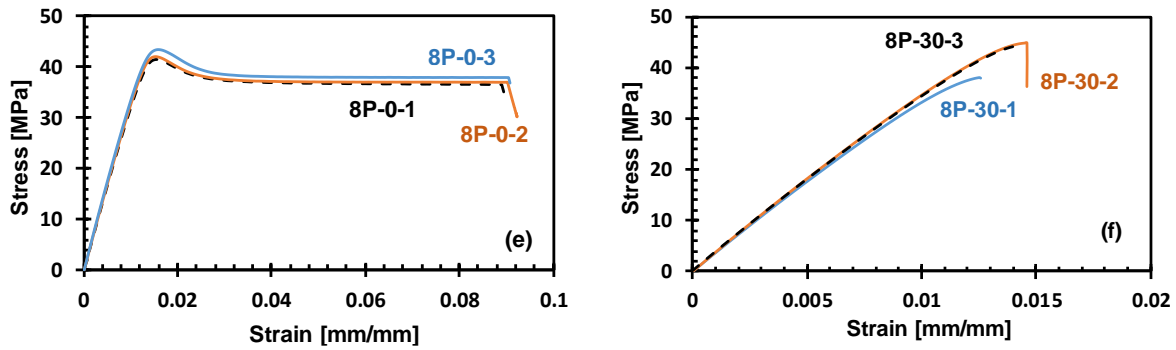


Figure 6.2 Stress vs. strain for plain samples under tension for different t_s and θ_p , a) $t_s = 0$, $\theta_p = 0^\circ$; b) $t_s = 0$, $\theta_p = 30^\circ$; c) $t_s = 0.4 \text{ mm}$, $\theta_p = 0^\circ$; d) $t_s = 0.4 \text{ mm}$, $\theta_p = 0^\circ$; e) $t_s = 0.8 \text{ mm}$, $\theta_p = 0^\circ$; f) $t_s = 0.8 \text{ mm}$, $\theta_p = 30^\circ$

The literature suggests that it is good practice for additive manufacturing of polymeric components to use a shell thickness equal to the printing nozzle diameter. Accordingly, for all notched PLA components, the shell thickness was invariably kept equal to 0.4 mm, which is equal to the nozzle size. Also noteworthy is that the results for the behaviour and mechanical properties of the samples with θ_p equal to 0° and 30° , were significantly the same as samples with θ_p equal to 90° and 60° , respectively (see Figures 6.3-6.5). For this reason, the strength of the notched samples was investigated with manufacturing angles equal to 0° , 30° , and 45° only. This testing plan reduces the number of samples needed to characterise the behaviour of the notched AM PLA components being investigated.

It is worth noting that the mechanical properties obtained for PLA components produced by conventional fabrication, such as σ_{UTS} , are in the range (45-80) MPa, and E are in the range (3200-4500) MPa [108][42][109]. However, these values for the PLA commercial product depend on several parameters such as the molecular weight, crystallinity level, and the manufacturing method. Comparing these values with the mechanical properties observed in Figures 6.3-6.5, it turns out that PLA fabricated by additive manufacturing can be produced with very similar properties to those obtained by injection moulding, notwithstanding the marked difference in the meso-structure of the two products. This outcome is certainly interesting and auspicious, especially when the AM technique can produce complex parts at a lower price than conventional manufacturing.

Table 6.1 Results of solid plain specimens under tension

Code	θ_p [Deg]	t_s [mm]	w [mm]	t [mm]	F_r [N]	E [MPa]	$\sigma_{0.2\%}$ [MPa]	σ_{UTS} [MPa]
nsP_0_1	0	0	15.25	4.13	3538	3599	43.0	44.9
nsP_0_2	0	0	15.00	4.07	3597	3700	45.0	46.5
nsP_0_3	0	0	14.93	4.18	3504	3602	44.5	45.7
nsP_30_1	30	0	15.11	4.20	3680	3685	39.0	40.0
nsP_30_2	30	0	15.03	4.09	3787	3808	40.5	41.0
nsP_30_3	30	0	14.95	4.08	3662	3676	40.0	41.0
nsP_45_1	45	0	14.98	4.17	3569	3596	38.5	39.7
nsP_45_2	45	0	14.92	4.15	3554	3562	38.5	39.6
nsP_45_3	45	0	14.99	4.22	3415	3434	36.5	37.7
nsP_60_1	60	0	15.16	4.14	3487	3501	37.0	38.0
nsP_60_2	60	0	15.11	4.16	3484	3491	37.0	38.3
nsP_60_3	60	0	15.11	4.15	3529	3540	37.0	38.3
nsP_90_1	90	0	15.14	4.20	3434	3453	39.0	40.8
nsP_90_2	90	0	15.19	4.20	3435	3437	40.0	41.3
nsP_90_3	90	0	15.15	4.21	3520	3536	39.5	41.1
P_0_2	0	0.4	14.95	4.08	3189	3288	40.9	42.1
P_0_3	0	0.4	14.93	4.07	3265	3304	42.2	43.0
P_0_4	0	0.4	14.97	4.21	3251	3245	42.0	43.4
P_30_1	30	0.4	14.85	4.11	3136	3206	35.1	37.3
P_30_2	30	0.4	15.09	4.10	3450	3502	40.1	40.8
P_30_3	30	0.4	14.92	4.04	3347	3405	40.3	44.2
P_45_1	45	0.4	14.87	4.09	3426	3413	38.6	43.0
P_45_2	45	0.4	15.15	4.07	3342	3367	40.7	42.1
P_45_3	45	0.4	15.03	4.04	3348	3371	39.1	42.1
P_60_1	60	0.4	15.06	4.13	3180	3215	40.0	39.6
P_60_2	60	0.4	15.06	4.18	3251	3302	40.1	40.9
P_60_3	60	0.4	15.00	4.08	3235	3229	40.1	42.1
P_90_1	90	0.4	15.16	3.99	3421	3448	42.4	46.5
P_90_2	90	0.4	14.95	3.98	3399	3400	42.3	47.5
P_90_3	90	0.4	15.10	4.15	3193	3187	40.7	42.7
8P_0_1	0	0.8	15.22	4.25	3369	3384	41.0	41.4
8P_0_2	0	0.8	15.16	4.22	3438	3497	41.5	42.2
8P_0_3	0	0.8	15.19	4.17	3540	3558	42.0	43.6
8P_30_1	30	0.8	15.22	4.19	3530	3547	37.8	38.0
8P_30_2	30	0.8	15.22	4.20	3651	3672	44.0	44.8
8P_30_3	30	0.8	15.19	4.17	3609	3627	44.0	44.3
8P_45_1	45	0.8	15.07	4.06	3778	3791	44.0	45.0
8P_45_2	45	0.8	15.17	4.09	3710	3729	45.5	46.4
8P_45_3	45	0.8	15.09	4.14	3688	3724	45.5	46.4
8P_60_1	60	0.8	15.05	4.20	3597	3633	44.0	45.2
8P_60_2	60	0.8	15.03	4.28	3578	3598	44.5	45.9
8P_60_3	60	0.8	15.02	4.28	3607	3638	44.0	44.8
8P_90_1	90	0.8	15.14	4.23	3585	3600	48.0	50.2
8P_90_2	90	0.8	15.09	4.20	3681	3695	47.0	50.6
8P_90_3	90	0.8	15.13	4.24	3573	3592	47.0	49.8

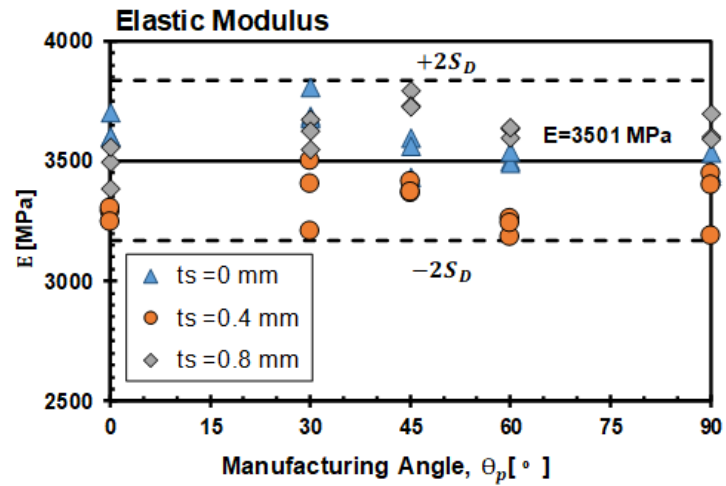
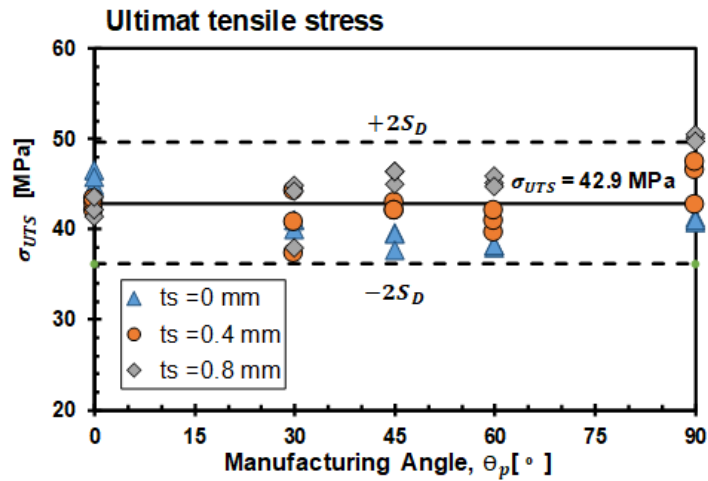
Figure 6.3 Effect of shell thickness on (E) for different θ_p 

Figure 6.4 Strength distribution of plain specimens

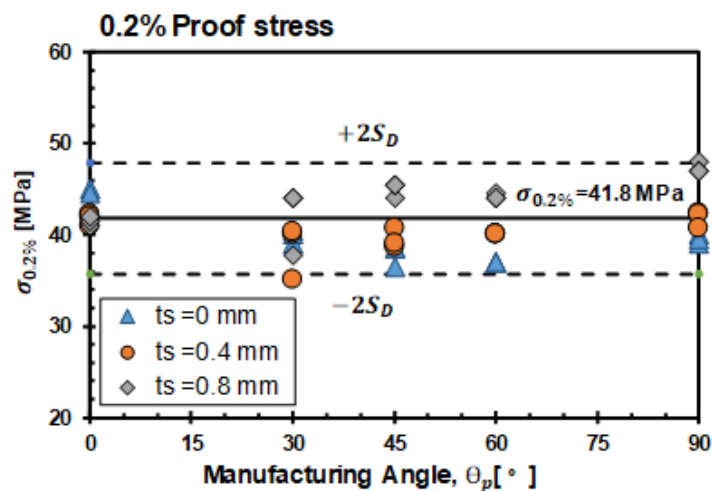


Figure 6.5 Distribution of 0.2% proof stress for plain specimens

6.2 Behaviour of AM PLA notched samples under static loading

In order to investigate the behaviour of the U-notched and the open notched PLA solid specimens under tensile and bending load, the samples were manufactured by keeping the shell thickness t_s invariably equal to 0.4 mm, while θ_p varied from 0° , 30° to 45° , as shown in Figures A.1.4-A.1.7. The notches' root radius ranged between (1, 0.5 and 3) mm, as can be seen from Table 6.2 (see also Tables A.2.1-A.2.4).

Figure 6.6 presents some samples of the load vs displacement for notched specimens under tension and 3-point bending, with different root radiuses (see also Figures A.3.2-A.3.5). For notched samples under tension, the figures show a bilinear relation of load vs displacement, independent of the profile. Specifically, the first linear region of the relation is followed by another linear part with a lower slope, and this slope change always occurs with approximately 0.5 mm displacement regardless of notch geometry. This value is related to the crack initiation of the shell thickness t_s which equals 0.4 mm. We will later see when presenting the behaviour of the crack-like specimens that this value increases with higher shell thickness.

Regarding the notched components under three-point loading, the load vs vertical displacement curves were all distinguished by an initial nonlinear trend followed by almost linear behaviour up to the final failure. The non-linear part was expected for both U-notches and V-notches due to the initial seating of specimens at the beginning of the loading process.

To investigate the behaviour of the notched AM PLA components under the tensile load, crack-like notched specimens were first tested under tension, Figure 6.7 (see also Figure A.1.8). These samples were manufactured with a deposition angle θ_p ranging from 0° , to 90° , and shell perimeter thickness t_s ranging from 0 to 0.8 mm, as shown in Table A.6.

Figure A.14 shows the load vs. displacement for crack-like notched specimens. The Figures evidence the same bilinear behaviour for the load vs displacement as the notched samples before the finale breakage. The points of slope change of the curves were affected by the shell thickness of the samples. The displacement of the slope change increased from 0.4 mm; 0.5 mm; to 0.65 mm for shell thickness t_s equal to 0 mm; 0.4 mm; and 0.8 mm respectively. This confirms that the point of changing slope of the load vs displacement is related to the crack initiation at the shell perimeter of the PLA parts under loading. Also, noteworthy is the higher failure strength mostly showed by the samples manufactured with θ_p equal to 0° , and 90° , for the same reasons as for plain samples.

The results of the failure net stress σ_f , vs. deposition angle θ_p for crack-like notched AM PLA samples are shown in Figure 6.8. It is clear that higher shell thickness gives a higher static strength for all values of θ_p , while the deposition angle has no clear influence on the failure stress of the samples with t_s equal to 0.8 mm, due to the shell thickness delaying the crack initiation at the notch's tip. Whereas the effect of θ_p on the strength of PLA parts manufactured with t_s equal to 0 mm and 0.4 mm, is clearer;

and the samples with θ_p equal to 0° and 90° showed higher failure stress due to the same reasons explained for plain AM PLA specimens.

Table 6.2 Results of U-notched specimens under tension

Code	θ_p [Deg]	t_s [mm]	r_n [mm]	W_n [mm]	W_g [mm]	t [mm]	F_r [N]	σ_f [MPa]
S04_0_1	0	0.4	0.51	15.32	24.90	4.21	3234	50.1
S04_0_2	0	0.4	0.50	15.39	24.98	4.25	3212	49.1
S04_0_3	0	0.4	0.52	15.32	24.99	4.23	3123	49.7
S04_30_1	30	0.4	0.49	15.34	24.90	4.19	2861	44.5
S04_30_2	30	0.4	0.49	15.35	24.92	4.22	2815	43.5
S04_30_3	30	0.4	0.48	15.34	24.92	4.22	2824	43.6
S04_45_1	45	0.4	0.50	15.42	24.97	4.21	2777	42.8
S04_45_2	45	0.4	0.52	15.59	25.01	4.2	2861	43.7
S04_45_3	45	0.4	0.50	15.38	24.91	4.19	2713	42.1
I04_0_1	0	0.4	0.97	15.2	24.81	4.22	3355	52.3
I04_0_2	0	0.4	1.00	15.26	24.82	4.24	3311	51.2
I04_0_3	0	0.4	0.98	15.27	24.84	4.2	3327	51.9
I04_30_1	30	0.4	0.99	15.26	24.97	4.12	3274	52.1
I04_30_2	30	0.4	1.00	15.28	24.98	4.18	3262	51.1
I04_30_3	30	0.4	0.99	15.27	24.96	4.16	3260	51.3
I04_45_1	45	0.4	1.01	15.38	25.00	4.18	3206	49.9
I04_45_2	45	0.4	1.02	15.29	24.98	4.12	3182	50.5
I04_45_3	45	0.4	1.03	15.26	24.99	4.16	3174	50
B04_0_1	0	0.4	3.00	15.09	24.93	4.32	3330	51.1
B04_0_2	0	0.4	3.00	15.21	24.90	4.26	3307	51
B04_0_3	0	0.4	3.00	15.12	24.92	4.3	3294	50.7
B04_30_1	30	0.4	3.00	15.16	25.10	4.39	2986	44.9
B04_30_2	30	0.4	3.00	15.2	25.60	4.3	2706	41.4
B04_30_3	30	0.4	3.00	15.16	25.09	4.32	3099	47.3
B04_45_1	45	0.4	3.00	15.18	25.07	4.2	3179	49.9
B04_45_2	45	0.4	3.00	15.15	25.12	4.22	3230	50.5
B04_45_3	45	0.4	3.00	15.19	25.12	4.26	3163	48.9

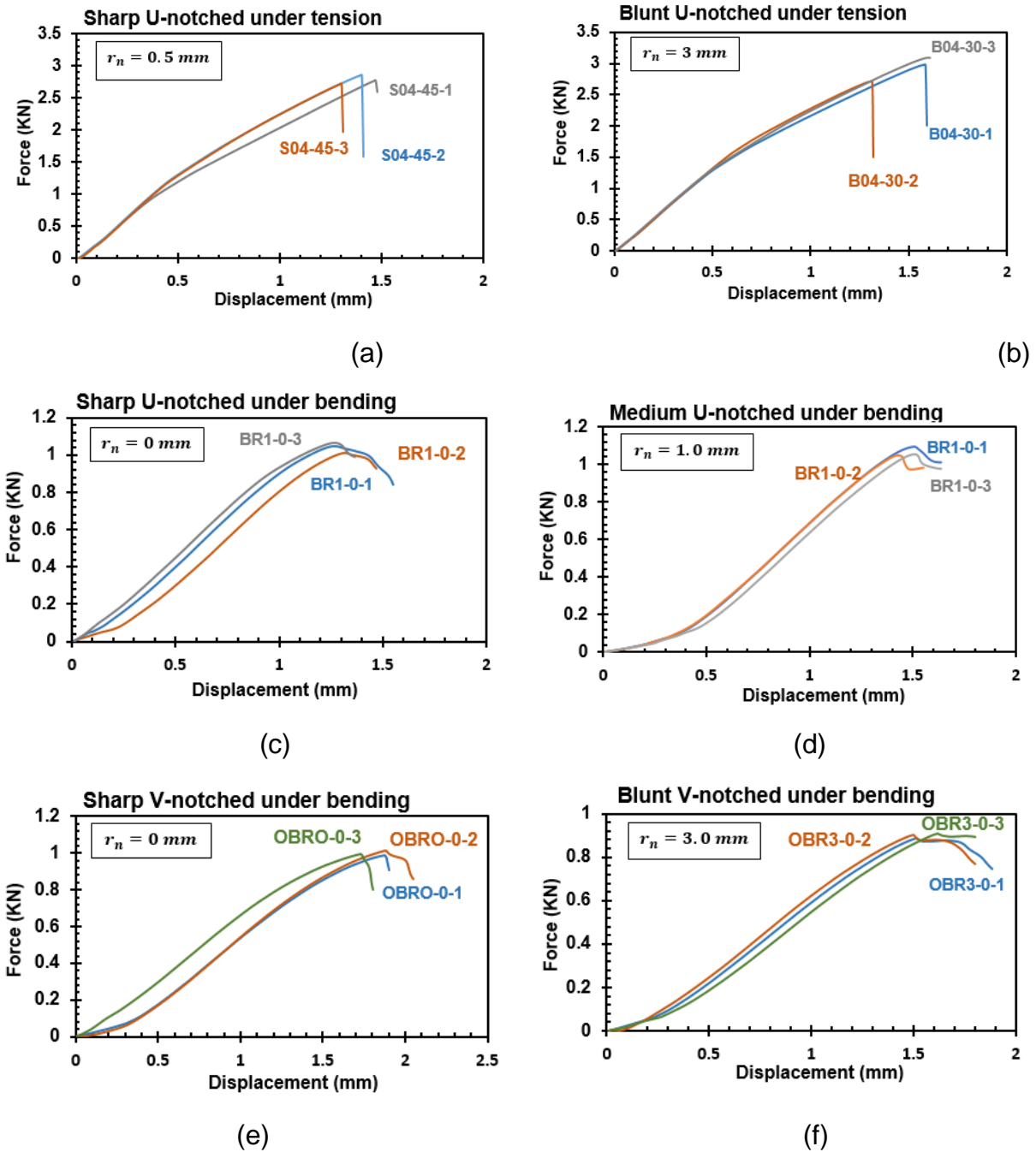


Figure 6.6 load vs displacement for notched specimens, a) $\theta_p = 45^\circ$; b) $\theta_p = 30^\circ$; c) $\theta_p = 0^\circ$; d) $\theta_p = 0^\circ$; e) $\theta_p = 0^\circ$; f) $\theta_p = 0^\circ$

Unlike the plain specimens, the relationship for the failure stress and the deposition angle (Figures 6.9 to 6.12) showed a clear effect of θ_p on the failure strength for U-notched and open notched specimens tested under tensile and 3-point bending. This influence was clearer for the samples under the bending test (Figure 6.10 and Figure 6.12).

Comparing the notched samples (Figures 6.9-6.11) with the plain specimens in Figure 6.4, we see mostly the same trend for the samples with a θ_p equal to 30° , which showed lower failure strength due to the crack pattern following the fused filament direction at a 15° inclination. This means that the failure is controlled by the de-bonding mechanism which is weaker than the failure by direct tension of the filament (see Figure 5.3). This fracture behaviour is mostly the same as the failure of plain specimens under tension with a shell thickness of 0.4 mm. While the samples with a θ_p equal 0° and 45° showed mode I cracking, leading to higher failure strength (see Figure 6.13); nevertheless, samples manufactured with $\theta_p = 45^\circ$, showed a lower failure strength than specimens fabricated with $\theta_p = 0^\circ$, due to less contribution of the fibres to the direct tension failure (see Figure 5.3). This behaviour is not consistent across all samples due to the complicated behaviour of the AM PLA parts under investigation (see Figure 6.10).

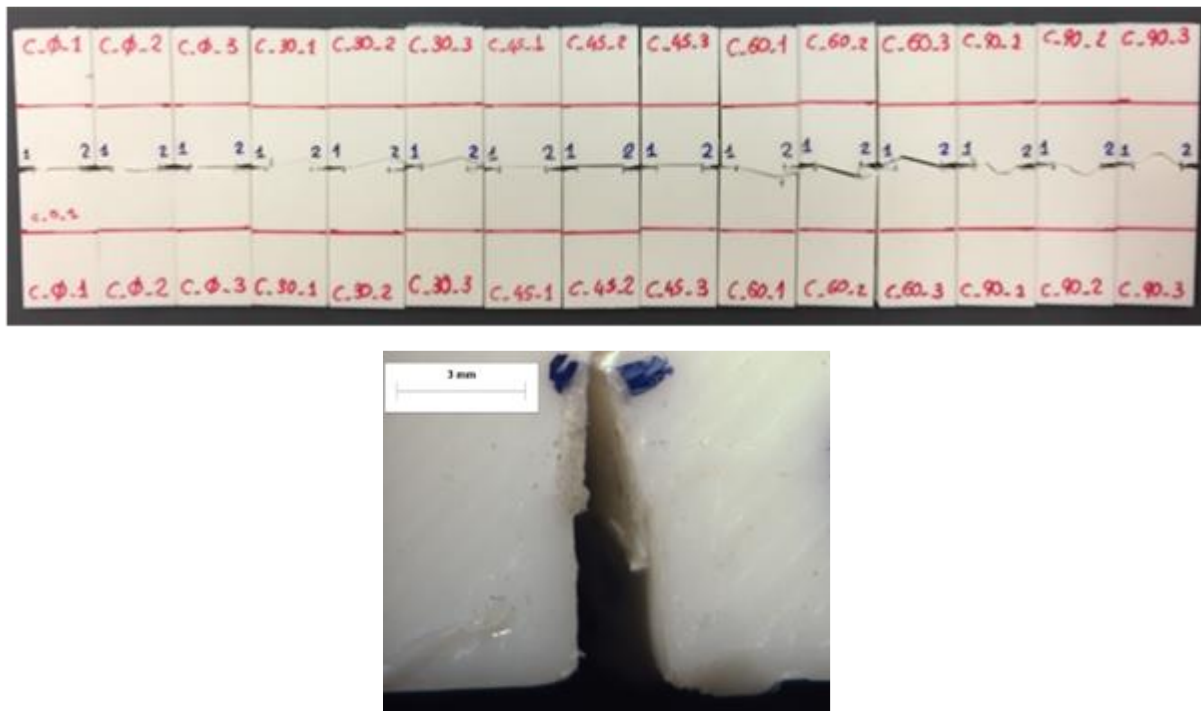


Figure 6.7 Cracked specimens with microscope picture for the crack tip, $t_s = 0 \text{ mm}$

It is worth pointing that the sharpest notches did not always demonstrate less strength, which was uncommon trend, as shown in the results of V-notched and U-notched samples under tension, particularly for a θ_p to equal 30° . It can be seen from Figures 6.9-6.12 that the average of the failure stress, for different θ_p values is represented by a straight horizontal line for every value of the root radius. Due to the unclear and complex behaviour of the notched samples under loading, these lines purport to present the general trend in a simple way.

Finally, considering the contour plot in Figures 6.14-6.17, the higher strength of notched specimens was noticed when the θ_p was equal to 0° , and the notch was blunt. This happens because the direct tension failure was the dominant on the two orthogonal deposited filaments in every layer (which is stronger than de-bonding failure as explained for plain samples), and the blunt notch presents less stress concentration. This correlation is not clear for V-notched specimens under 3-point bending, however (Figure 6.17).

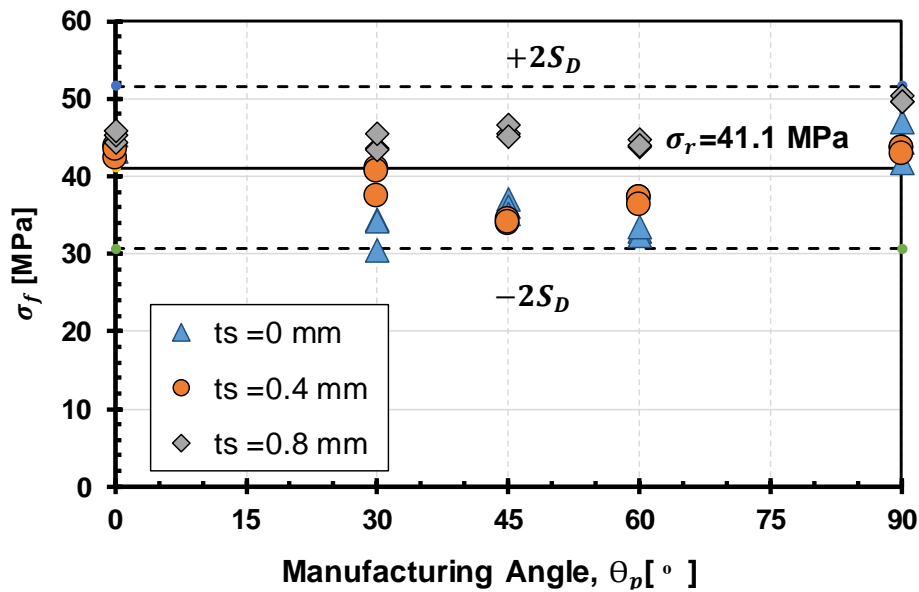


Figure 6.8 Ultimate strength vs. θ_p for crack-like specimens

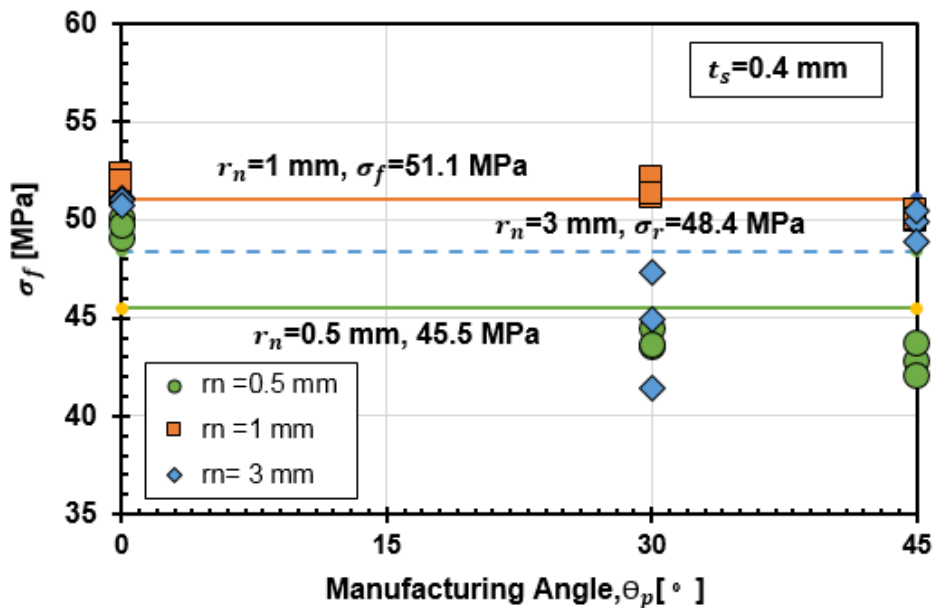


Figure 6.9 Failure strength for U-notches specimens under tension

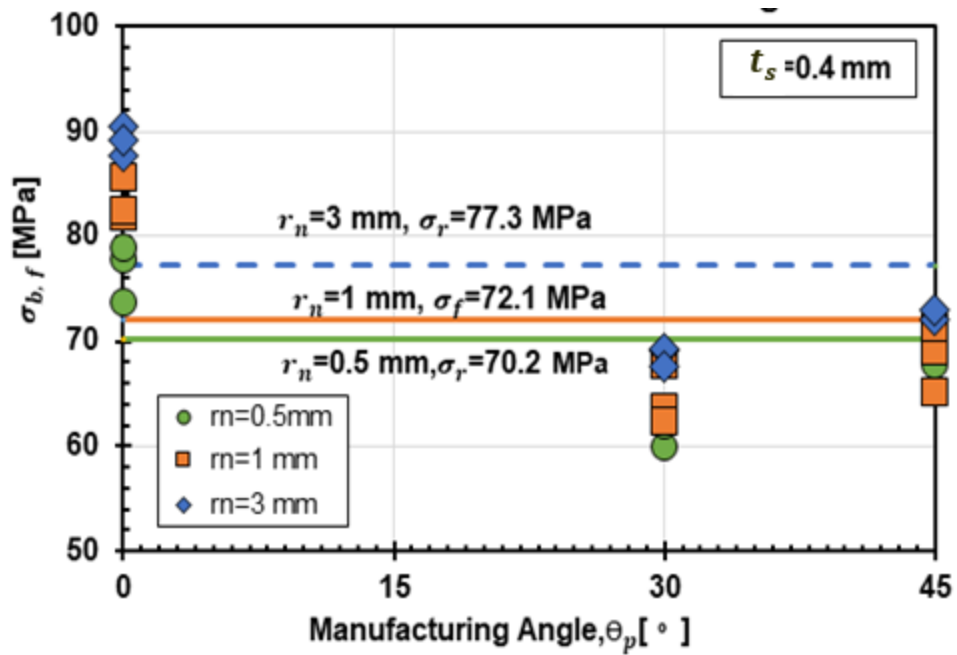


Figure 6.10 Failure stress for U-notched specimens under 3-point bending

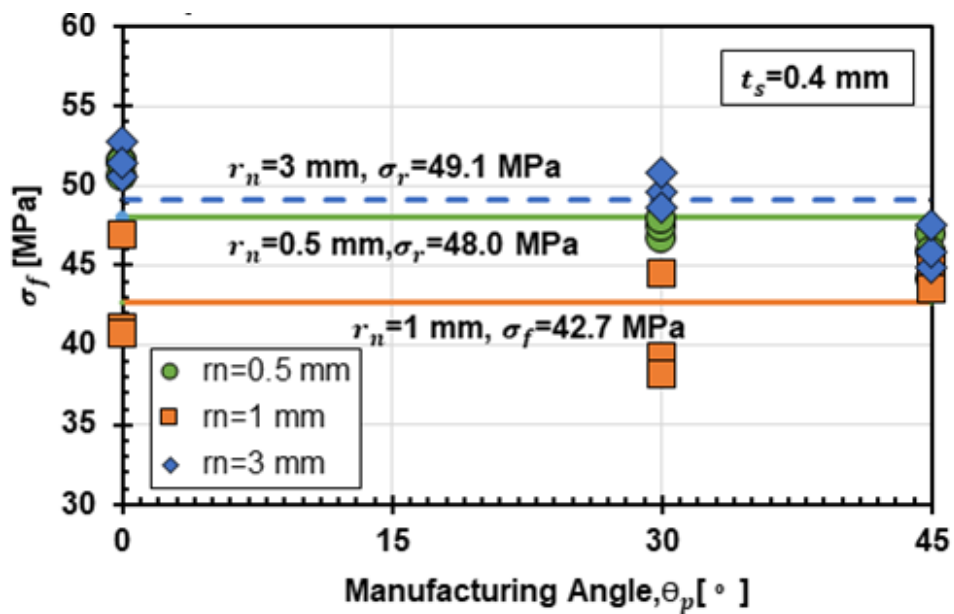


Figure 6.11 Failure strength for open notched specimens under tension

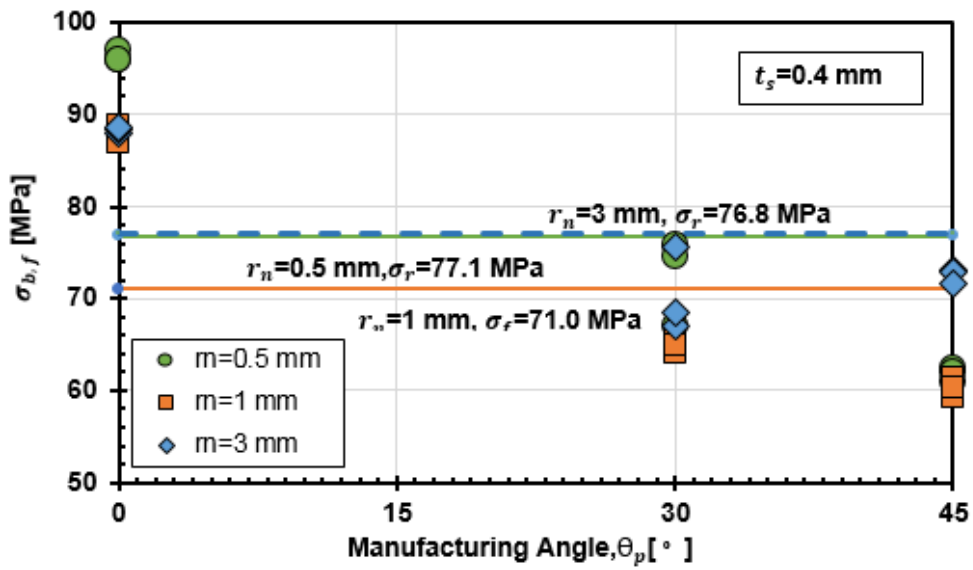


Figure 6.12 Failure strength for open notched specimens under 3-point bending

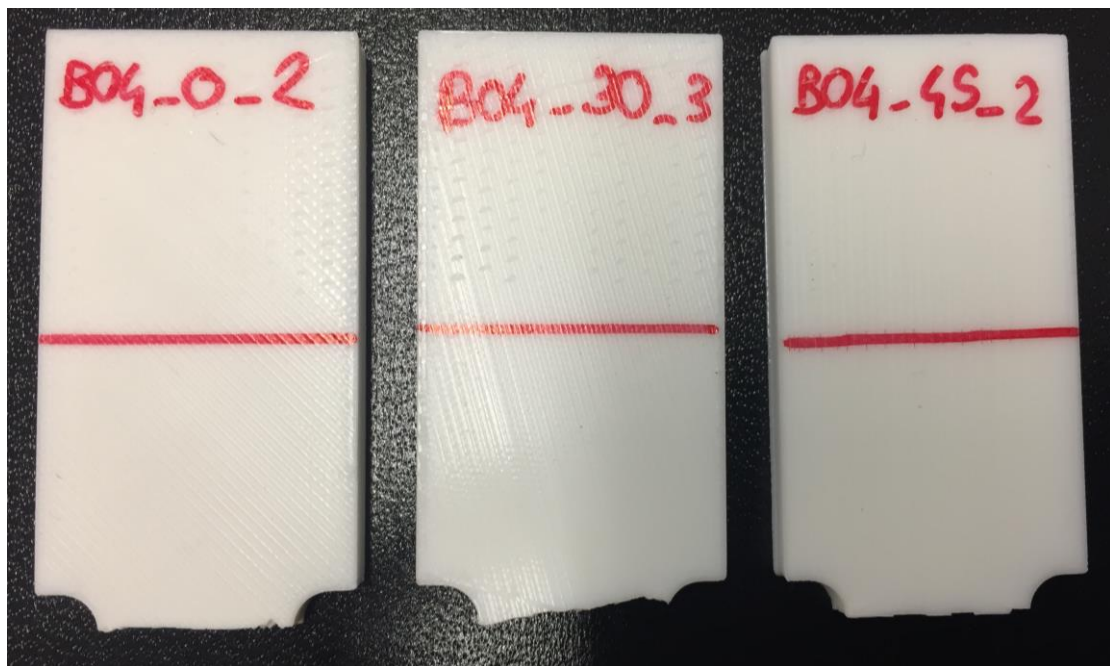


Figure 6.13 Crack path of u-notched parts under tension

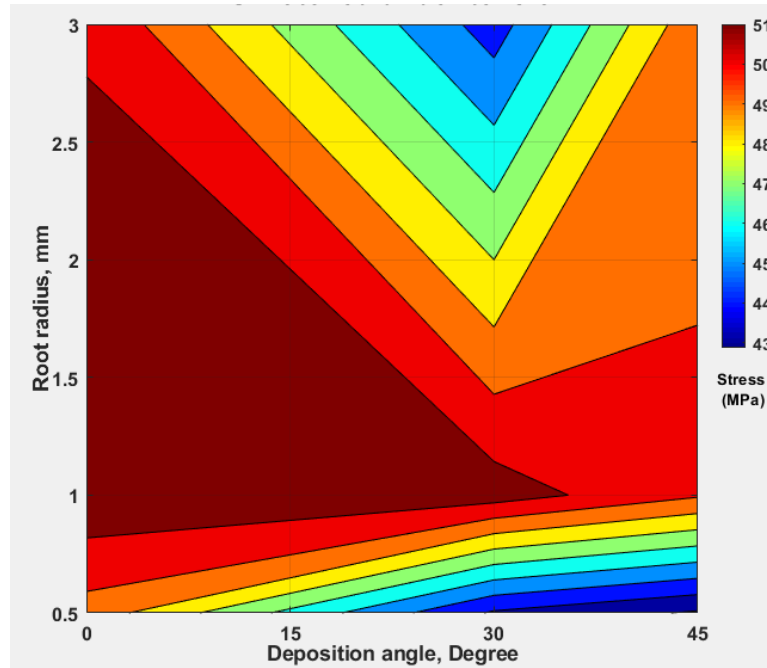


Figure 6.14 Contour plot of failure stress vs. t_s and θ_p for U-notches under tension

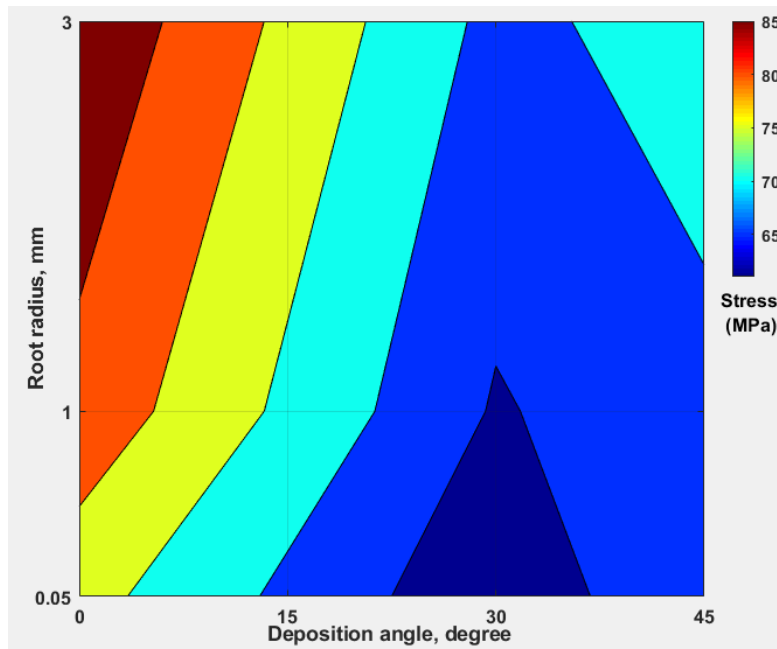


Figure 6.15 Contour plot of the ultimate stress vs. θ_p and r_n for U-notches under 3-point bending

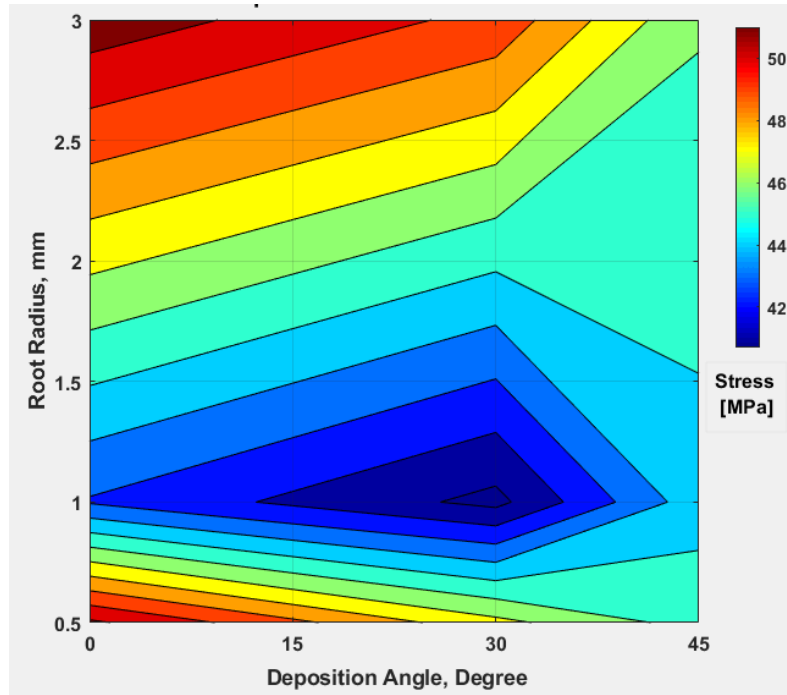


Figure 6.16 Contour plot of ultimate stress vs. θ_p and r_n for U-notches under tension

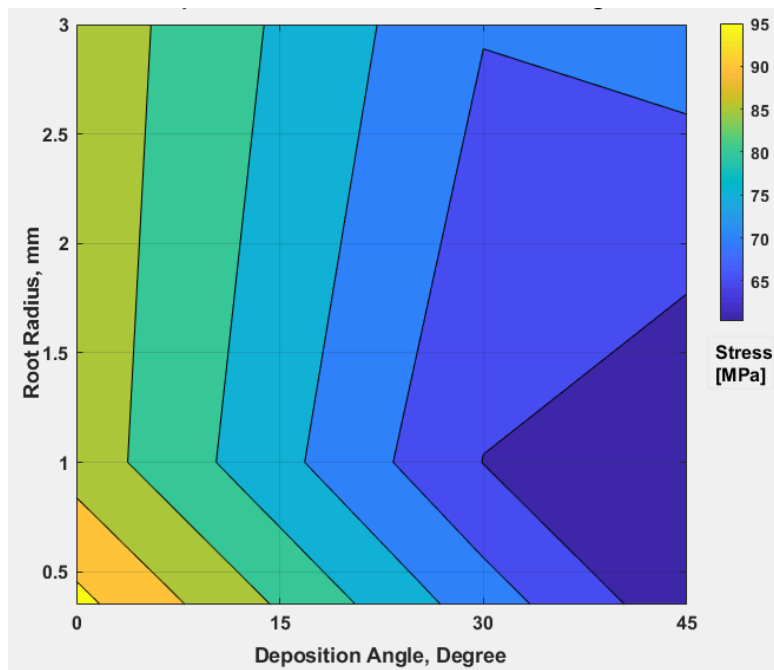


Figure 6.17 Contour plot of failure stress vs. t_s and θ_p for V-notches under 3-point bending

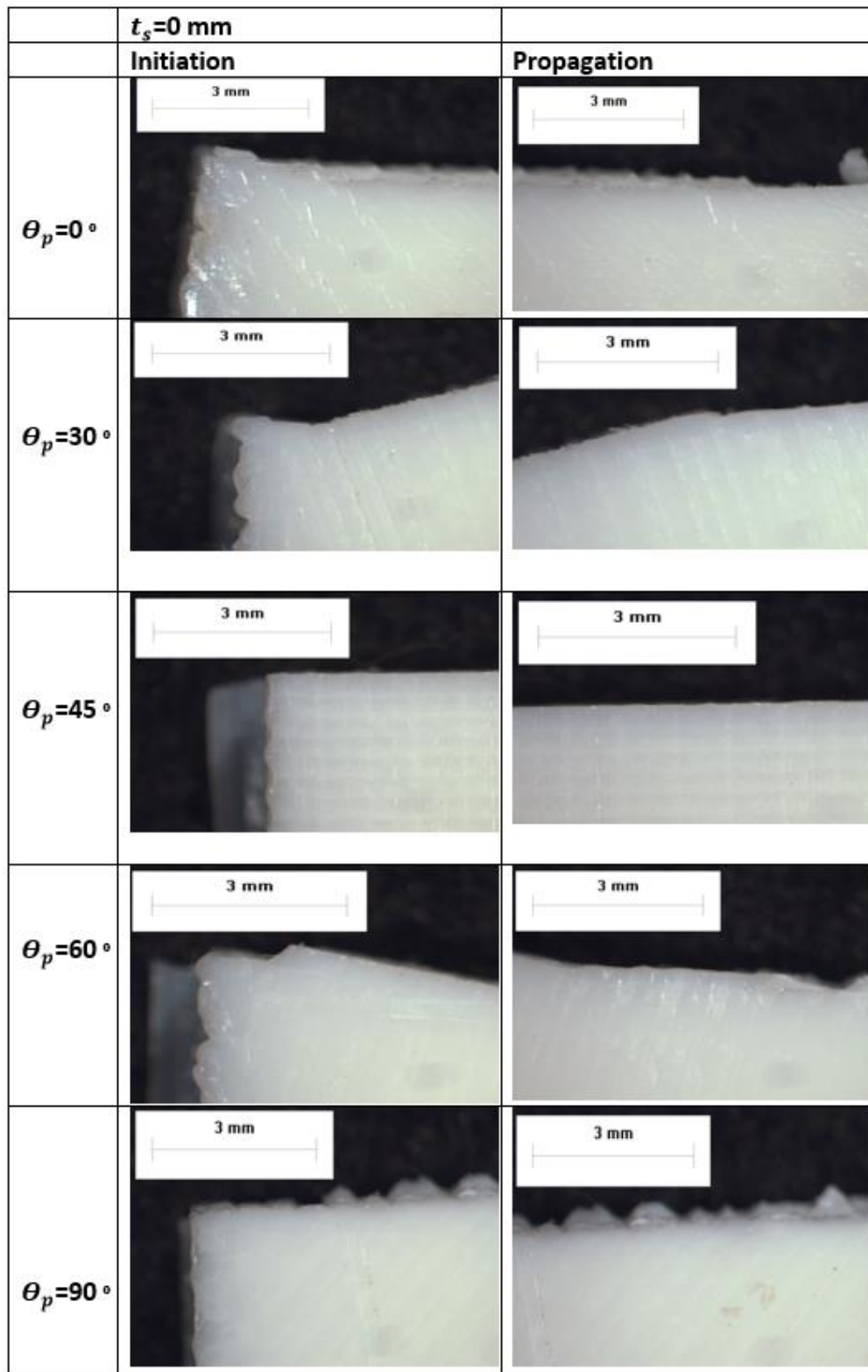
6.3 Cracking behaviour

By considering the effect of the deposition angle and the shell thickness on the cracking behaviour of AM PLA components, the final breakage of plain specimens was examined. The crack initiation and the propagation of specimens without notches under tensile loading, are shown in Figure 6.18 (see also Figures A.4.1 and A.4.2) The general crack initiation trend, independent of the fibre orientation, θ_p , and shell thickness, t_s , was perpendicular to the applied load direction. In samples with no shell thickness, the length of the initial crack was about 0.25 mm; while in specimens with a shell thickness of 0.4 mm and 0.8 mm, the length of this crack was equal to the shell thickness (Figure A.1.8).

The next crack propagation process followed the direction of the deposited filament in a zigzag path. The estimated crack pattern supports the idea that cracking is controlled by two failure mechanism, i.e., de-bonding between fibres and rectilinear cracking failure of the filaments, which is holding true irrespectively of the deposition angle and shell thickness.

To investigate the crack behaviour for specimens with crack-like notches, it is noteworthy that the samples with $t_s = 0$, were manufactured by cutting the plain specimens with a thin knife resulting in a root radius of 0.04 mm; whereas the samples with t_s equal to 0.4 mm and 0.8 mm were made by setting the root radius equal to zero in the CAD model that sent to the 3D printer. The crack initiation shown in Figure 6.19, is not steady due to the sharpness of the notches, but in general, the profile of the cracks followed the direction of the deposition angle θ_p . This crack behaviour robustly advocates the suggested concept of fracture, fibre de-bonding and rectilinear fibres cracking. Unexpected cracking behaviour was shown in some crack-like notched specimens with t_s equal to 0.4 mm and 0.8 mm (In Figure 6.19, θ_p equals 45° , and 90°). The cracks in these samples started in the flank of the notches which attributed to the adhesion defect between the shell and the inside fibres near the notch due to the performance limitation of the 3D printer.

For notched specimens under tension and 3-point bending, the crack profiles are shown in Figure 6.20 (see also Figures A.4.3-A.4.5). The initiation of cracks was similar to what was seen in the plain samples. The crack tip started in the direction normal to the applied load, irrespectively of the deposition angle, notch geometry, and loading type. The premature cracks extended to a length equal to 0.4 mm, the same as the shell thickness. The subsequent crack propagation followed the direction of the fused filament θ_p . It can be observed that the same presumption for crack propagation, fibre de-bonding and rectilinear fibre cracking applies also to notched PLA components.

Figure 6.18 Microscopic pictures of plain specimens, $t_s=0$ mm

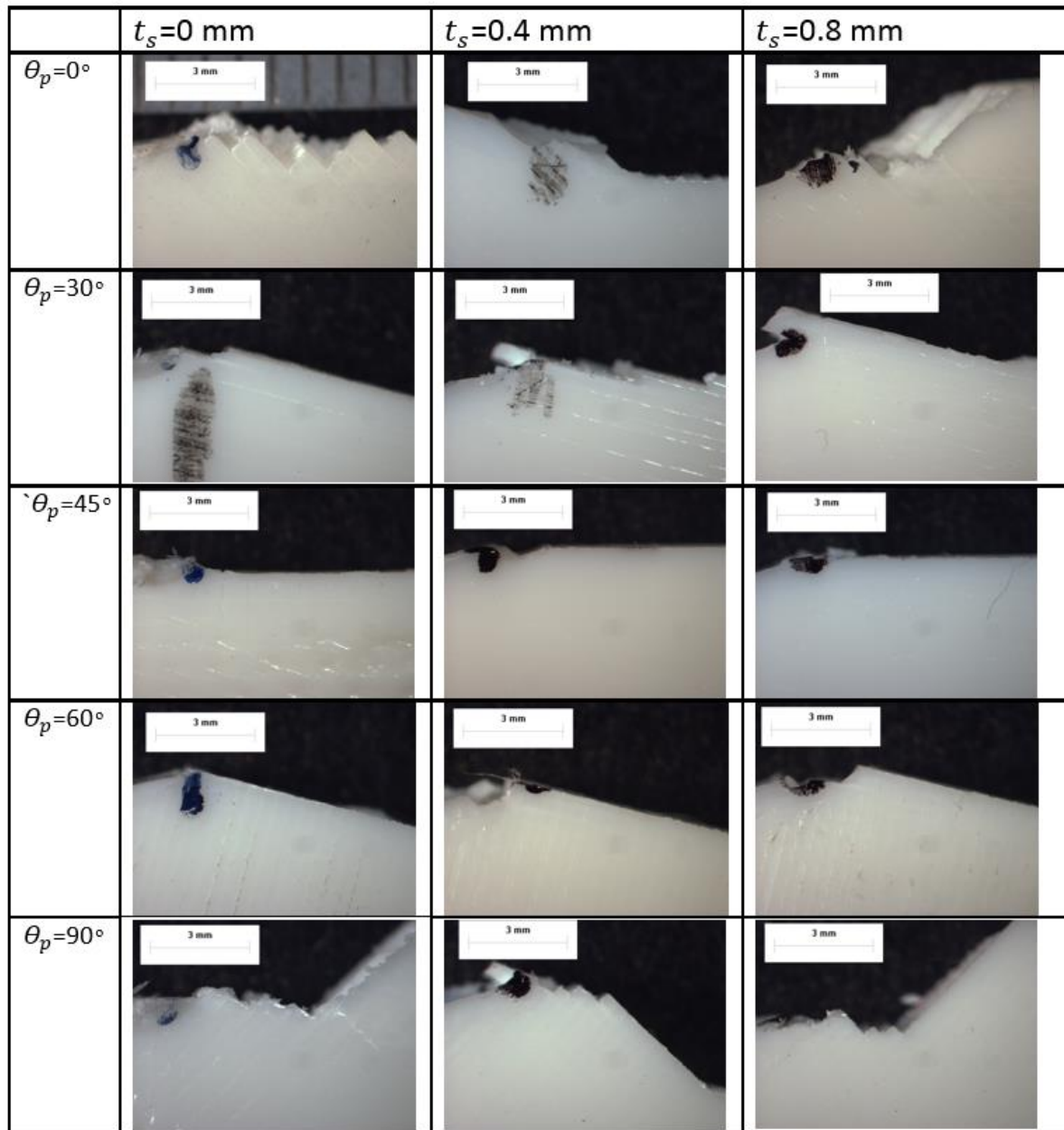


Figure 6.19 Microscopic pictures of crack-Like specimens

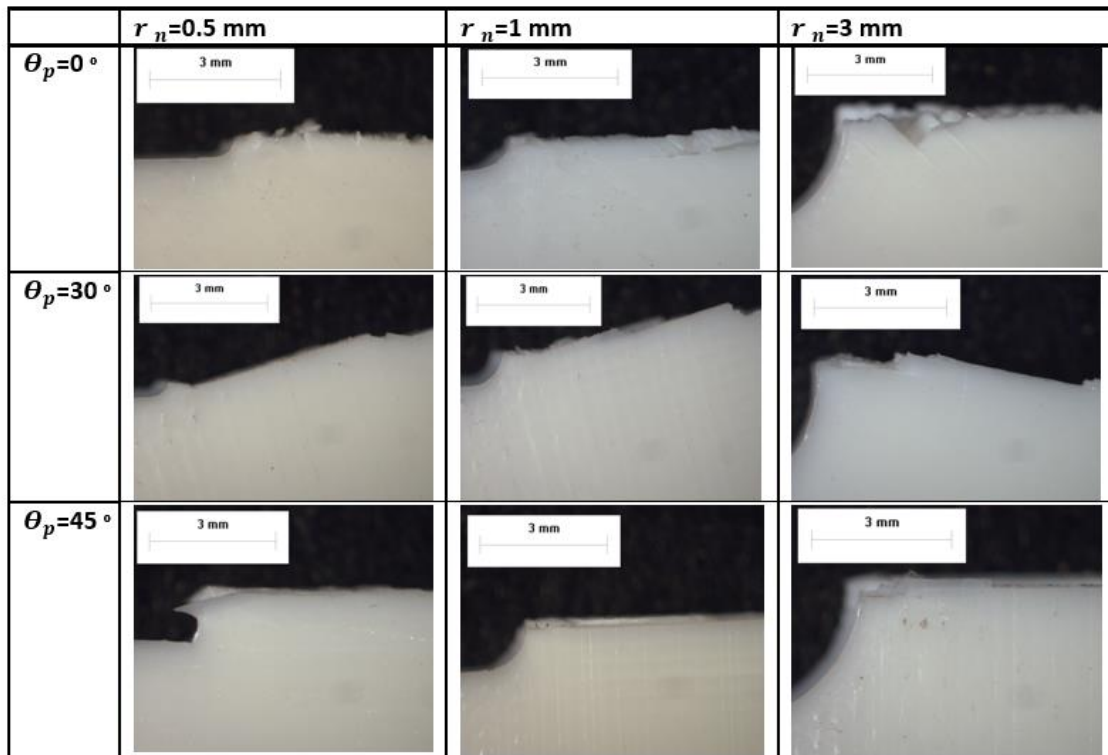


Figure 6.20 Microscopic pictures of U-notches under tension

6.4 Fracture toughness

To study the effect of the deposition angle θ_p and the shell thickness t_s on the behaviour of notched AM PLA components under static tensile loading, 45 crack-like notched specimens were tested, as shown in Figure 5.6, with θ_p ranging from 0° to 90° , and t_s between 0 and 0.8 mm. The specification and the net failure stress of these specimens are listed in Table A.2.4. The load vs displacement for the tested crack-like specimens are shown in Figure A.3.6.

The crack-like notched specimens were tested under a tensile load to estimate the fracture toughness K_C for notches with 4 mm thickness. The shape factor required for the classical formula to estimate the K_C values were computed according to Figure 4.5. The distribution of K_C values versus θ_p is shown in Figure 6.21 (see also Table A.2.4). Noteworthy is that the deposition angle θ_p considerably affects the K_C values for samples with 4 mm thickness.

The influence of θ_p may be attributed to the crack propagation, which follows a zigzag path according to the manufacturing angle θ_p that refers to a crack expanding due to mode I-loading at the macroscopic level, while the real meso-structure exposed to local mixed-Mode I /II loading. This fracture behaviour is not available in the $\theta_p = 45^\circ$ samples, however, because the fibre orientation was either parallel or normal to the main direction of the applied load. Nevertheless, the distribution of the K_C showed

no clear trend, and the experimental K_C values (see Figure 6.21) fall within two standard deviations ($\mp 2SD$) of the mean value of $3.5 \text{ MPa} \cdot \text{m}^{1/2}$.

The next group of AM PLA specimens was made according to ASTM D5045-14 in order to estimate the plane strain fracture toughness. We conducted the CT test. The thickness of the specimens is 20 mm (Figure 6.22), and the shell thickness t_s equals 0.4 mm. Contrary to the ASTM D5045-14 recommendation, no pre-crack involved in CT specimens in order to estimate the fracture toughness of AM PLA components by incorporating the influence of shell thickness.

Table A.2.5, Appendix A, summarises the test results, while Figure A.3.7, shows the estimating of P_Q , (needed to find the K_{IC} value) according to Equation (5.1). The results show that the higher values of K_C were presented by the samples produced with θ_p equals 0° (Figure 6.23), and that ascribed to the dominant rectilinear crack mode, due to the allocation of the fibre at 45° , to the direction of the applied load, which displayed higher strength than the de-bonding mode, as observed in other samples made with different θ_p values. The distribution of K_C for a 20 mm thickness still falls within $\mp 2SD$ from the mean, however.

The propagation of cracks followed the filament orientation, especially for an θ_p equal to 0° , and 30° , (Figures 6.24a and 6.24b). While for an θ_p equal to 45° , the crack generated by Mode-I loading, started away from the notch root and followed the profile of the shell thickness (Figure 6.24c).

In order to estimate the plane strain fracture toughness, K_{IC} of AM PLA, the CT specimen thickness was increased to 30 mm (Figure 6.25). The specimens were manufactured with solely θ_p equal to 45° , to promote Mode-I cracking, while t_s remained 0.4 mm. The displacement vs load relationship is shown in Figure 6.26. Estimating P_Q , (needed to find the K_{IC} value) according to Equation (5.1) is depicted in Figure A.3.8, Appendix A. The details and the results of the tested samples are listed in Table A.2.5. The values of K_{IC} were computed according to the ASTM D5045-14 method, and equal to $3.7 \text{ MPa} \cdot \text{m}^{1/2}$. The crack propagation followed Mode I cracking as expected, Figure 6.25, with an initiation away from the notch apex.

To conclude, different experimental strategies for estimating the fracture toughness of AM PLA material have produced different values, which were affected by the geometry and thickness of the samples. Also, noteworthy is that the fracture toughness results conflicted with the conventional engineering material behaviour and did not increase gradually with thickness. The behaviour is clear from comparing the fracture toughness of the specimens with 20 mm thickness ($4.24 \text{ MPa} \cdot \text{m}^{1/2}$), and samples with thickness 30 mm thickness ($3.7 \text{ MPa} \cdot \text{m}^{1/2}$).

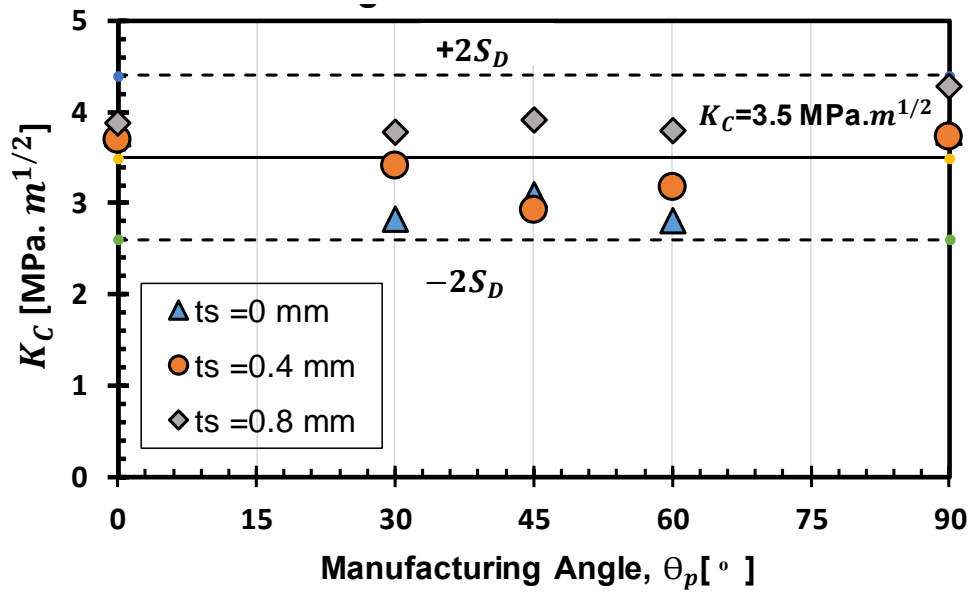


Figure 6.21 Distribution of K_c for crack-like notched specimens, $t=4$ mm



Figure 6.22 CT-20 mm specimens

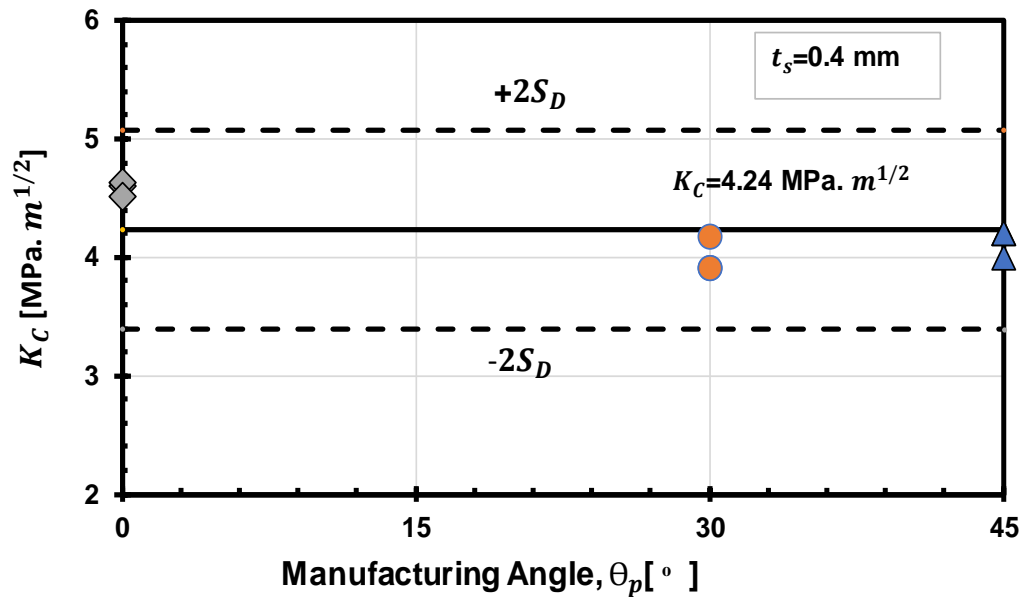
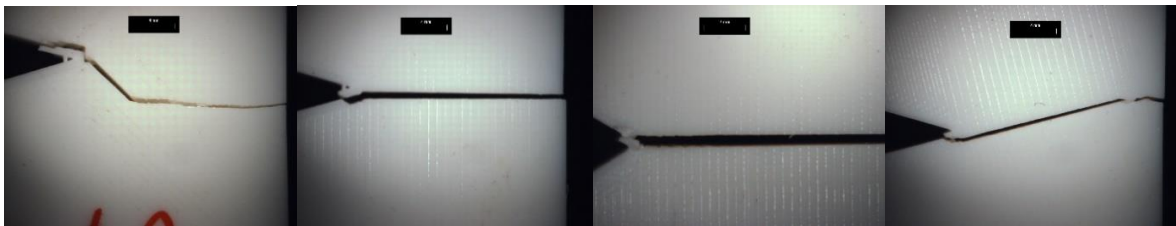


Figure 6.23 Distribution of fracture toughness of CT specimens, $t=20$ mm



(a) CT-0-20 mm (b) CT-30-20 mm (c) CT-45-20 mm (d) CT-45-30 mm

Figure 6.24 Example of cracking behaviour of CT specimens, $t=20$ mm and $t=30$ mm

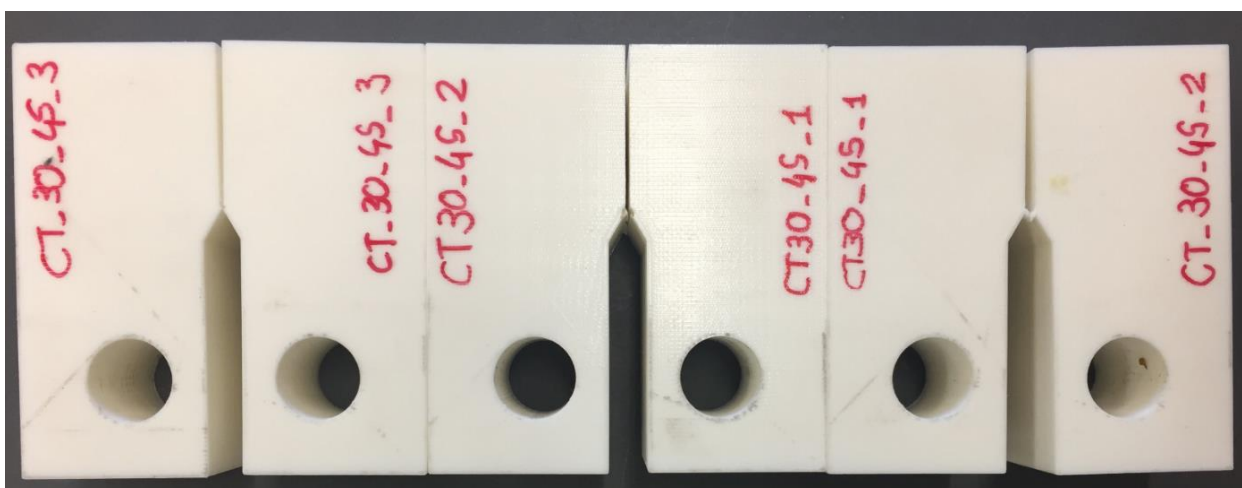


Figure 6.25 CT-30 mm specimens

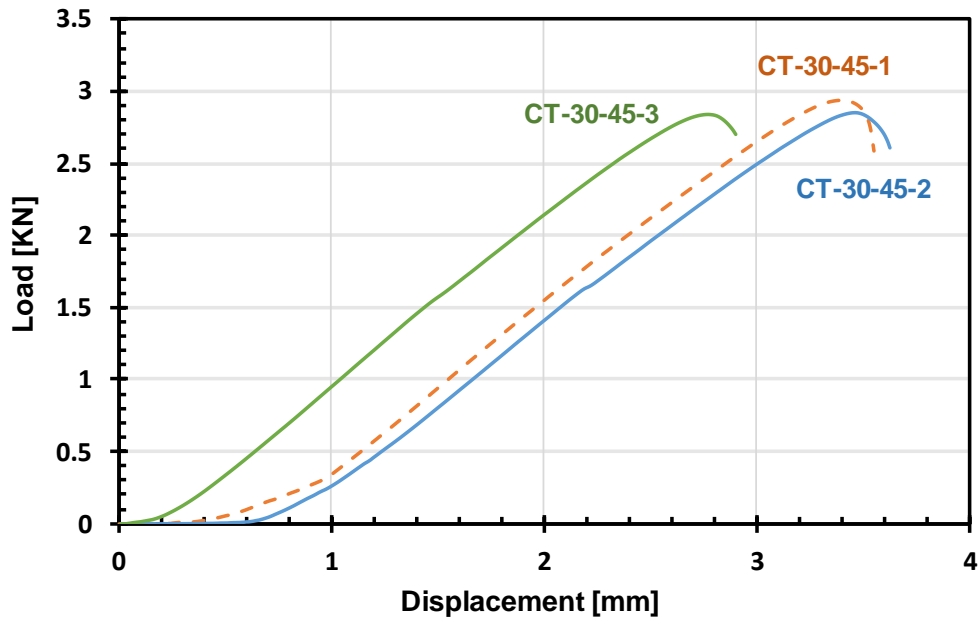


Figure 6.26 CT specimens test with a thickness of 30 mm and θ_p equals 45°

6.5 Static strength of notched PLA parts

To validate the use of TCD in estimating the static strength of the AM PLA notched components, and due to the complex notch-cracking behaviour observed in the specimens being tested, some simplifying assumptions are made. The first assumption can be validated from Figures 6.3 to 6.5, where the experimental values of the mechanical properties (σ_{ult} , E and $\sigma_{0.2\%}$) fall within $\mp 2SD$ of the mean. As a result, and from an engineering point of view, the effect of θ_p and t_s can be neglected with little loss of accuracy. So, the AM PLA behaviour can be considered as a homogeneous and isotropic material.

The second assumption is that the behaviour of the material follows the linear–elastic constitutive law. This presumption is supported by the linear stress vs strain relation before the max stress (Figure 6.2), irrespective of the angle θ_p , and t_s . The importance of this simplification is to consider the material as brittle, and the inherent material strength σ_o (material strength without defects) equals the ultimate tensile strength of the plain specimen σ_{UTS} [8][24].

Within this framework, ANSYS software was used to estimate the stress field near the notch tip, by simple linear elastic axisymmetric bi-dimensional modelling of the quarter of the specimens under tension; and by bi-dimensional model with full geometry for specimens under 3-point bending, using 183 Plane elements. The stress values were taken from FE simulation, on a line that represents the expected crack propagation path, in order to validate the accuracy of the TCD approach with regard to the regarding experimental results. TCD effective stress σ_{eff} is taken after the process of the mapped mesh refining will not affect the magnitude of the maximum stress at the notch tip, Figure 6.27 (see also. Figures A.5.1-A.5.4).

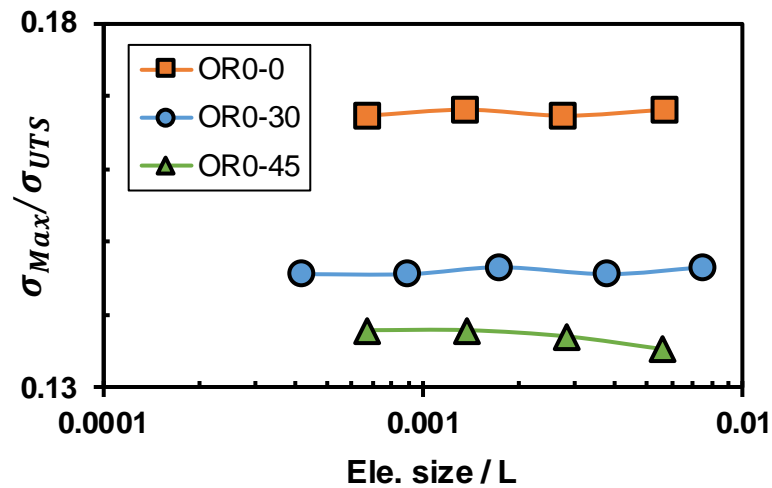


Figure 6.27 Stress convergence in FE modelling

The most important parameter in the application of the TCD is the critical distance L , which is considered a material characteristic. The direct estimation of the L value, using Equation (4.22), is not possible valid due to the uncertainty of K_{IC} , as explained in Section 6.4. An alternative is to obtain the L value from the intersection of the stress vs distance curve (for the sharp notch with the horizontal line which represents the ultimate tensile strength of the material. The results obtained from testing the sharp U-notched samples (see Table 6.2), under tension, were post-processed to determine the local linear elastic stress field in the incipient failure state. The stress vs distance curves were drawn, (see Figure 6.28) by taking the average result of three repeated tests for every tested deposition angle θ_p (i.e., 0° , 30° , and 45°).

Then, the critical distance L is taken as the average values from the intersection of the horizontal line (representing the σ_{UTS} of the plain material) with the three stress-distance curves (representing the local stress field near the notch) for three deposition angles. The computed L value is 4.48 mm. This value, together with σ_o equal to 42.9 MPa, σ_{UTS} , was used to predict the static strength of the notched specimens listed in Table 6.2 and Tables A.2.1 - A.2.3.

It is important to recall that the strength of engineering material, within the TCD framework, is presumed to be based on the stress value acting on a small finite part of the material which is vulnerable to crack initiation. Thus, the process zone size is related to the material length scale L [8][110], which in turn, is affected by the microstructure of the material under investigation[110] [111]. Taylor [112] showed that the L value of engineering materials is an order of magnitude greater than the material's microstructure size.

Because the dominant microstructural heterogeneity in the AM PLA material being tested in this work is the fused filament size, which is equal to 0.4 mm (printing nozzle size) it is reasonable to take the characteristic length appropriate to evaluate the static strength of AM PLA, as ten times the fused filament size. The notched specimen's

test results reported in Tables 6.2 and A.2.1-A.2.3, Appendix A, fully support this assertion.

By returning to the strength prediction of the notched PLA samples, and verifying the TCD procedure concluded in the current section; and having computed the L value, the effective stress in the primary failure condition can be evaluated from the linear elastic stress field, estimated by FE analysis, for every sample geometry and loading type. The effective stress is computed according to the point method, Equation (4.18), and the area method, Equation (4.27). According to the point method, the effective stress for the examined specimens is produced by intersecting the vertical line of $(L/2)$ with the stress distance curve in the incipient failure condition. For the area method, meanwhile, the effective stress is taken as averaged stress over a semi-circular area centred on the emanating point of the focus line at the notch apex (see Figure 4.8a). Unfortunately, it was not possible to verify the accuracy of TCD in the form of LM (Equation 4.25), because the length of the linear integration domain (i.e., $2L = 9.2$ mm) was larger than the half-width of the tested specimens.

The evaluated static strength prediction error for the notched specimens is calculated according to the following equation:

$$\text{Error} = \frac{\sigma_{eff} - \sigma_{UTS}}{\sigma_{UTS}} [\%] \quad (6.1)$$

According to Equation (6.1), a positive error refers to conservative strength values, while a negative error denotes a non-conservative estimate. The accuracy summary of applying the point method and area method to predict the static strength of notched specimens, shown in Figure 5.7, is presented in Figures 6.29 and 6.30, respectively (see also Tables A.6.1-A.6.8).

From Figure 6.29 we see that the strength estimates of the AM PLA samples tested under tension had mainly positive prediction errors, while the specimens examined under 3-point bending had a negative error. It is clear from Figure 6.29 that the U-notched samples (denoted as U-N, 3PB, $r_n=0.05$ mm) under the 3-point bending are predicted non-conservatively due to the behaviour of the notch as a sharp crack which presented less effective stress, given that the opening angle was 30° and the root radius was equal to 0.05 mm (see Figure A.1.6a). On the other hand, Figure 6.30 showed good strength prediction for the area method with a few conservative results for the open notched PLA samples.

Despite the intricate mechanical and cracking behaviour of the AM PLA material under investigation, Figures 6.29 and 6.30 confirm the remarkable accuracy of the TCD approach in predicting the static strength of the notched samples, resulting in the error estimates falling mostly within the interval $\pm 20\%$. Due to problems during the experimental test and numerical analysis, this accuracy level is acceptable, since differences between 0% error and the 20% error can in any case not be identified when using conventional engineering materials [8].

To summarise, the validity verification of the TCD methodology discussed in the current section strongly suggests that the linear elastic approach with TCD can be used in practical applications to design AM PLA components under static loading. The essence of TCD assumes the material as isotropic and homogenous when directly post-processing the linear elastic stress field from FE modelling.

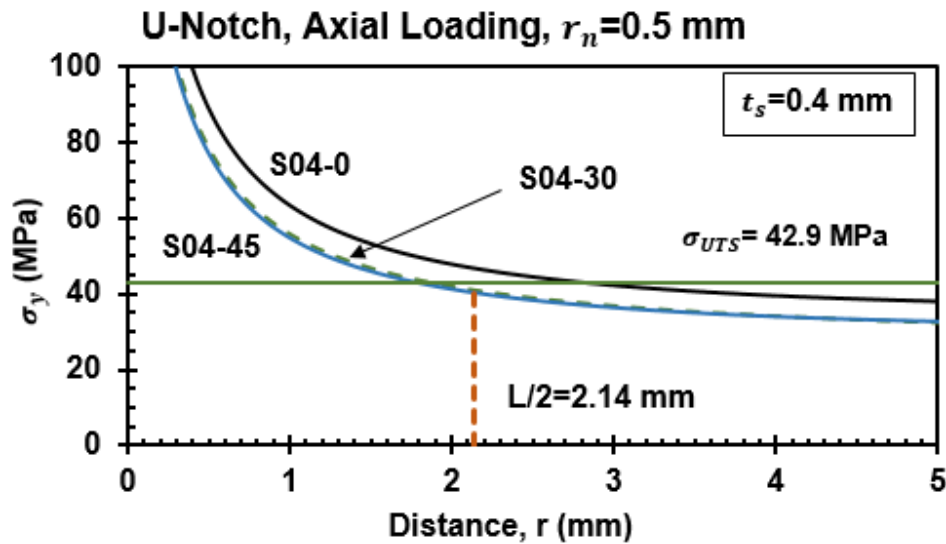


Figure 6.28 Estimating (L) value for solid AM PLA

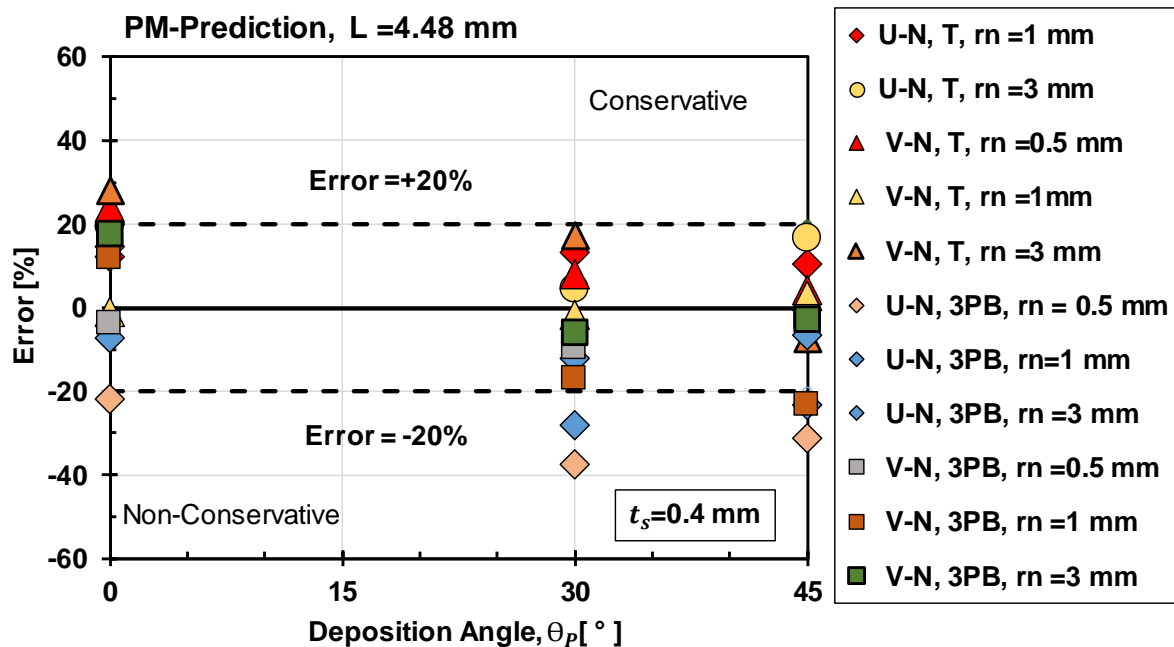


Figure 6.29 PM strength prediction error for notched solid AM PLA

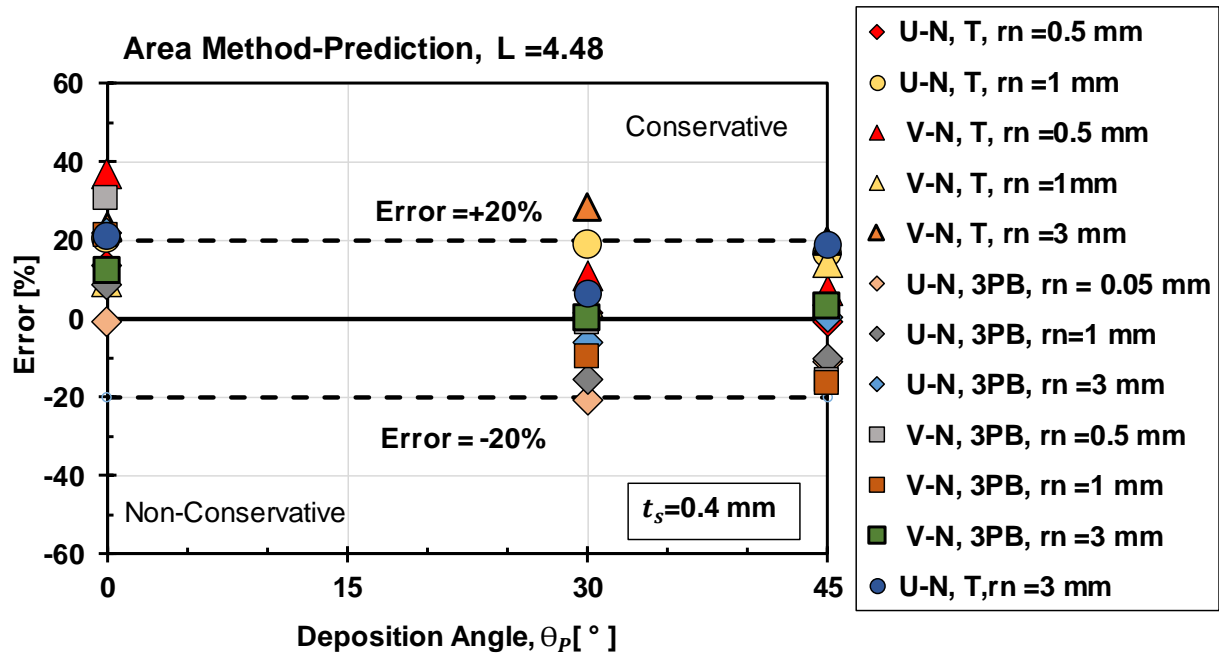


Figure 6.30 Area method strength prediction error for notched solid AM PLA

6.6 Conclusion

The mechanical properties and crack behaviour of the AM PLA material were investigated with different deposition angles and shell perimeter thickness.

The validation of simple linear elastic TCD to predict the static strength of AM PLA components, weakened by different stress risers and loading types, were implemented.

A large number of AM PLA samples, with various geometric discontinuities, were manufactured and tested under tensile loading and 3-points bending as well, to check the accuracy of the TCD in assessing the static strength for specimens under investigation.

Regarding the PLA materials produced by the additive manufacturing technology with 100% infill level, the following points can be made based on the results of this study:

- The material can be modelled using the linear elastic approach, up to ultimate strength, regardless of the deposition angle θ_p and the shell thickness t_s .
- The mechanical properties of the AM PLA material (E , $\sigma_{0.2\%}$ and σ_{uts}) vary within two standard deviations of the mean, for values of θ_p and t_s .

-
- The lowest static strength of the notched PLA samples is not always related to the lowest root radius.
 - The cracking of the AM PLA material under loading follows the fused filament orientation.
 - The thickness and geometry of the AM PLA specimens noticeably influence the results of fracture toughness K_C test.
 - The TCD with the linear elastic approach showed reliable static strength prediction for the notched samples with error estimates falling mainly within an $\pm 20\%$ range.
 - The characteristic length L to evaluate the static strength of AM PLA is ten times the fused filament size.

Chapter 7-Results and discussion of AM PLA porous parts

7.1 Plain PLA porous components

This chapter will discuss the results of 81 porous plain AM PLA samples manufactured with less than 100% infill level and different deposition angles. An electronic microscope was used to measure the vertical and horizontal dimensions of the voids for plain porous samples for three adjacent selected voids, as shown in Table 7.1 and Figure 7.1. The final void's size is taken as the average of six readings.

The pictures of the plain porous samples before testing are shown in Figures B.1.1-B.1.3. The plain porous specimens have the same dimensions as the plain solid samples, and the deposition angle θ_p varied from 0° , 30° and 45° . Nine specimens were tested for every deposition angle with the infill level changed from 10% to 90%, as shown in Table 7.2 (see also Tables B.2.1 and B.2.2). As the tables show, the void sizes ranged from 10.72 mm (for a 10% infill level) to 0.11 mm (for a 90% infill level). The mechanical properties showed an increasing trend with the infill level and the fictitious failure stress (the applied load divided by the cross-sectional area calculated by neglecting the existence of voids) ranged between 8.7-23 MPa, as shown in the tables above.

Figure 7.2 (see also Figure B.3.1) shows the relationship of fictitious stress vs. strain for three infill levels of plain porous AM PLA specimens. As evidenced, the response was almost linear up to the maximum stress recorded during the test. In relation to the non-linear part: the samples with a deposition angle, θ_p , equal to 0° show the largest amount of ductility, leading to a horizontal plateau, for all values of the infill levels. This is due to fibres participating in every fused layer in the rectilinear cracking mechanism. For the samples fabricated with θ_p equal to 30° and 45° , the curves showed some non-linear behaviour after the maximum stress. This is due to the fibres, in one deposited layer, bearing the applied load by direct tension while the adhesion between adjacent fibres will withstand the rest portion of the applied load in the adjacent layer (Figure 5.3). This is weaker than the former force and mostly showed brittle fracture.

Comparing the stress/strain curves of the solid PLA specimens manufactured with a 100% infill level and with θ_p equal to 0° , (see Figure A.3.1), with the nearest corresponding porous samples fabricated with 90% infill (Figure B.3.1), it can be seen that, after the maximum stress had been reached, the solid PLA parts showed decreasing stress before the plateau stage (this refers to the onset of necking despite it was unclear in the cracked parts). For the porous PLA samples, however, the plateau of the stress-strain curve started after the maximum stress without noticeably lowering the stress level. Overall, the solid ones had a higher elongation (1.2%) before the final breakage while the porous PLA showed a lower elongation (8%). This confirms the significant difference in the ductile behaviour between the two kinds of manufacturing.

Table 7.1 An example for the measurements of the voids' dimensions

Code	θ [Deg]	dh1 [mm]	dh2 [mm]	dh3 [mm]	dv1 [mm]	dv2 [mm]	dv3 [mm]	tf [mm]	dh-av [mm]	dv-av [mm]
P0_10-1	0	10.42	10.5	10.9	10.6	10.9	10.90	0.46	10.6	10.80
P0_20_1	0	4.86	4.83	5.1	5.03	5.04	5.00	0.51	4.9	5.02
P0_30_1	0	1.3	1.3	1.35	1.46	1.4	1.36	0.27	1.3	1.41
P0_40_1	0	0.9	0.87	0.7	1.1	0.83	0.90	0.33	0.8	0.94
P0_50_3	0	0.56	0.67	0.64	0.55	0.66	0.61	0.33	0.6	0.61
P0_60_1	0	0.44	0.44	0.43	0.47	0.46	0.44	0.27	0.4	0.46
P0_70_1	0	0.35	0.29	0.3	0.38	0.31	0.37	0.31	0.31	0.35
P0_80_1	0	0.19	0.2	0.22	0.23	0.24	0.34	0.33	0.20	0.27
P0_90_1	0	0.11	0.14	0.14	0.14	0.16	0.12	0.41	0.13	0.14

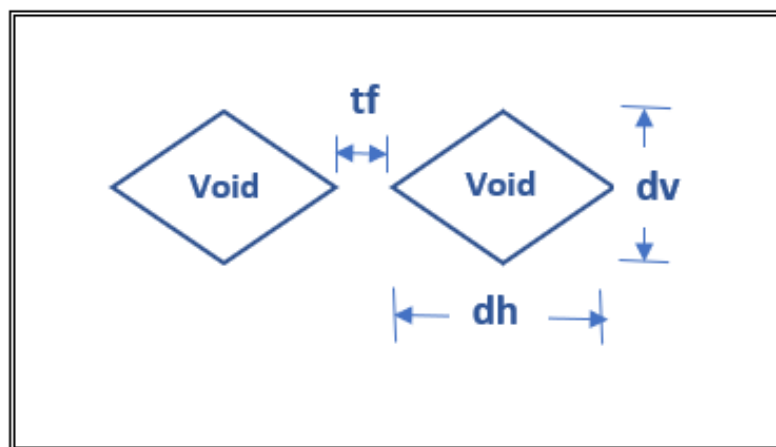


Figure 7.1 Measurements of Void's dimensions

Figure 7.3 presents the dominant crack pattern for the AM PLA porous specimens. The cracking behaviour reveals rectilinear cracking of the PLA filament, which occurs regardless of the deposition angle and the infill ratio. The initial crack starts with crack thickness of 4 mm and occurs on an almost perpendicular plane to the applied load. Irrespective of the macroscopic geometry, the manufacturing angle θ_p , and infill level, crack initiation as well as propagation occurred on planes that were mostly perpendicular to the direction of the applied tensile force. The subsequent crack propagation follows the internal wall path, which forms a net-like structure.

Table 7.2 The dimension and test results for plain porous specimens

Code	θ_p [Deg]	Infill %	W_n [mm]	t [mm]	F_f [N]	E [MPa]	$\sigma_{0.2\%}$ [MPa]	σ_f [MPa]	d_v [mm]
P0_10_1	0	10	14.99	4.07	505	591	7.9	8.3	10.70
P0_10_2	0	10	15.03	4.05	531	622	8.1	8.2	
P0_10_3	0	10	15.05	4.05	529	647	8.4	8.7	
P0_20_1	0	20	14.98	4.00	562	687	8.7	9.4	4.98
P0_20_2	0	20	14.92	3.95	538	673	8.6	9.1	
P0_20_3	0	20	14.96	3.98	537	658	8.4	9.0	
P0_30_1	0	30	14.94	4.07	599	706	8.8	9.9	1.36
P0_30_2	0	30	14.92	4.02	641	731	9.5	10.7	
P0_30_3	0	30	14.99	4.02	638	734	9.5	10.6	
P0_40_1	0	40	15.02	4.00	721	836	10.5	12.0	0.88
P0_40_2	0	40	15.00	4.08	723	822	10.0	11.8	
P0_40_3	0	40	14.97	4.05	726	862	11.0	12.0	
P0_50_1	0	50	14.95	4.06	829	953	12.0	13.7	0.62
P0_50_2	0	50	15.00	4.04	842	940	12.5	13.9	
P0_50_3	0	50	15.03	4.07	816	916	11.3	13.3	
P0_60_1	0	60	15.10	4.05	971	1078	13.3	15.9	0.45
P0_60_2	0	60	15.03	4.03	1004	1041	14.0	16.6	
P0_60_3	0	60	15.03	3.98	1001	1147	14.5	16.7	
P0_70_1	0	70	15.04	4.01	1182	1354	17.0	19.6	0.33
P0_70_2	0	70	15.02	4.04	1237	1434	18.0	20.4	
P0_70_3	0	70	15.03	4.04	1186	1364	17.0	19.5	
P0_80_1	0	80	15.12	4.03	1356	1638	20.3	22.3	0.24
P0_80_2	0	80	15.09	4.05	1401	1660	20.5	22.9	
P0_80_3	0	80	15.05	4.07	1372	1633	19.7	22.4	
P0_90_1	0	90	15.08	4.02	1577	2006	23.5	26.0	0.14
P0_90_2	0	90	15.12	4.09	1618	2030	23.5	26.2	
P0_90_3	0	90	15.07	4.09	1551	1912	22.5	25.2	

The relationship of the mechanical properties vs. the infill level are shown in Figure 7.4. The curves show an increase in the mechanical properties (σ_f , $\sigma_{0.2\%}$ and E) with an increase in the infill level. It is evident from Figure 7.4 that the magnitudes of σ_f , $\sigma_{0.2\%}$ and E increased markedly from the 90% to the 100% fill density. The reason is due to the meso-structure characteristics of the AM PLA parts. Specifically, the mechanical behaviour of the solid PLA parts fabricated with a 100% infill level depends on three aspects: a) the properties of the raw material of the fused filaments, b) the adhesion forces between the adjacent filaments in the same layer, and c) the bonding forces between the neighbouring layers. Accordingly, the fracture mechanism of the solid AM PLA will be controlled by three specific behaviours: a) the rectilinear cracking of the fused filaments, b) the de-bonding between neighbouring filaments, and c) the de-bonding between adjacent deposited layers.

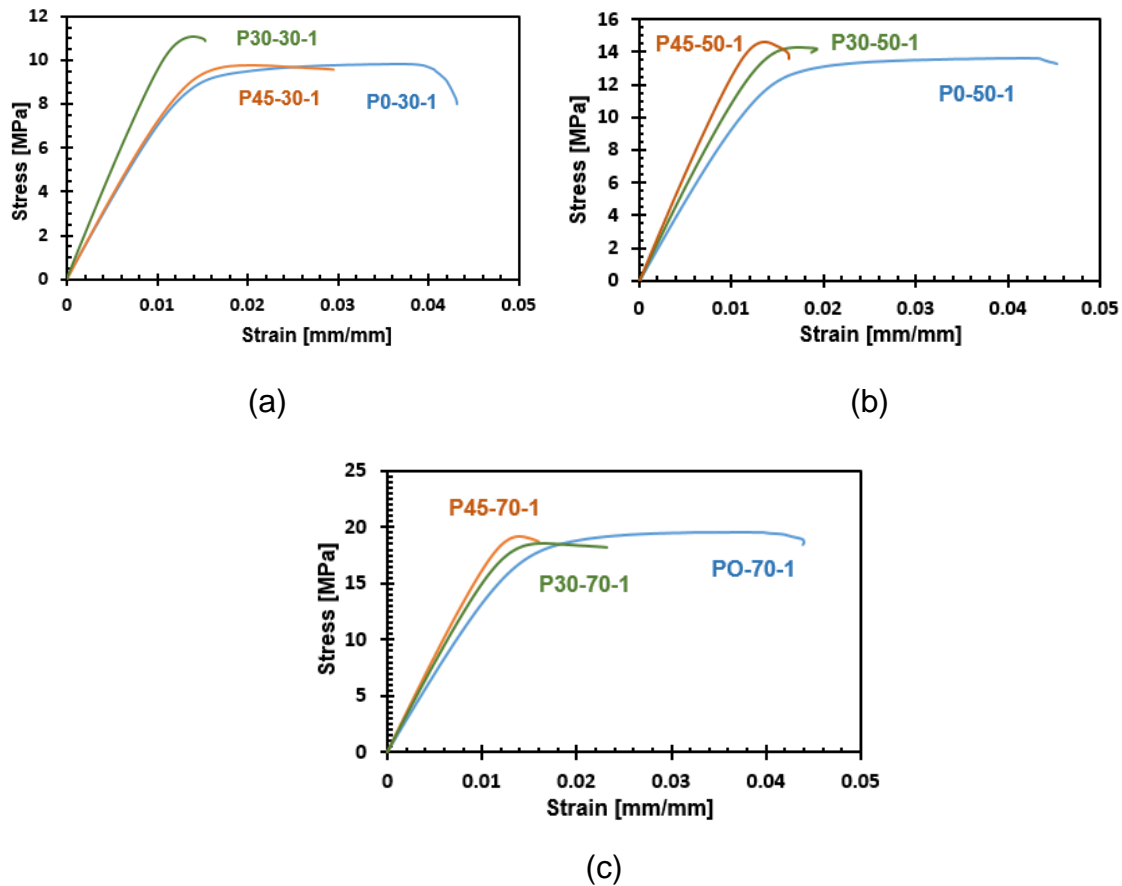


Figure 7.2 Examples of fictitious stress vs. strain for plain porous PLA specimens: a) with 30% infill; b) with 50% infill; and c) with 70% infill.

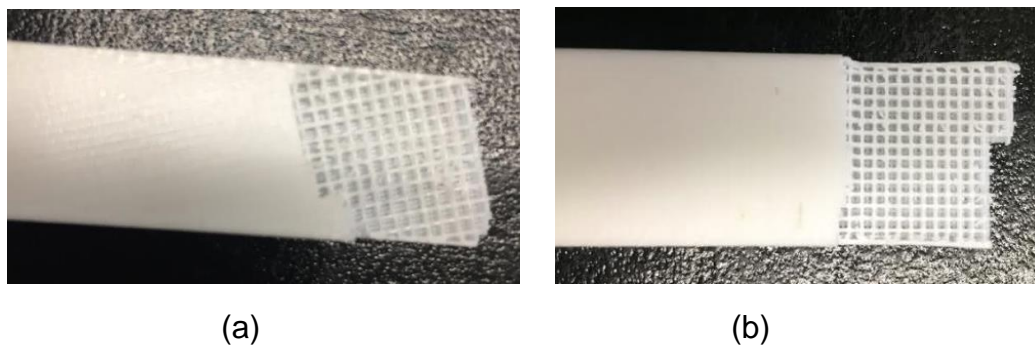


Figure 7.3 Crack propagation in plain porous PLA, a) $\theta_p = 30^\circ$; b) $\theta_p = 45^\circ$

By observing the meso-structure of the PLA parts fabricated with an infill level of less than 100%, the adhesion forces between the adjacent fused filaments in the same layer, are not effective, negatively influencing the mechanical properties of the porous AM PLA parts. This explains the significant reduction in the mechanical properties of

PLA samples when moving from 100% to 90% fill density, which is true for even a very small size of the fabricated internal voids (90% infill level).

It is clear from Figure 7.4a that the samples with a θ_p equal to 45° presented the highest elastic modulus, while those with θ_p equal to 0° showed the lowest E value. This behaviour demonstrates the fracture mechanism of AM PLA material. Specifically, the elongation in the former samples (θ_p equal to 45°) started with the fibre stretching in the direction of the applied load before the failure in adhesion between the adjacent fibres, resulting in less elongation in the elastic range of the curve. On the contrary, the elongation in the later specimens is likely initiated by the debonding failure in the neighbouring fibres before the stretching in the deposited fibres, which leads to higher strain within the elastic part of the curve. Consequently, the highest 0.2% proof stress $\sigma_{0.2\%}$ was shown by AM PLA samples fabricated with a θ_p equal to 45° (Figure 7.4c.)

Also noteworthy is the highest failure strength evidenced by the PLA porous specimens manufactured with a 0° deposition angle (Figure 7.4b), which occurs for the same reasons explained for the solid samples (see Chapter 6). In contrast, the fracture mechanism of the AM PLA parts is responsible of the low failure strength of porous specimens manufactured with θ_p equal to 30° and 45° , (Figure 7.4b).

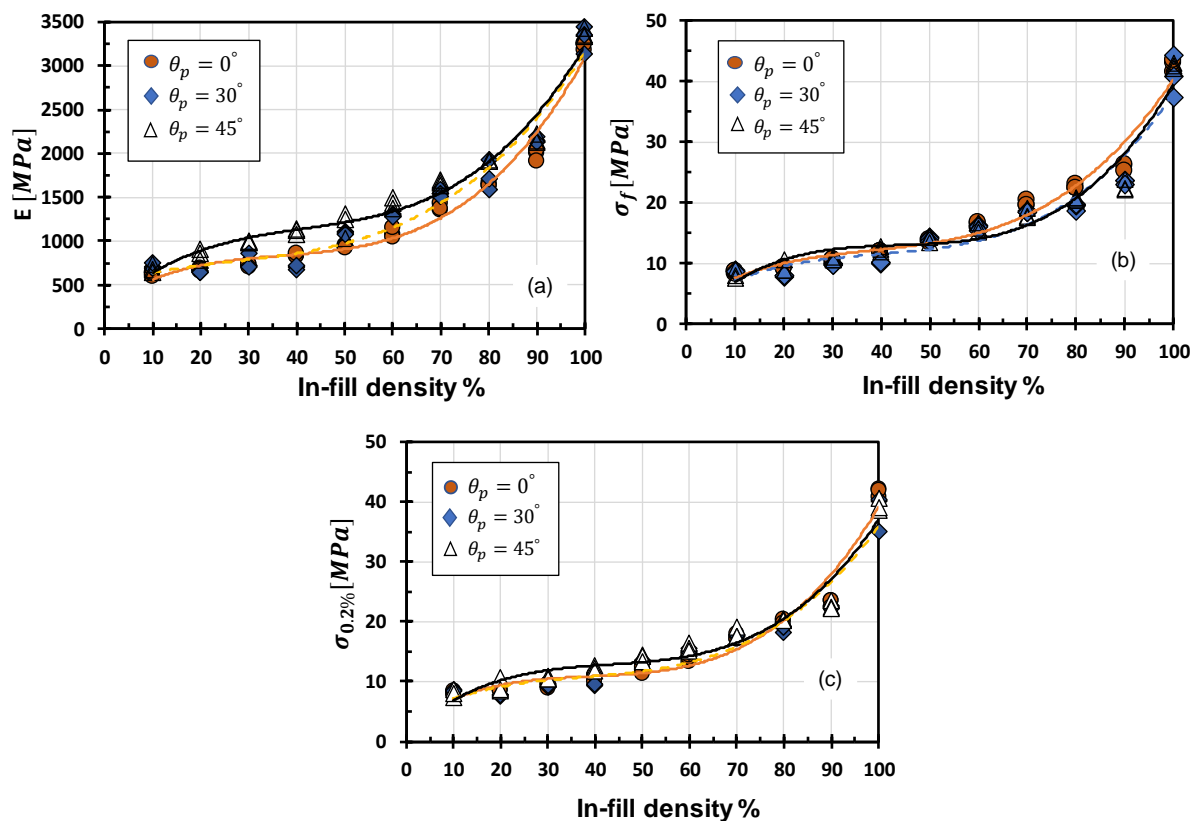


Figure 7.4 The relationship of the infill ratio of PLA parts with: a) Elastic modulus, b) Failure stress, and c) Proof yield stress,

7.2 Notched PLA porous components

This section will discuss the results of 54 porous notched AM PLA tested samples, manufactured with different deposition angles and variable infill level. All samples were tested under tension in order to investigate the influence of the above variables (θ_p and infill ratio) on the mechanical behaviour and the failure strength. The deposition angle was changed between 0° , 30° and 45° with the infill level varying between 30%, 50%, and 70%. The investigation comprised U-notched samples in addition to open-notched samples with different root radii for each notch. The size of the internal manufactured voids was measured by electronic microscope as was done for the plain specimens. The pictures of the tested AM PLA porous notched parts are displayed in Figure B.1.4. In addition to the fracture behaviour, the prediction of static strength under tension for the porous notched samples, will be presented according to the Theory of Critical Distance (TCD).

The measured dimensions and the test results for the notched porous AM PLA specimens are displayed in Tables 7.3 (see also Tables B.2.3-B2.7). The size of the voids in these tables ranged between 0.33-1.54 mm and the fracture stress between 400-1220 N.

There were two aspects to the behaviour of the notched porous AM PLA components under tension (see Figure 7.5; also Figures B.3.2 and B.3.3). The initial part of the curve was mostly linear, followed by non-linear behaviour before failure. The crack initiation and propagation in the notched sample was similar to the plain samples: starting in the shell thickness near the notch root perpendicular to the applied load direction, then following the path of the walls for every deposition angle, as shown in Figure 7.6. As the crack path is longer for the sample with the infill angle θ_p equal to 0° , and the predominant rectilinear cracking mechanism, they showed the highest degree of nonlinearity.

Table 7. 3 The test results for the U-notched porous PLA samples

Code	θ [Deg]	Infill [%]	R_n [mm]	W_n [mm]	W_g [mm]	t [mm]	F_f [N]	d_v [mm]
S0_30_1	0	30	0.50	15.23	24.94	4.14	730	1.42
S0_30_2	0	30	0.51	15.29	24.79	4.11	533	
S0_30_3	0	30	0.49	15.28	24.78	4.09	566	
S0_50_1	0	50	0.51	15.28	24.78	4.09	790	0.69
S0_50_2	0	50	0.51	15.27	24.81	4.09	793	
S0_50_3	0	50	0.48	15.28	24.81	4.15	879	
S0_70_1	0	70	0.53	15.31	24.78	4.16	1221	0.33
S0_70_2	0	70	0.51	15.28	24.76	4.10	1023	
S0_70_3	0	70	0.50	15.32	24.82	4.11	1046	
I0_30_1	0	30	1.01	15.31	24.73	4.03	504	1.45
I0_30_2	0	30	1.03	15.31	24.72	4.04	545	
I0_30_3	0	30	0.99	15.19	24.86	4.04	714	
I0_50_1	0	50	1.00	15.19	24.77	4.06	817	0.66
I0_50_2	0	50	1.02	15.16	24.71	4.06	841	
I0_50_3	0	50	1.00	15.21	24.75	4.05	884	
I0_70_1	0	70	1.01	15.27	24.81	4.08	1047	0.35
I0_70_2	0	70	1.04	15.14	24.75	4.08	930	
I0_70_3	0	70	1.00	15.08	24.75	4.04	1151	
B0_30_1	0	30	3.07	15.16	24.82	4.10	723	1.35
B0_30_2	0	30	3.06	15.26	24.88	4.10	718	
B0_30_3	0	30	3.04	15.29	24.82	4.12	599	
B0_50_1	0	50	3.04	15.19	24.86	4.15	893	0.67
B0_50_2	0	50	3.06	15.29	24.97	4.12	871	
B0_50_3	0	50	3.06	15.19	24.88	4.10	957	
B0_70_1	0	70	3.05	15.17	24.94	4.12	1222	0.33
B0_70_2	0	70	3.06	15.20	24.94	4.12	1055	
B0_70_3	0	70	3.08	15.14	24.82	4.07	1195	

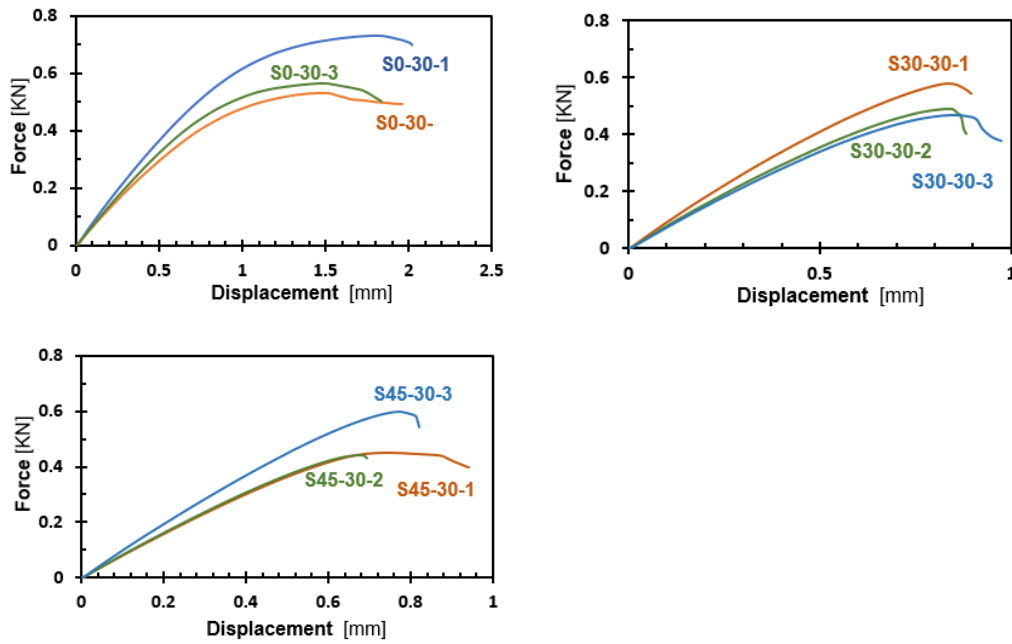


Figure 7.5 Selection of load vs. displacement curves displayed by notched porous AM PLA samples

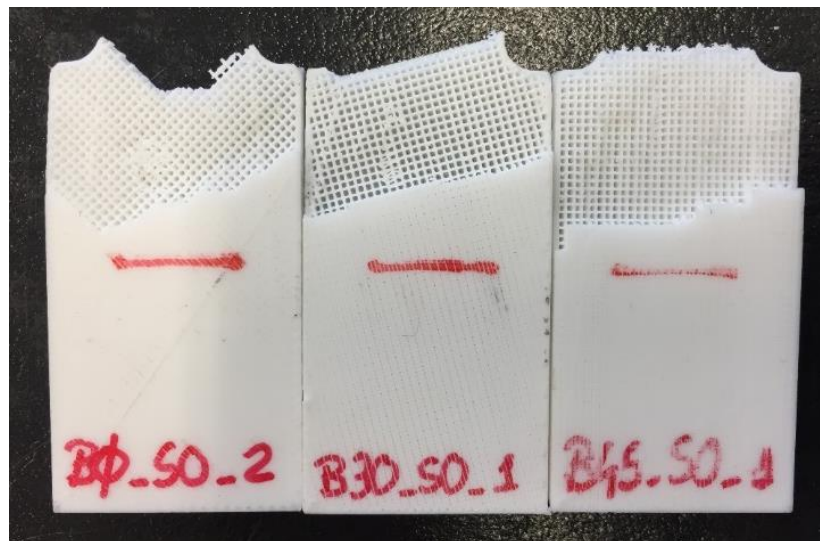


Figure 7.6 Crack pattern for notched samples

Figure 7.7 displays the failure factitious stress vs. infill level for the porous notched AM PLA specimens fabricated with different deposition angles θ_p and with various root radii for the notches. For U-notched samples the higher static strength of all θ_p values were shown by the higher infill ratio. Specifically, the specimens manufactured with θ_p equal to zero degrees, presented higher failure strength due to the contribution of both deposited filaments bearing the applied stress (see Figures 7.7a to 7.7c). In contrast,

for V-notched samples, by setting θ_p equal to 45° , the samples showed the highest strength. Notice from Figure 7.7 that the static strength of notched porous AM PLA parts is not clearly affected by the notches' root radius, which means that the existence of a notch does not influence the stress concentration, in PLA porous parts. In contrast, the in-fill porosity was the preponderant factor on the static strength of the AM PLA porous samples under tension.

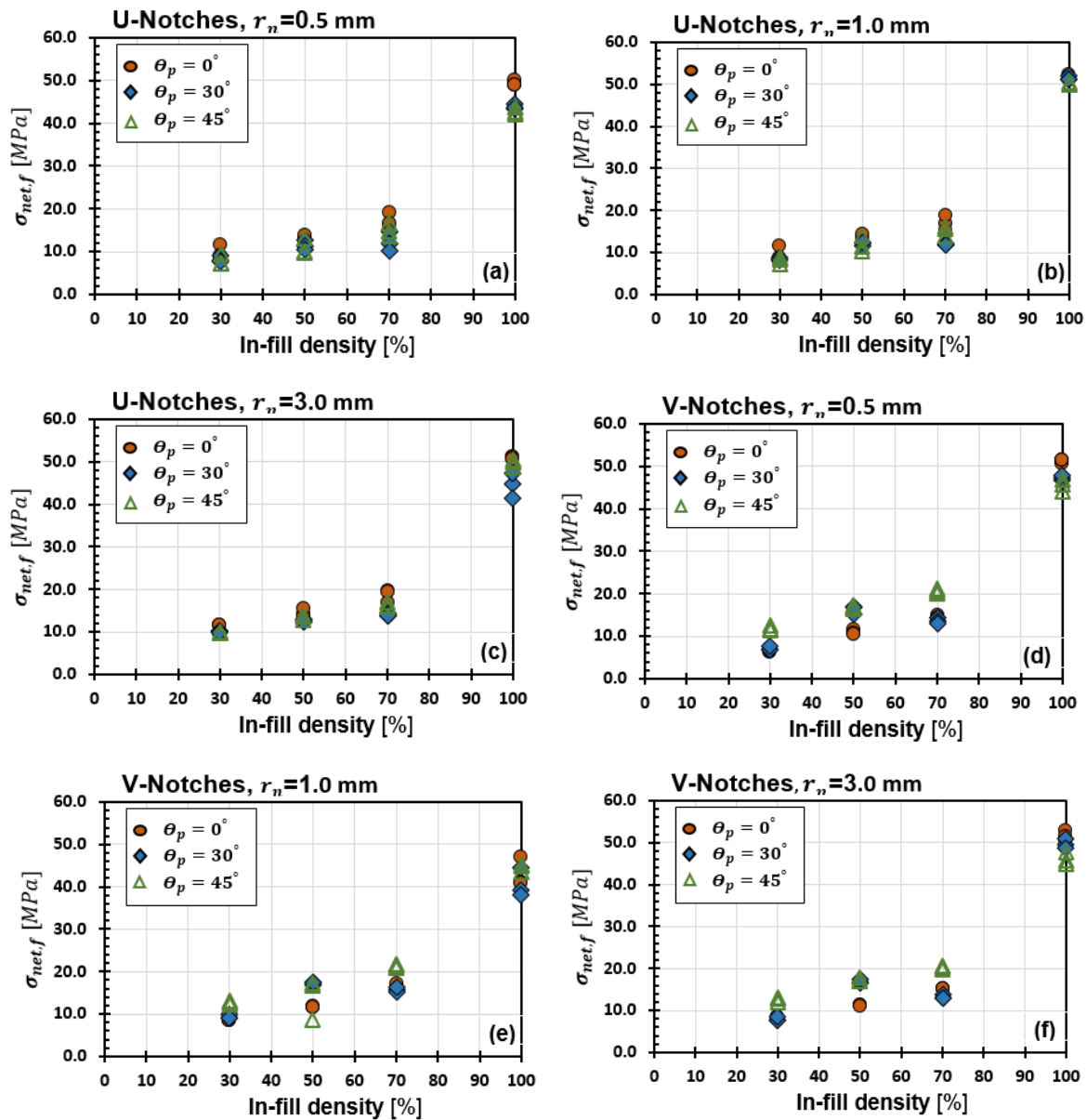


Figure 7.7 Factitious stress vs in-fill density for notched specimens

7.3 Mechanical behaviour in terms of the Equivalent Homogenised Material Concept

The most important finding from the previous investigation about PLA components with a fill density of 100%, is that the influence of the manufacturing angle on the mechanical properties could be neglected with little loss of accuracy. The experimental results showed that the mechanical properties of these specimens fell within $\mp 2SD$ of the mean value. The average values obtained were: $\sigma_{UTS} = 42.9$ MPa; $\sigma_{0.2\%} = 41.7$ MPa; $E = 3500$ MPa; and $K_{IC} = 3.7$ MPa·m^{0.5}

Regarding the fracture toughness test K_{IC} , it is noteworthy that, despite the effect of filament orientation on crack propagation, the values of K_{IC} fell within $\mp 2SD$ of the mean value. To involve the effect of the shell thickness on the K_{IC} value estimation, the CT test was conducted for the AM PLA specimens that had a shell perimeter, which means that the test achieved without any pre-cracks, as required by ASTM D5045 specification.

The static evaluation of the porous AM PLA components with infill levels lower than 100% was done with an equivalent homogenised material concept, considered an alternative TCD-based design approach capable of assessing the strength of these materials under static uniaxial loading. The TCD formulation depends on modelling the 3D printed PLA parts with lower than 100% infill ratio, as an equivalent material with an isotropic, homogeneous, continuum, and linear elastic behaviour.

The initial presumption is that the force vs. displacement relationship is re-analysed in terms of factitious stress σ_{fs} , and the measured strain, ε_{exp} (i.e., experimental strain from the extensometer reading). In other words, by disregarding the fabricated voids, σ_{fs} is taken as the applied load over the cross-sectional area:

$$\sigma_{fs} = \frac{F}{t \cdot w_n} \quad (7.1)$$

Where F is the applied load; t is the thickness; and w_n is the width of the sample within the extensometer length. Figure 7.2 showed the curves for σ_{fs} vs. ε_{exp} according to this simple procedure (see also Figure B.3.1). It is evident that the AM PLA material could be considered as purely linear elastic up to the highest stress recorded while testing the samples. This finding comports with the literature [53][107]. The porous PLA material with θ_p equal to 0° showed a high level of ductile behaviour after the maximum stress. In contrast, the porous PLA components with a deposition angle of 30° and 45° mainly failed directly after the maximum stress. All curves obtained from the experiments testing the plain porous specimens (Table 7.2, Table B.2.1 and B.2.2), had the same type of profile as those for conventional materials when the problem is addressed using standard engineering stresses and strains.

In this respect, the experimental results for the plain porous samples were re-analysed according to the fictitious stress, σ_{fs} , and the experimental strain, ε_{exp} , to find the failure stress σ_f , and fictitious 0.2% proof stress $\sigma_{0.2\%}$, and fictitious elastic modulus E (see Figures 7.4a – 7.4c). The results of the plain specimens with a 100% infill ratio, from the previous group of tested samples, were added for the sake of completeness. When the infill density was increased, the mechanical properties gradually increased, as expected. Also, Figure 7.4 evidences a palpable decrease in σ_f , $\sigma_{0.2\%}$, and E when moving from the infill level of 100% to 90%. The meso-structure of the 3D printed PLA material justifies this behaviour (see Section 7.1).

All mentioned above leads to the hypothesis of the effective modelling of AM PLA components, disregarding the in-fill density, by utilising an equivalent material that is homogenous, isotropic and continuum. Within this framework, the equivalent method will be explained in the next Section.

7.4 Static strength modelling of plain porous AM PLA

To develop a novel methodology for static strength assessment, it is appropriate to relate the strength of the plain porous PLA components to the variable internal fabricated void size, since failure stress increases with the in-fill density (evidenced in Figure 7.4). The specific formulation can be seen by taking the uniformly loaded PLA strip (see Figure 7.8A) with the equivalent void size d_v . It is presumed that the strip is in the incipient failure condition with fictitious stress of σ_f . The strip can be transformed to the infinite plate (Figure 7.8B) with a central through-thickness crack and has the same fracture toughness value K_{IC} and ultimate tensile strength σ_{UTS} of the same PLA material manufactured with an infill level of 100%. The material of the infinite plate is isotropic, homogenous and linear elastic.

The length of the central crack $2a_{eq}$ is established so that the failure of the plate occurs when the remotely applied stress on the plate equals the fictitious stress σ_f , causing the PLA plain strip to break in Figure 7.8A. In other words, the infinite plate with a central crack is also assumed to be in an initial crack state.

It is well known that the LEFM shape factor for a plate with a through-thickness central crack is equal to one, regardless of the crack length. According to the hypotheses being formed, LEFM postulates that the cracked plate in Figure 7.8B fails as soon as the resulting stress intensity factor equals the material fracture toughness K_{IC} . Accordingly, the failure condition for the homogenised equivalent cracked material can be expressed as:

$$K_{IC} = \sigma_f \sqrt{\pi \cdot a_{eq}} \quad (7.2)$$

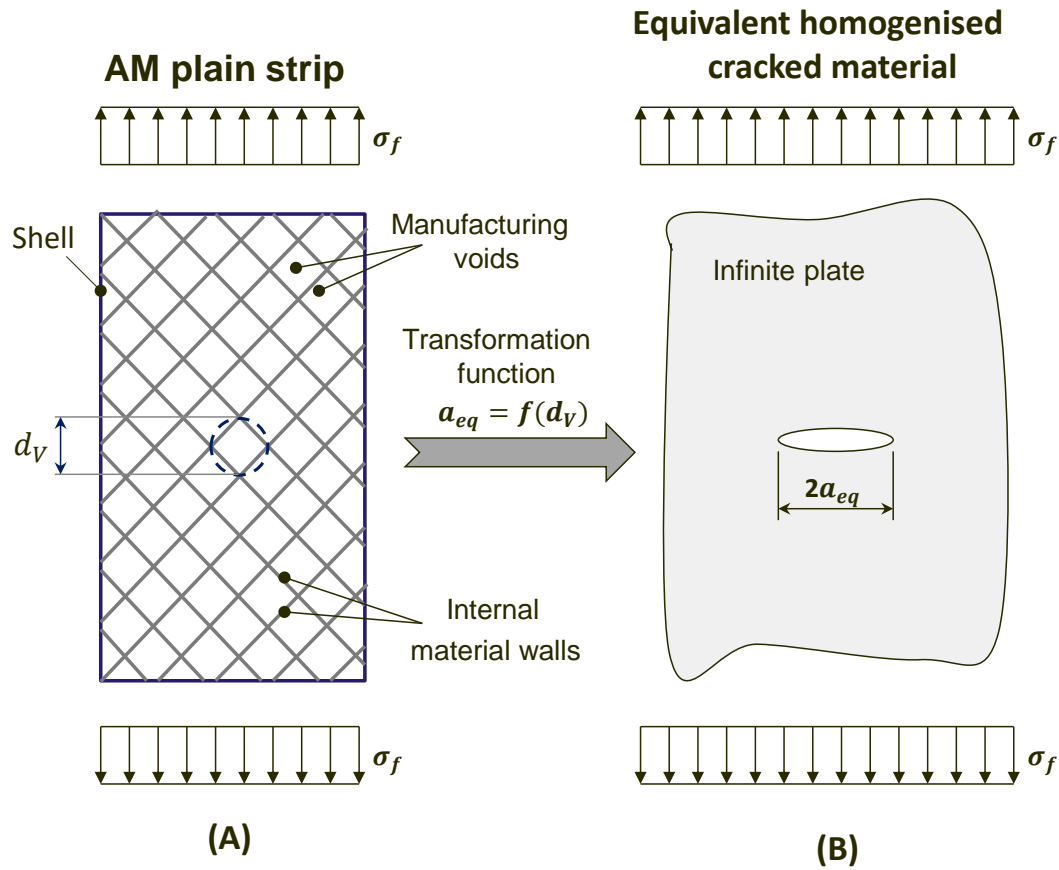


Figure 7.8 The transformation process to estimate the static strength of the plain porous AM PLA parts

The application of Equation (7.2) is valid if the plate in Figure 7.8B has a long crack. As a result, the crack length a_{eq} , can be written as:

$$a_{eq} = \frac{1}{\pi} \left(\frac{K_{IC}}{\sigma_f} \right)^2 \quad (7.3)$$

The next step in the procedure is to propose a relationship between the void size in the PLA strip (Figure 7.8A) and the length of the central crack in the infinite plate (Figure 7.8B), which can be expressed as follows:

$$a_{eq} = f(d_v) \quad (7.4)$$

where $f(d_v)$ is a conversion function, transferring the AM PLA plain strip (Figure 7.8A) to an equivalent, isotropic, homogeneous, continuum, and linear elastic cracked material (Figure 7.8B).

The importance of this transformation is to equalise the PLA strip and the cracked plate when they fail under the same applied stress, σ_f . This works under two conditions: (a) the stress for the cracked PLA plate is computed with regard to the gross area and disregarding the presence of a crack, (b) neglecting the existence of manufactured voids when defining the stress according to Equation (7.1), for the AM PLA strip.

As mentioned earlier, Equation (7.3) can be used to estimate a_{eq} as long as the size of the AM voids results, via Function (7.4), in an equivalent homogenised material weakened by the long crack. It is clear that when the infill level approaches 100%, the PLA voids will more likely behave as short cracks, rendering Equation (7.3) invalid. Alternatively, TCD can be used to activate the transition modelling from the short to the long-crack regime (see Section 4.7). In other words, the TCD methods PM and LM, via Equations (4.53) and (4.54), can be used directly to achieve the transition between the two regimes in an infinite plate with a through-thickness central crack.

Let's consider the PM formalisation, Equation (4.53), for a through-cracked plate under tension. Replacing the half-crack length (a), by the semi-crack length (a_{eq}), the equation can be solved to obtain a_{eq} :

$$a_{eq} = f(d_V) = \frac{L}{2\sigma_f^2} \left\{ (\sigma_{UTS}^2 - \sigma_f^2) + \sqrt{(\sigma_f^2 - \sigma_{UTS}^2)^2 - \sigma_f^2(\sigma_f^2 - \sigma_{UTS}^2)} \right\} \quad (7.5)$$

The equivalent semi-crack length for LM formula, Equation (7.4), is as follows:

$$a_{eq} = f(d_V) = L \left\{ \left(\frac{\sigma_{UTS}}{\sigma_f} \right)^2 - 1 \right\} \quad (7.6)$$

As stated above, the constants that quantify the static strength of the equivalent homogenised cracked material used in the transformation process of Figure 7.8 are assumed to be equal to the corresponding strength properties that are determined experimentally from 100% infill specimens made of the AM PLA material under investigation. In other words, the values for σ_{UTS} and K_{IC} , estimated from testing AM PLA with a 100% infill level, will be used to calculate the critical distance L , which in turn is used to evaluate a_{eq} from Equations (7.5) and (7.6).

The final step is to present the transformation function $f(d_V)$ that leads to good estimates. Optimising this process is important to minimize the effort for the $f(d_V)$ calculation. Thus, it is useful to assume the following linear relation between d_V and a_{eq} :

$$a_{eq} = f(d_V) = k_{tr} \cdot d_V \quad (7.7)$$

k_{tr} being the dimensionless transformation constant. The benefit of a simple linear relation is that we obtain a constant value of k_{tr} for a specific value of d_V . So, k_{tr} can be obtained from either from Equation (7.5) or Eq. (7.6) as:

$$k_{tr} = \frac{a_{eq}}{d_V} = \frac{L}{2 \cdot d_V \cdot \sigma_f^2} \left\{ (\sigma_{UTS}^2 - \sigma_f^2) + \sqrt{(\sigma_f^2 - \sigma_{UTS}^2)^2 - \sigma_f^2 (\sigma_f^2 - \sigma_{UTS}^2)} \right\} \quad (7.8)$$

$$k_{tr} = \frac{a_{eq}}{d_V} = \frac{L}{d_V} \left\{ \left(\frac{\sigma_{UTS}}{\sigma_f} \right)^2 - 1 \right\} \quad (7.9)$$

Where σ_f is the experimentally fictitious stress determined for the component with the size of voids d_V . After calculating the k_{tr} values, the failure strength of any infill ratio for PLA components can be estimated directly by using the PM and LM by rewriting Equations (4.53) and (4.54) as:

$$\sigma_f = \sigma_{UTS} \sqrt{1 - \left(\frac{k_{tr} \cdot d_V}{k_{tr} \cdot d_V + \frac{L}{2}} \right)^2} \quad (7.10)$$

$$\sigma_f = \sigma_{UTS} \sqrt{\frac{L}{k_{tr} \cdot d_V + L}} \quad (7.11)$$

The evaluation of the static strength of the plain PLA components was achieved according to Equations (7.10) and (7.11) using the experimental results in Table 7.2 (in addition to Tables B.2.1 and B.2.2). This was done to check the validity and accuracy of the equivalent homogenised material approach presented in this section. Specifically, the mechanical properties for PLA with a 100% infill level ($\sigma_{UTS} = 42.9$ MPa, $K_{IC} = 3.7$ MPa·m^{0.5}), were used to estimate the critical distance $L = 2.4$ mm, according to the following formula:

$$L = \frac{1}{\pi} \left(\frac{K_{IC}}{\sigma_{UTS}} \right)^2 \quad (7.12)$$

Next, calculating the conversion function $f(d_V)$ from Equation (7.4), was done by using the results of all specimens (all voids sizes) with three manufacturing angles ($\theta_p = 0^\circ, 30^\circ$ and 45°). According to Equations (7.8) and (7.9), the conversion constant k_{tr} for the PM and LM approaches were computed. The average value of k_{tr} for PM and LM are 32.6 and 29.3 subsequently.

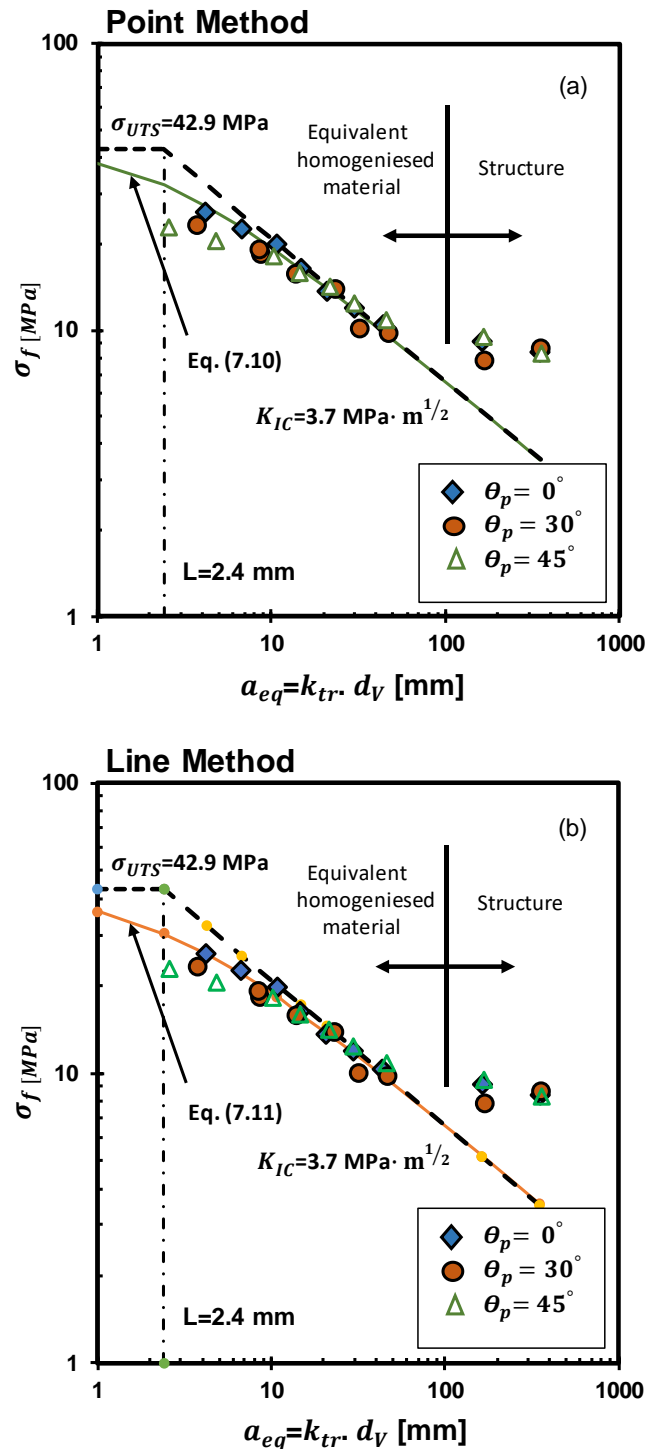


Figure 7.9 Accuracy of the proposed methodology in modelling static strength of plain porous AM PLA: a) PM, b) LM

By drawing the results of failure strength via Equations (7.10) and (7.11), according to Kitagawa-Takahashi diagrams (Figure 7.9), it is clear that these equations accurately predict the static strength of the plain porous AM PLA components. The two charts in Figure 7.9 (see also Tables B.5.1-B.5.3), showed noticeable accuracy in strength estimation until reaching the 30% infill level by using the suggested approach. The estimated results of samples with 20% and 10% infill, however, did not follow the predicted trend. The behaviour of AM parts, with a very coarse mesh of the internal walls, as lattice structures, explains this expected deviation [113]. Consequently, the proposed equivalent homogenised material approach is limited and no longer verified for 3D-printed components with a very low in-fill density. This fact presents the lower limit in the practical application of the suggested methodology.

To summarise, the high accuracy of the formulated approach was achieved by the simple linear transformation in Equation (7.7). And, the theoretical framework can be extended to assess the static strength of other net-like components by using other kind of functions to express $f(d_V)$.

7.5 Static strength of notched porous AM PLA components

It is well known that the AM technique can easily fabricate components with complex geometries at a high level of accuracy in dimensions and shapes. Complex features, however, produce a very complicated stress concentration that markedly affect the overall object strength. It is therefore important to use a reliable and simple design method to evaluate the static strength of AM material accurately. Thus, the equivalent homogenised material concept, in combination with the TCD, will be extended in this section to evaluate the static strength of notched porous AM PLA objects. The details of the tested notched porous PLA specimens are shown in Figure 7.10.

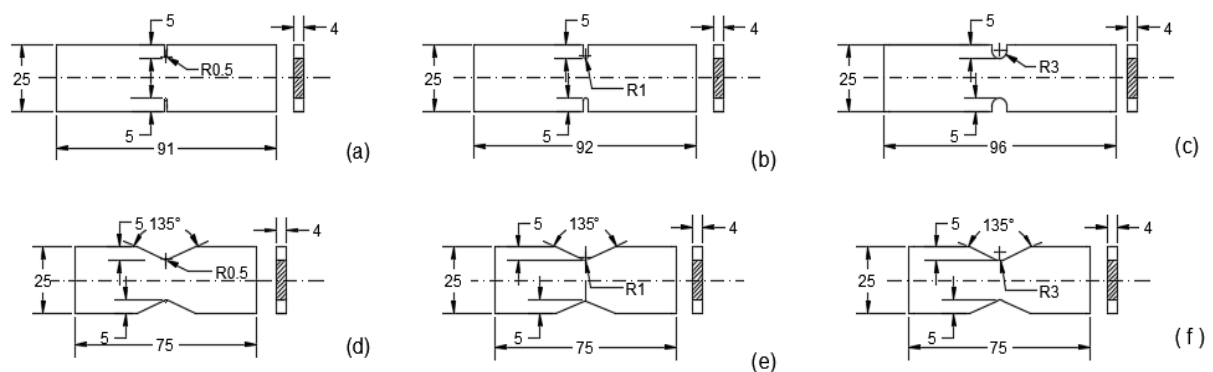


Figure 7.10 The notched AM PLA samples with manufactured voids, dimensions are in mm

Let us consider the loaded notched component in Figure 7.11. The voids are representing the spaces produced by an AM PLA with an infill level lower than 100%. Evaluating the strength of the notched AM PLA parts by the TCD approach must model the notched object in Figure 7.11A as a homogeneous, continuum, and isotropic material with linear elastic behaviour (Figure 7.11B).

With these assumptions, the static strength of the sample can be estimated by PM, LM, and the area method assuming a fixed size of the process zone near the notch tip which does not change with the void size. The value of the critical distance L is computed by Equation (7.12), taking the experimental values of K_{IC} and σ_{UTS} for PLA material with an infill level of 100% (Figure 7.11B). It is clear from Equations (7.10) and (7.11) that the size of the void influences the material intrinsic static strength, and the L value is constant for specific AM material.

According to this procedure, the fictitious stress near the notch tip (Figure 7.11C) is calculated by FE modelling or by analytical solution, since the material is assumed homogenous, isotropic, and linear elastic. Once the fictitious stress field is known, TCD is applied according to Equations (4.18), (4.25), and (4.27) for the PM, LM and area methods, respectively, to find the effective stress σ_{eff} . Due to the presence of manufacturing voids in the PLA material, the incipient failure case can be represented as:

$$\sigma_{eff} = \sigma_f \quad (7.13)$$

Where σ_f is the failure strength within the process zone, which can be directly evaluated according to Equations (7.10) or (7.11). In other words, by combining Equation (4.18) and Equation (7.10) according to the failure condition (7.13), the material failure can be expressed by PM as:

$$\sigma_{eff} = \sigma\left(\theta = 0, r = \frac{L}{2}\right) = \sigma_{UTS} \sqrt{1 - \left(\frac{k_{tr} \cdot d_V}{k_{tr} \cdot d_V + \frac{L}{2}}\right)^2} \quad (7.14)$$

Similarly, combining Equation (4.25) with Equation (7.11) shows the condition (7.13) according to LM as:

$$\sigma_{eff} = \frac{1}{2L} \int_0^{2L} \sigma_y(\theta = 0, r) dr = \sigma_{UTS} \sqrt{\frac{L}{k_{tr} \cdot d_V + L}} \quad (7.15)$$

The experimental results of the tested notched porous PLA samples (Table 7.3, and Tables B.2.3 to B.2.7) were used to check the validity and accuracy of the novel

reformulation of the TCD proposed in this section. In this regard, the elastic stress field needed for the TCD application is determined from bi-dimensional modelling of the samples using an ANSYS program. The mapped meshing near the notch tip was refined until the stress convergence occur, by utilising the Plane 183 elements.

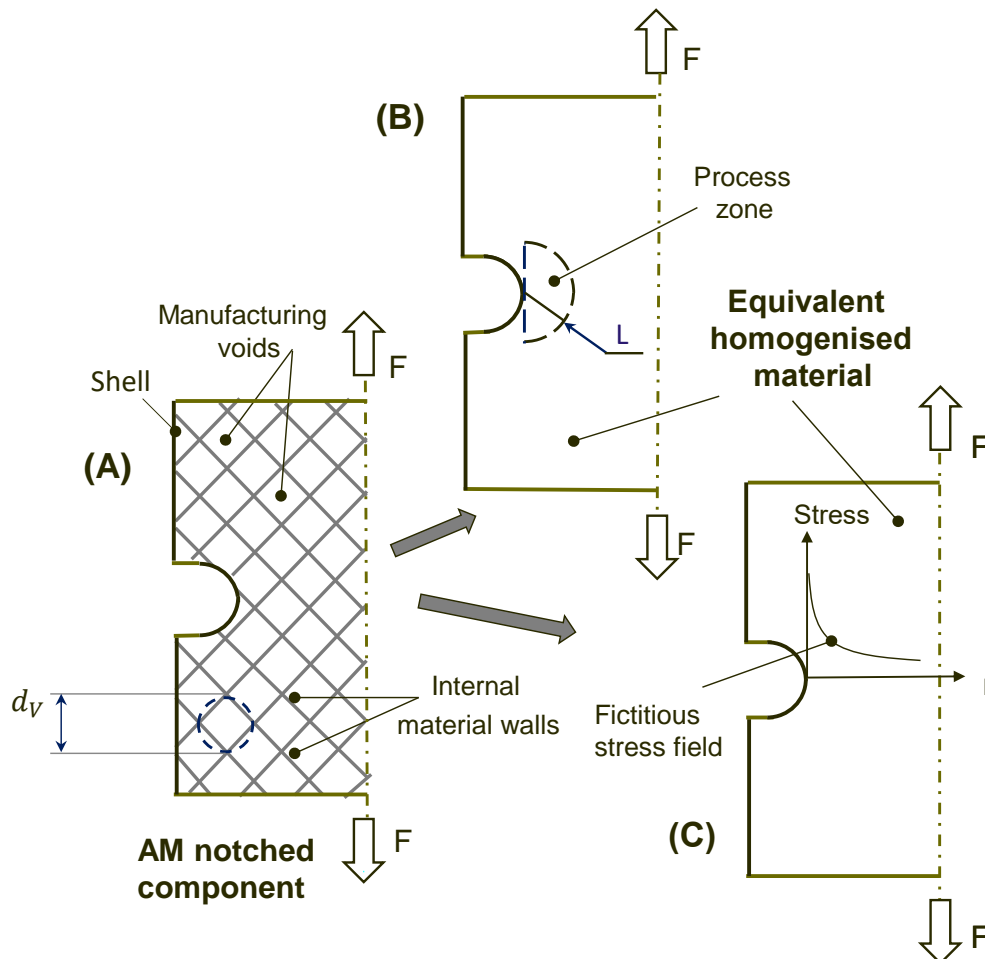


Figure 7.11 Notched porous AM PLA components with the suggested process zone and fictitious linear elastic stress

It is worth pointing out that the existence of the voids in the PLA parts is neglected when modelling the specimens for FE analysis, because the material is assumed homogeneous, continuum, isotropic and linear elastic. The critical distance, according to Equation (7.12), is equal to 2.4 mm. The $\sigma_{UTS} = 42.9$ MPa, and the fracture toughness $K_{IC} = 3.7$ MPa \cdot m $^{1/2}$, are the values estimated for PLA parts with a 100% infill level. The next step after estimating the L value is post-processing the FE analysis results to find σ_{eff} according to PM, Equation (4.18); the LM, Equation (4.25); and the area method, Equation (4.27).

Then, by taking the transformation factor k_{tr} equal to 32.6 for the PM and to 29.3 for LM, the failure stress for the transformed models based on Equations (7.14) and

(7.15) can be estimated. Regarding the area method, the effective stress σ_{eff} was determined from the linear elastic field, according to Equation (4.27), while the failure stress is computed by PM Equation (7.14) with the corresponding value of transformation factor k_{tr} equal to 32.6.

Figure 7.12 presents the error percentage from applying the new formulation of the three TCD methods: PM, LM, and area method, compared with the results of the tested PLA AM notched specimens (see also Tables B.5.4 – B.5.9). The error in these diagrams was evaluated as:

$$Error = \frac{\sigma_{eff} - \sigma_f}{\sigma_f} [\%] \quad (7.16)$$

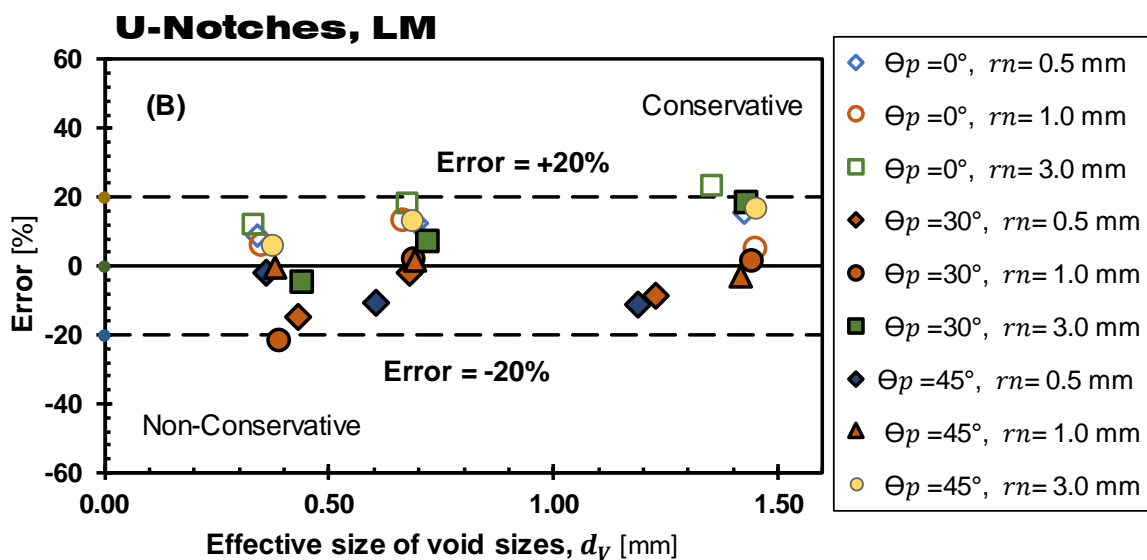
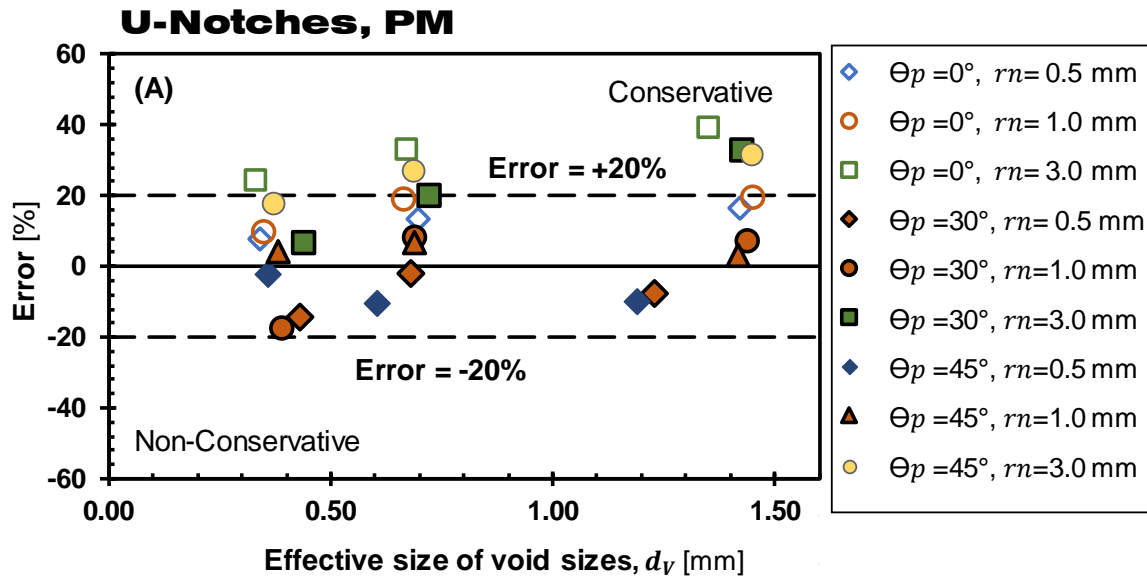
The conservative estimation is shown by a positive error, whereas the non-conservative prediction is shown by a negative error. It is noteworthy that every prediction was taken from three repeated experimental tests for every specimen's geometry (see Tables 7.3). It can be seen from Figures 7.12A- 7.12C that evaluating the static strength of the U-notched additively manufactured components with lower than a 100% infill level, can be successfully implemented by applying TCD with the equivalent homogenised material concept. Specifically, the regular employment of the suggested design procedure, for these notches, had showed an error estimate mainly within $\mp 20\%$ intervals.

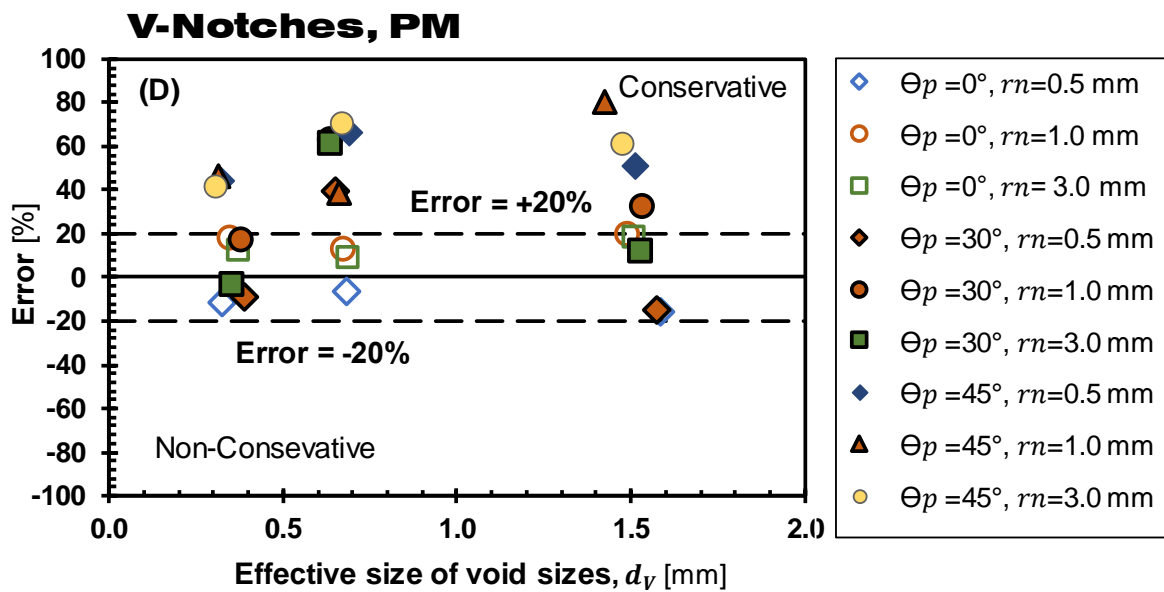
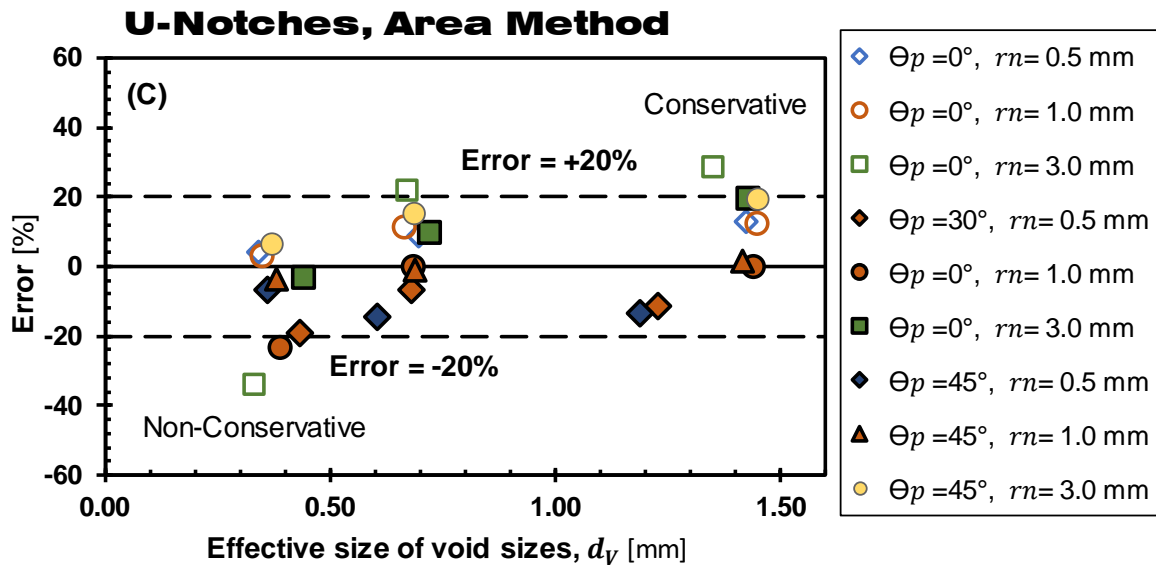
Regarding the U-notched samples, the static strength was not at all influenced by the deposit angle θ_p , according to Figures 7.7a-7.7c. This explains the consistency of the estimates falling mainly within an error of $\mp 20\%$ intervals by applying the suggested approach (Figures 7.12A - 7.12C).

By contrast, the open notched samples (Figures 7.7e-7.7g) showed a noticeable effect of the deposition angle θ_p , on the static strength. In particular, the estimated static strength for specimens with a θ_p equal to 45° was higher than the corresponding strength of samples with a θ_p equal to 0° and 30° , by 25% to 50%, (Figure 7.4b and Tables B.2.5- B.2.7). The increase in the static strength can be explained by careful checking of the broken specimens, which reveals that it is related to how the 3D printer deposits the fused filament. The shell thickness in samples with θ_p equal to 45° was doubled due to the internal walls being deposited very close to the notch tip. That means that the region of crack initiation for a θ_p equal to 45° was twice the thickness of the corresponding region for samples with a θ_p equal to 0° and 30° .

This explains the reason for the accurate estimation when applying the novel TCD formulation for a θ_p equal 0° and 30° open notched samples, while specimens with a θ_p equal to 45° showed a conservative estimate (Figures 7.12D - 7.12F). Nevertheless, the presented accuracy level in Figure 7.12 is acceptable due to the complex micro/meso-structure characterising the AM PLA materials. In addition, due

to problems commonly experienced during the experimental test and numerical analysis post-processing, this accuracy level is satisfactory since even with conventional engineering materials there is an error of between 0% and 20% [8].





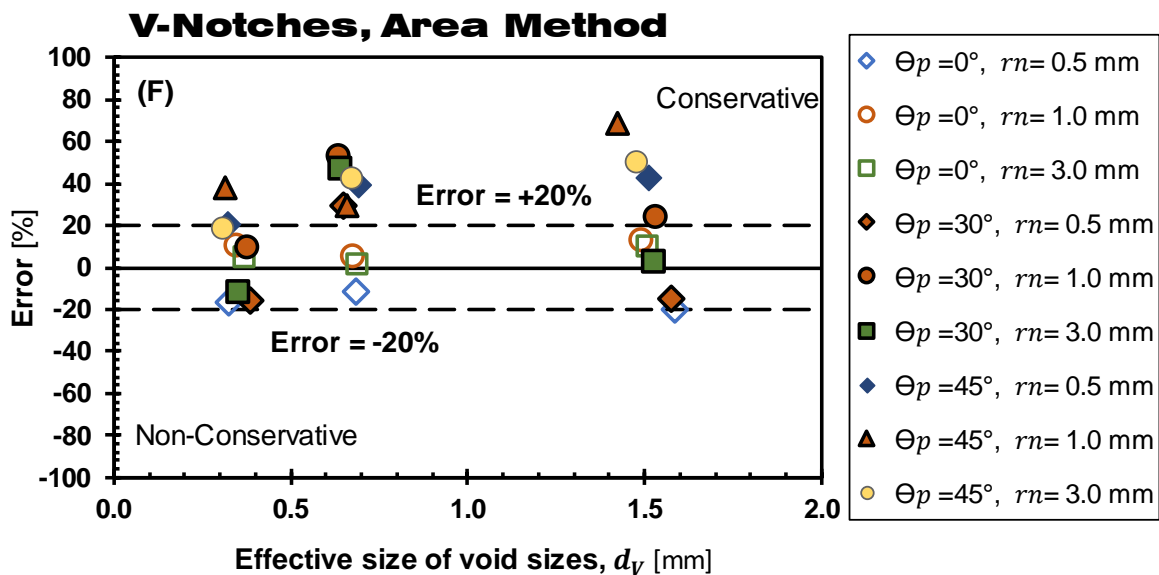
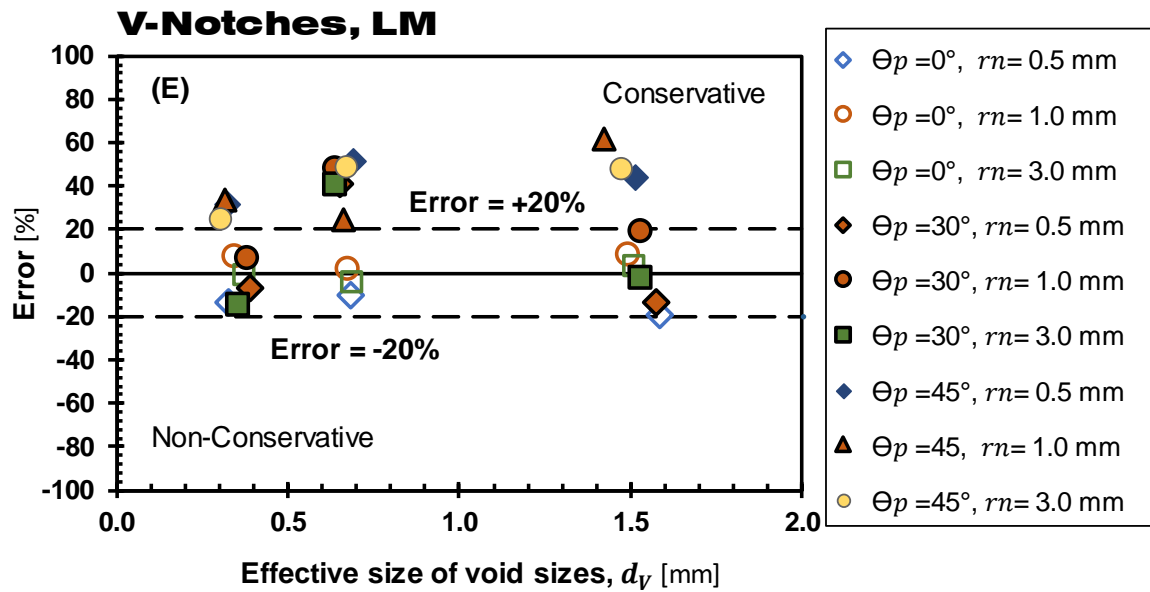


Figure 7.12 The accuracy of the proposed approach in evaluating the static strength of notched porous AM PLA, A) PM for U-notched samples, B) LM for U-notched samples, C) Area method for U-notched samples, D) PM for V-notched samples, E) LM for V-notched samples, and F) Area method for V-notched samples.

7.6 Conclusion

This investigation formulated a novel approach to perform the static strength evaluation of plain and notched AM PLA parts fabricated with various infill levels. It is based on the combination of TCD and the equivalent homogenised material concept.

AM PLA specimens with different geometrical discontinuities, infill levels and manufacturing angles, were tested under tension to verify the accuracy of the proposed approach against the results of the samples tested.

According to the outcomes obtained from the verification exercise with the experimental results, the following key points were obtained:

- The behaviour of additive manufactured PLA components can be modelled as linear elastic material up to the ultimate strength, regardless of the deposition angle θ_p and infill level, only producing a slight loss of precision.
- The internal walls' orientation controls the cracking pattern and the behaviour of plain and notched additively manufactured PLA porous components.
- As the void size increases, the static strength of AM PLA porous parts for both plain and notched objects, decreases.
- The static strength of plain additively manufactured PLA can be successfully predicted by the equivalent homogenised material hypothesis along with TCD, as the in-fill density decreases.
- The proposed approach can successfully assess the static strength of notched porous AM PLA objects with estimates error falling mainly within a $\pm 20\%$ interval.
- The key concept in the estimation of the AM PLA static strength by the equivalent homogenised material concept along with TCD is to assume that the AM PLA parts behave as homogeneous, continuum, isotropic, and linear elastic material when evaluating the requisite stress field by conventional FE modelling.
- The proposed approach is invalid in modelling the mechanical behaviour and static strength of 3D-printed parts when the infill level is very low, giving very coarse mesh for the internal wall.
- Due to time constraints, I was not able to estimate the strength of porous AM PLA under three-point bending, but perhaps this can be a subject for future research.

Chapter 8- General discussion, conclusion and future work

8.1 Discussion

This research investigated the accuracy of the linear elastic TCD approach in designing the 3D printed notched PLA components under static loading. The effect of different manufacturing parameters on the mechanical properties and fracture behaviour of AM PLA was first examined.

In contrast with 3D printed polymer fabricated with mono-directional filling [67-69], the experimental result of a large number of tested plain PLA specimens manufactured with orthogonal deposition, showed that the deposition angle and shell thickness showed a minor effect on the mechanical properties of the AM PLA components, tested under tension.

For both plain and notched AM PLA samples, the general crack initiation trend, independent of fibre orientation θ_p and shell thickness t_s , was perpendicular to the applied load. The subsequent crack propagation followed the direction of the fused filament θ_p . This crack behaviour robustly advocates the suggested mechanism of the fracture, fibres de-bonding and rectilinear fibres cracking. This fracture behaviour is similar to that of the fibrous material. Owing to the absence of matrix in AM PLA material, the de-bonding happens between adjacent fibres in the AM PLA components.

Regarding the fracture toughness test K_{IC} , it is noteworthy that despite the effect of filament orientation on crack propagation, the values of K_{IC} for AM PLA parts were within $\mp 2SD$ of the mean value. The (CT) test was conducted according to ASTM D5045-14 specifications to find the plane strain fracture toughness K_{IC} for the AM PLA, by manufacturing the specimens with solely θ_p equal to 45° , in order to promote mode-I cracking. The average computed value of K_{IC} equals $3.7 \text{ MPa} \cdot \text{m}^{1/2}$, which is nearly the same value found for PLA produced by injection moulding [58].

Regarding the strength prediction of the notched AM PLA manufactured with a 100% infill level, the validity verification of TCD methodology suggests that the linear elastic approach with TCD can be used in practical applications to design AM PLA components under static loading, for both tension and three-point loading. The key concept of TCD is to consider the material as isotropic and homogenous when evaluating the linear elastic stress field by FE modelling. This is true independent of the 3D printed deposition angle θ_p . Although the TCD approach has been used with polymeric materials manufactured by traditional injection moulding, this is the first use of the TCD to evaluate the strength of the 3D printed polymer.

By drawing the results of failure strength for porous plain AM PLA specimens (printed with less than 100% infill level), according to the Kitagawa-Takahashi diagrams, clearly, the proposed formula for this kind of specimens was accurate in predicting the static strength of plain porous PLA components. The equivalent homogenised material

concept along with TCD showed noticeable accuracy in strength estimation until the 30% infill level. However, the estimated results of samples with 20% and 10% were not the same. The AM PLA parts, with a very coarse mesh of the internal walls, behave as lattice structures, precipitated this behaviour.

It can be seen that it is possible to evaluate the static strength of notched AM PLA components manufactured with lower than a 100% infill level by applying TCD with the equivalent homogenised material hypotheses. The key concept of applying this novel formalisation is assuming the material as linear, elastic, homogeneous, and isotropic; and the process zone is not affected by the existence of the voids. The strength prediction estimates fell mostly within an error of ± 20 intervals. However, the open notched samples, especially for deposition angle equal to 45° , showed conservative estimates due to how the printer deposits the fused filament.

To conclude, this thesis is the first research to evaluate the static strength of 3D printed notched polymer components by TCD methodologies. In addition, the proposed approach, by utilising the TCD alongside the equivalent homogenised material concept, showed reliable and acceptable accuracy in estimating the static strength of the 3D printed notched and plain porous PLA components.

8.2 Conclusion

According to this research on PLA materials produced by 3D printing technology, and contingent on processing the experimental results of AM PLA parts and analysis, the following points can be summarised:

- The behaviour of the additive manufactured PLA components can be modelled as linear elastic material up to the ultimate strength, regardless of the deposition angle θ_p and the infill level, only resulting in a slight loss of precision.
- The mechanical properties results of PLA material (E , $\sigma_{0.2\%}$ and σ_{uts}), with 100% infill level, falls within two standard deviations of the mean for different values of θ_p and t_s , showing that these printing variables do not considerably influence on PLA AM strength properties, and the material behaves like homogenous and isotropic material.
- The critical distance L for AM PLA material, manufactured with 100% infill level, can be estimated from post-processing the results of samples with sharp notches and inherent material strength σ_o according to TCD, considering that the PLA objects is a brittle material by taking σ_o equal to σ_{uts} . The resulting L value is thus ten times the fused filament size.

- The TCD with the linear elastic approach, utilising the PM and area method, showed a reliable static strength prediction for the notched samples manufactured with 100% infill level, with error estimates falling mainly within $\pm 20\%$ interval.
- The static strength of plain PLA additively manufactured with infill level less than 100%, can be successfully predicted by the equivalent homogenised material hypothesis alongside with TCD, as the fill density decreases.
- Applying TCD with the equivalent homogenised material hypotheses can successfully assess the static strength of notched porous AM PLA objects manufactured with different infill levels, with error estimates falling mainly within $\pm 20\%$ interval, by applying the three TCD methods: PM, LM, and area method.
- The key concept in the estimation of the porous AM PLA static strength by the proposed approach is assuming the material as homogeneous, continuum, isotropic, and linear elastic when evaluating the requisite stress field by conventional FE modelling and taking the L value according to the process zone characteristics.
- The limits on the validity of the proposed equivalent homogenised material concept with TCD in predicting the strength of PLA material manufactured with less than 100% infill level, is when the mesh of the internal void is very coarse leading the material to behave as a lattice structure.

8.3 Recommendations for future work

Suggestions for future work include:

- Further investigation on understanding the effect of other printing parameters such as nozzle size, and layer thickness on the characteristic material length and strength of notched AM PLA components.
- Utilise other approaches (for instance, the strain energy density method) alongside the TCD, to confirm more accurate values for the AM PLA material characteristic length and inherent material strength, i.e., considering the 3-D printed PLA as a ductile material.

- Validating the proposed equivalent homogenised material concept with TCD, in evaluating the strength of porous AM PLA notched parts under 3-point bending.
- Verify the use of equivalent homogenised material method along with TCD in estimating the strength of AM parts manufactured with different infill pattern such as hexagonal and iso-grid infill.
- Checking the accuracy of the TCD in predicting the strength of 3D PLA notched components subject to other types of loading such as static multiaxial and fatigue loading.

References

- [1] D. Dimitrov, K. Schreve, and N. De Beer, "Advances in three dimensional printing - state of the art and future perspectives," *Rapid Prototyp. J.*, vol. 12, no. 3, pp. 136–147, 2006.
- [2] D. Croccolo, M. De Agostinis, and G. Olmi, "Experimental characterization and analytical modelling of the mechanical behaviour of fused deposition processed parts made of ABS-M30," *Comput. Mater. Sci.*, vol. 79, pp. 506–518, 2013.
- [3] C. Casavola, A. Cazzato, V. Moramarco, and C. Pappalettere, "Orthotropic mechanical properties of fused deposition modelling parts described by classical laminate theory," *Mater. Des.*, vol. 90, pp. 453–458, 2016.
- [4] Z. B. Mustafa, "Multiaxial Fatigue Characterization of Self-Reinforced Poly(lactic Acid-Calcium Phosphate Composite)," 2012.
- [5] Z. B. Velioglu, D. Pulat, B. Demirbakan, B. Ozcan, E. Bayrak, and C. Eriskan, "3D-printed poly(lactic acid) scaffolds for trabecular bone repair and regeneration: scaffold and native bone characterization.," *Connect. Tissue Res.*, vol. 00, no. 00, pp. 1–9, 2018.
- [6] M. I. Mohammed, B. Cadd, G. Peart, and I. Gibson, "Augmented patient-specific facial prosthesis production using medical imaging modelling and 3D printing technologies for improved patient outcomes," *Virtual Phys. Prototyp.*, vol. 13, no. 3, pp. 164–176, 2018.
- [7] K. Kim, S. Kim, J. Suk, J. Ahn, N. Kim, and B. S. Kim, "Flight test of flying-wing type unmanned aerial vehicle with partial wing-loss," *Proc. Inst. Mech. Eng. Part G J. Aerosp. Eng.*, vol. 0, no. 0, pp. 1–18, 2018.
- [8] D. Taylor, *Theory of critical distance*, vol. 53, no. 9. 2007.
- [9] P. Mm. L. T. Besuner, D. O. Harris, and J. M. Thomas, *Mechanics Life Technology*. 2018.
- [10] H. Neuber, *Theory of notch stresses*. 1938.
- [11] R. E. Peterson, *Methods of correlating data from fatigue tests of stress concentration specimens*. New York, 1938.
- [12] R. E. Peterson, *Notch-sensitivity in Metal Fatigue*. 1959.
- [13] H. Neuber, *Theory of notch stresses : principle for exact calculation of strength with reference to structural form and material,* in *Theory of notch stresses*. 1961.
- [14] G. R. Irwin, "Analysis of stresses and strains near the end of crack traversing a plate," *J. Appl. Mech.*, vol. 24, pp. 361–364, 1957.
- [15] V. V. Novozhilov, "On a necessary and sufficient criterion for brittle strength," *J. Appl. Math. Mech.*, vol. 33, no. 2, pp. 201–210, 2003.
- [16] G. . McClintock, F.A. and Irwin, "Plasticity aspects of fracture mechanics," *ASTM STP 381*, 1965.

-
- [17] J. M. Whitney and R. Nuismer, "Stress fracture criteria for laminated composites containing stress concentrations," *J. Compos. Mater.*, vol. 8, no. 8, pp. 253–265, 1974.
- [18] R. Louks, H. Askes, and L. Susmel, "A generalised approach to rapid finite element design of notched materials against static loading using the Theory of Critical Distances," *Mater. Des.*, vol. 108, pp. 769–779, 2016.
- [19] D. Taylor, M. Merlo, R. Pegley, and M. P. Cavatorta, "The effect of stress concentrations on the fracture strength of polymethylmethacrylate," *Mater. Sci. Eng. A*, vol. 382, no. 1–2, pp. 288–294, 2004.
- [20] L. Susmel and D. Taylor, "The Theory of Critical Distances to estimate the static strength of notched samples of Al6082 loaded in combined tension and torsion. Part I: Material cracking behaviour," *Eng. Fract. Mech.*, vol. 77, no. 3, pp. 452–469, 2010.
- [21] L. Susmel and D. Taylor, "The Theory of Critical Distances to estimate the static strength of notched samples of Al6082 loaded in combined tension and torsion. PartII: Material cracking behaviour," *Eng. Fract. Mech.*, vol. 77, no. 3, pp. 452–469, 2010.
- [22] W. Li, L. Susmel, H. Askes, F. Liao, and T. Zhou, "Assessing the integrity of steel structural components with stress raisers using the Theory of Critical Distances," *Eng. Fail. Anal.*, vol. 70, pp. 73–89, 2016.
- [23] L. Susmel and D. Taylor, "On the use of the Theory of Critical Distances to predict static failures in ductile metallic materials containing different geometrical features," *Eng. Fract. Mech.*, vol. 75, no. 15, pp. 4410–4421, 2008.
- [24] L. Susmel and D. Taylor, "The theory of critical distances to predict static strength of notched brittle components subjected to mixed-mode loading," *Eng. Fract. Mech.*, vol. 75, no. 3–4, pp. 534–550, 2008.
- [25] J. B. D. and L. S. A. A. H. Ameri and Department, "On the use of linear-elastic local stress to design load-carrying fillet-welded steel joints against static loading," 2015.
- [26] J. W. Stansbury and M. J. Idacavage, "3D printing with polymers: Challenges among expanding options and opportunities," *Dent. Mater.*, vol. 32, no. 1, pp. 54–64, 2016.
- [27] B. McKenna, "The Next Big Thing in 3-D Printing: Big Area Additive Manufacturing, or BAAM," *The Motley fool*, 2014. [Online]. Available: <http://www.fool.com/investing/general/2014/04/26/the-next-big-thing-in-3-d-printing-big-area-addi-2.aspx>.
- [28] EOS, "E-Manufacturing Solution," 2016. [Online]. Available: http://www.eos.info/industries_markets/medical/medical_devices.
- [29] Ultimaker, "Ultimaker, 'Cura software,'" 2016. [Online]. Available: <https://ultimaker.com/en/products/cura-software>.
- [30] M. Gebler, A. J. M. Schoot Uiterkamp, and C. Visser, "A global sustainability perspective on 3D printing technologies," *Energy Policy*, vol. 74, no. C, pp. 158–167, 2014.

- [31] M. Hofmann, "3D printing gets a boost and opportunities with polymer materials," *ACS Macro Lett.*, vol. 3, no. 4, pp. 382–386, 2014.
- [32] 3DEO, "Costs of Traditional vs. Additive Manufacturing," *Metal and 3d printing*. [Online]. Available: <https://news.3deo.co/strategy/costs-traditional-vs-additive-manufacturing>.
- [33] Fabbaloo, "How Additive Manufacturing Complements Conventional Plastics Production," 2019. [Online]. Available: <https://www.fabbaloo.com/blog/2019/8/16/how-additive-manufacturing-complements-conventional-plastics-production>.
- [34] Hopkinson, *Rapid Manufacturing. An Industrial Revolution for the Digital Age*. 2006.
- [35] M. Boston, "'Additive manufacturing,' AM 3D," 2016. .
- [36] ORD, "'RoVa3D 5 Extruder 3D Printer,' ORD solution," 2019. [Online]. Available: <https://www.ordsolutions.com/rova3d-5-extruder-3d-printer-package/>.
- [37] J. De Ciurana, L. Serenó, and È. Vallès, "Selecting process parameters in RepRap additive manufacturing system for PLA scaffolds manufacture," *Procedia CIRP*, vol. 5, pp. 152–157, 2013.
- [38] Winson, "all3dp," 2018. [Online]. Available: <https://all3dp.com/topic/winsun/>.
- [39] D. Carothers, "Studies of polymerization and ring formation," *J. Am. Chem. Soc.*, vol. 54, pp. 761–772, 1932.
- [40] R. Zhu, "Preparation of Maleic Anhydride Grafted Poly(Lactid Acid) (Pla) and Its Compatibilization Effects on Pla/Soy Protein Composites," *Thesis*, no. May, 2011.
- [41] K. L. Owen, "Control of Microstructure in Poly-Lactic Acid and the Effect on Biodegradation," *Master thesis*, no. September, 2012.
- [42] M. Jamshidian, E. A. Tehrany, M. Imran, M. Jacquot, and S. Desobry, "Poly-Lactic Acid: Production, applications, nanocomposites, and release studies," *Compr. Rev. Food Sci. Food Saf.*, vol. 9, no. 5, pp. 552–571, 2010.
- [43] S.-D. Park, M. Todo, and K. Arakawa, "Effects of isothermal crystallization on fracture toughness and crack growth behavior of poly (lactic acid)," *J. Mater. Sci.*, vol. 40, no. 4, pp. 1055–1058, 2005.
- [44] advisor, "GRANTA," 2012. [Online]. Available: <http://inventor.grantadesign.com/en/index.asp>.
- [45] Z. Grigale and M. Kalnins, "Biodegradable Plasticized Poly (lactic acid) Films," *Sci. J. Riga Tech. Univ. Mater. Sci. Appl. Chem.*, vol. 21, pp. 97–103, 2010.
- [46] Chilson, "The difference Between ABS and PLA for 3D printing," 2013. [Online]. Available: <http://2015.igem.org/wiki/images/2/24/CamJIC-Specs-Strength.pdf>.
- [47] G. Kfoury *et al.*, "Recent advances in high performance poly(lactide): from 'green' plasticization to super-tough materials via (reactive) compounding.," *Front. Chem.*, vol. 1, no. December, pp. 1–46, 2013.

-
- [48] D. Taylor, "The theory of c ," *Eng. Fract. Mech.*, vol. 75, no. 7, pp. 1696–1705, 2008.
- [49] MATTER, "3D Matter, Unlocking Material Properties," 2015. .
- [50] Leapfrog, "Architectuer / Leapfrog 3D Printers," 2015. [Online]. Available: www.ipfrg.com.
- [51] B. Wittbrodt and J. M. Pearce, "The Effects of PLA Color on Material Properties of 3-D Printed Components Department of Materials Science & Engineering , Michigan Technological University , Department of Electrical & Computer Engineering , Michigan Technological * Corresponding author :," vol. 116, pp. 110–116, 2015.
- [52] J. F. Rodríguez, J. P. Thomas, and J. E. Renaud, "Design of Fused-Deposition ABS Components for Stiffness and Strength," *J. Mech. Des.*, vol. 125, no. 3, p. 545, 2003.
- [53] A. Lanzotti, M. Grasso, G. Staiano, and M. Martorelli, "The impact of process parameters on mechanical properties of parts fabricated in PLA with an open-source 3-D printer," *Rapid Prototyp. J.*, vol. 21, no. 5, pp. 604–617, 2015.
- [54] J. M. Chacón, M. A. Caminero, E. García-Plaza, and P. J. Núñez, "Additive manufacturing of PLA structures using fused deposition modelling: Effect of process parameters on mechanical properties and their optimal selection," *Mater. Des. J.*, vol. 124, pp. 143–157, 2017.
- [55] T. Letcher, "Material property testing of 3D-Printed specimen in PLA on an entry-level 3D printer," *Proc. ASME 2014 Int. Mech. Eng. Congr.*, pp. 1–8, 2016.
- [56] L. Wang, W. M. Gramlich, and D. J. Gardner, "Improving the impact strength of Poly(lactic acid) (PLA) in fused layer modeling (FLM)," *Polym. (United Kingdom)*, vol. 114, pp. 242–248, 2017.
- [57] B. M. Tymrak, M. Kreiger, and J. M. Pearce, "Mechanical properties of components fabricated with open-source 3-D printers under realistic environmental conditions," *Mater. Des.*, vol. 58, pp. 242–246, 2014.
- [58] Y. Jin, Y. He, and A. Shih, "Process Planning for the Fuse Deposition Modeling of Ankle-Foot-Othoses," *Procedia CIRP*, vol. 42, no. Isem Xviii, pp. 760–765, 2016.
- [59] S. Ravindrababu, Y. Govdeli, Z. W. Wong, and E. Kayacan, "Evaluation of the influence of build and print orientations of unmanned aerial vehicle parts fabricated using fused deposition modeling process," *J. Manuf. Process.*, vol. 34, no. December 2017, pp. 659–666, 2018.
- [60] Gravity, "Zero-Gravity 3D Printer, Made in space," 2015.
- [61] Q. Deng, S. Li, and Y. Chen, "Mechanical properties and failure mechanism of wood cell wall layers," *Comput. Mater. Sci.*, vol. 62, pp. 221–226, 2012.
- [62] S. Amada and S. Untao, "Fracture properties of bamboo," *Compos. Part BEngineering*, vol. 32, no. 5, pp. 451–459, 2001.
- [63] D. Huang, Y. Bian, A. Zhou, and B. Sheng, "Experimental study on stress-strain

- relationships and failure mechanisms of parallel strand bamboo made from phyllostachys," *Constr. Build. Mater.*, vol. 77, pp. 130–138, 2015.
- [64] R. Z. Yang, Y. Xiao, and F. Lam, "Failure analysis of typical glubam with bidirectional fibers by off-axis tension tests," *Constr. Build. Mater.*, vol. 58, pp. 9–15, 2014.
- [65] C. S. Verma and V. M. Chariar, "Stiffness and strength analysis of four layered laminate bamboo composite at macroscopic scale," *Compos. Part B Eng.*, vol. 45, no. 1, pp. 369–376, 2013.
- [66] Z. X. Guo and B. Derby, "Solid-state fabrication and interfaces of fibre reinforced metal matrix composites," *Prog. Mater. Sci.*, vol. 39, no. 4–5, pp. 411–495, 1995.
- [67] A. Matzenmiller, J. Lubliner, and R. L. Taylor, "A constitutive model for anisotropic damage in fiber-composites," *Mech. Mater.*, vol. 20, no. 2, pp. 125–152, 1995.
- [68] R. Talreja and C. V. Singh, "Damage and Failure of Composite Materials," p. 315, 2012.
- [69] A. Griffith, *The phenomena of rupture and flow in solids*, philosophical transactions. 1920.
- [70] Broberg, *Linear Elastic Fracture Mechanics*. 1999.
- [71] Anderson, *Fracture Mechanics*. 1995.
- [72] D. Roylance, *Introduction to Fracture Mechanics*, Massachusetts Institute of Technology. Cambridge, 2001.
- [73] S. Kasiri, D. J. Kelly, and D. Taylor, "Can the theory of critical distances predict the failure of shape memory alloys?," *Comput. Methods Biomech. Biomed. Engin.*, vol. 14, no. 6, pp. 491–496, 2011.
- [74] C. Inglis, "stress in plate due to presence of cracks and sharp corners," transaction of the institute of naval architects," 1913.
- [75] G. Irwin, *Fracture Mechanics*. 1948.
- [76] A. Seweryn, *Fracture Mechanics*. 1998.
- [77] P. Arthur, R. J. Schmidt, J. Hayton, and K. Hepburn, *Advanced Mechanics OF MATERIALS*. 2002.
- [78] L. Susmel, "The theory of critical distances: a review of its applications in fatigue," *Eng. Fract. Mech.*, vol. 75, no. 7, pp. 1706–1724, 2008.
- [79] R. J. Nuismer, "Stress Fracture Criteria for Laminated Composites Containing Nonmetallic Materials Division Air Force Materials Laboratory," 1996.
- [80] H. . Westergaard, "Bearing Pressures and Cracks.," *J. Appl. Mech.* 6, pp. A49–A53, 1939.
- [81] S. Cicero, V. Madrazo, and I. A. Carrascal, "Analysis of notch effect in PMMA using the Theory of Critical Distances," *Eng. Fract. Mech.*, vol. 86, pp. 56–72, 2012.

-
- [82] D. Bellett, D. Taylor, S. Marco, E. Mazzeo, J. Guillois, and T. Pircher, "The fatigue behaviour of three-dimensional stress concentrations," *Int. J. Fatigue*, vol. 27, no. 3, pp. 207–221, 2005.
- [83] M. H. E. Haddad, K. N. Smith, and T. H. Topper, "Fatigue Crack Propagation of Short Cracks," *J. Eng. Mater. Technol.*, vol. 101, no. 1, pp. 42–46, 1979.
- [84] T. Voiconi, R. Negru, E. Linul, L. Marsavina, and H. Filipescu, "The notch effect on fracture of polyurethane materials," *Frat. ed Integrita Strutt.*, vol. 30, pp. 101–108, 2014.
- [85] K. Tsuji, K. Iwase, and K. Ando, "Investigation into the location of crack initiation sites in alumina, polycarbonate and mild steel," *Fatigue Fract. Eng. Mater. Struct.*, vol. 22, no. 6, pp. 509–517, 1999.
- [86] P. C. Creager, M. and Paris, "Elastic field equations for blunt cracks with reference to stress corrosion cracking," *Int. J. Fract. Mech.* 3, vol. 3, 1967.
- [87] H. D. Kinloch, "Crack propagation in rubber-toughened epoxy," *Int. Conf. yield, Deform. Fract.*, 1982.
- [88] F. J. Gómez, G. V. Guinea, and M. Elices, "Failure criteria for linear elastic materials with U-notches," *Int. J. Fract.*, vol. 141, no. 1–2, pp. 99–113, 2006.
- [89] A. Seweryn, "Brittle fracture criterion for structures with sharp notches," *Eng. Fract. Mech.*, vol. 47, no. 5, pp. 673–681, 1994.
- [90] A. A. H. Ameri, J. B. Davison, and L. Susmel, "On the use of linear-elastic local stresses to design load-carrying fillet-welded steel joints against static loading," *Eng. Fract. Mech.*, vol. 136, pp. 38–57, 2015.
- [91] D. Taylor, "Geometrical effects in fatigue: a unifying theoretical model," *Int. J. Fatigue*, vol. 21, no. 5, pp. 413–420, 2000.
- [92] D. Taylor, "Predicting the fracture strength of ceramic materials using the theory of critical distances," *Eng. Fract. Mech.*, vol. 71, no. 16–17, pp. 2407–2416, 2004.
- [93] H. Askes, P. Livieri, L. Susmel, D. Taylor, and R. Tovo, "Intrinsic material length, theory of critical distances and gradient mechanics: Analogies and differences in processing linear-elastic crack tip stress fields," *Fatigue Fract. Eng. Mater. Struct.*, vol. 36, no. 1, pp. 39–55, 2013.
- [94] L. Susmel, H. Askes, T. Bennett, and D. Taylor, "Theory of Critical Distances versus Gradient Mechanics in modelling the transition from the short to long crack regime at the fatigue limit," *Fatigue Fract. Eng. Mater. Struct.*, vol. 36, no. 9, pp. 861–869, 2013.
- [95] Westergaard, "Bearing Pressure and cracks," *J. Appl. Mech.*, pp. A48–A53, 1939.
- [96] J. F. K. Ritchie, "On The relationship between Critical Tensile Stress and Fracture Toughness in Mild Steel.pdf," *J. Me&. Phys. Solids*, 21, vol. 21, pp. 395–410, 1973.
- [97] W. Weibull, "The phenomenon of rupture in solids," *Proc. R. Swedish Inst. Eng.*

- Res., 1939.
- [98] B. Y. M. L. Williams, "Stress Singularities Resulting From Various Boundary Conditions in Angular Corners of Plates in Extension," *J. Appl. Mech.*, pp. 526–528, 1952.
- [99] R. A. Smith and K. J. Miller, "Prediction of fatigue regimes in notched components," *Int. J. Mech. Sci.*, vol. 20, no. 4, pp. 201–206, 1978.
- [100] A. Hillerborg, M. Modéer, and P. E. Petersson, "Analysis of crack formation and crack growth in concrete by means of fracture mechanics and finite elements," *Cem. Concr. Res.*, vol. 6, no. 6, pp. 773–781, 1976.
- [101] J. Grenestedt, *Engineering Fracture Mechanics*. 1996.
- [102] ASTM D638-14, "Standard Test Method for Tensile Properties of Plastics," *Annu. B. ASTM Stand.*, pp. 1–15, 2004.
- [103] L. Susmel, D. Taylor, and R. Tovo, "On the Estimation of Notch Fatigue Limits by Using the Theory of Critical Distances: L, a_0 and Open Notches," *SDHM*, vol. 4, no. 1, pp. 81–86, 2008.
- [104] ASTM D5045, "Standard Test Methods for Plane-Strain Fracture Toughness and Strain Energy Release Rate of Plastic Materials 1," *ASTM J.*, vol. 99, no. C, pp. 1–9, 2014.
- [105] L. Kuentz, A. Salem, M. Singh, M. C. Halbig, and J. A. Salem, "Additive Manufacturing and Characterization of Polylactic Acid (PLA) Composites Containing Metal Reinforcements," *Natl. Aeronaut. Sp. Adm.*, pp. 1–22, 2017.
- [106] PLANE183, "PLANE183 Element Description," *Release 18.2 - © ANSYS, Inc.* [Online]. Available: http://www.mm.bme.hu/~gyebro/files/ans_help_v182/ans_elem/Hlp_E_PLANE183.html.
- [107] Y. Song, Y. Li, W. Song, K. Yee, K. Y. Lee, and V. L. Tagarielli, "Measurements of the mechanical response of unidirectional 3D-printed PLA," *Mater. Des.*, vol. 123, pp. 154–164, 2017.
- [108] D. Garlotta, "A Literature Review of Poly (Lactic Acid)," vol. 9, no. 2, 2002.
- [109] F. Carrasco, P. Pagès, J. Gámez-Pérez, O. O. Santana, and M. L. Maspoch, "Processing of poly(lactic acid): Characterization of chemical structure, thermal stability and mechanical properties," *Polym. Degrad. Stab.*, vol. 95, no. 2, pp. 116–125, 2010.
- [110] H. Askes and L. Susmel, "Understanding cracked materials: Is Linear elastic fracture mechanics obsolete?," *Fatigue Fract. Eng. Mater. Struct.*, vol. 38, no. 2, pp. 154–160, 2015.
- [111] C. Bagni, H. Askes, and L. Susmel, "Gradient elasticity: a transformative stress analysis tool to design notched components against uniaxial/multiaxial high-cycle fatigue," *Fatigue Fract. Eng. Mater. Struct.*, vol. 39, no. 8, pp. 1012–1029, 2016.
- [112] D. Taylor, "The Theory of Critical Distances: A link to micromechanisms," *Theor.*

-
- Appl. Fract. Mech.*, vol. 90, pp. 228–233, 2017.
- [113] T. D. Ngo, A. Kashani, G. Imbalzano, K. T. Q. Nguyen, and D. Hui, “Additive manufacturing (3D printing): A review of materials, methods, applications and challenges,” *Compos. Part B Eng.*, vol. 143, no. December 2017, pp. 172–196, 2018.

Appendix A. AM PLA solid samples

The experimental program results of PLA tested parts, manufactured with 100% infill level, will be presented in the current appendix. This include the pictures of the specimens, tables of the results, load vs displacement curves, microscopic images and FE modeling scheme for every tested sample.

A.1 The pictures of the PLA specimens

The pictures of AM PLA samples after testing will be shown including plain and notched parts fabricated with different deposition angle and tested under tension and 3-point bending.

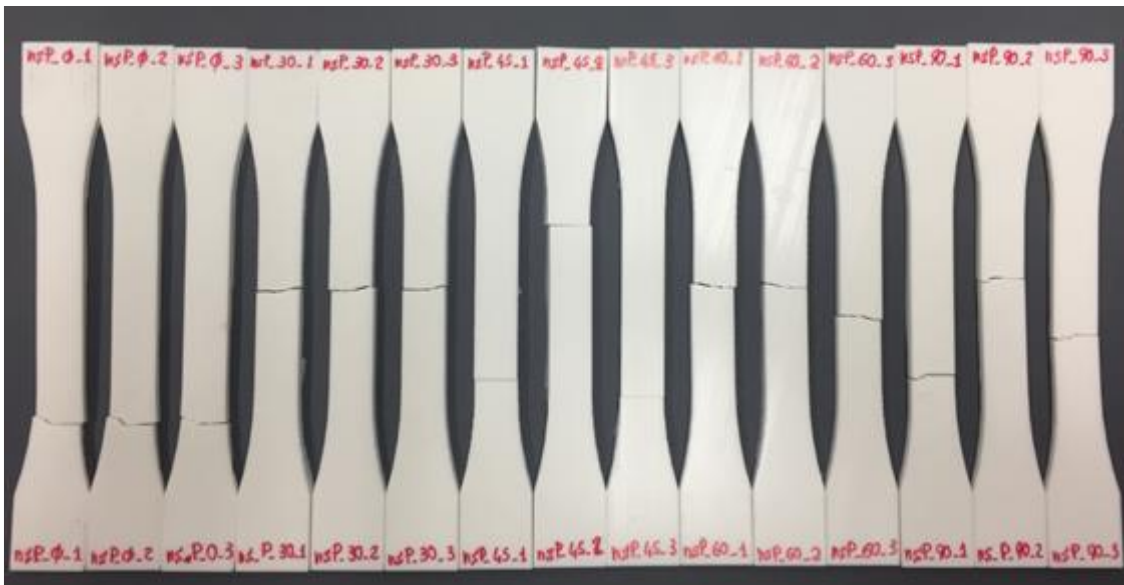


Figure A.1.1 Plain specimens with t_s equal 0 mm

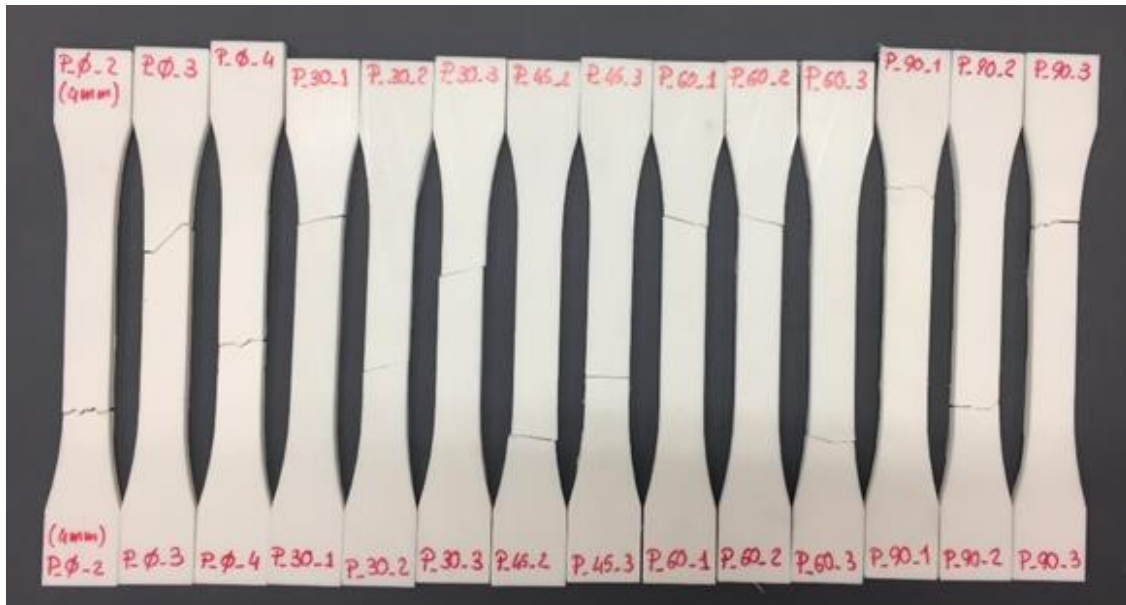


Figure A.1.2 Plain specimens with t_s equal to 0.4 mm

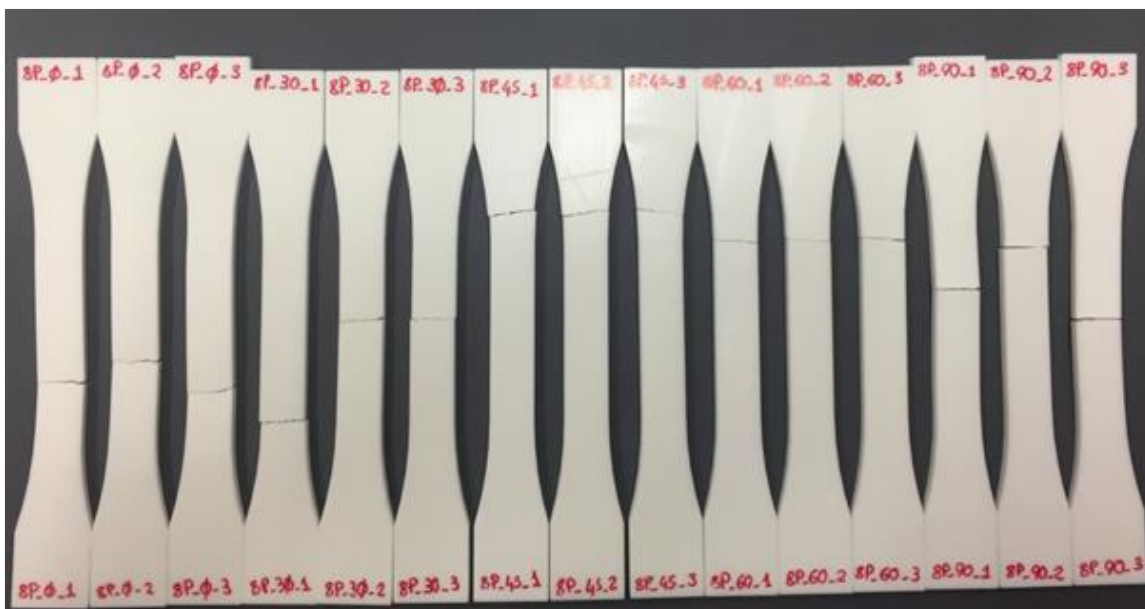
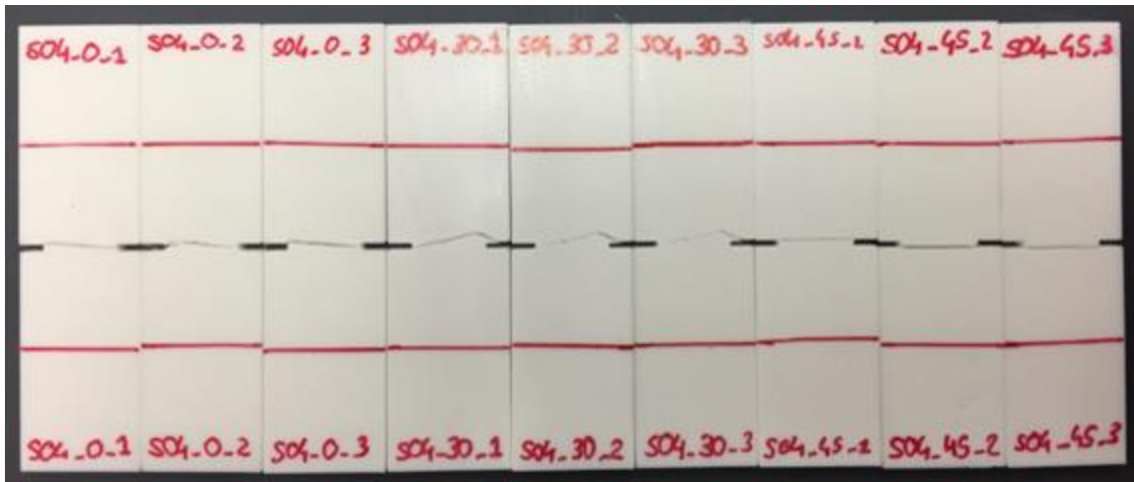
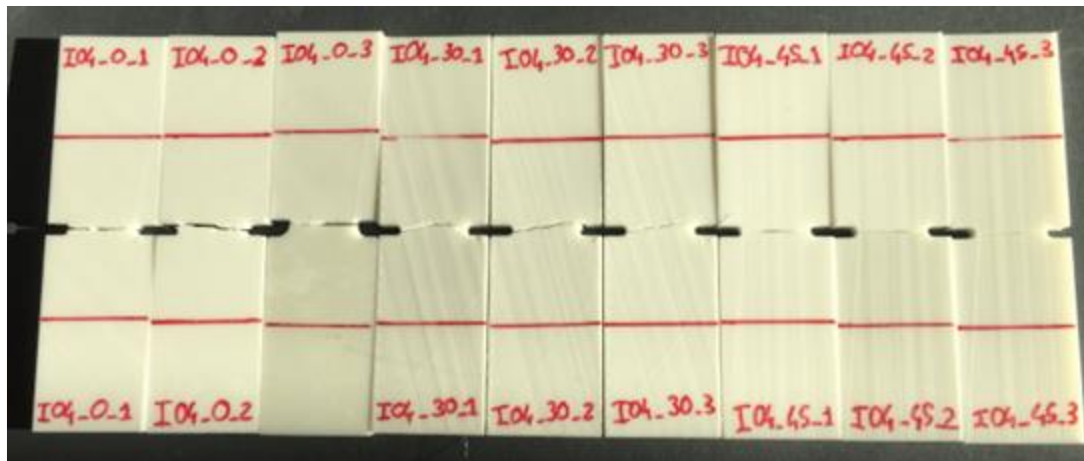


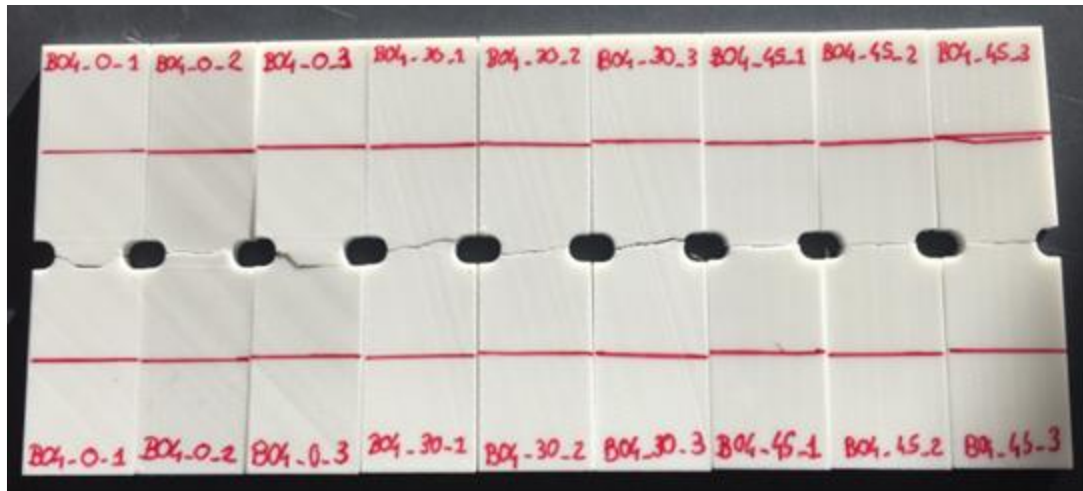
Figure A.1.3 plain specimens with t_s equal to 0.8 mm



(a)



(b)

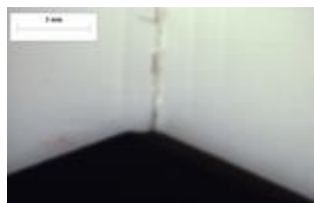
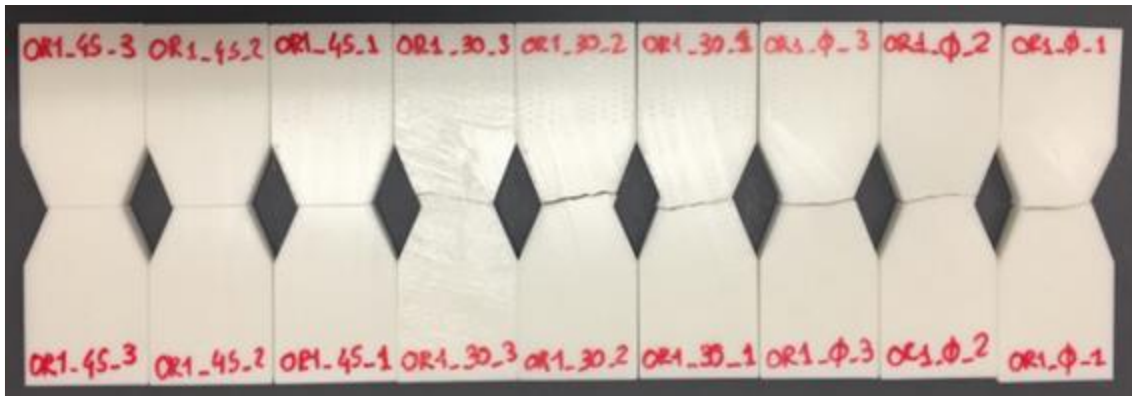


(c)

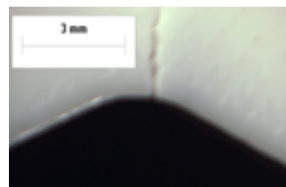
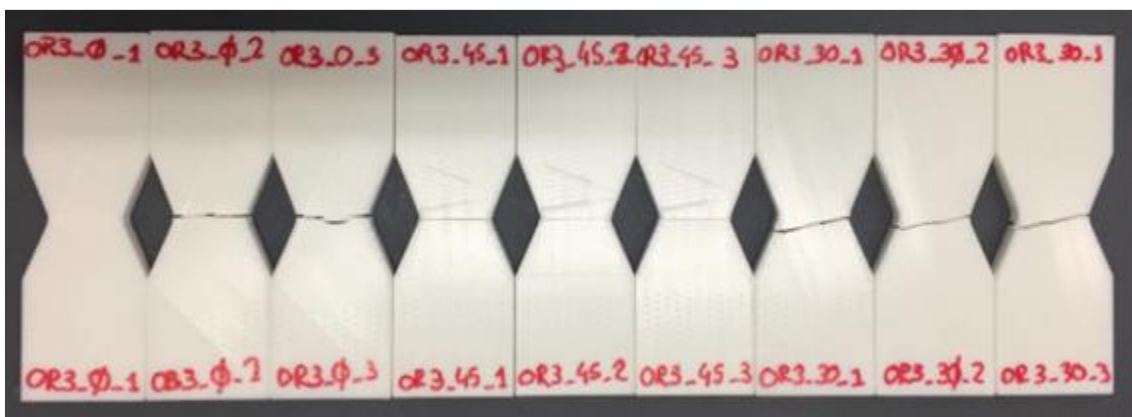
Figure A.1.4 U-notched specimens under tension (a) Sharp notches (b) Medium notches (c) Blunt notches



(a)

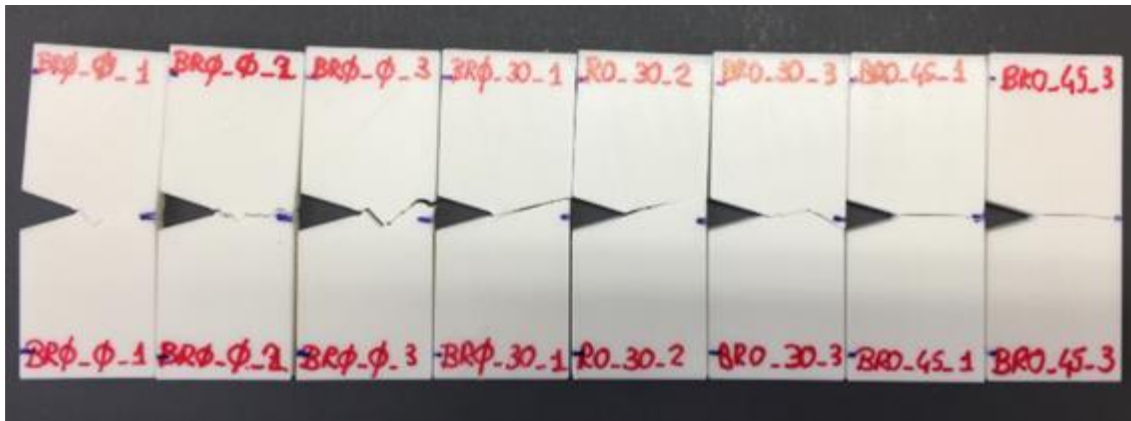


(b)



(c)

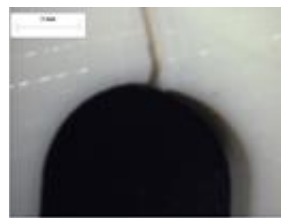
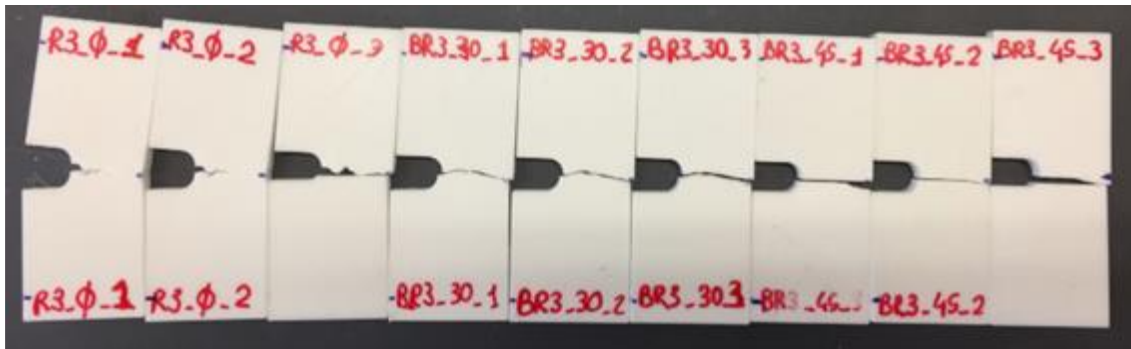
Figure A.1.5 Open notched specimens tested under tension (a) Sharp notches
 (b) Medium notches (c) Blunt notches



(a)

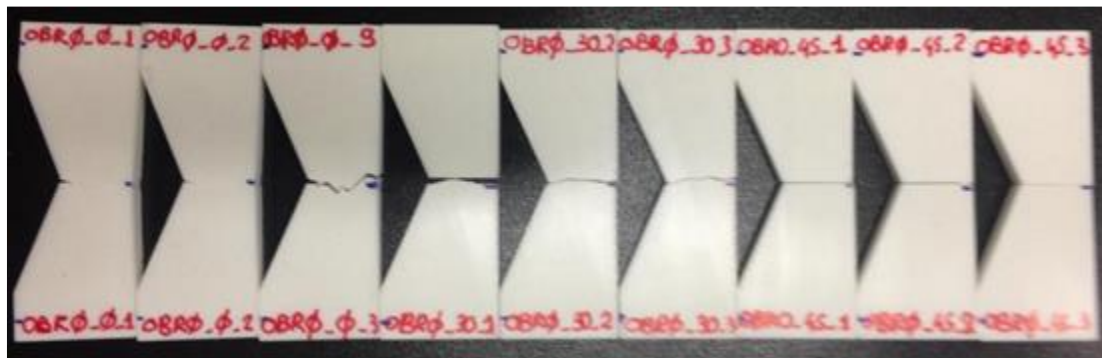


(b)

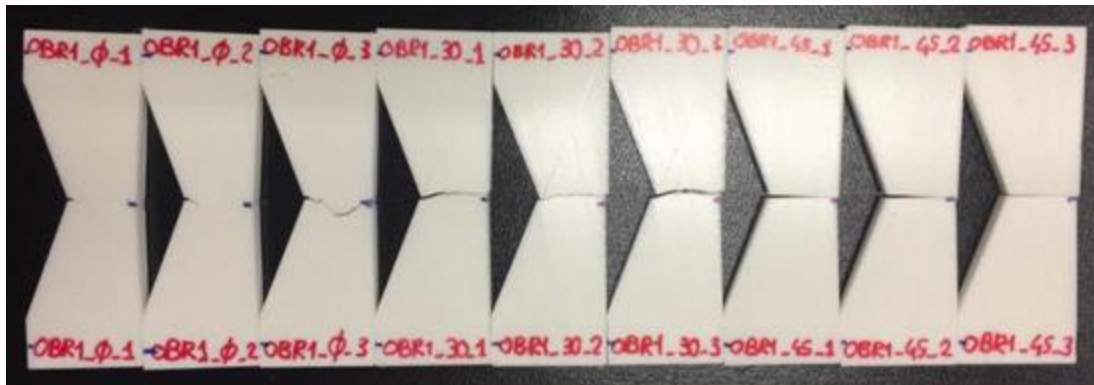


(c)

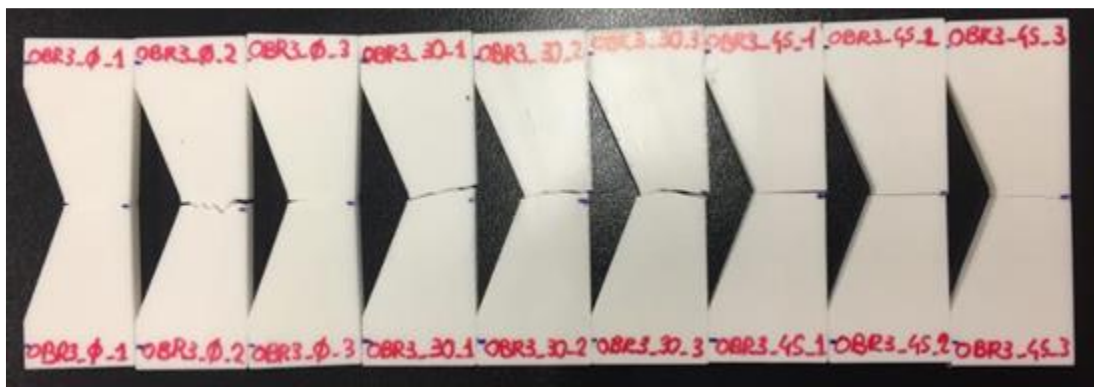
Figure A.1.6 U-notched specimens tested under 3-point bending (a) Sharp notches (b) Medium notches (c) Blunt notches



(a)

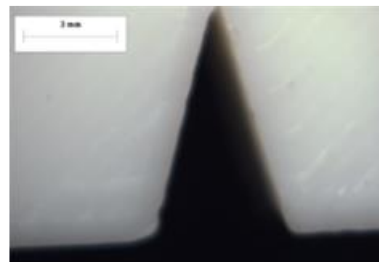


(b)

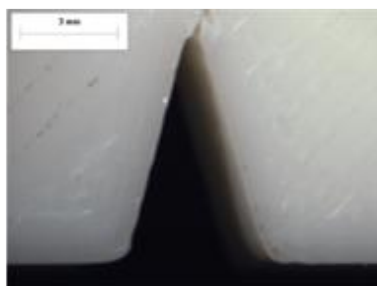
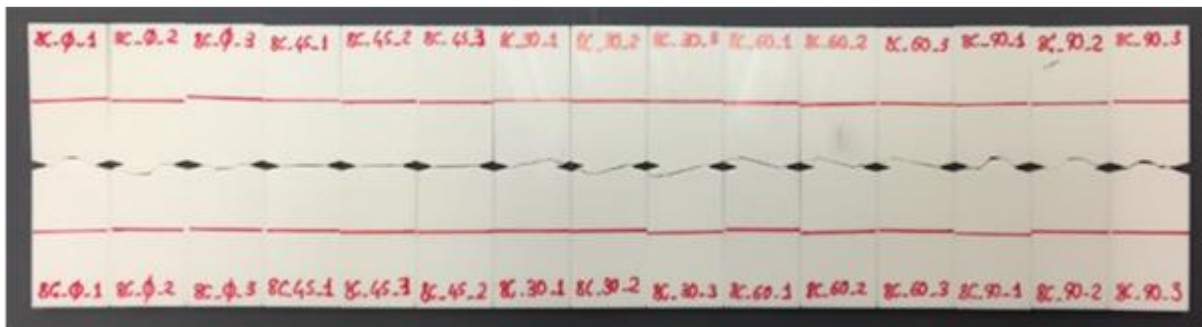


(c)

Figure A.1.7 Open-notched specimens tested under 3-point bending, (a) Sharp notches (b) Medium notches (c) Blunt notches



(a)



(b)

Figure A.1.8 Crack-like notched specimens with microscopic picture for the crack tip, (a) $t_s = 0.4$ mm, (b) $t_s = 0.8$ mm

A.2 The tables of results for the tested solid AM PLA samples

The measurements of PLA specimens' dimensions and the test results will be listed in the tables for the notched and the CT samples.

Table A.2.1 Results of open notched specimens under tension

Code	Θ_p [Deg]	t_s [mm]	α [Deg]	r_n [mm]	w_n [mm]	w_g [mm]	t [mm]	F_r (N)	σ_f (Mpa)
OR0-0-1	0	0.4	135.00	0.46	15.50	25.1	4	3302	50.6
OR0-0-2	0	0.4	135.00	0.475	15.44	25.02	4	3329	51.6
OR0-0-3	0	0.4	135.00	0.515	15.46	25.13	4	3325	51.4
OR0-30-1	30	0.4	135.00	0.44	15.67	25.21	4	3057	46.7
OR0-30-2	30	0.4	135.00	0.435	15.61	25.22	4	3108	47.4
OR0-30-3	30	0.4	135.00	0.475	15.30	25.1	4	3068	47.9
OR0-45-1	45	0.4	135.00	0.56	15.44	24.98	4	2858	44.1
OR0-5-2	45	0.4	135.00	0.565	15.39	25.03	4	3015	47
OR0-45-3	45	0.4	135.00	0.475	15.46	25.04	4	2960	45.8
OR1-0-1	0	0.4	135.00	1.01	15.32	24.92	4	2670	41.1
OR1-0-2	0	0.4	135.00	1.05	15.34	25.4	4	3031	46.9
OR1-0-3	0	0.4	135.00	1.005	15.54	25.14	4	2669	40.8
OR1-30-1	30	0.4	135.00	1.035	15.40	25.09	4	2543	39.3
OR1-30-2	30	0.4	135.00	0.995	15.40	25.1	4	2889	44.5
OR1-30-3	30	0.4	135.00	1.04	15.34	25.06	4	2472	38.2
OR1-45-1	45	0.4	135.00	1.035	15.44	25.12	4	2939	45.3
OR1-45-2	45	0.4	135.00	1.005	15.28	25.06	4	2893	45
OR1-45-3	45	0.4	135.00	1.05	15.48	25.28	4	2825	43.6
OR3_0_1	0	0.4	135.00	3.01	15.28	25.04	4	3195	50.6
OR3_0_2	0	0.4	135.00	3.015	15.18	24.99	4	3297	52.8
OR3_0_3	0	0.4	135.00	3.03	15.22	25.04	4	3216	51.4
OR3_30_1	30	0.4	135.00	3	15.38	25.15	4	3142	49.6
OR3_30_2	30	0.4	135.00	3.045	15.38	25.26	4	3195	50.8
OR3_30_3	30	0.4	135.00	2.975	15.36	25.14	4	3069	48.6
OR3_45_1	45	0.4	135.00	3.015	15.47	25.3	4	2826	44.9
OR3_45_2	45	0.4	135.00	2.985	15.25	25.1	4	2872	45.9
OR3_45_3	45	0.4	135.00	3.035	15.44	25.18	4	2997	47.6

Table A.2.2 Results of U-notched specimens under 3-point bending

Code	θ_p [Deg]	t_s [mm]	α [Deg]	r_n [mm]	W_n [mm]	W_g [mm]	t [mm]	F_r [N]	σ_f [MPa]
BR0_0_1	0	0.4	30	0.05	15.44	24.95	4.30	1009	73.8
BR0_0_2	0	0.4	30	0.04	15.46	24.96	4.23	1049	77.8
BR0_0_3	0	0.4	30	0.05	15.44	25.02	4.24	1063	78.9
BR0_30_1	30	0.4	30	0.06	15.48	25.2	4.23	810	60.0
BR0_30_2	30	0.4	30	0.05	15.42	25.27	4.26	-	-
BR0_30_3	30	0.4	30	0.05	15.50	25.12	4.26	847	62.1
BR0_45_1	45	0.4	30	0.04	14.78	25.14	4.28	879	70.5
BR0_45_2	45	0.4	30	0.04	14.80	25.06	4.26	884	71.0
BR0_45_3	45	0.4	30	0.06	14.91	25.13	4.29	862	67.8
BR1_0_1	0	0.4	0	1.02	14.98	25.08	4.28	1096	85.6
BR1_0_2	0	0.4	0	1.01	14.98	25.03	4.28	1050	82.0
BR1_0_3	0	0.4	0	0.98	14.96	25	4.28	1054	82.5
BR1_30_1	30	0.4	0	0.97	14.97	25.04	4.28	813	63.6
BR1_30_2	30	0.4	0	0.99	14.96	25.06	4.28	865	67.7
BR1_30_3	30	0.4	0	1.00	14.96	24.92	4.32	803	62.3
BR1_45_1	45	0.4	0	1.01	15.06	24.68	4.28	895	69.1
BR1_45_2	45	0.4	0	1.01	15.04	24.89	4.31	926	71.3
BR1_45_3	45	0.4	0	0.97	15.04	24.82	4.32	850	65.2
R3_0_1	0	0.4	0	3.11	14.98	24.88	4.23	1144	90.4
R3_0_2	0	0.4	0	3.03	15.07	24.9	4.26	1131	87.7
R3_0_3	0	0.4	0	2.91	15.07	24.9	4.20	1134	89.2
BR3_30_1	30	0.4	0	2.95	15.08	24.89	4.18	875	69.0
BR3_30_2	30	0.4	0	2.98	15.08	24.9	4.16	873	69.2
BR3_30_3	30	0.4	0	3.07	15.09	24.88	4.26	874	67.6
BR3_45_1	45	0.4	0	3.09	15.09	24.92	4.22	923	72.0
BR3_45_2	45	0.4	0	3.01	15.09	24.94	4.20	930	72.9
BR3_45_3	45	0.4	0	2.94	15.08	25.02	4.17	-	-

Table A.2.3 Results of V-notched specimens under 3-point bending

Code	Θ_p [Deg]	t_s [mm]	α [Deg]	r_n [mm]	W_n [mm]	W_g [mm]	t [mm]	F_r [N]	σ_f [MPa]
OBR0-0-1	0	0.4	135	0.35	14.92	25.09	4.17	990	96.0
OBR0-0-2	0	0.4	135	0.33	14.98	24.92	4.19	1015	97.1
OBR0-0-3	0	0.4	135	0.34	14.98	25.01	4.16	996	96.0
OBR0_30_1	30	0.4	135	0.35	15.00	25.06	4.18	701	67.1
OBR0_30_2	30	0.4	135	0.39	15.01	25.18	4.14	786	75.8
OBR0_30_3	30	0.4	135	0.34	15.00	25.02	4.16	776	74.6
OBR0_45_1	45	0.4	135	0.37	15.14	24.93	4.16	660	62.3
OBR0_45_2	45	0.4	135	0.39	15.12	24.94	4.14	640	60.9
OBR0_45_3	45	0.4	135	0.31	15.01	24.97	4.18	647	61.9
OBR1_0_1	0	0.4	135	0.99	14.99	24.72	4.19	919	87.8
OBR1_0_2	0	0.4	135	1.02	15.08	24.72	4.18	939	88.9
OBR1_0_3	0	0.4	135	1.01	15.16	24.88	4.16	924	86.9
OBR1_30_1	30	0.4	135	0.98	15.14	24.82	4.16	696	65.7
OBR1_30_2	30	0.4	135	1.01	15.28	24.88	4.16	690	64.0
OBR1_30_3	30	0.4	135	1.03	15.18	24.88	4.16	693	65.0
OBR1_45_1	45	0.4	135	0.99	15.06	24.76	4.20	649	61.3
OBR1_45_2	45	0.4	135	0.99	15.12	24.78	4.22	636	59.3
OBR1_45_3	45	0.4	135	1.02	15.03	24.78	4.24	641	60.3
OBR3_0_1	0	0.4	135	3.01	14.88	24.9	4.10	887	87.9
OBR3_0_2	0	0.4	135	3.02	14.98	24.9	4.09	902	88.4
OBR3_0_3	0	0.4	135	2.99	14.98	24.96	4.10	907	88.7
OBR3_30_1	30	0.4	135	2.99	15.03	24.99	4.07	773	75.6
OBR3_30_2	30	0.4	135	3.00	15.04	25	4.11	692	67.0
OBR3_30_3	30	0.4	135	3.01	15.02	25.01	4.09	701	68.4
OBR3_45_1	45	0.4	135	3.02	15.02	25.06	4.11	753	73.1
OBR3_45_2	45	0.4	135	2.98	15.02	24.9	4.08	744	72.8
OBR3_45_3	45	0.4	135	2.99	15.04	24.94	4.08	734	71.6

Table A.2.4 Results of crack-like notched specimens under tension

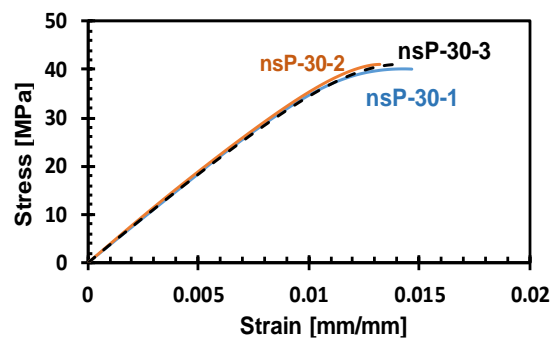
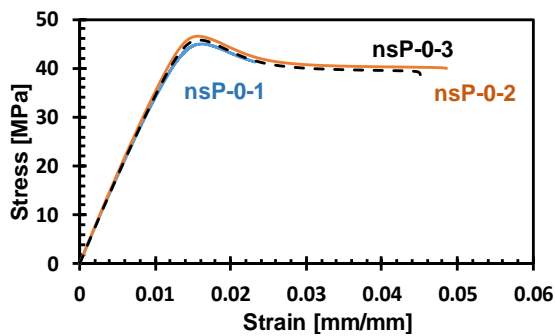
Code	θ_p [Deg]	t_c [mm]	a [Deg]	w_z [mm]	t_z [mm]	F_r [N]	σ_r [MPa]	K_C [MPa.m ^{1/2}]
C_30_1	30	0	0	24.98	4.21	2209	34.4	2.95
C_30_2	30	0	0	24.98	4.18	1973	30.4	2.61
C_30_3	30	0	0	24.92	4.18	2207	34.2	2.95
C_45_1	45	0	0	24.93	4.16	2386	37	3.19
C_45_2	45	0	0	24.90	4.18	2273	36	3.09
C_45_3	45	0	0	24.88	4.16	2216	35.1	3.01
C_60_1	60	0	0	24.83	4.18	2139	32.8	2.83
C_60_2	60	0	0	24.80	4.14	2026	32.3	2.77
C_60_3	60	0	0	24.82	4.08	2079	33.4	2.86
C_90_1	90	0	0	25.06	4.04	2616	41.6	3.59
C_90_2	90	0	0	25.06	4.11	2600	44.3	3.75
C_90_3	90	0	0	24.74	4.08	2863	46.9	4.00
sC_0_1	0	0.4	30	24.79	4.21	3003	43.8	3.77
sC_0_2	0	0.4	30	24.77	4.26	2946	42.2	3.63
sC_0_3	0	0.4	30	24.76	4.2	2996	43.4	3.73
sC_30_1	30	0.4	30	24.88	4.18	2839	41	3.53
sC_30_2	30	0.4	30	24.88	4.22	2823	40.6	3.50
sC_30_3	30	0.4	30	24.92	4.21	2626	37.4	3.22
sC_45_1	45	0.4	30	24.89	4.22	2389	33.7	2.90
sC_45_2	45	0.4	30	24.90	4.23	2426	34.4	2.97
sC_45_3	45	0.4	30	24.90	4.2	2369	33.9	2.93
sC_60_1	60	0.4	30	24.82	4.2	2556	37.2	3.21
sC_60_2	60	0.4	30	24.84	4.18	2512	37.1	3.20
sC_60_3	60	0.4	30	24.83	4.18	2503	36.6	3.15
sC_90_1	90	0.4	30	24.92	4.2	2960	43.6	3.76
sC_90_2	90	0.4	30	24.90	4.19	2973	43.5	3.75
sC_90_3	90	0.4	30	24.88	4.22	2928	42.9	3.70
8C_0_1	0	0.8	30	24.76	4.2	3064	44.4	3.81
8C_0_2	0	0.8	30	24.70	4.19	3099	45.3	3.89
8C_0_3	0	0.8	30	24.74	4.16	3083	45.9	3.94
8C_30_1	30	0.8	30	25.03	4.18	2982	43.6	3.70
8C_30_2	30	0.8	30	24.99	4.2	2968	43.3	3.74
8C_30_3	30	0.8	30	25.04	4.18	3067	45.4	3.92
8C_45_1	45	0.8	30	24.81	4.22	3133	45.4	3.91
8C_45_2	45	0.8	30	24.86	4.19	3161	46.5	4
8C_45_3	45	0.8	30	24.64	4.2	3115	45.1	3.86
8C_60_1	60	0.8	30	24.56	4.04	2900	44.7	3.83
8C_60_2	60	0.8	30	24.88	4.04	2868	43.8	3.78
8C_60_3	60	0.8	30	24.84	4.04	2846	43.9	3.78
8C_90_1	90	0.8	30	24.90	4.03	3297	50.3	4.34
8C_90_2	90	0.8	30	24.95	4.07	3307	49.6	4.28
8C_90_3	90	0.8	30	24.96	4.07	3268	49.5	4.27

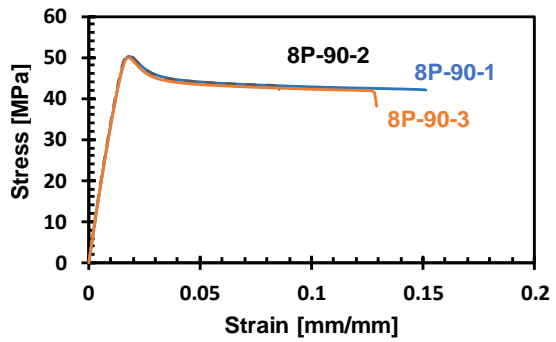
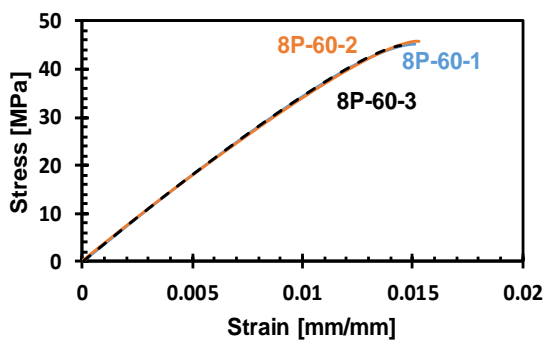
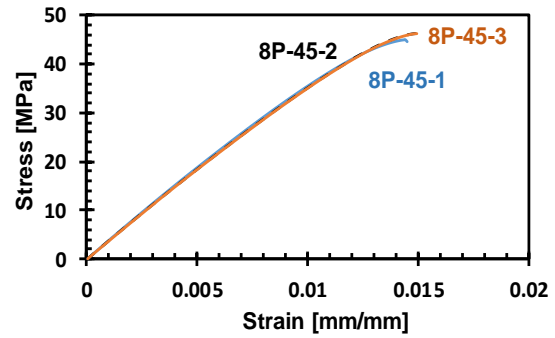
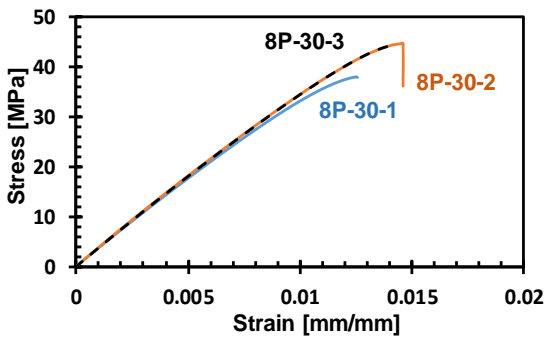
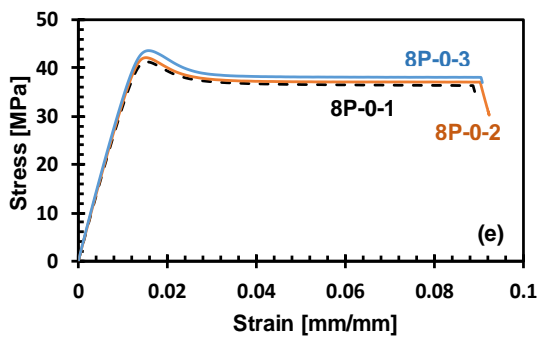
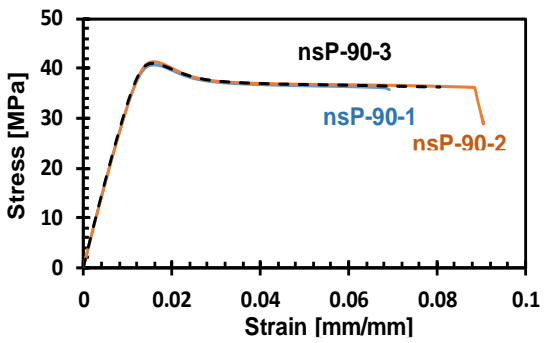
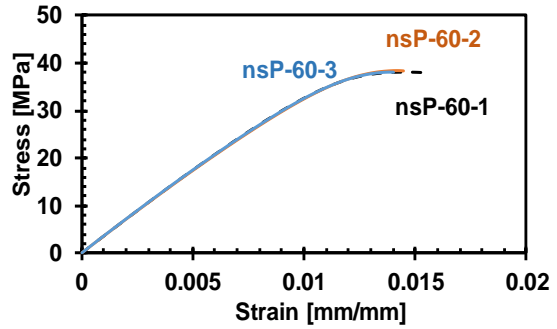
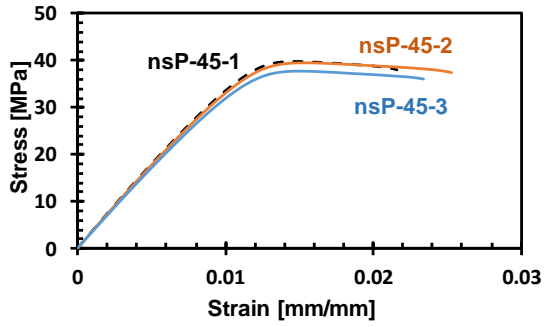
Table A.2.5 Plane strain fracture toughness, t=20 mm and t=30 mm

Code	Θ_p [Deg]	t_s [mm]	B [mm]	W [mm]	P_{max} [N]	P_Q [N]	P_{max}/P_Q	K_C [MPa.m ^{1/2}]
CT_0_1	0	0.4	20	40.05	2022	2017	1.00	4.6
CT_0_2	0	0.4	20	39.98	2039	1920	1.06	4.6
CT_0_3	0	0.4	20	40.03	1920	1870	1.02	4.5
CT_30_1	30	0.4	20	40.02	1774	1730	1.03	4.2
CT_30_2	30	0.4	20	40.11	1731	1620	1.07	3.9
CT_30_3	30	0.4	20	39.96	1640	1620	1.01	3.9
CT_45_1	45	0.4	20	40.02	1760	1660	1.06	4.0
CT_45_2	45	0.4	20	39.98	1752	1690	1.04	4.2
CT_45_3	45	0.4	20	39.97	1790	1750	1.02	4.2
CT30-45-1	0	0.4	30	60.04	2932	2906	1.01	3.8
CT30-45-2	0	0.4	30	60.03	2849	2800	1.02	3.7
CT30-45-3	0	0.4	30	60.03	2849	2783	1.02	3.7

A.3 Figures of tested AM PLA solid samples

The stress/ strain curves for the tested plain PLA parts and the load vs displacement for notched samples in addition to the figures of fracture toughness calculation, will be presented below.





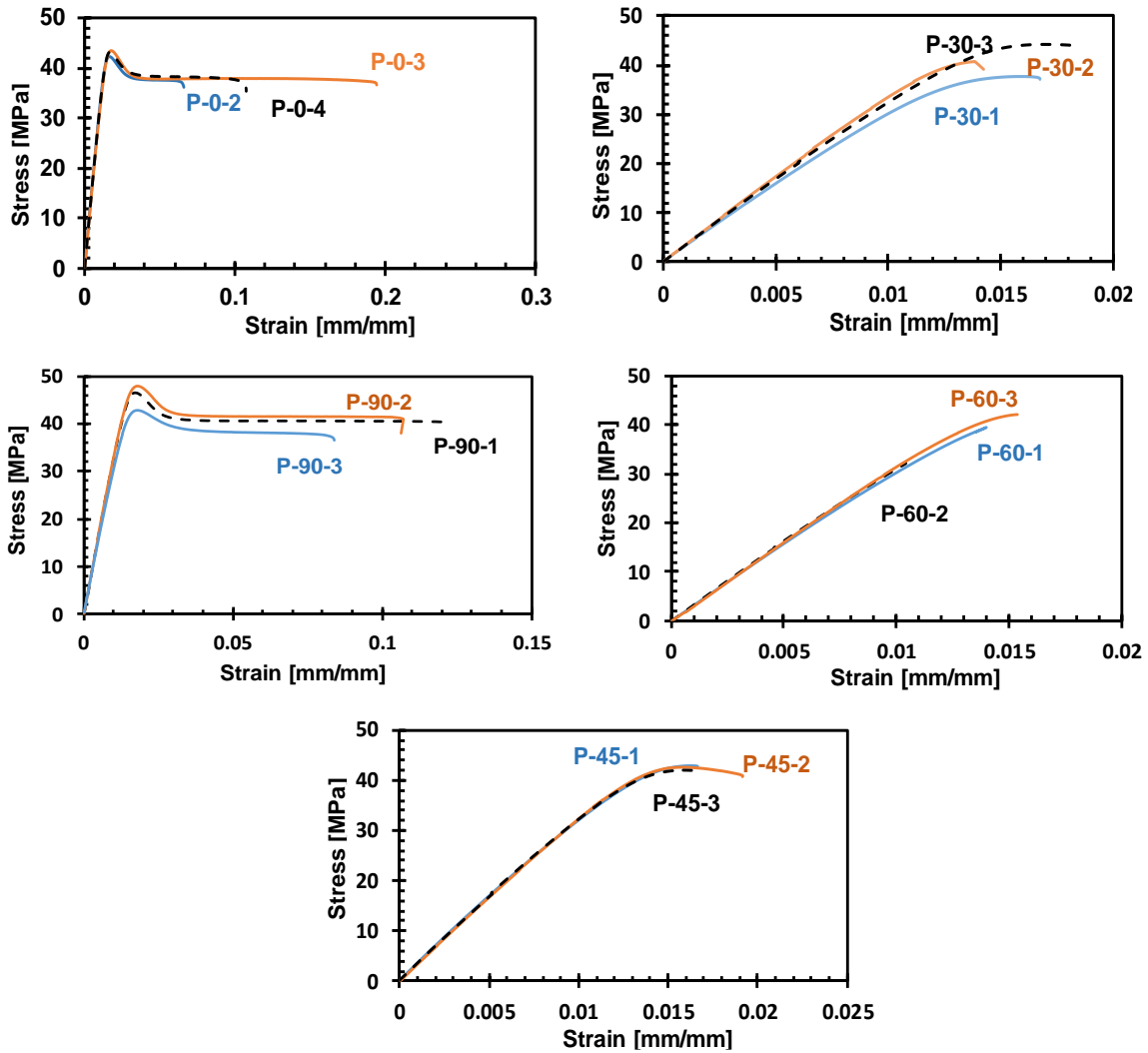
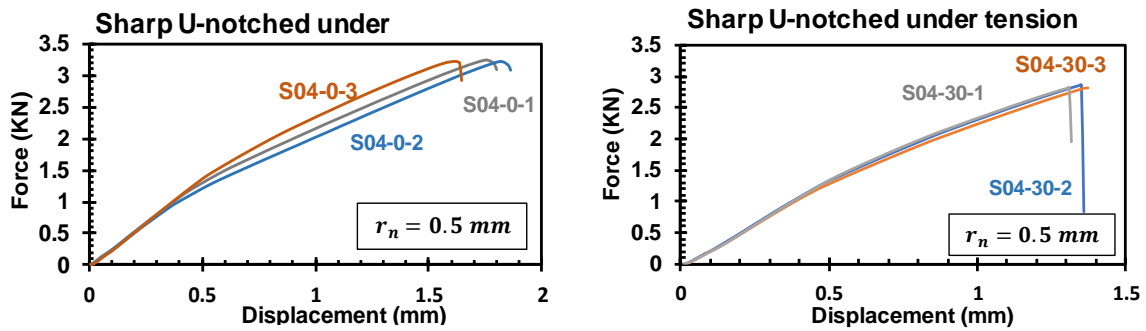


Figure A.3.1 Stress vs. strain curves for plain specimens, $t_s = (0, 0.4, 0.8)$ mm



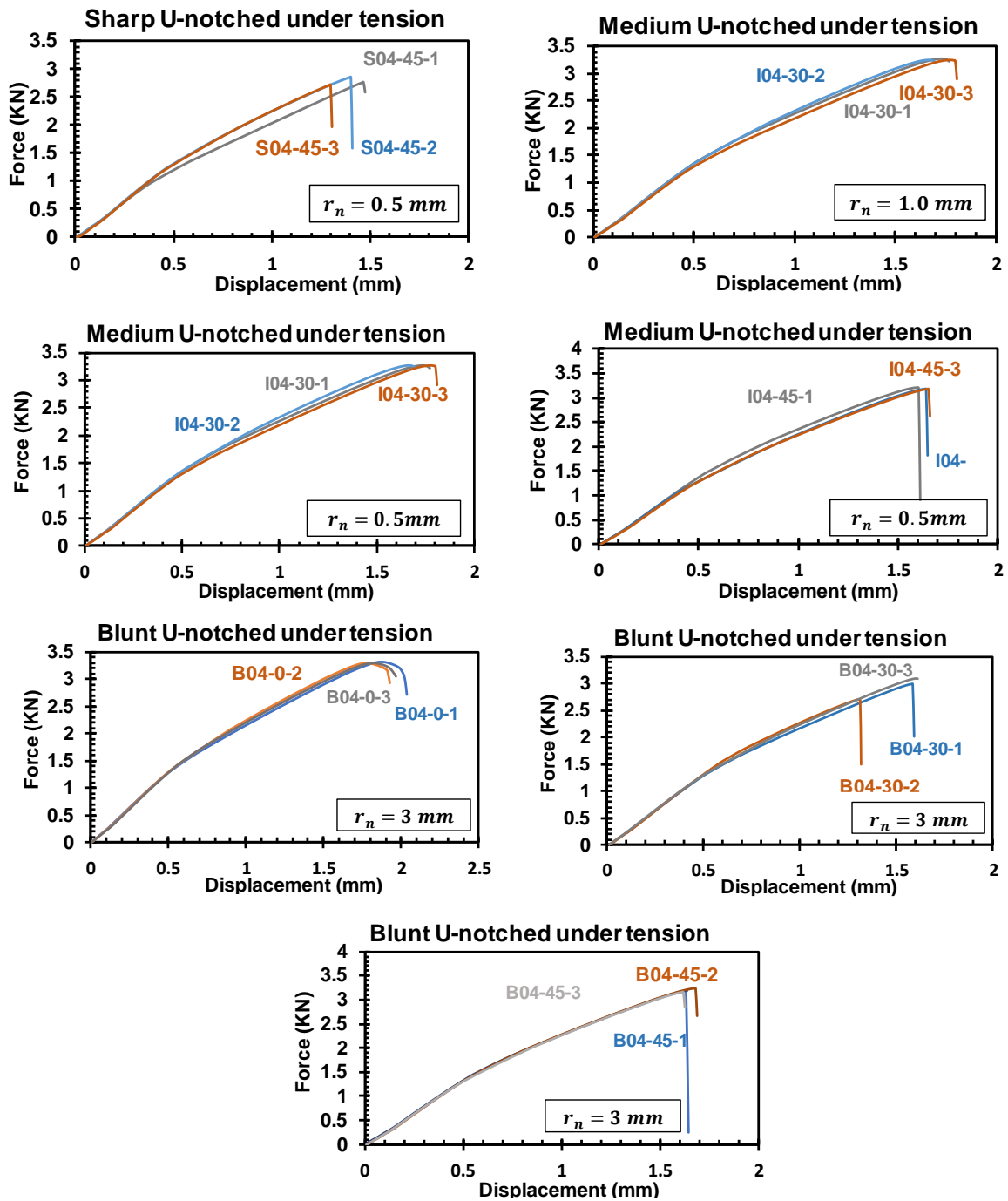
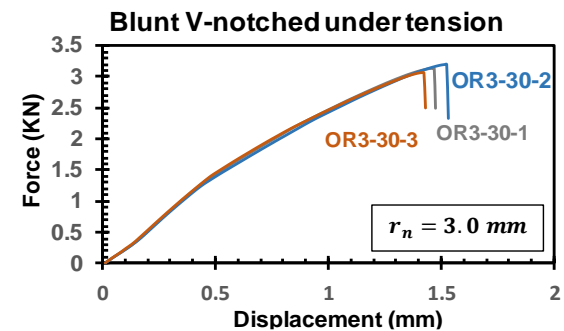
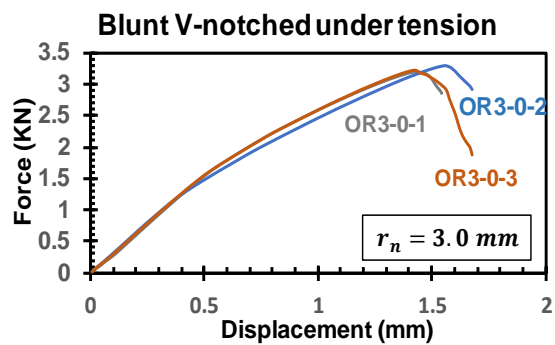
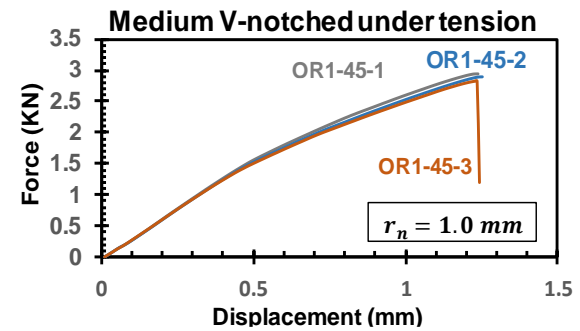
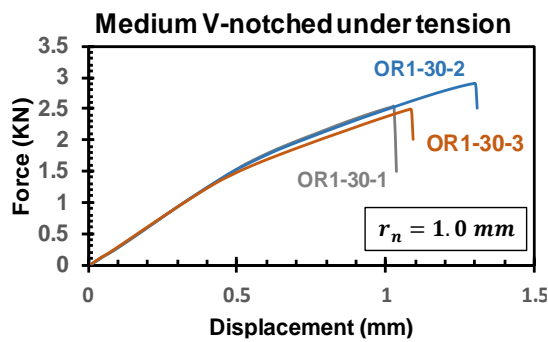
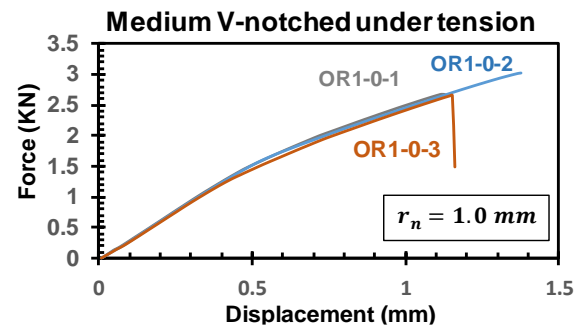
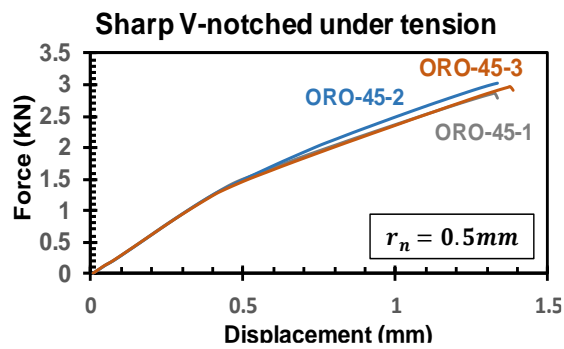
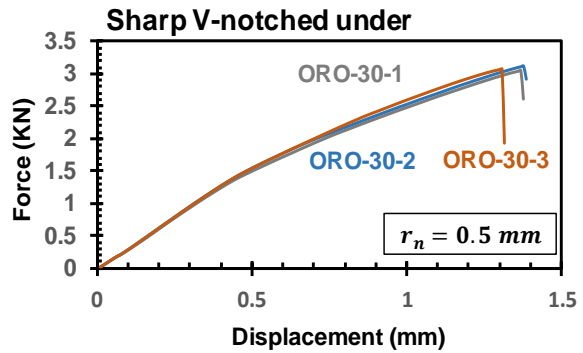
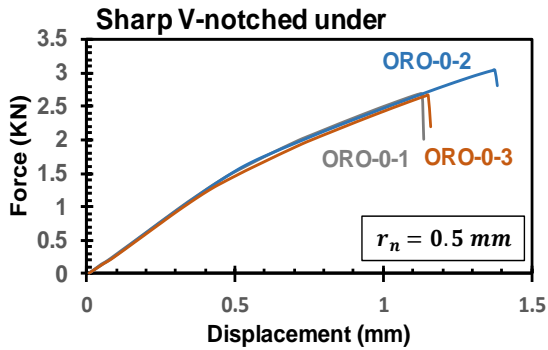


Figure A.3.2 Force vs. displacement for U-notched specimens under tension



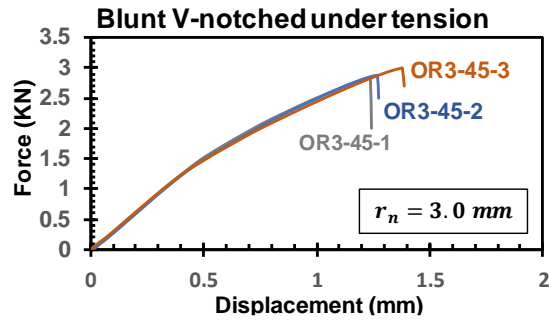
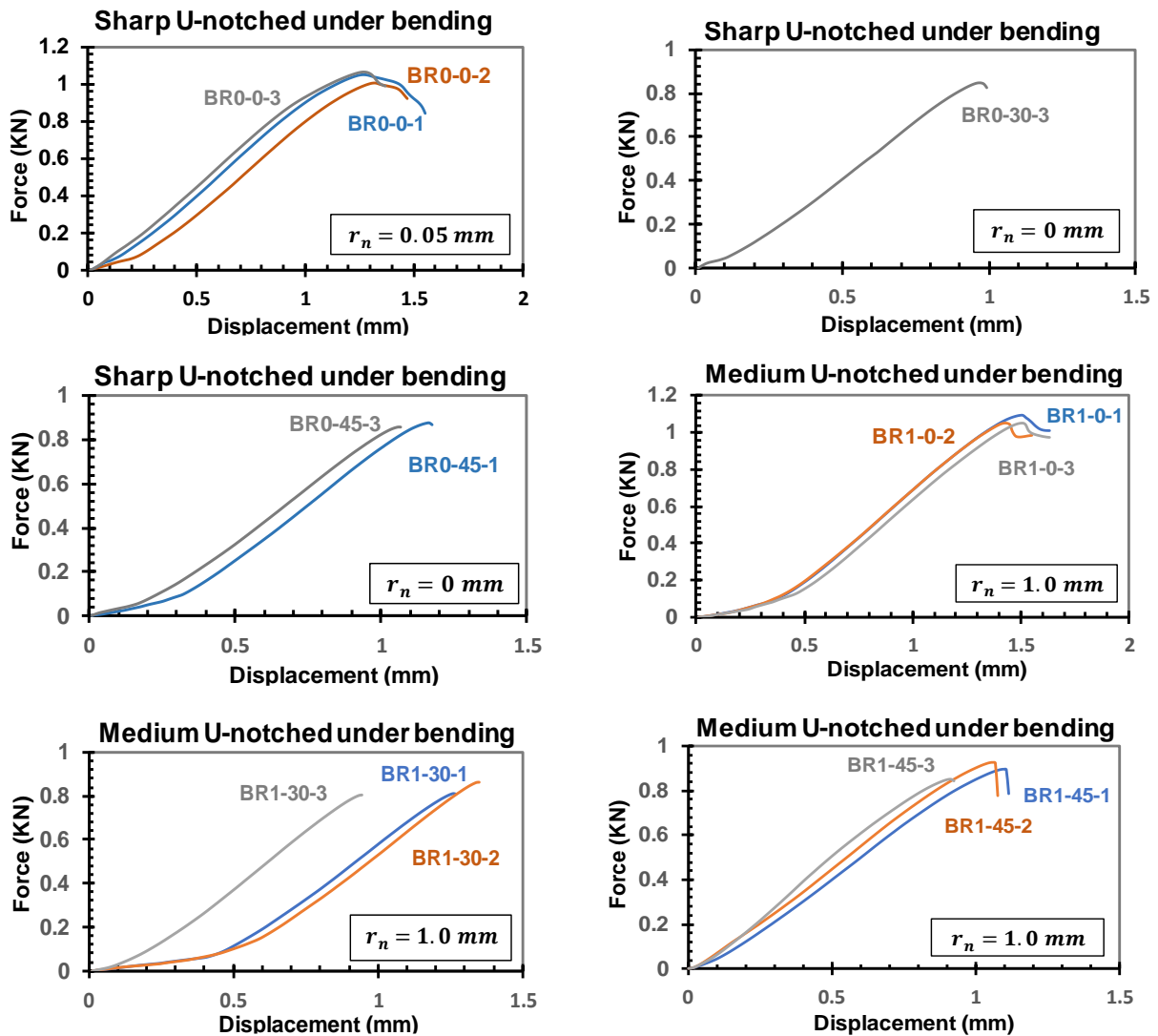


Figure A.3.3 Force vs. displacement for V-notched specimens under tension



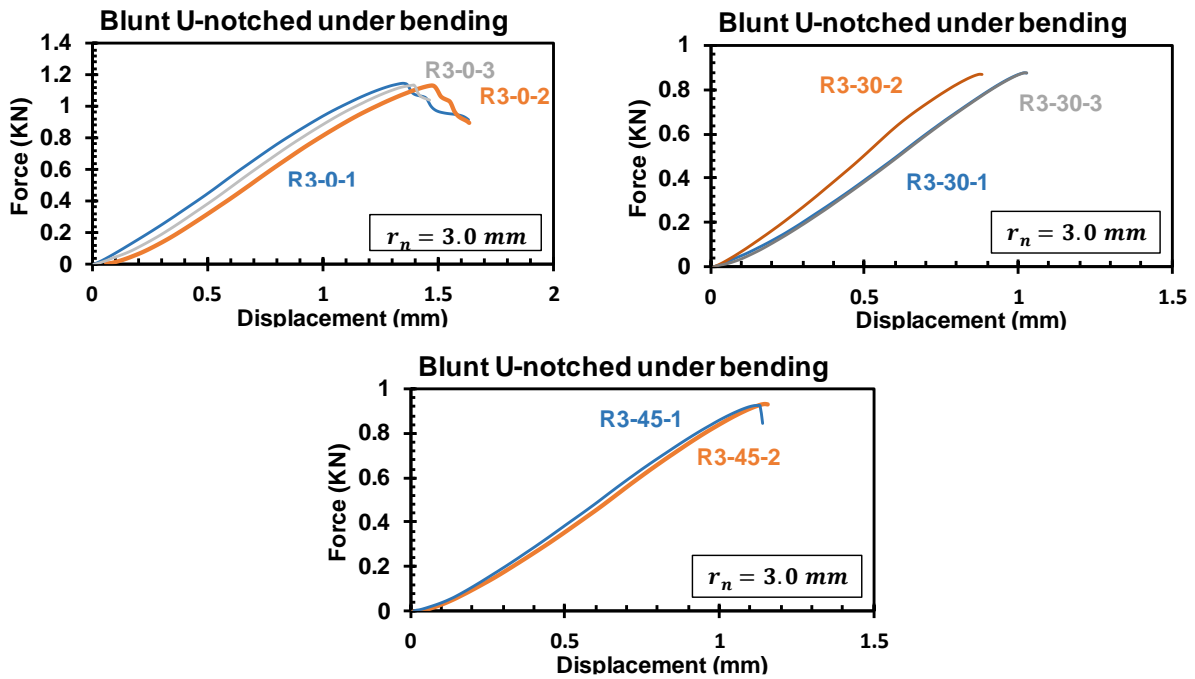
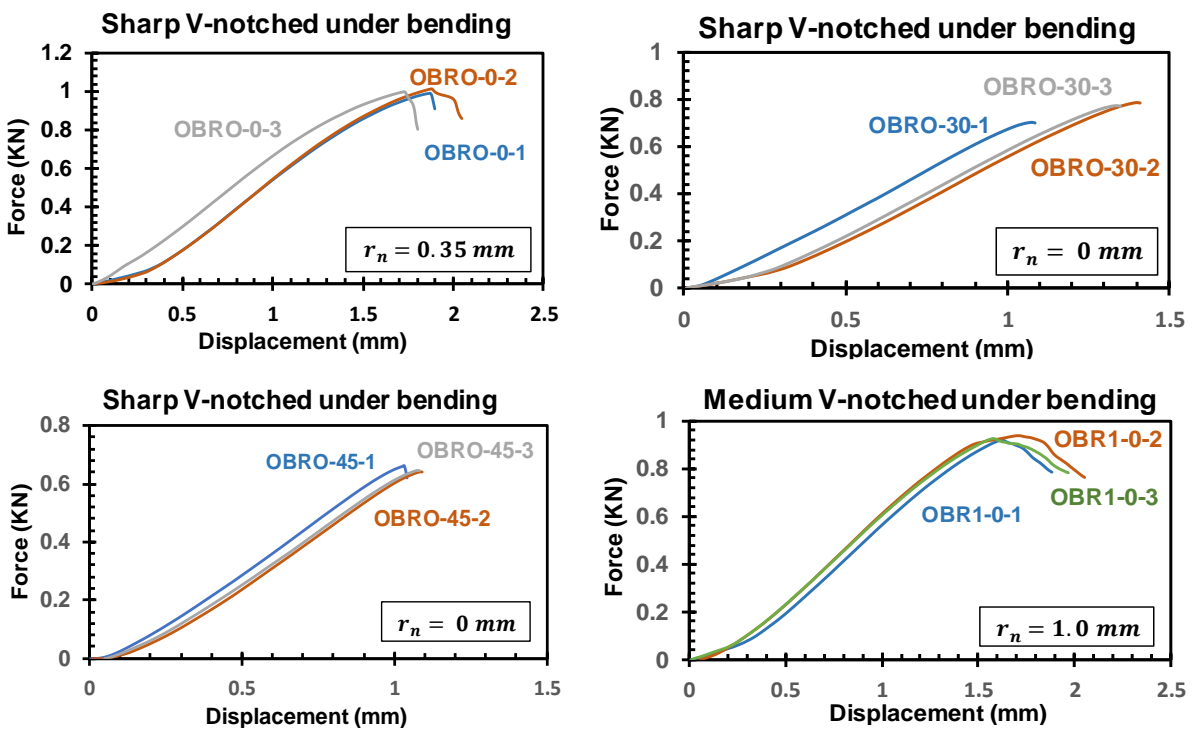


Figure A.3.4 Force vs. displacement for U-Notched specimens under 3-point bending



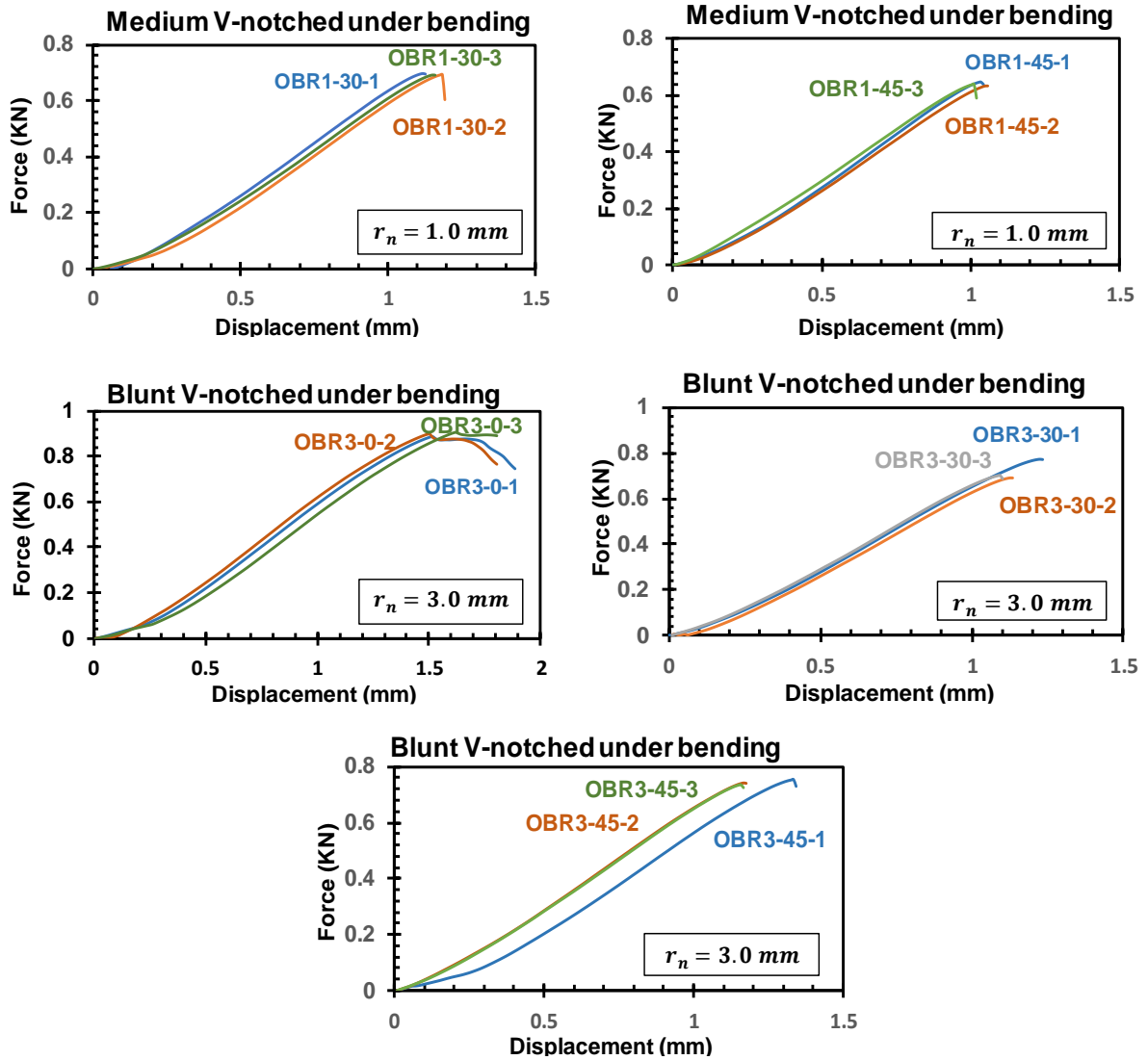
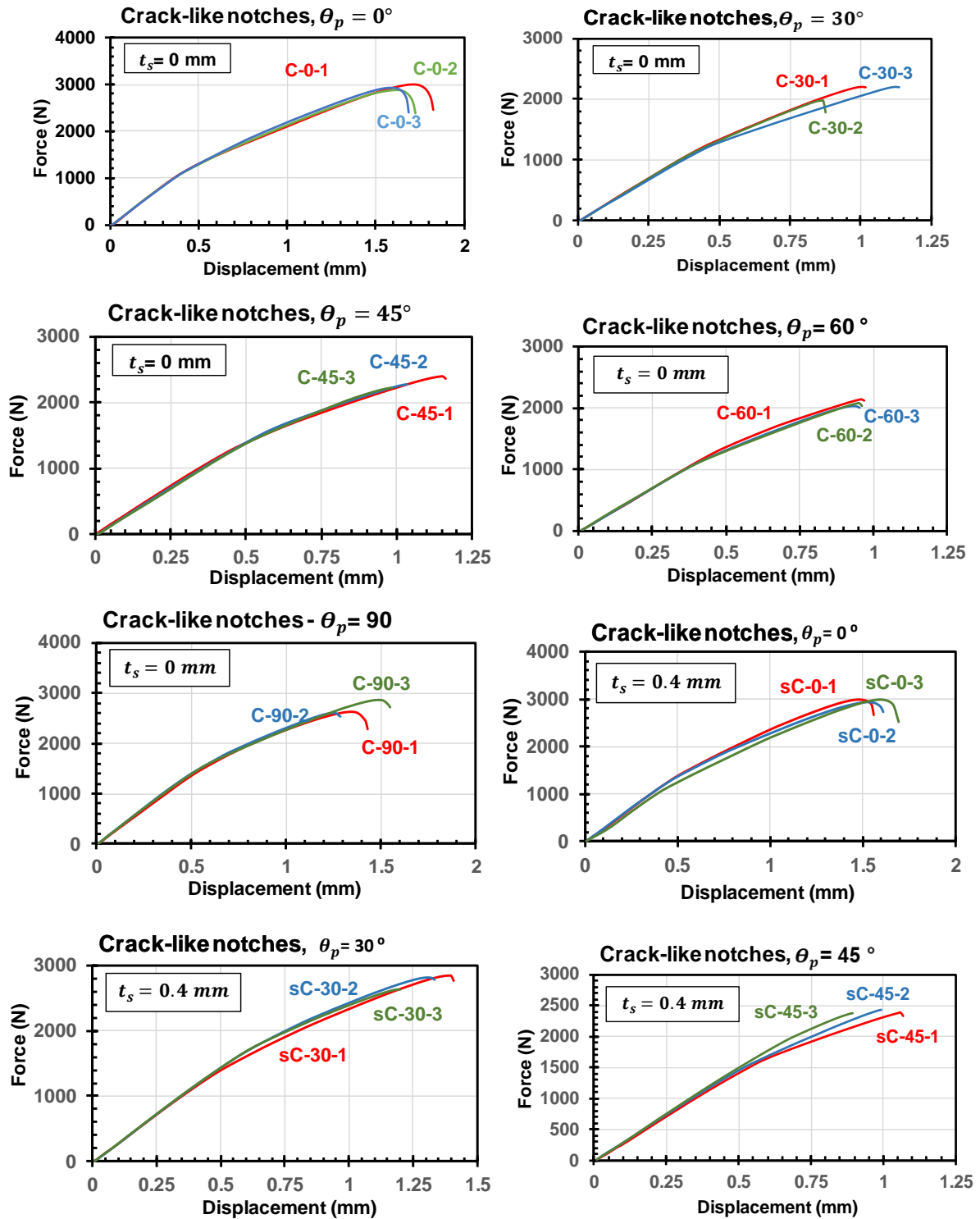


Figure A.3.5 Force vs. displacement for V-notched specimens under 3-point bending



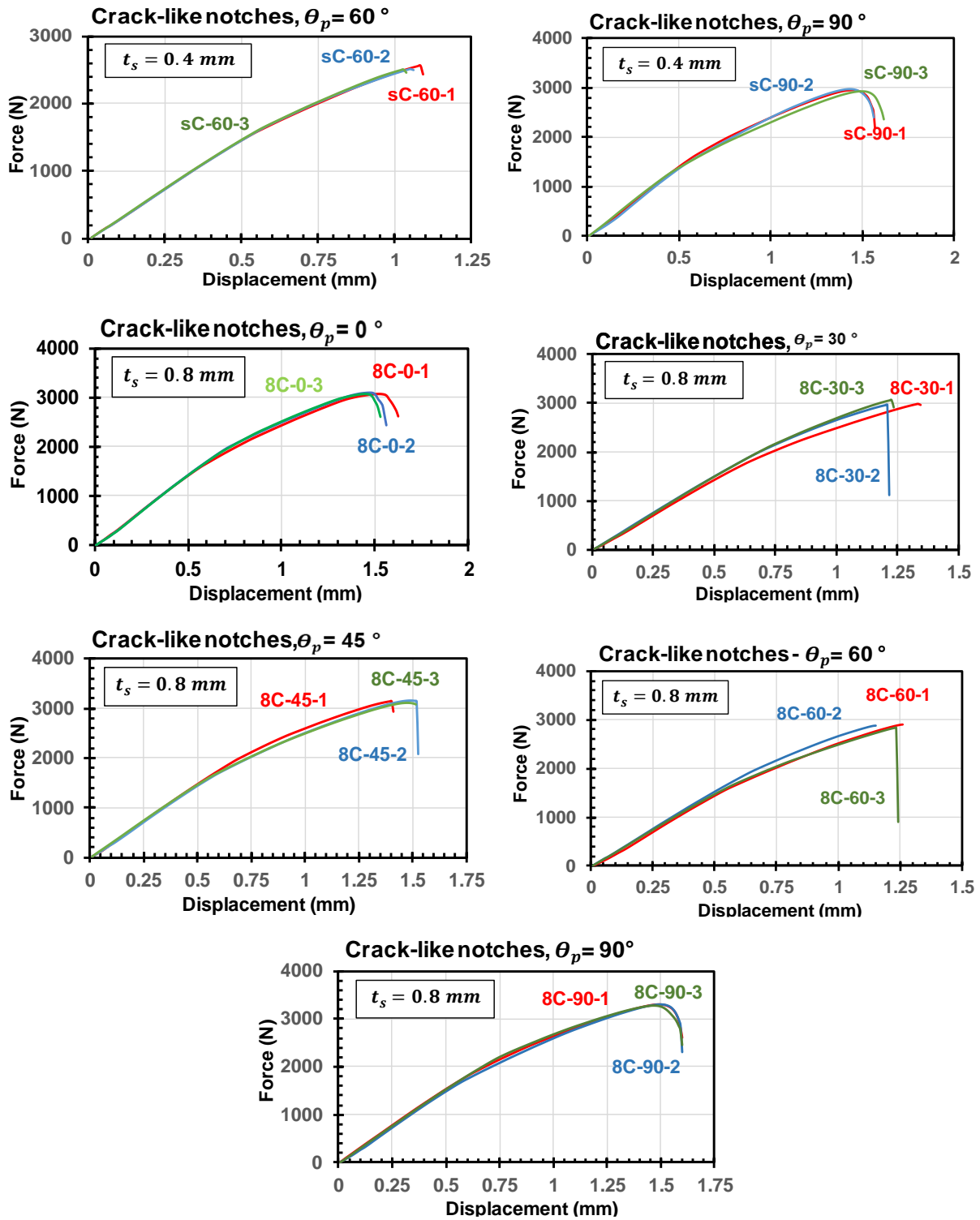
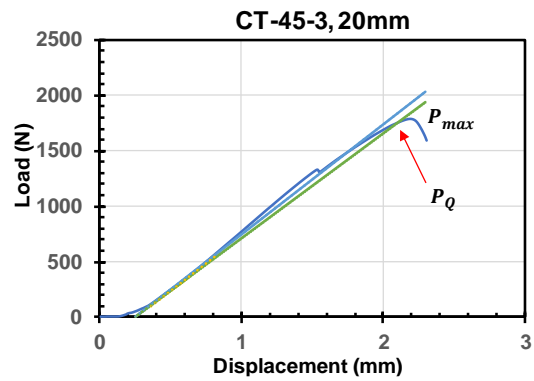
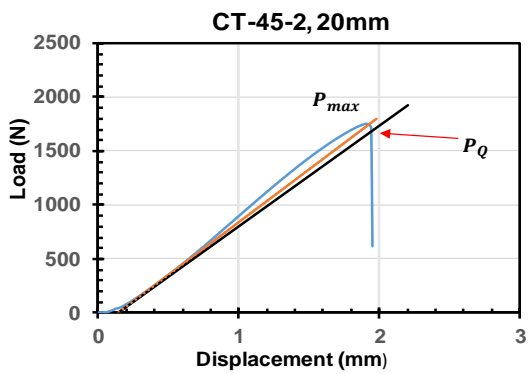
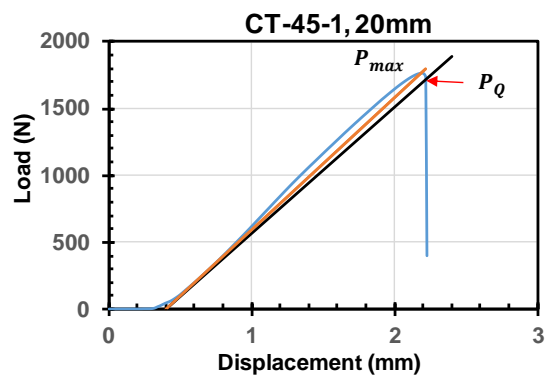
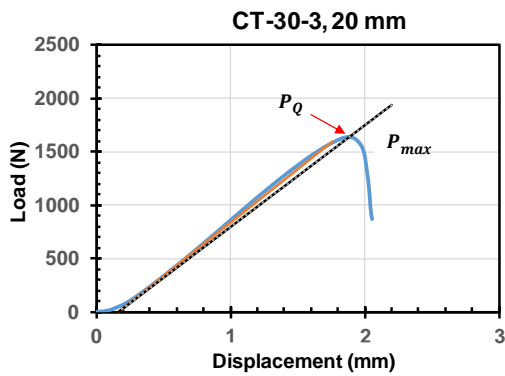
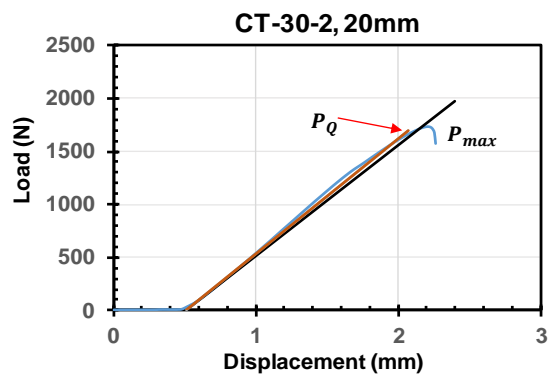
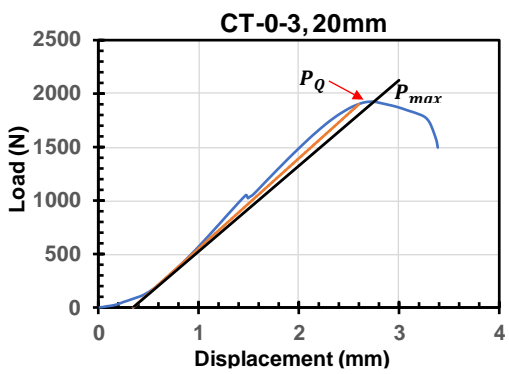
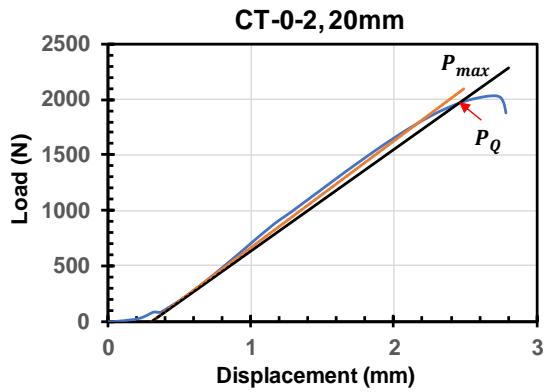
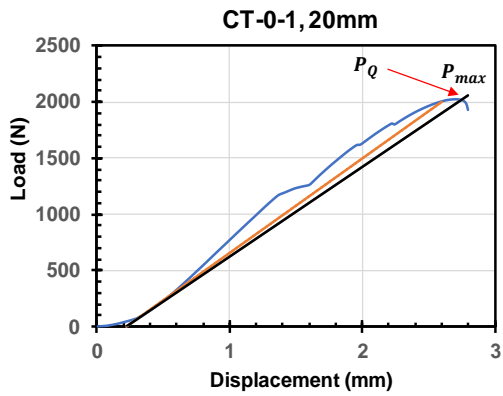


Figure A.3.6 Load vs. displacement for crack-like notched specimens, $t_s = (0, 0.4, 0.8)$ mm



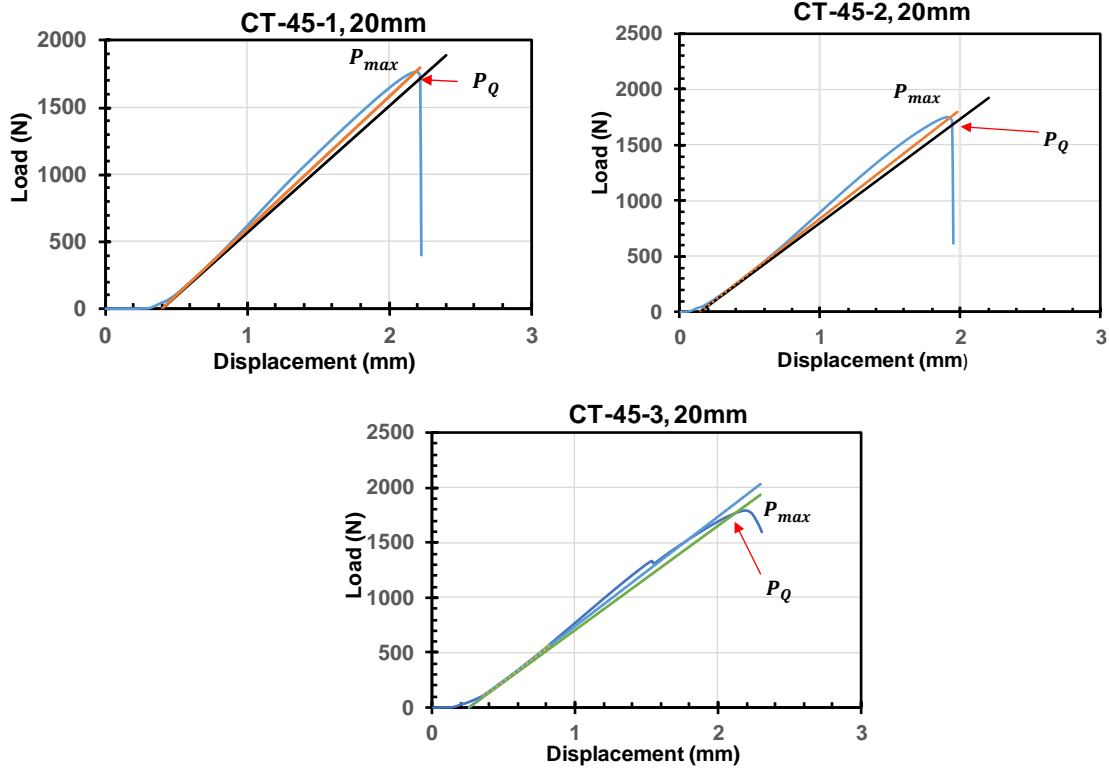


Figure A.3.7 Evaluating P_Q for CT-20 mm specimens

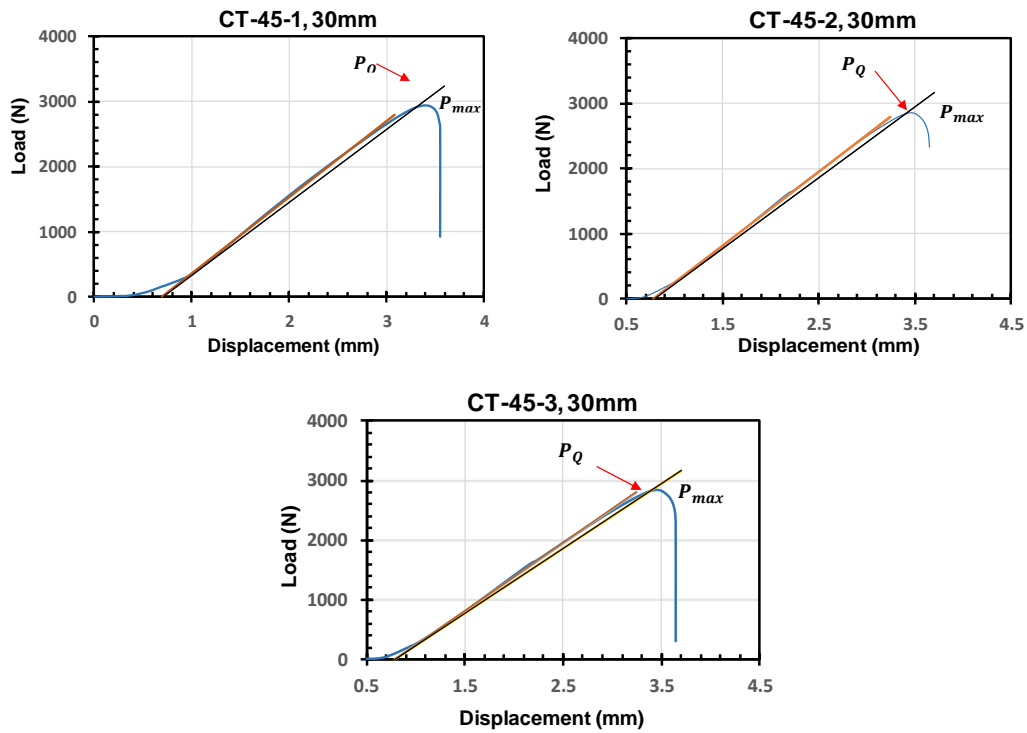


Figure A.3.8 Evaluating P_Q for CT-30 mm specimens

A.4 Microscopic pictures of tested PLA specimens

The microscopic images for plain and notched samples printed with different deposition angles, after failure, will be shown below.

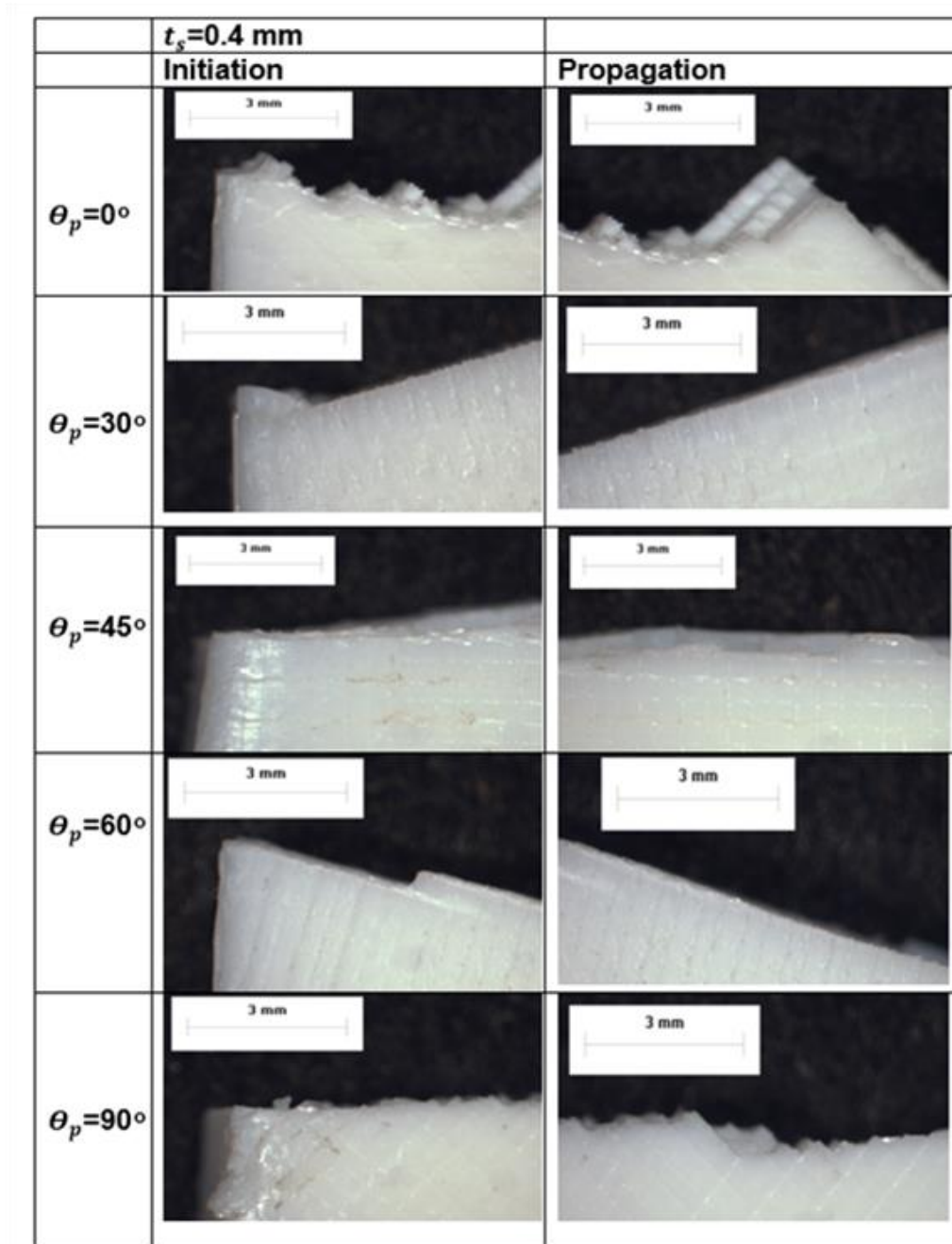
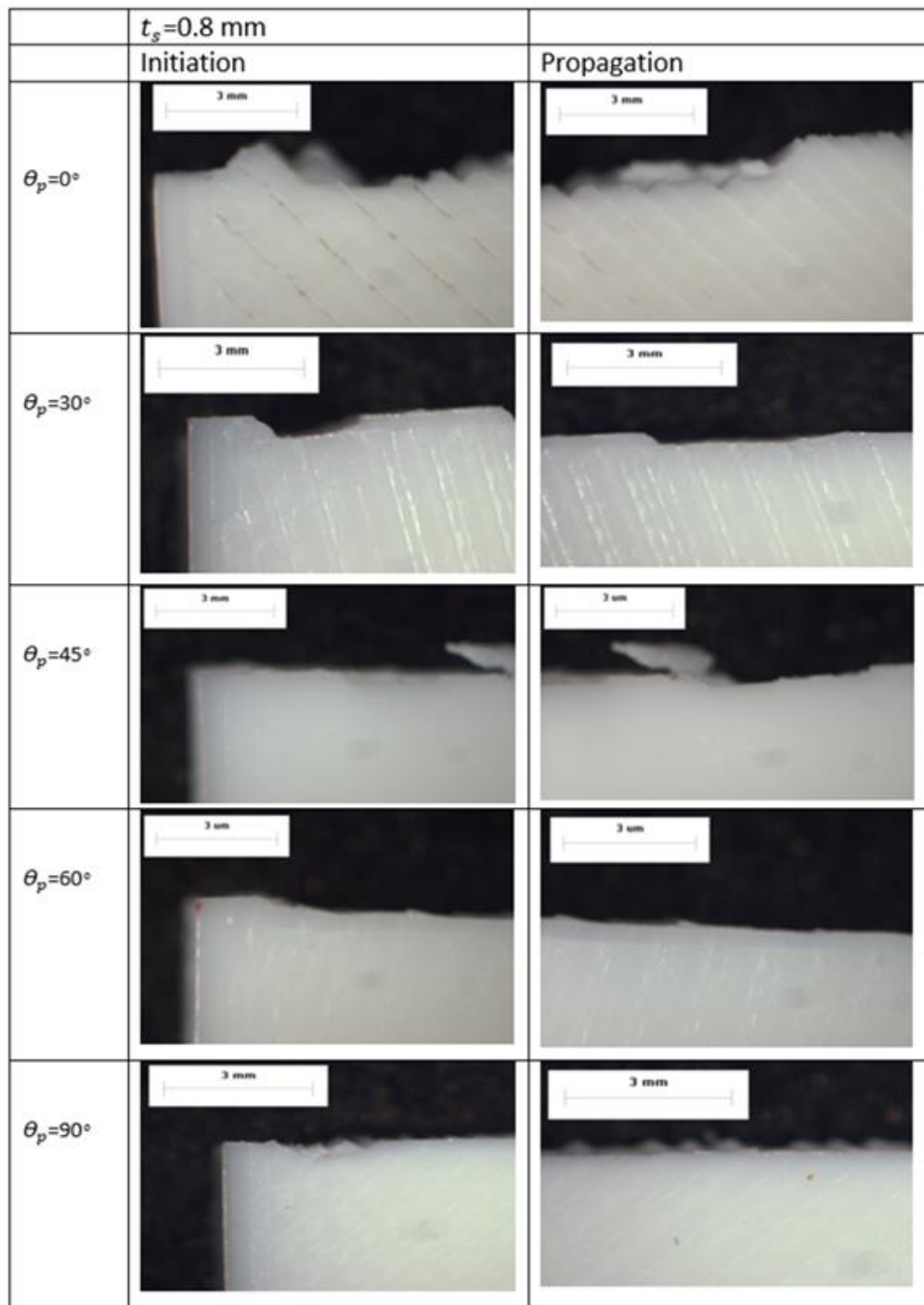


Figure A.4.1 Plain specimens, $t_s=0.4$ mm

Figure A.4.2 Plain specimens, $t_s=0.8$ mm

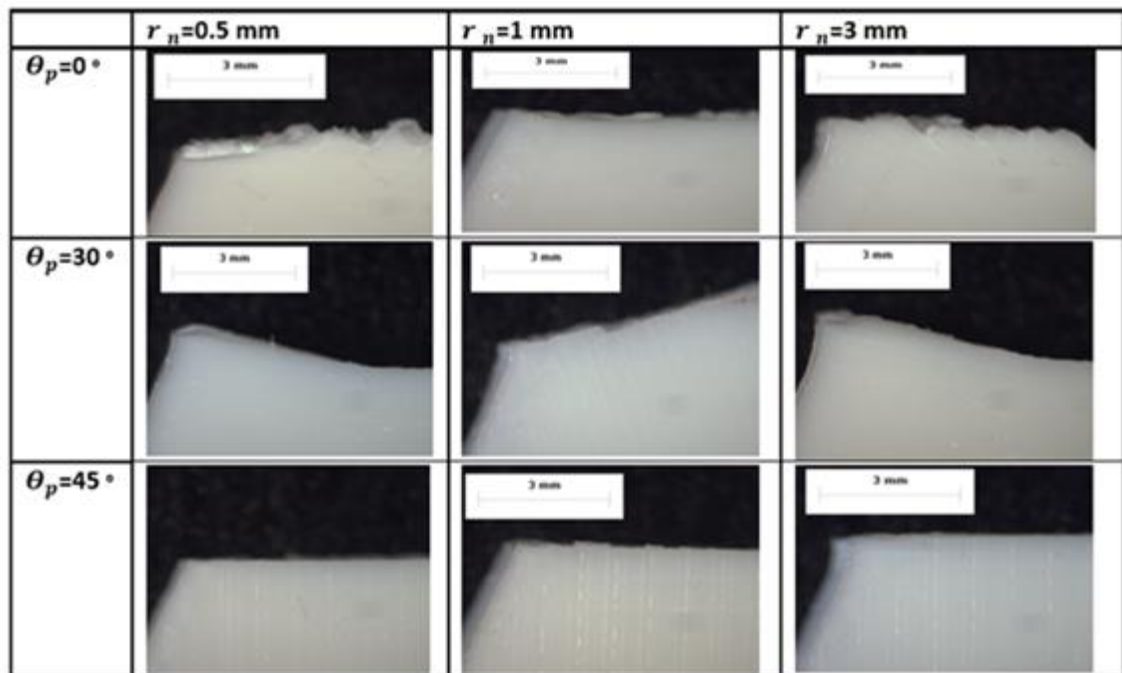


Figure A.4.3 Open notches under tension

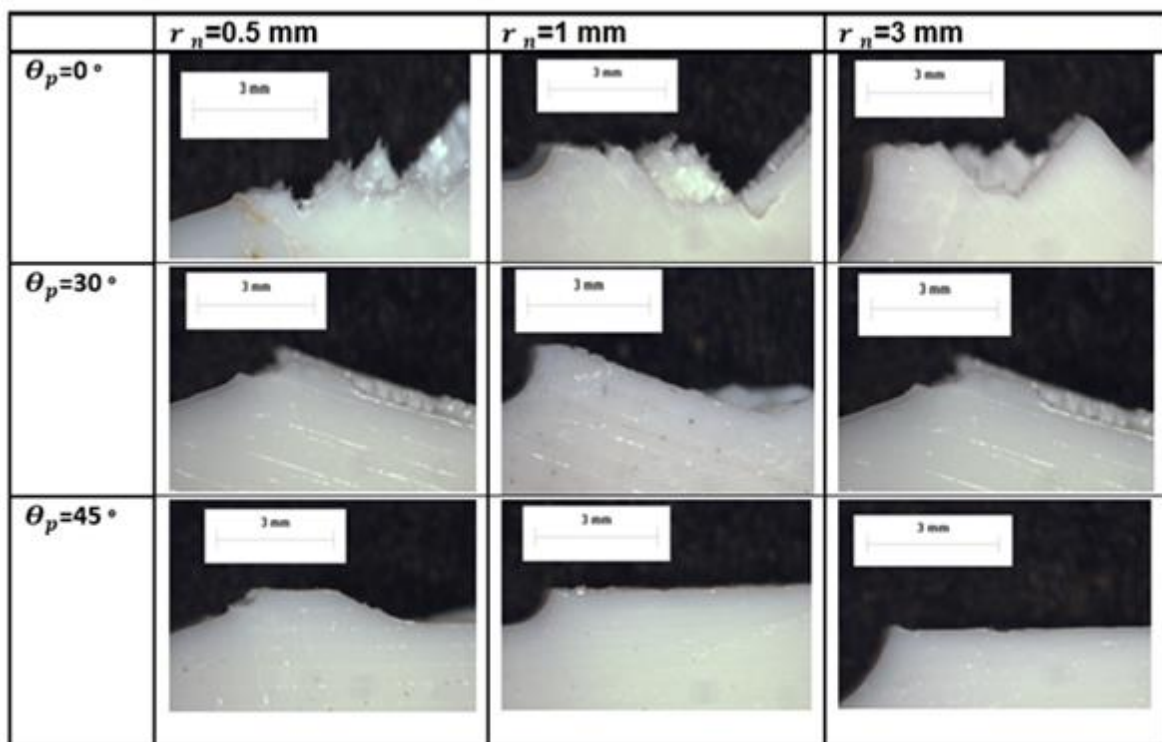


Figure A.4.4 U-notches under 3-point bending

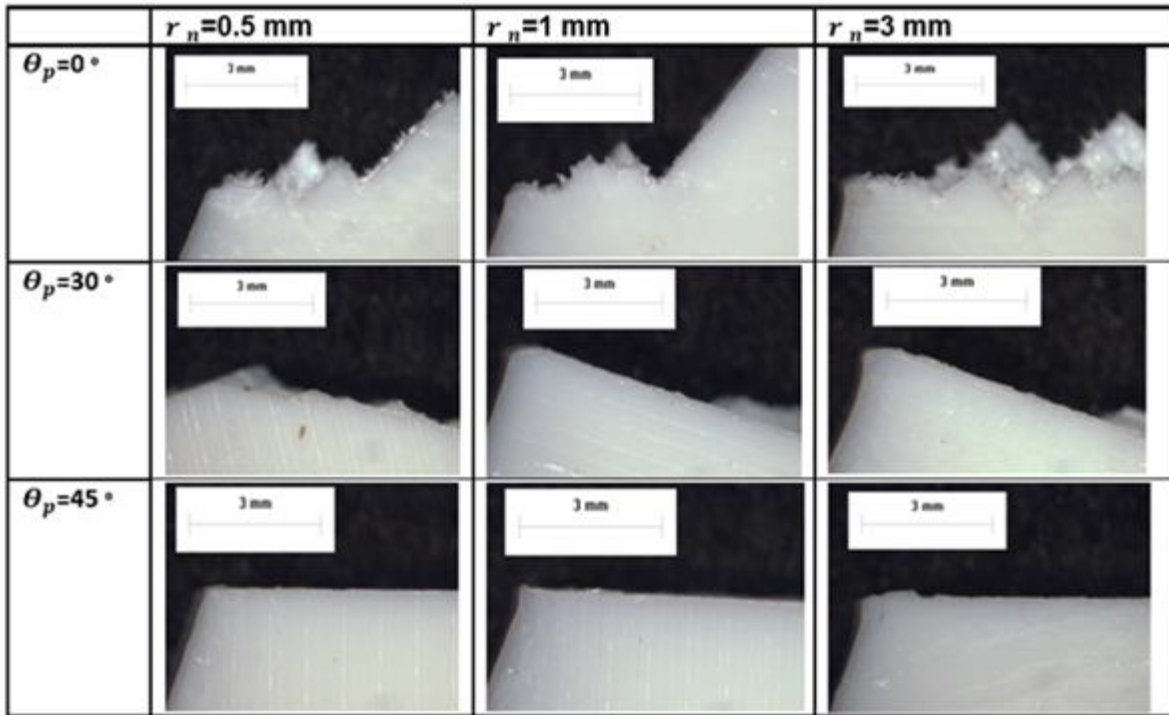
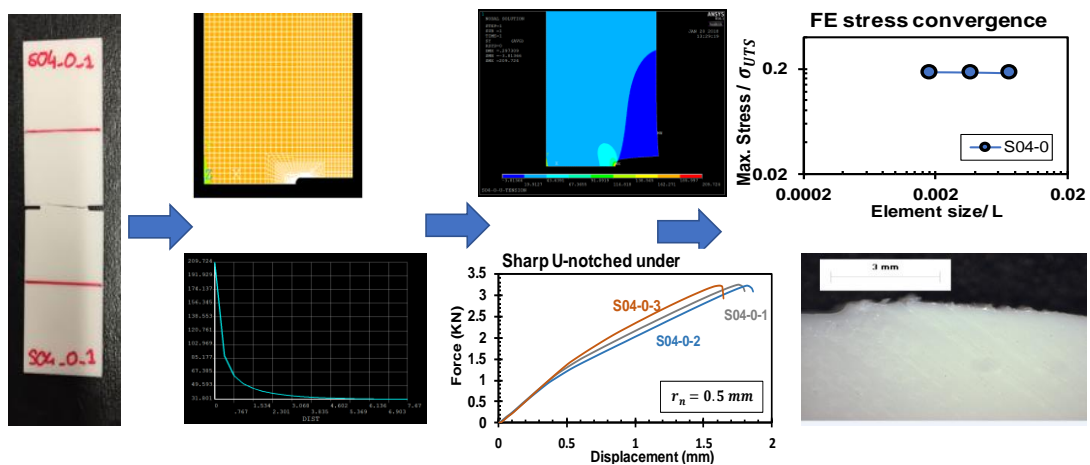
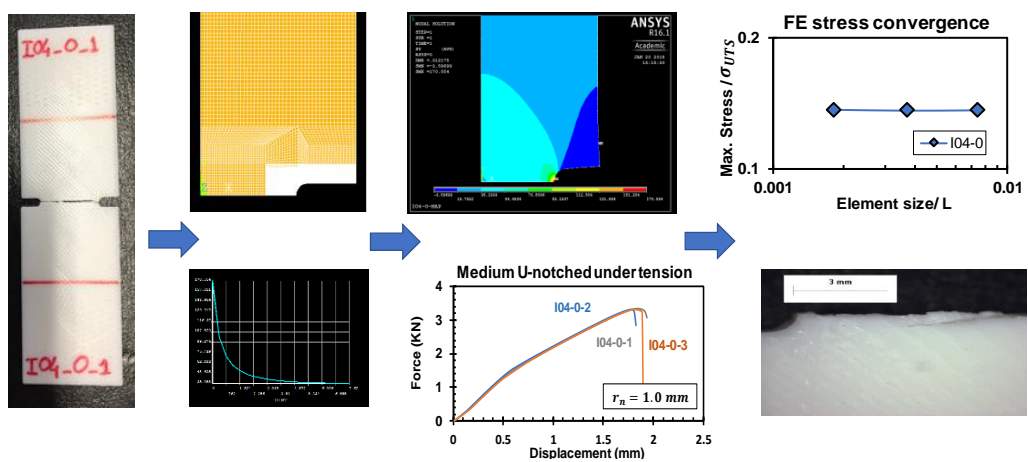
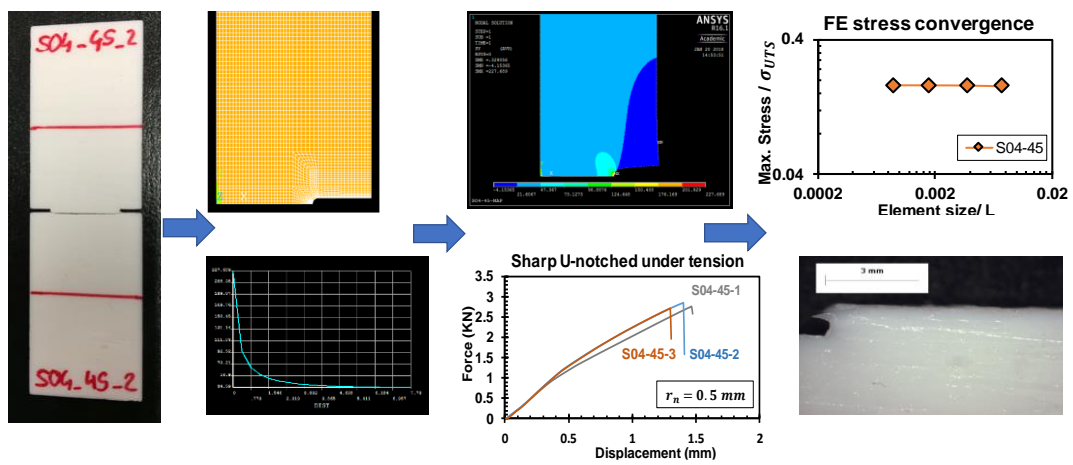
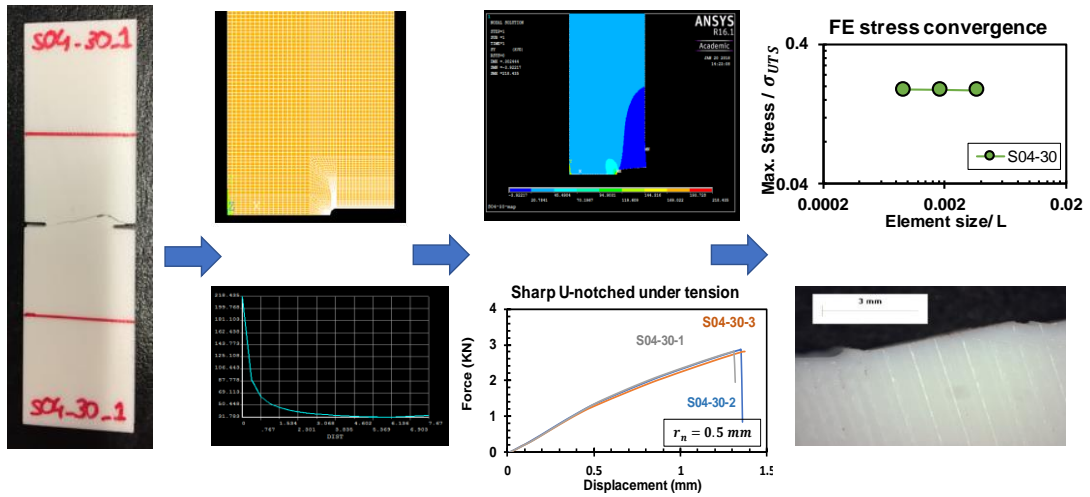


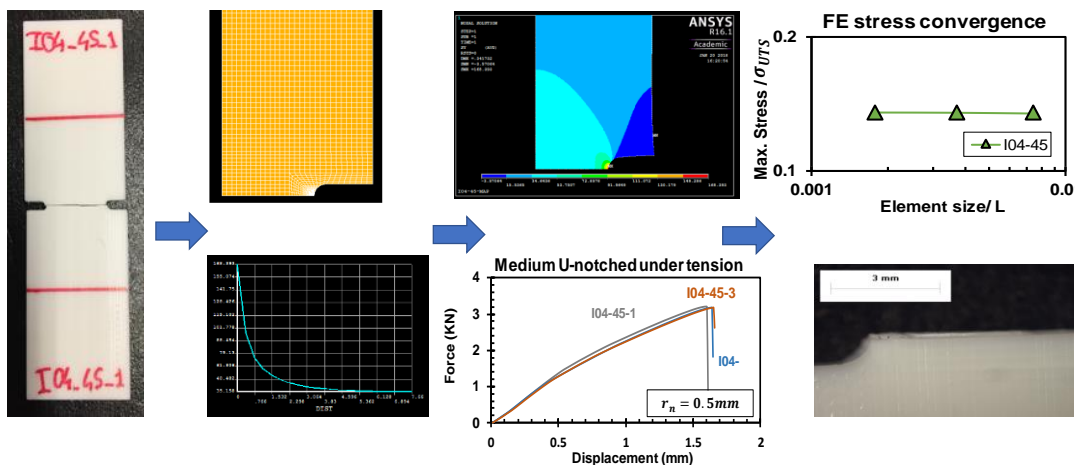
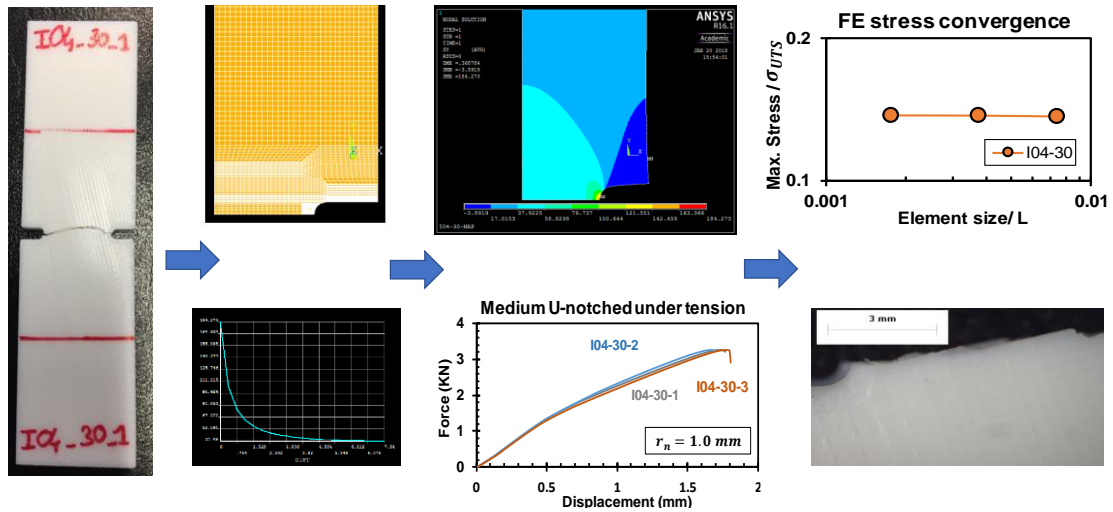
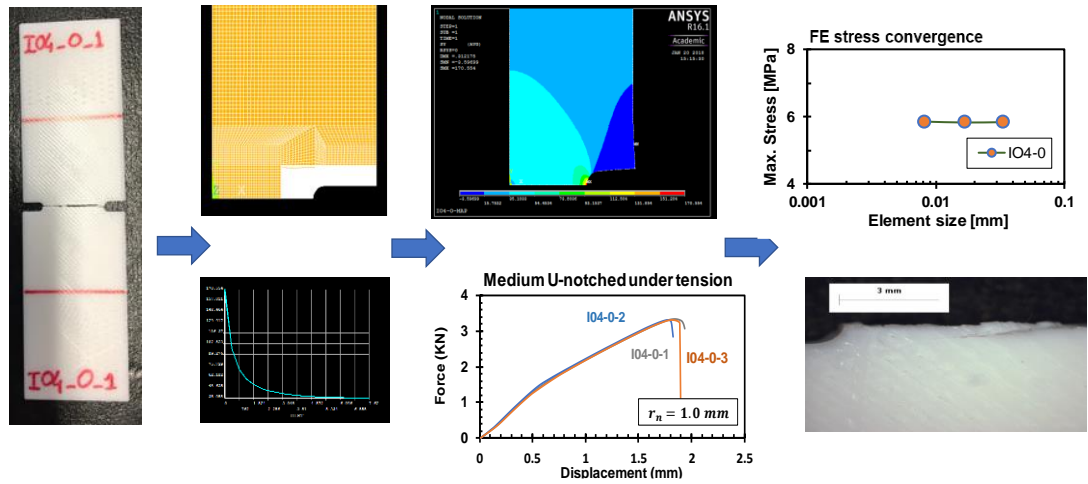
Figure A.4.5 Open notches under 3-point bending

A.5 FE modelling scheme and test figures for solid PLA samples

The FE modelling process and the stress convergence for every notched solid PLA specimen are listed in the scheme below. The average failure stress result of three repeated samples for every deposition angle, was considered in estimating the stress field in the FE modelling.







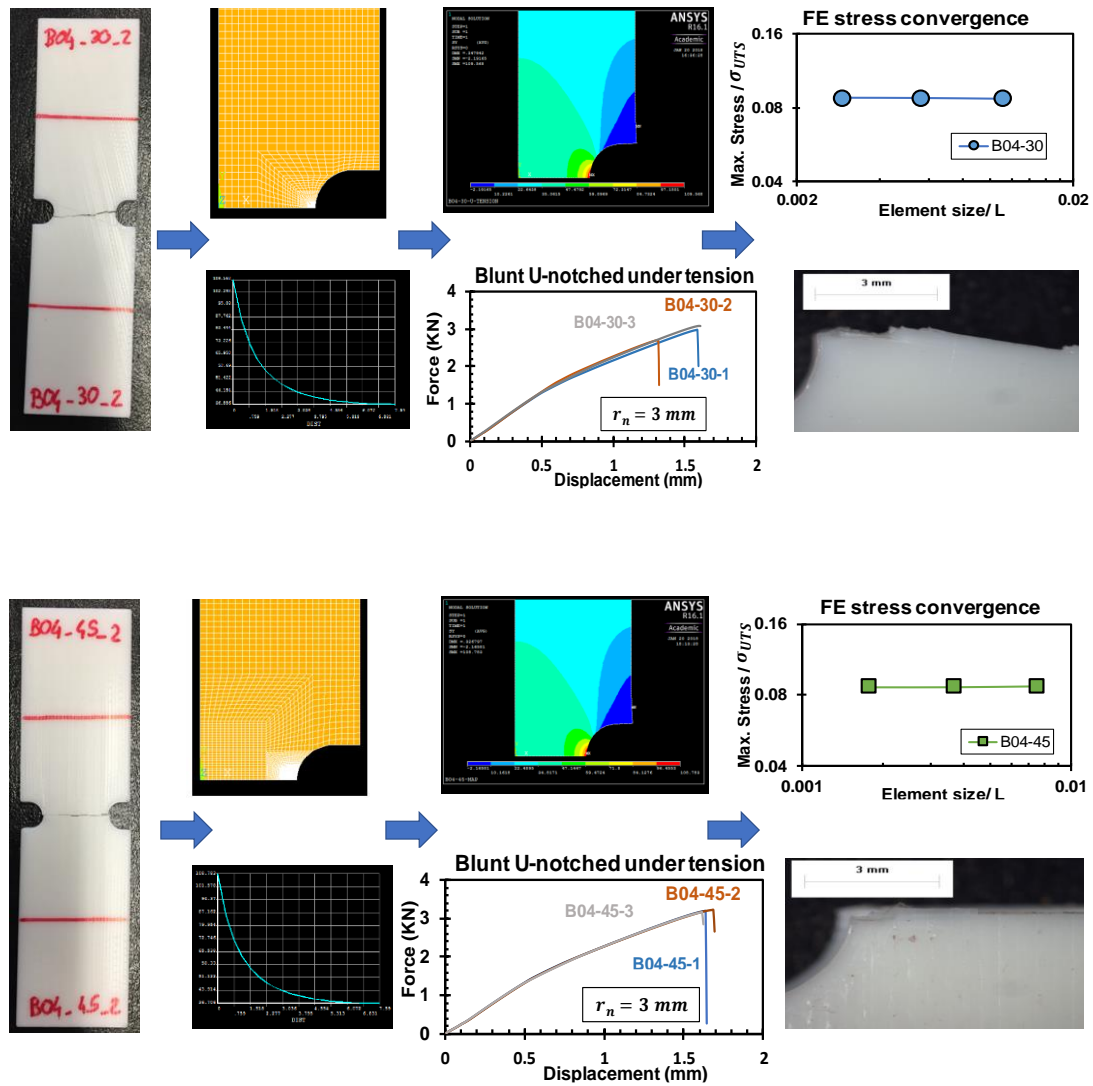
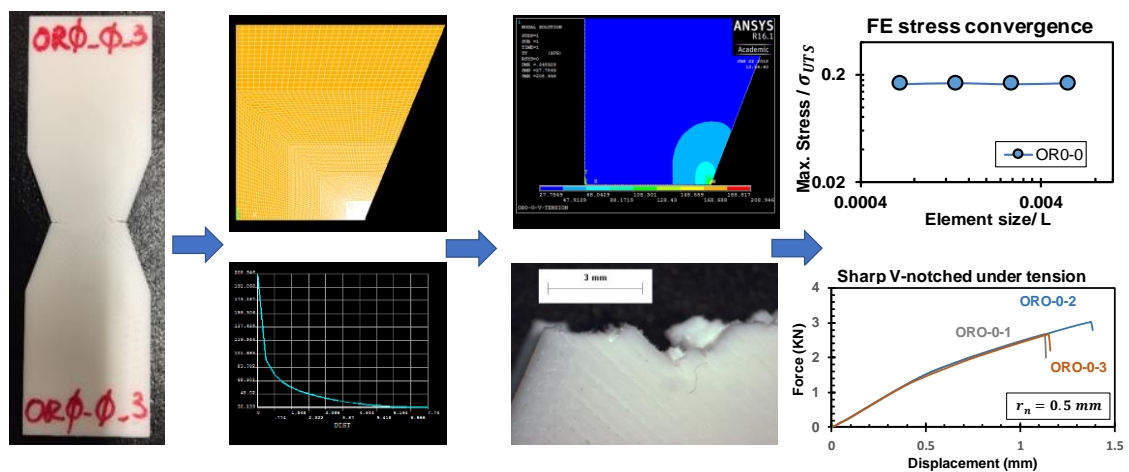
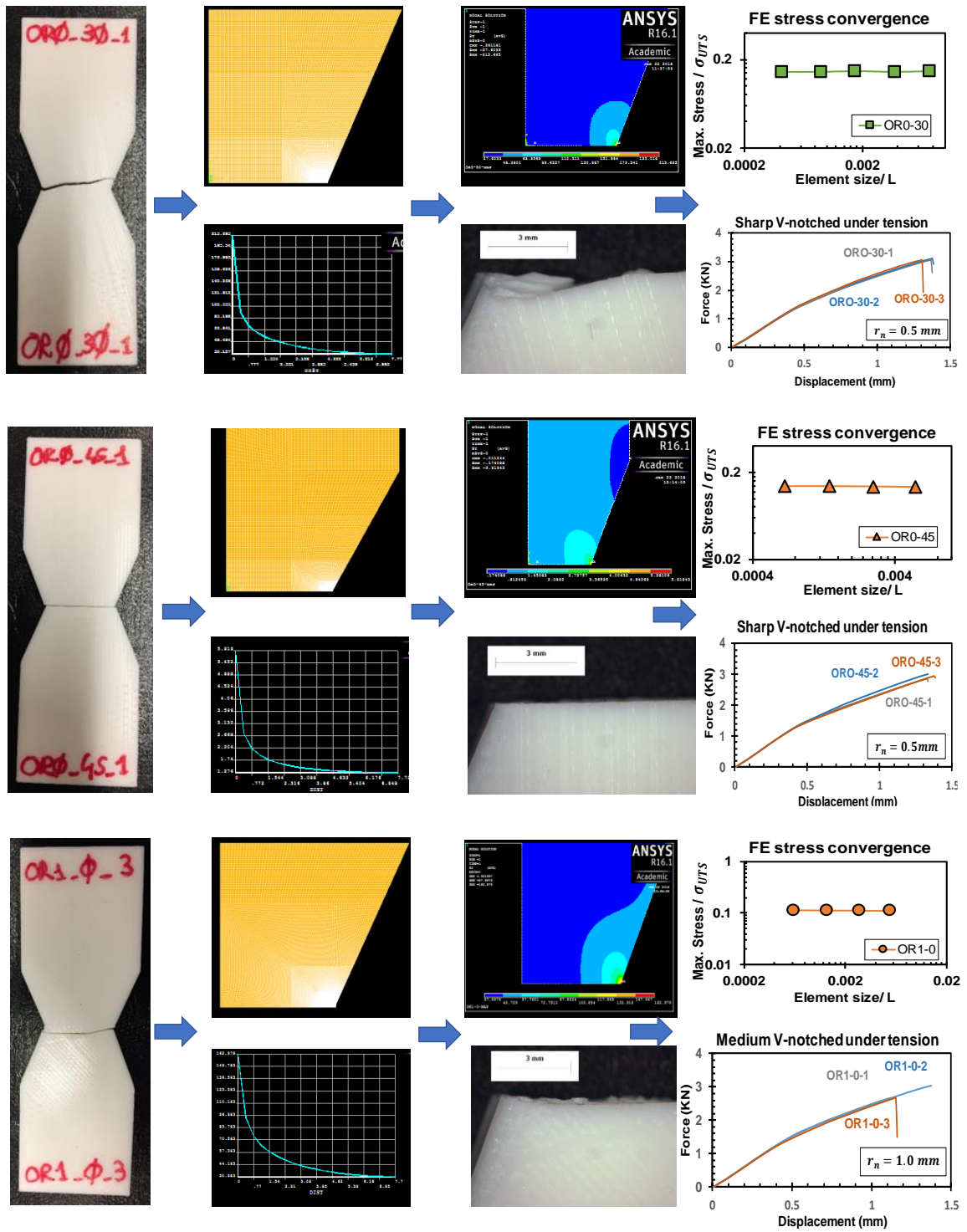
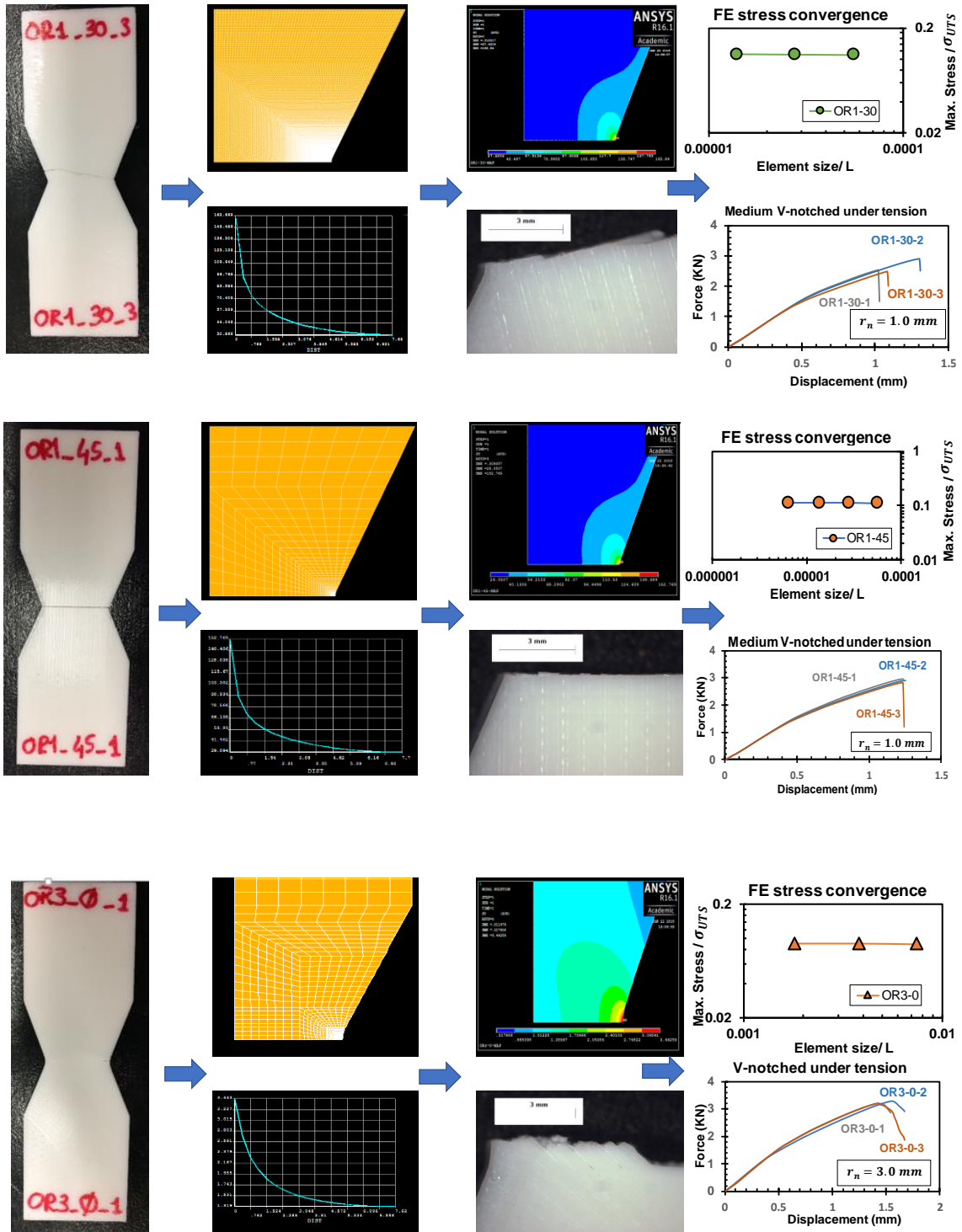


Figure A.5.1 Test scheme of U-notches under tension







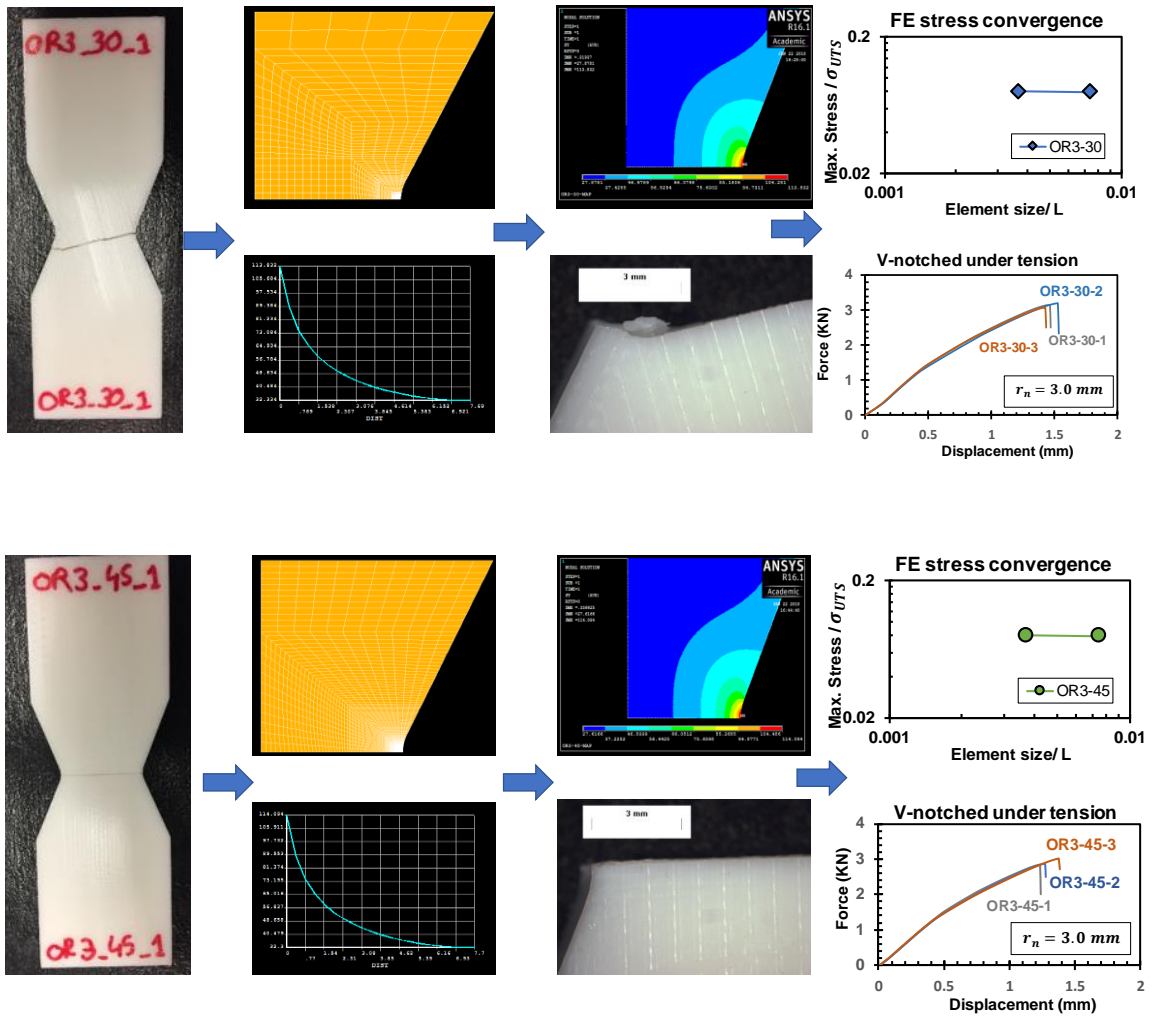
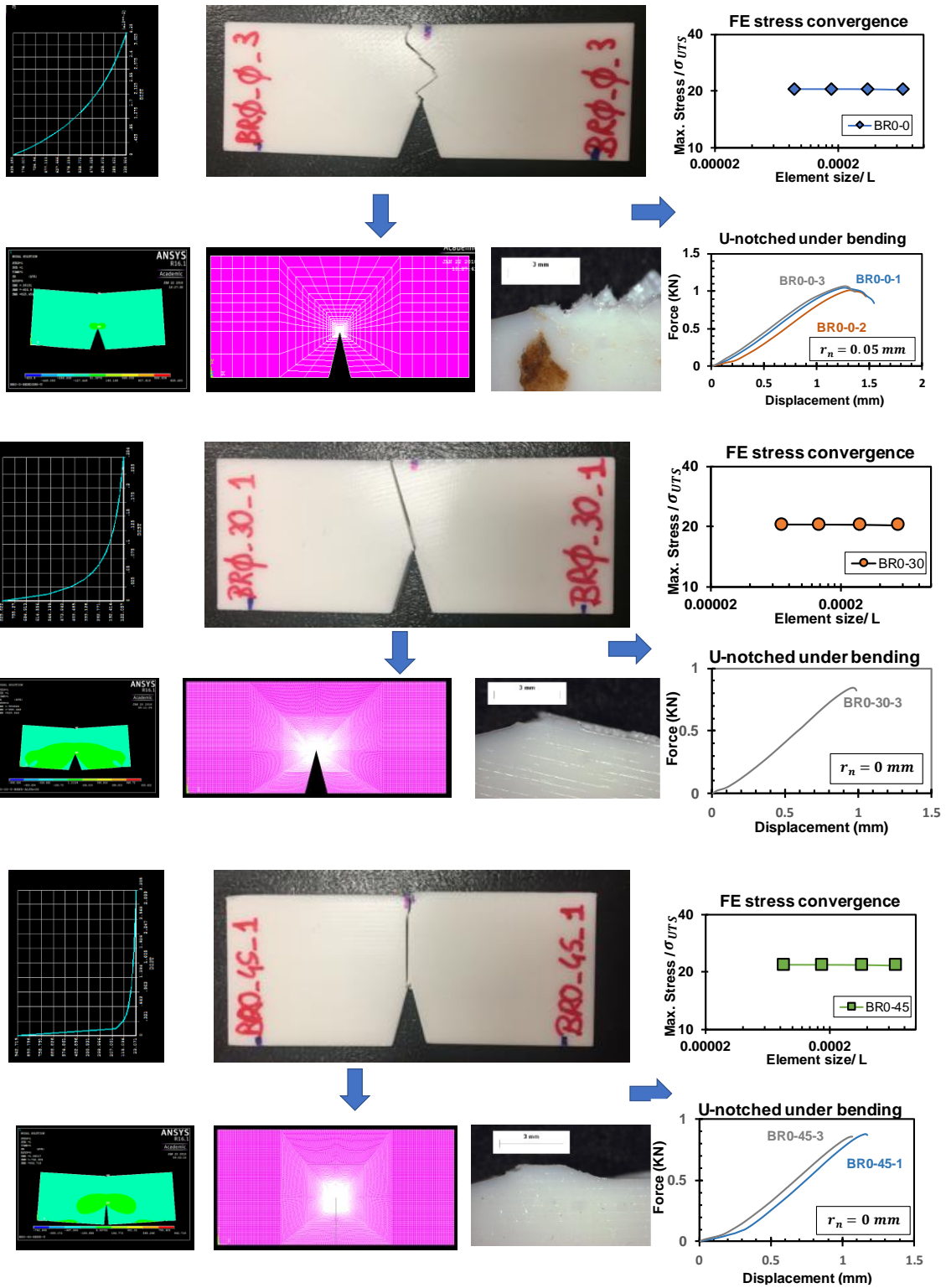
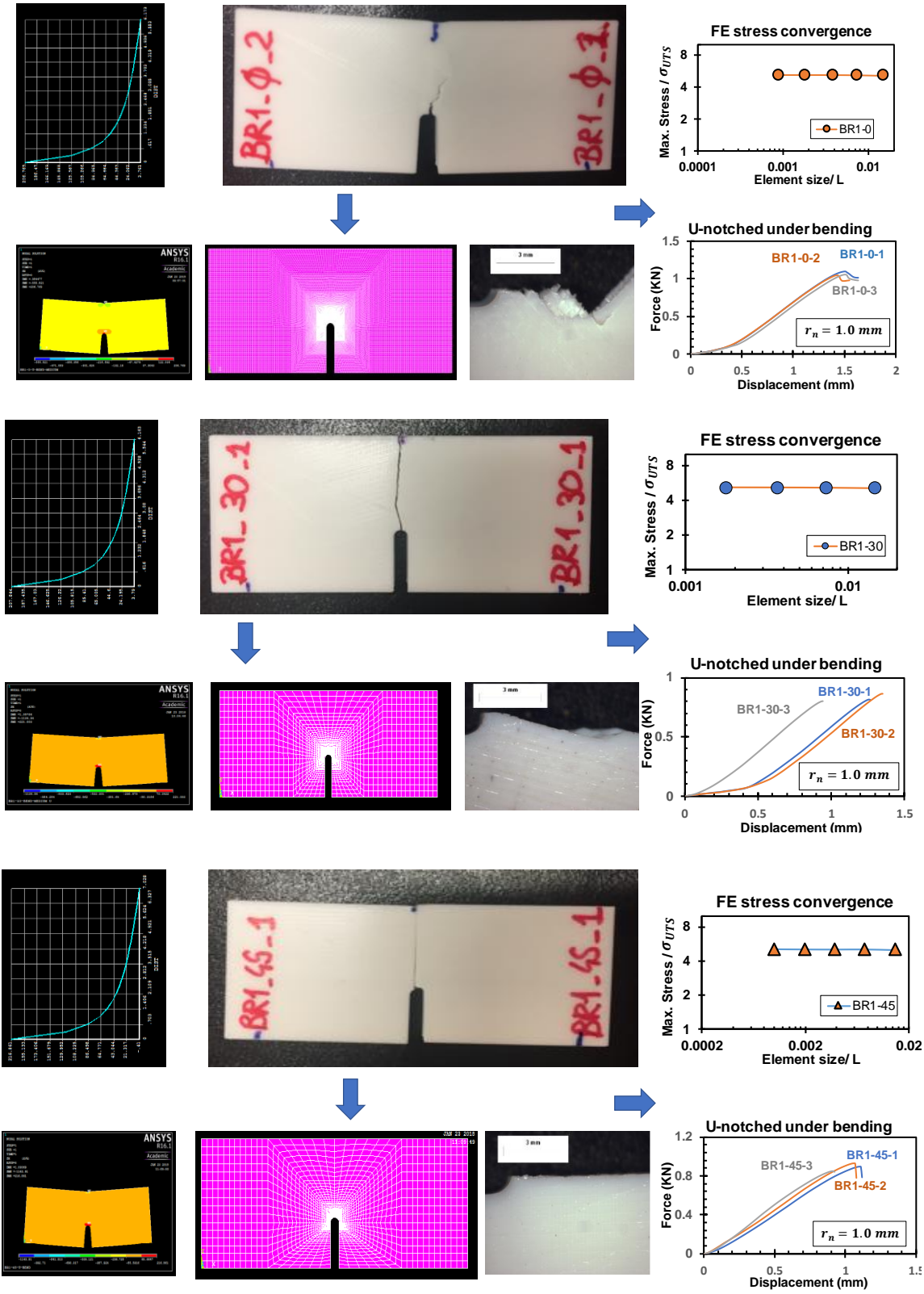


Figure A.5.2 Test scheme of open notches under tension





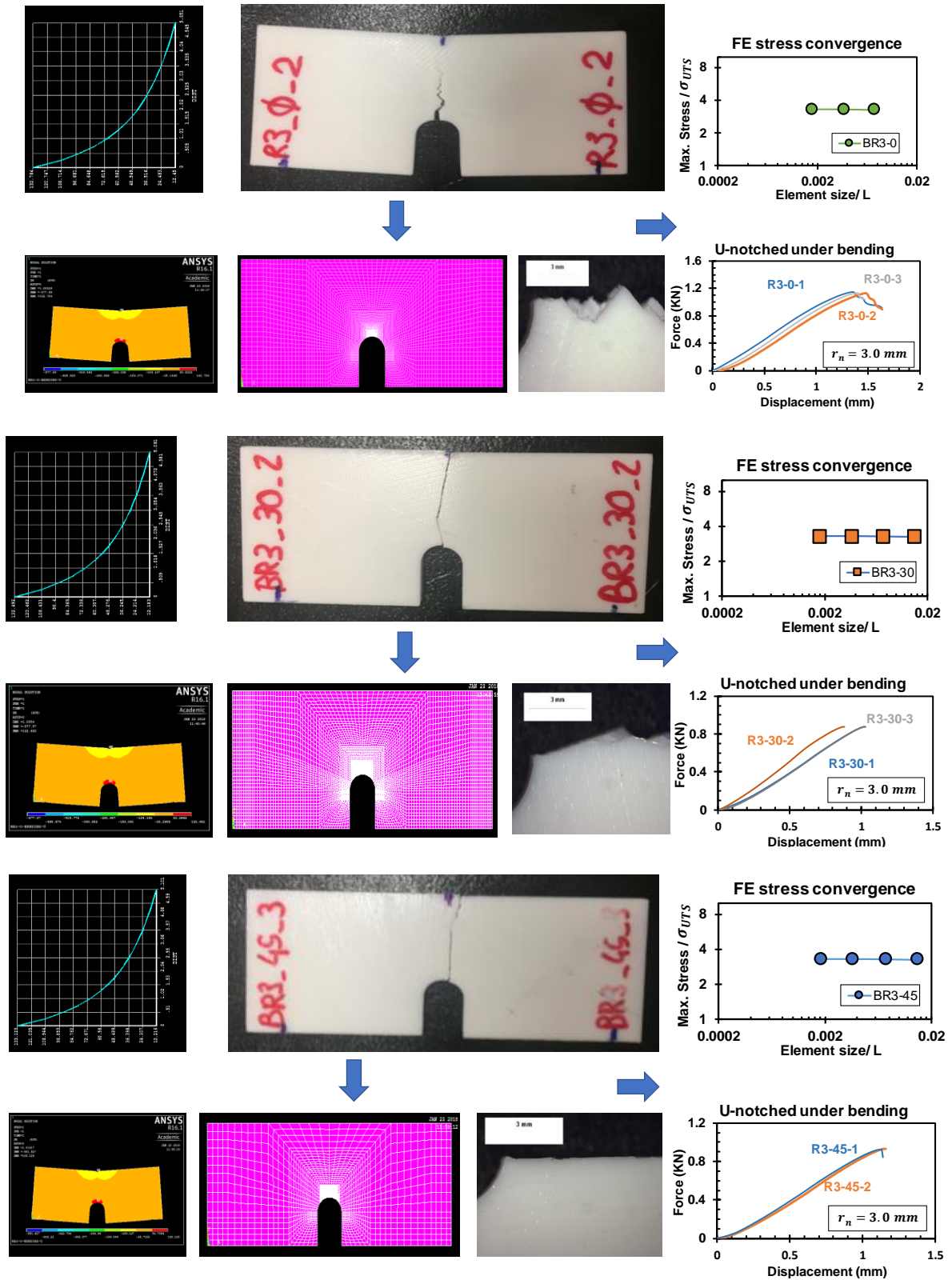
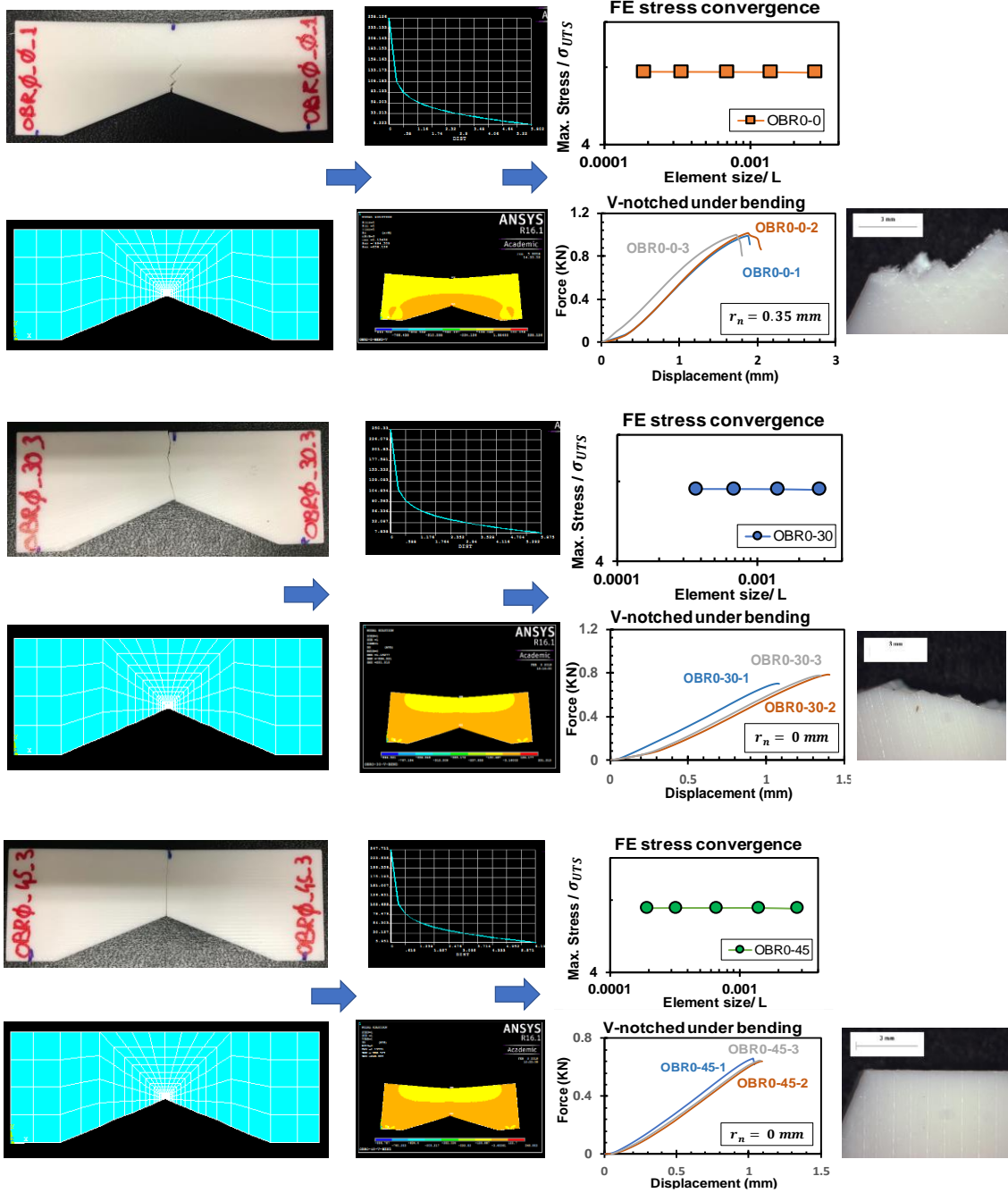
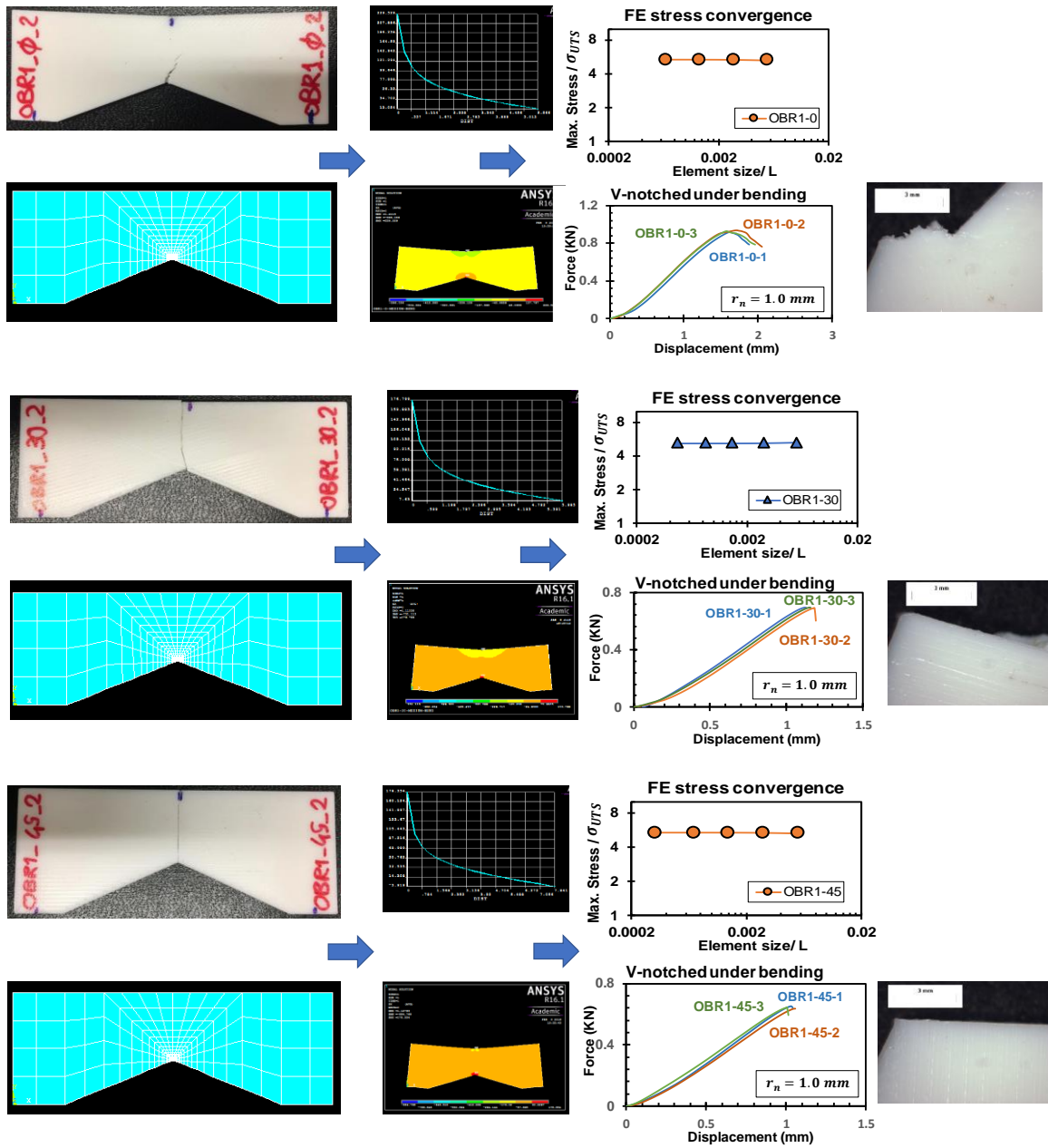


Figure A.5.3 Test scheme of U-notches under 3-point bending





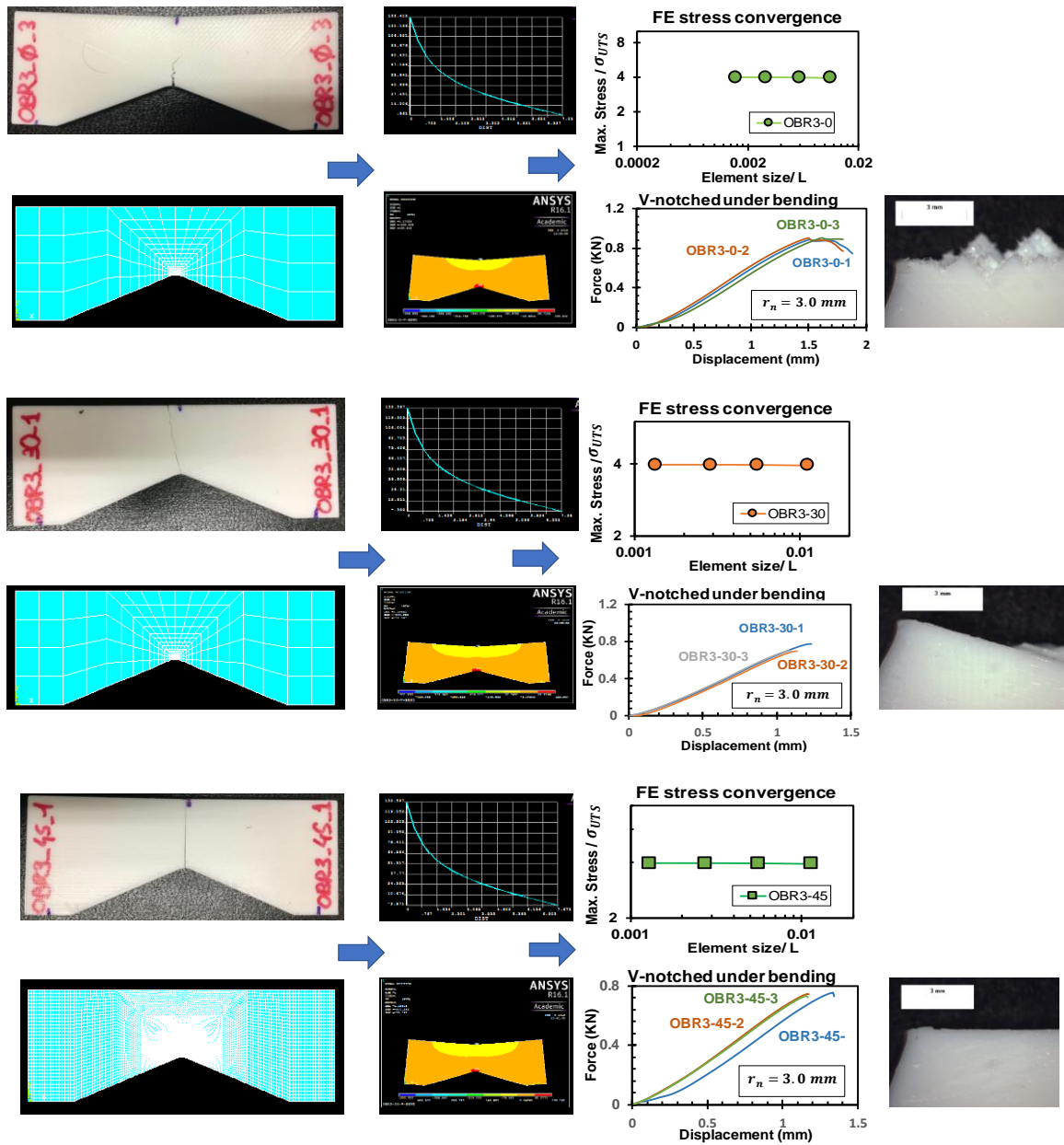


Figure A.5.4 Test scheme of V-notches under 3- point bending

A.6 Tables of PLA strength prediction by the TCD

The results of strength estimation of the notched AM PLA parts by utilising the point method and area method, are shown in the below tables.

Table A.6.1 PM prediction for U-notches under tension

U-notches under tension			POINT METHOD		
Code	$\sigma_{ult}[MPa]$	L [mm]	$\sigma_0 [MPa]$	$\sigma_{eff}[MPa]$	Error [%]
B04-0	30.95	4.48	42.9	51.4	19.8
B04-30	26.75	4.48	42.9	44.9	4.6
B04-45	30.07	4.48	42.9	50.25	17
I04-0	31.801	4.48	42.9	48.18	12.4
I04-30	31.487	4.48	42.9	48.65	13.3
I04-45	30.736	4.48	42.9	47.46	10.6

Table A.6.2 PM prediction for V-notches under tension

V-notches under tension			POINT METHOD		
Code	$\sigma_{ult}[MPa]$	L [mm]	$\sigma_0 [MPa]$	$\sigma_{eff}[MPa]$	Error [%]
ORO-0	31.54	4.48	42.9	53.2	24
ORO-30	29.171	4.48	42.9	46.4	8.1
ORO-45	28.15	4.48	42.9	44.8	4.4
OR1-0	26.287	4.48	42.9	42.48	-0.9
OR1-30	24.954	4.48	42.9	40.2	-1.6
OR1-45	27.318	4.48	42.9	44.12	2.8
OR3-0	31.39	4.48	42.9	55.06	28.3
OR3-30	30.3	4.48	42.9	50.35	17.3
OR3-45	28.2	4.48	42.9	46.8	-7.2

Table A.6.3 AM prediction for U-notches under tension

U-notches under tension			AREA METHOD		
Code	σ_{ult} [MPa]	L [mm]	σ_o [MPa]	σ_{eff} [MPa]	Error [%]
S04-0	30.2	4.48	42.9	48.7	13.5
S04-30	27	4.48	42.9	43.6	1.6
S04-45	26.5	4.48	42.9	42.5	-0.9
I04-0	31.8	4.48	42.9	51.7	20.5
I04-30	31.5	4.48	42.9	51	19
I04-45	30.7	4.48	42.9	50	16.5
B04-0	31.0	4.48	42.9	52	21
B04-30	26.8	4.48	42.9	45.6	6.3
B04-45	30.1	4.48	42.9	51	19

Table A.6.4 AM prediction for V-notches under tension

V-notches under tension			AREA METHOD		
Code	σ_{ult} [MPa]	L [mm]	σ_o [MPa]	σ_{eff} [MPa]	Error [%]
ORO-0	31.54	4.48	42.9	58.8	37
ORO-30	29.17	4.48	42.9	47.7	11
ORO-45	28.2	4.48	42.9	46	7.2
OR1-0	26.3	4.48	42.9	47	9.5
OR1-30	25.0	4.48	42.9	44.7	4.2
OR1-45	27.3	4.48	42.9	49	14.2
OR3-0	31.4	4.48	42.9	53	23.5
OR3-30	30.3	4.48	42.9	55.2	28.6
OR3-45	28.2	4.48	42.9	51.4	19.8

Table A.6.5 AM prediction for U-notches under 3-point bending

U-notches under bending			AREA METHOD		
Code	F_r [N]	L [mm]	σ_o [MPa]	σ_{eff} [MPa]	Error [%]
BRO-O	1040.5	4.48	42.9	42.56	-0.8
BRO-30	828.9	4.48	42.9	34	-20.7
BRO-45	874.8	4.48	42.9	38.1	-11
BR1-O	1,066.6	4.48	42.9	46.7	8.8
BR1-30	827.1	4.48	42.9	36.22	-15.5
BR1-45	890.3	4.48	42.9	38.5	-10.2
BR3-O	1,136.5	4.48	42.9	52.4	22
BR3-30	873.9	4.48	42.9	40.2	-6.3
BR3-45	926.3	4.48	42.9	43	0.2

Table A.6.6 AM prediction for V-notches under 3-point bending

V-notches under bending			AREA METHOD		
Code	F_r [N]	L [mm]	σ_o [MPa]	σ_{eff} [MPa]	Error [%]
OBRO-O	1000.1	4.48	42.9	56	30.5
OBRO-30	754.1	4.48	42.9	42.3	-1.3
OBRO-45	649.2	4.48	42.9	36.1	-16
OBR1-O	927.2	4.48	42.9	52	21
OBR1-30	693.0	4.48	42.9	38.5	-10
OBR1-45	642.2	4.48	42.9	35.7	-16.7
OBR3-O	804.7	4.48	42.9	48.2	12.3
OBR3-30	722.1	4.48	42.9	43	0.2
OBR3-45	743.6	4.48	42.9	44.3	3.2

Table A.6.7 PM prediction for U-notches under 3-point bending

U-notches under bending			PIONT METHOD		
Code	$F_r [N]$	L [mm]	$\sigma_o [MPa]$	$\sigma_{eff} [MPa]$	Error [%]
BRO-O	1040.5	4.48	42.9	33.6	-21.6
BRO-30	828.9	4.48	42.9	26.8	-37.5
BRO-45	874.75	4.48	42.9	29.52	-31
BR1-O	1066.55	4.48	42.9	39.9	-7
BR1-30	827.12	4.48	42.9	30.9	-27.9
BR1-45	890.34	4.48	42.9	32.4	-23
BR3-O	1136.46	4.48	42.9	49.2	14.7
BR3-30	873.93	4.48	42.9	37.7	-12
BR3-45	926.33	4.48	42.9	40.2	-6.3

Table A.6.8 PM prediction for V-notches under 3-point bending

V-notches under bending			PIONT METHOD		
Code	$F_r [N]$	L [mm]	$\sigma_o [MPa]$	$\sigma_{eff} [MPa]$	Error [%]
OBRO-O	1000.1	4.48	42.9	41.3	-3.7
OBRO-30	754.1	4.48	42.9	38.85	-9.4
OBRO-45	649.2	4.48	42.9	33.1	-2.3
OBR1-O	927.2	4.48	42.9	48.1	12
OBR1-30	693	4.48	42.9	35.58	-17
OBR1-45	642.2	4.48	42.9	33	-23
OBR3-O	804.7	4.48	42.9	50.5	17.7
OBR3-30	722.1	4.48	42.9	40.4	-5.8
OBR3-45	743.6	4.48	42.9	41.7	-2.8

Appendix B. AM PLA porous samples

The results of porous PLA parts manufactured with less than 100% infill level, will be presented in the current appendix. This include the pictures, the tables, the load vs displacement, and the microscopic images. Finally, the tables of strength prediction for the samples, by using TCD method, will be shown.

B.1 The pictures of PLA porous samples

The pictures of the plain and notched porous specimens printed with variable infill level and different deposition angle, are shown below. The whole samples were tested under tension.

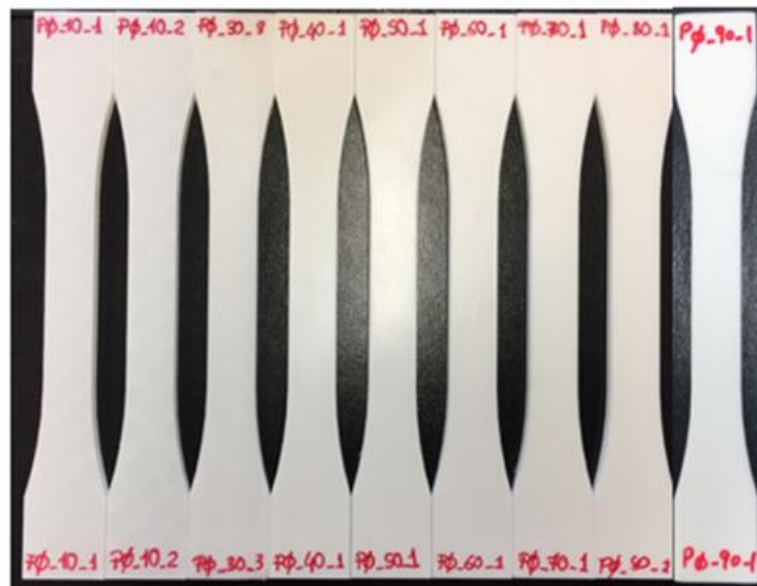


Figure B.1.1 Plain porous specimens with 0° deposit angle

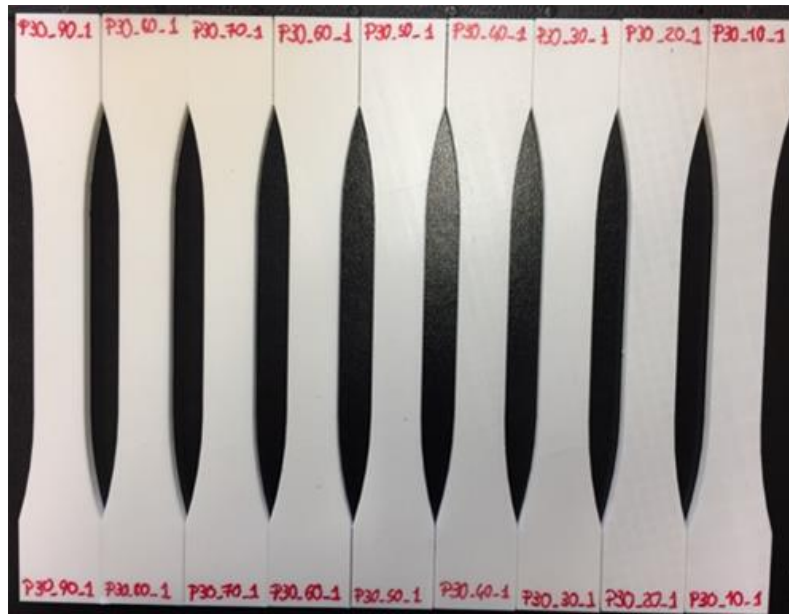


Figure B.1.2 Plain porous specimens with 30° deposit angle

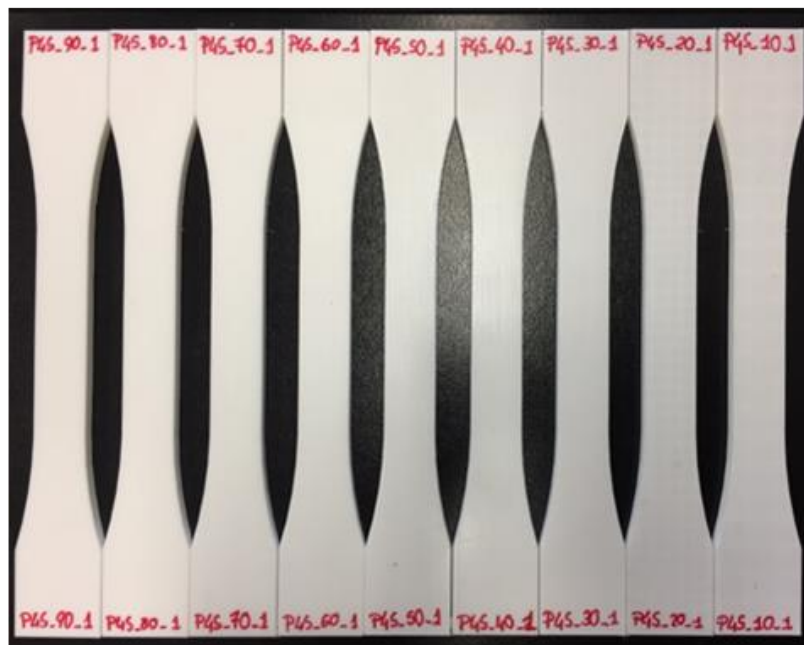
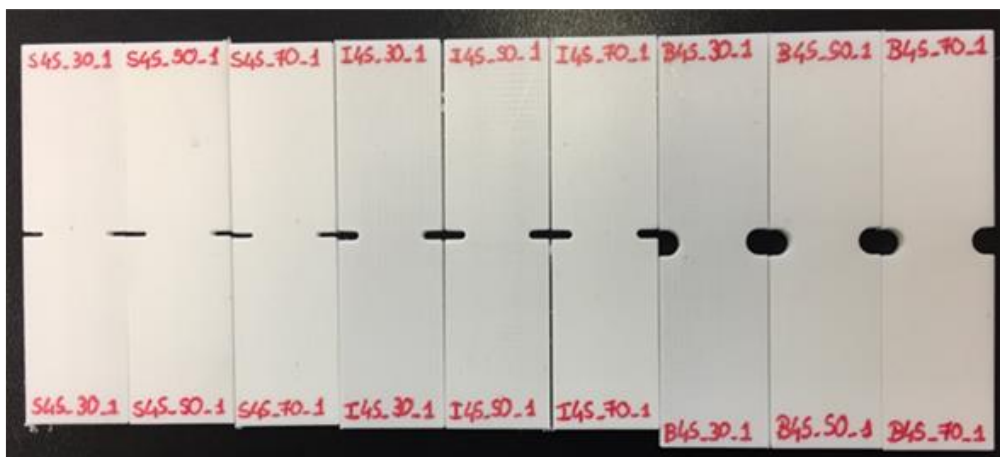


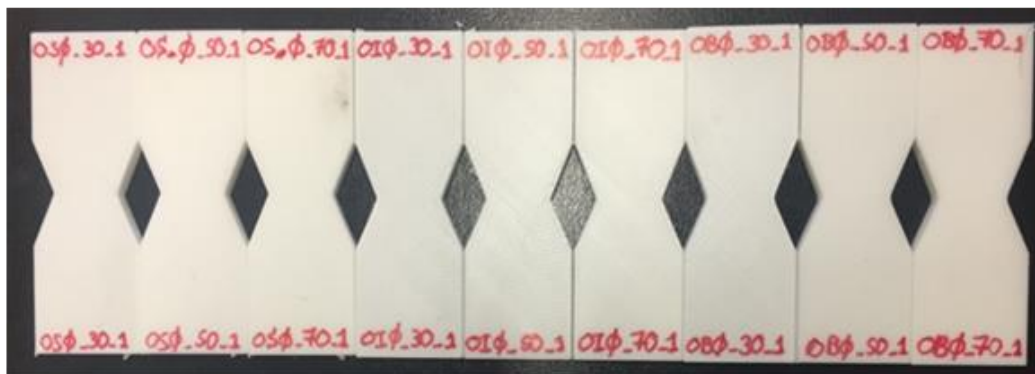
Figure B.1.3 Plain porous specimens with 45° deposit angle



(a)



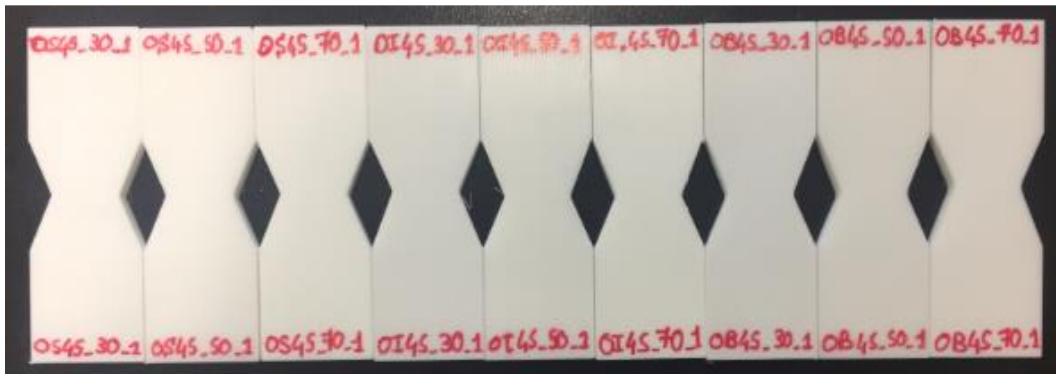
(b)



(c)



(d)



(e)

Figure B.1.4 Notched PLA samples manufactured with different infill levels, a) U-notches, $\theta_p=0^\circ$, b) U-notches, $\theta_p=45^\circ$, c) V-notches, $\theta_p=0^\circ$, d) V-notches, $\theta_p=30^\circ$, e) V-notches, $\theta_p=45^\circ$

B.2 Tables of the test results for AM PLA porous parts

The following tables will show the measured dimensions and the test results of the plain and notched porous samples, manufactured with different deposition angles and variable infill levels.

Table B.2.1 Results of plain porous PLA samples with $\theta_p = 30^\circ$

Code	θ_p [Deg]	Infill %	W_n [mm]	t [mm]	F_f [N]	E [MPa]	$\sigma_{0.2\%}$ [MPa]	σ_f [MPa]	d_V [mm]
P30_10_1	30	10	15.10	4.01	527	704	8.5	8.7	10.72
P30_10_2	30	10	15.09	4.05	538	688	8.6	8.8	
P30_10_3	30	10	15.11	4.04	531	744	8.5	8.7	
P30_20_1	30	20	15.05	4.00	473	642	7.5	7.9	5.06
P30_20_2	30	20	15.09	4.03	480	663	7.9	7.9	
P30_20_3	30	20	15.10	4.01	480	649	7.9	7.9	
P30_30_1	30	30	15.08	4.06	599	723	9.2	9.8	1.39
P30_30_2	30	30	15.02	4.01	596	710	9.2	9.9	
P30_30_3	30	30	15.03	4.03	591	863	9.3	9.8	
P30_40_1	30	40	15.03	4.04	614	698	9.5	10.1	0.96
P30_40_2	30	40	15.01	4.06	613	675	9.3	10.1	
P30_40_3	30	40	15.00	4.04	618	726	9.6	10.2	
P30_50_1	30	50	15.10	3.99	860	1107	13.5	14.3	0.66
P30_50_2	30	50	15.08	3.97	840	1095	13.3	14.0	
P30_50_3	30	50	15.04	3.95	810	1071	13.2	13.6	
P30_60_1	30	60	15.04	4.02	980	1305	15.5	16.2	0.41
P30_60_2	30	60	15.05	4.01	964	1292	15.2	16.0	
P30_60_3	30	60	15.00	4.00	927	1275	14.8	15.5	
P30_70_1	30	70	15.01	4.03	1122	1584	17.7	18.5	0.29
P30_70_2	30	70	15.05	4.03	1113	1541	17.5	18.4	
P30_70_3	30	70	15.04	4.01	1116	1513	17.7	18.5	
P30_80_1	30	80	14.98	4.04	1133	1594	18.3	18.7	0.25
P30_80_2	30	80	15.03	4.04	1191	1934	19.0	19.6	
P30_80_3	30	80	14.96	4.03	1186	1705	19.1	19.7	
P30_90_1	30	90	15.09	4.04	1438	2152	22.7	23.6	0.11
P30_90_2	30	90	15.00	4.02	1422	2193	22.5	23.6	
P30_90_3	30	90	14.99	4.02	1384	2133	22.3	23.0	

Table B.2.2 Results of plain porous PLA samples with $\theta_p = 45^\circ$

Code	θ_p [Deg]	Infill [mm]	W_n [mm]	t [mm]	F_r [N]	E [MPa]	$\sigma_{0.2\%}$ [MPa]	σ_f [MPa]	d_v [mm]
P45_10_1	45	10	15.09	4.04	552	738	8.7	9.1	10.65
P45_10_2	45	10	15.01	4.05	462	646	7.3	7.6	
P45_10_3	45	10	14.95	4.05	492	677	7.9	8.1	
P45_20_1	45	20	15.06	4.09	661	911	10.7	10.7	5.12
P45_20_2	45	20	14.93	4.14	548	852	8.4	8.9	
P45_20_3	45	20	14.93	4.16	551	787	8.7	8.9	
P45_30_1	45	30	14.97	4.07	674	1002	10.9	11.1	1.37
P45_30_2	45	30	14.94	4.16	661	981	10.4	10.6	
P45_30_3	45	30	14.90	4.02	640	979	10.5	10.7	
P45_40_1	45	40	15.02	4.04	773	1124	12.6	12.7	0.93
P45_40_2	45	40	15.03	4.01	747	1138	12.3	12.4	
P45_40_3	45	40	14.9	4.07	730	1075	11.8	12.0	
P45_50_1	45	50	14.98	4.07	892	1035	14.5	14.6	0.65
P45_50_2	45	50	14.98	4.01	856	1303	14.2	14.3	
P45_50_3	45	50	15.00	4.00	807	1240	13.4	13.4	
P45_60_1	45	60	14.98	4.06	1008	1494	16.5	16.6	0.43
P45_60_2	45	60	14.96	4.07	906	1428	15.6	15.8	
P45_60_3	45	60	14.94	4.04	916	1367	15.0	15.2	
P45_70_1	45	70	14.89	4.07	1160	1697	19.0	19.1	0.31
P45_70_2	45	70	14.99	4.12	1098	1630	17.5	17.8	
P45_70_3	45	70	14.93	4.04	1055	1669	17.5	17.5	
P45_80_1	45	80	14.97	4.08	1269	1925	20.5	20.8	0.22
P45_80_2	45	80	15.00	4.04	1243	1909	20.4	20.5	
P45_80_3	45	80	14.99	4.01	1228	1917	20.2	20.4	
P45_90_1	45	90	14.99	4.03	1437	2218	23.5	23.8	0.13
P45_90_2	45	90	14.96	4.08	1369	2150	22.4	22.4	
P45_90_3	45	90	15.01	4.07	1356	2123	22.2	22.2	

Table B.2.3 Results of U-notched PLA porous samples with $\theta_p = 30^\circ$

Code	θ [Deg]	Infill [%]	R_n [mm]	W_n [mm]	W_g [mm]	t [mm]	F_f [N]	d_v [mm]
S30_30_1	30	30	0.50	15.34	24.83	4.12	578	
S30_30_2	30	30	0.53	15.31	24.80	4.09	490	1.23
S30_30_3	30	30	0.51	15.34	24.77	4.04	470	
S30_50_1	30	50	0.51	15.32	24.86	4.15	810	
S30_50_2	30	50	0.53	15.29	24.79	4.08	700	0.68
S30_50_3	30	50	0.50	15.37	24.77	4.11	659	
S30_70_1	30	70	0.53	15.37	24.85	4.01	895	
S30_70_2	30	70	0.51	15.31	24.83	4.04	728	0.43
S30_70_3	30	70	0.51	15.32	24.78	4.07	640	
I30_30_1	30	30	1.01	15.16	24.72	4.03	503	
I30_30_2	30	30	1.03	15.17	24.74	4.04	539	1.44
I30_30_3	30	30	1.03	15.19	24.67	4.03	510	
I30_50_1	30	50	1.04	15.19	24.76	4.06	741	
I30_50_2	30	50	1.02	15.14	24.72	4.02	707	0.70
I30_50_3	30	50	1.01	15.24	24.76	4.04	768	
I30_70_1	30	70	1.02	15.11	24.72	4.00	739	
I30_70_2	30	70	1.03	15.19	24.77	4.04	718	0.39
I30_70_3	30	70	1.05	15.14	24.71	4.00	715	
B30_30_1	30	30	3.06	15.27	24.86	4.03	617	
B30_30_2	30	30	3.06	15.19	24.88	4.09	635	1.43
B30_30_3	30	30	3.07	15.20	24.85	4.06	608	
B30_50_1	30	50	3.07	15.25	24.82	4.05	797	
B30_50_2	30	50	3.07	15.07	24.86	4.08	767	0.72
B30_50_3	30	50	3.08	15.19	24.83	4.11	766	
B30_70_1	30	70	3.12	15.22	24.84	4.09	858	
B30_70_2	30	70	3.07	15.13	24.82	4.04	868	0.44
B30_70_3	30	70	3.09	15.16	24.98	4.06	848	

Table B.2.4 Results of U-notched porous PLA samples with $\theta_p = 45^\circ$

Code	θ [Deg]	Infill [%]	R_n [mm]	W_n [mm]	W_g [mm]	t [mm]	F_f [N]	d_v [mm]
S45_30_1	45	30	0.50	15.37	24.81	4.01	450	
S45_30_2	45	30	0.55	15.29	24.75	3.99	443	1.19
S45_30_3	45	30	0.51	15.45	24.85	4.06	597	
S45_50_1	45	50	0.52	15.43	24.95	4.05	822	
S45_50_2	45	50	0.56	15.34	24.75	4.08	629	0.56
S45_50_3	45	50	0.54	15.32	24.82	4.02	604	
S45_70_1	45	70	0.54	15.40	24.85	4.03	909	
S45_70_2	45	70	0.55	15.29	24.75	4.00	841	0.36
S45_70_3	45	70	0.51	15.46	24.88	4.14	1070	
I45_30_1	45	30	1.04	15.25	24.74	4.01	536	
I45_30_2	45	30	1.06	15.22	24.66	3.96	502	1.42
I45_30_3	45	30	1.06	15.30	24.655	3.94	435	
I45_50_1	45	50	1.03	15.11	24.67	3.97	623	
I45_50_2	45	50	1.04	15.19	24.64	4.04	706	0.69
I45_50_3	45	50	1.04	15.19	24.76	4.00	839	
I45_70_1	45	70	1.05	15.11	24.75	4.01	949	
I45_70_2	45	70	1.06	15.14	24.66	3.96	964	0.38
I45_70_3	45	70	1.06	15.17	24.69	4.03	843	
B45_30_1	45	30	3.09	15.17	24.80	4.00	612	
B45_30_2	45	30	3.08	15.12	24.89	4.03	596	1.46
B45_30_3	45	30	3.25	15.26	25.05	4.02	592	
B45_50_1	45	50	3.06	15.14	24.89	4.04	854	
B45_50_2	45	50	3.08	15.17	24.87	4.06	836	0.69
B45_50_3	45	50	3.09	15.19	24.87	4.07	794	
B45_70_1	45	70	3.08	15.17	24.82	4.08	998	
B45_70_2	45	70	3.08	15.16	25.02	4.08	1058	0.38
B45_70_3	45	70	3.06	15.09	24.88	4.08	977	

Table B.2.5 Results of V-notched porous PLA samples with $\theta_p = 0^\circ$

Code	θ [Deg]	Infill [%]	R_n [mm]	W_n [mm]	W_g [mm]	t [mm]	F_f [N]	d_v [mm]
OS0_30_1	0	30	0.55	15.20	24.73	3.96	381	
OS0_30_2	0	30	0.56	15.14	24.73	3.95	419	1.54
OS0_30_3	0	30	0.55	15.20	24.65	3.98	396	
OS0_50_1	0	50	0.53	15.09	24.61	4.02	706	
OS0_50_2	0	50	0.53	15.15	24.64	4.06	664	0.66
OS0_50_3	0	50	0.54	15.09	24.69	4.04	631	
OS0_70_1	0	70	0.49	15.16	24.67	4.00	909	
OS0_70_2	0	70	0.54	15.17	24.66	3.99	860	0.33
OS0_70_3	0	70	0.61	15.18	24.68	4.02	860	
OIO_30_1	0	30	1.04	15.12	24.82	4.02	522	
OIO_30_2	0	30	1.07	15.20	24.69	3.98	518	1.45
OIO_30_3	0	30	1.14	15.19	24.74	3.94	509	
OIO_50_1	0	50	1.06	15.19	24.92	4.04	712	
OIO_50_2	0	50	0.97	15.21	24.91	4.05	730	0.65
OIO_50_3	0	50	1.07	15.23	24.77	4.03	706	
OIO_70_1	0	70	1.05	15.16	24.73	4.06	977	
OIO_70_2	0	70	1.05	15.17	24.78	4.04	999	0.35
OIO_70_3	0	70	0.99	15.13	24.76	4.00	1044	
OB0_30_1	0	30	2.89	15.22	25.08	3.95	499	
OB0_30_2	0	30	2.80	15.06	24.87	3.97	493	1.44
OB0_30_3	0	30	3.03	14.98	24.76	4.01	508	
OB0_50_1	0	50	3.01	15.00	24.87	3.93	672	
OB0_50_2	0	50	2.99	14.99	24.82	3.93	657	0.67
OB0_50_3	0	50	3.05	14.98	24.80	4.00	658	
OB0_70_1	0	70	2.94	15.14	24.87	4.00	921	
OB0_70_2	0	70	3.08	15.03	24.76	4.04	919	0.37
OB0_70_3	0	70	3.04	15.05	24.80	4.07	929	

Table B.2.6 Results of V-notched porous PLA samples with $\theta_p = 30^\circ$

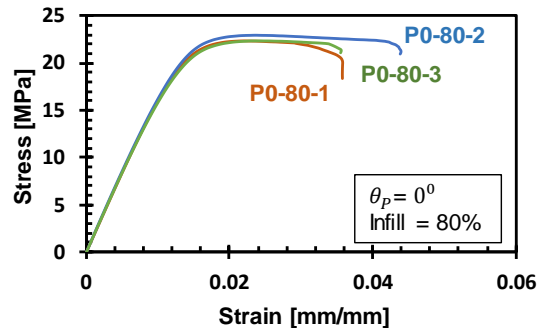
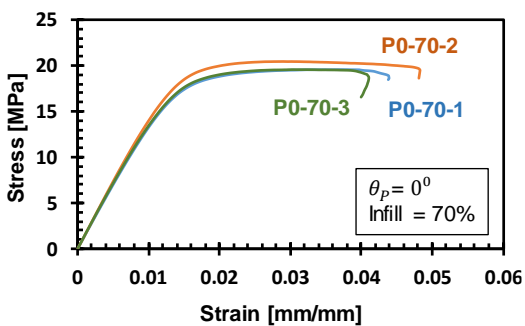
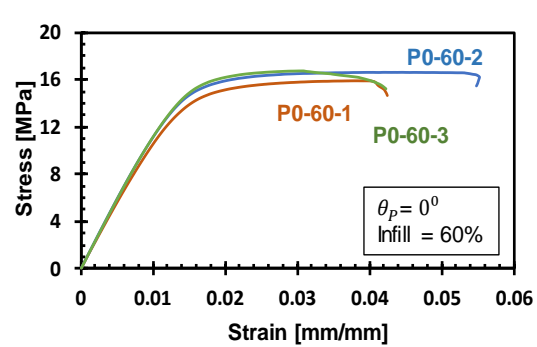
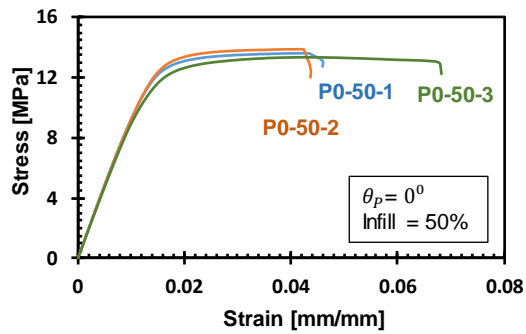
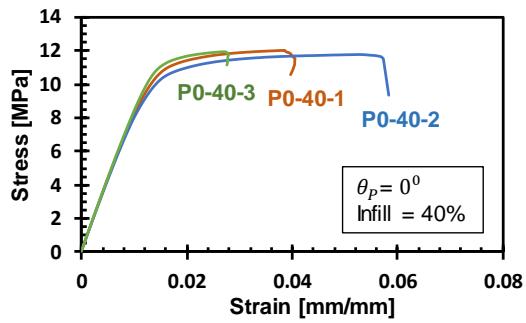
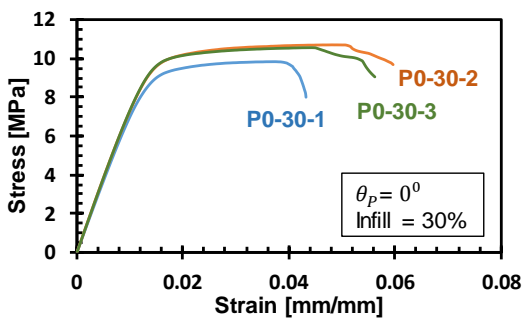
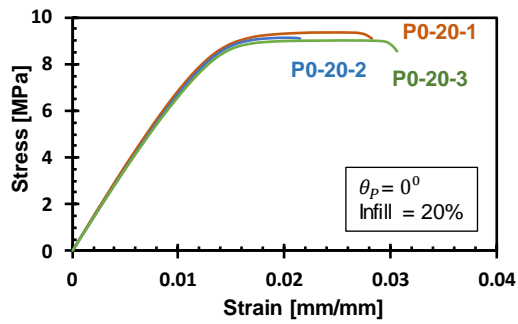
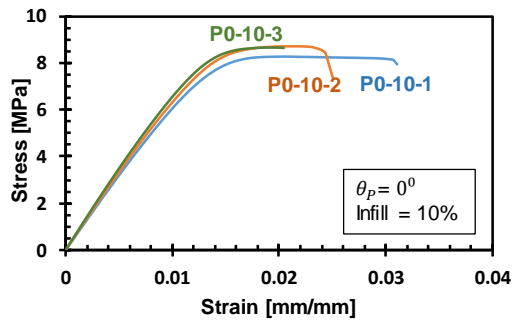
Code	θ [Deg]	Infill [%]	R_n [mm]	W_n [mm]	W_g [mm]	t [mm]	F_f [N]	d_v [mm]
OS30_30_1	30	30	0.55	15.29	24.65	4.02	420	
OS30_30_2	30	30	0.62	15.25	24.63	4.03	412	1.56
OS30_30_3	30	30	0.59	15.26	24.61	4.01	461	
OS30_50_1	30	50	0.50	15.33	24.89	4.07	1056	
OS30_50_2	30	50	0.50	15.27	24.85	4.08	944	0.65
OS30_50_3	30	50	0.49	15.30	24.81	4.11	1065	
OS30_70_1	30	70	0.54	15.03	24.63	4.01	861	
OS30_70_2	30	70	0.53	15.12	24.80	3.99	807	0.40
OS30_70_3	30	70	0.55	15.24	24.77	4.00	790	
OI30_30_1	30	30	1.02	15.25	24.85	4.04	554	
OI30_30_2	30	30	0.95	15.22	24.87	3.97	588	1.56
OI30_30_3	30	30	0.99	15.41	24.81	4.02	557	
OI30_50_1	30	50	1.03	15.38	24.84	4.11	1100	
OI30_50_2	30	50	0.97	15.33	24.79	4.09	1055	0.65
OI30_50_3	30	50	1.04	15.29	24.87	4.08	1088	
OI30_70_1	30	70	1.02	15.22	24.83	4.02	961	
OI30_70_2	30	70	1.02	15.05	24.75	4.05	923	0.38
OI30_70_3	30	70	1.07	15.32	24.75	4.01	997	
OB30_30_1	30	30	2.97	15.05	24.67	4.03	458	
OB30_30_2	30	30	2.98	15.00	24.82	4.00	452	1.50
OB30_30_3	30	30	3.06	15.03	24.89	4.06	510	
OB30_50_1	30	50	2.96	15.02	24.72	4.06	1005	
OB30_50_2	30	50	3.02	15.05	24.63	4.05	1009	0.68
OB30_50_3	30	50	2.96	15.07	24.75	4.09	1075	
OB30_70_1	30	70	3.04	15.10	24.88	4.09	858	
OB30_70_2	30	70	2.98	14.93	24.70	4.03	783	0.36
OB30_70_3	30	70	3.06	15.07	24.68	4.00	779	

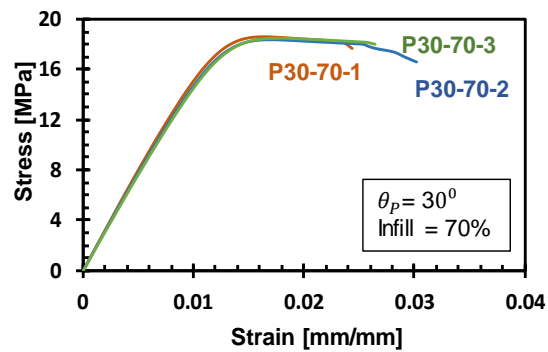
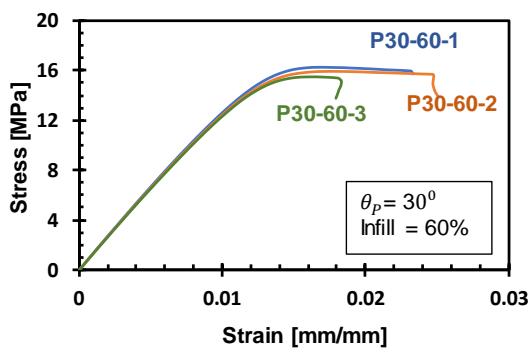
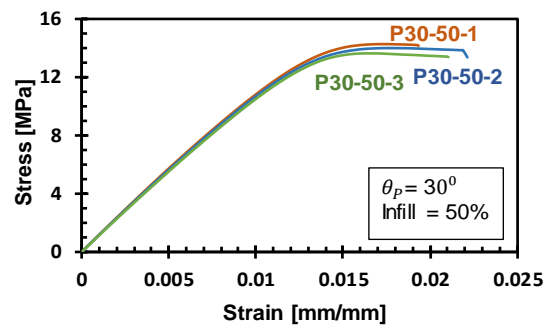
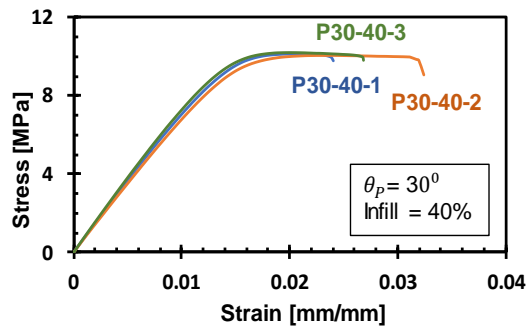
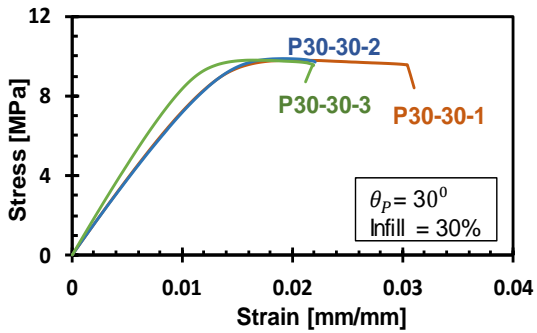
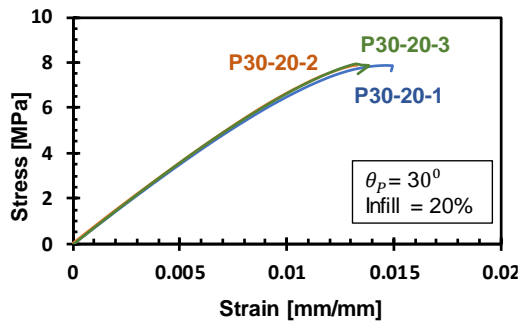
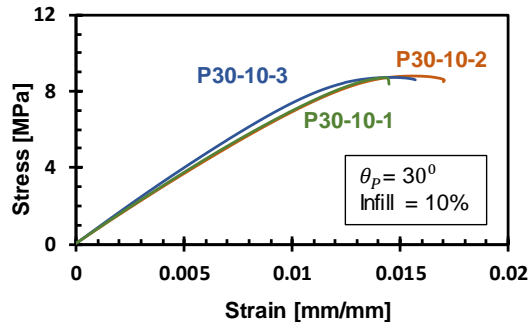
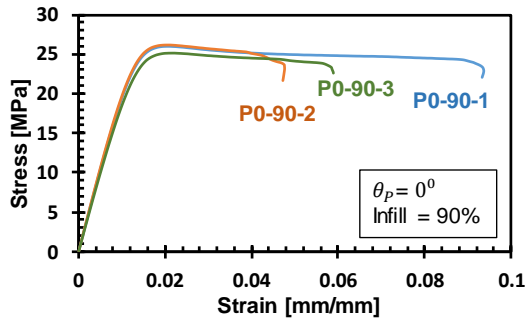
Table B.2.7 Results of V-notched porous PLA samples with $\theta_p = 45^\circ$

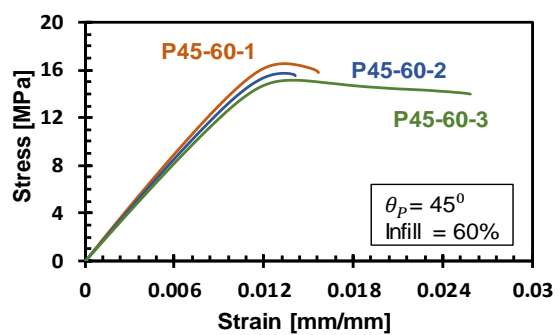
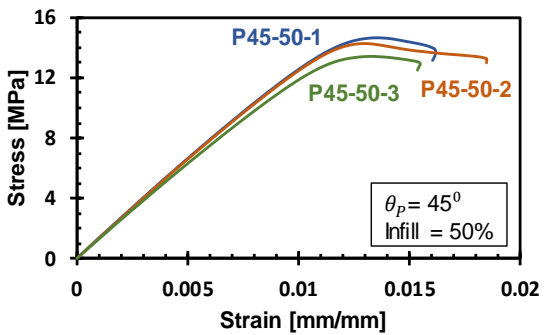
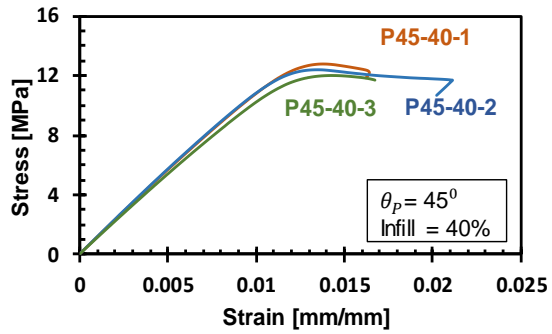
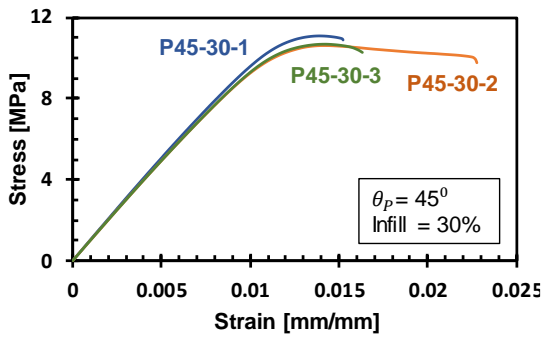
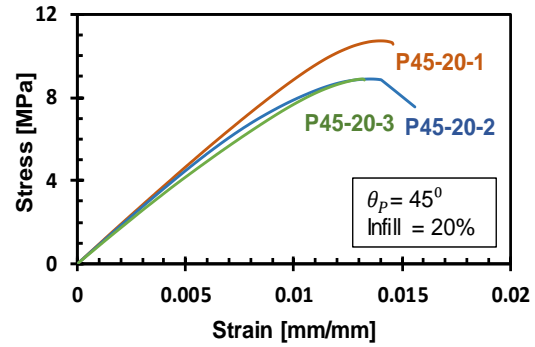
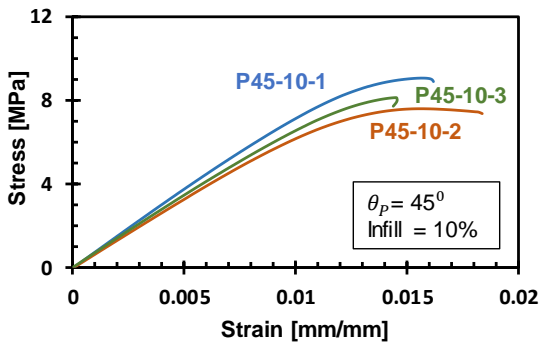
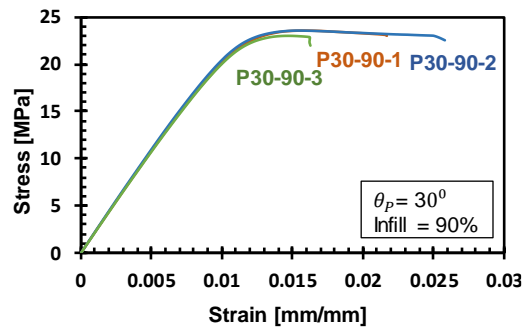
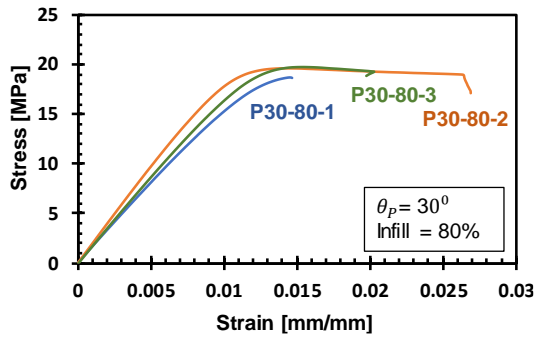
Code	θ [Deg]	t_s [mm]	R_n [mm]	W_n [mm]	W_g [mm]	t [mm]	F_f [N]	d_V [mm]
OS45_30_1	45	0.4	0.42	15.4	24.74	4.05	724	1.52
OS45_30_2	45	0.4	0.52	15.53	24.75	4.05	795	
OS45_30_3	45	0.4	0.47	15.65	24.73	4.08	726	
OS45_50_1	45	0.4	0.51	15.5	24.74	4.01	1013	0.70
OS45_50_2	45	0.4	0.52	15.27	24.76	4.01	1064	
OS45_50_3	45	0.4	0.50	15.6	24.78	4.05	1065	
OS45_70_1	45	0.4	0.49	15.42	24.74	4.08	1333	0.32
OS45_70_2	45	0.4	0.49	15.56	25.22	4.02	1283	
OS45_70_3	45	0.4	0.52	15.34	24.76	4.03	1235	
OI45_30_1	45	0.4	1.04	15.45	24.80	4.04	815	1.45
OI45_30_2	45	0.4	1.12	15.52	24.79	4.09	815	
OI45_30_3	45	0.4	1.01	15.59	24.85	4.05	780	
OI45_50_1	45	0.4	1.07	15.52	24.86	4.04	1086	0.69
OI45_50_2	45	0.4	0.99	15.31	24.90	4.06	537	
OI45_50_3	45	0.4	1.03	15.37	24.82	4.06	1038	
OI45_70_1	45	0.4	1.07	15.37	24.84	4.07	1353	0.31
OI45_70_2	45	0.4	1.10	15.18	24.88	4.08	1323	
OI45_70_3	45	0.4	1.03	15.13	24.94	4.11	1295	
OB45_30_1	45	0.4	3.03	15.06	24.84	4.06	732	1.49
OB45_30_2	45	0.4	3.01	15.00	24.84	4.05	789	
OB45_30_3	45	0.4	3.02	15.19	24.98	4.08	801	
OB45_50_1	45	0.4	2.94	15.06	24.85	4.01	1026	0.70
OB45_50_2	45	0.4	2.87	15.05	24.81	4.03	1024	
OB45_50_3	45	0.4	2.89	15.10	24.90	4.05	1094	
OB45_70_1	45	0.4	3.07	15.07	24.80	4.04	1256	0.32
OB45_70_2	45	0.4	3.00	15.05	24.80	4.06	1215	
OB45_70_3	45	0.4	2.89	15.02	24.77	4.02	1220	

B.3 Figures of the tested porous AM PLA samples

The stress vs strain curves for plain porous PLA samples, and the load vs displacement curve for the tested notched porous specimens will be shown below.







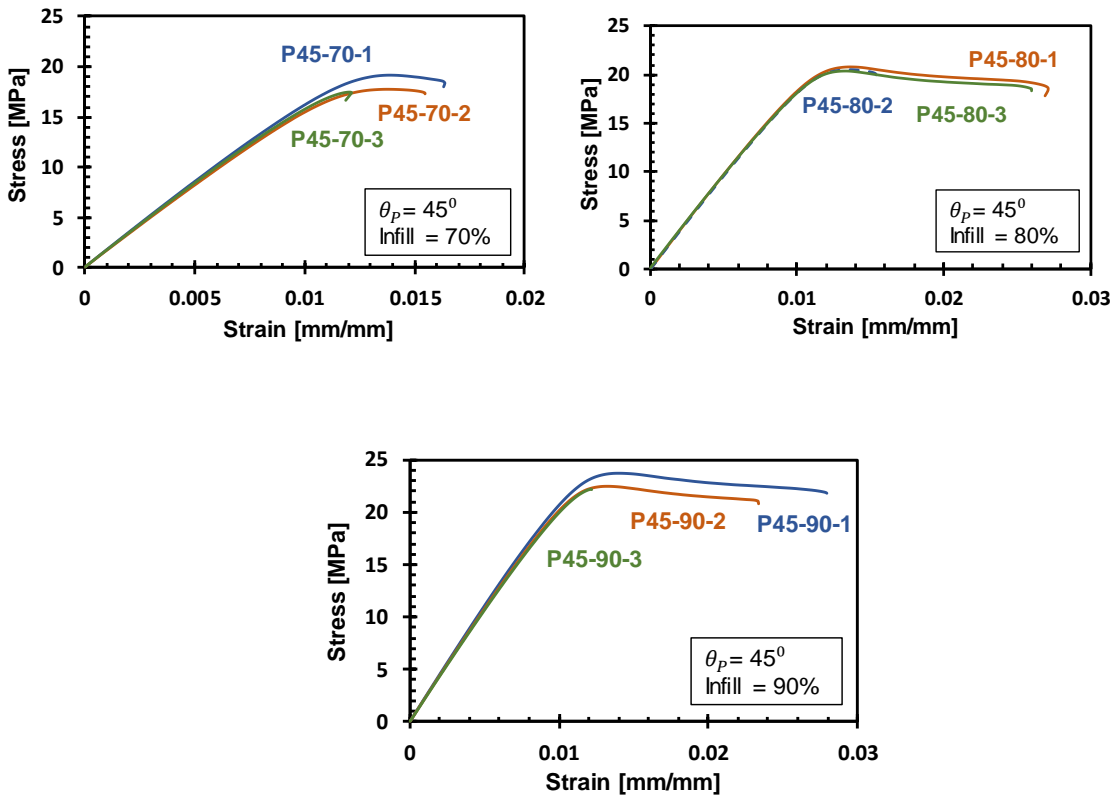
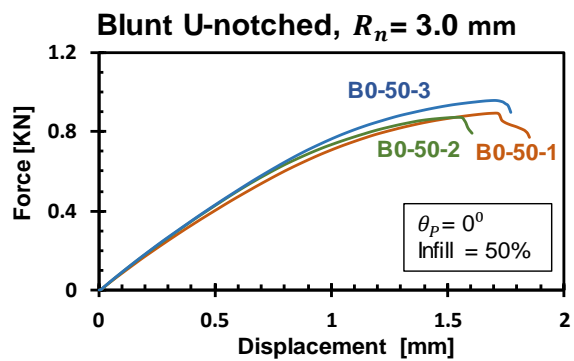
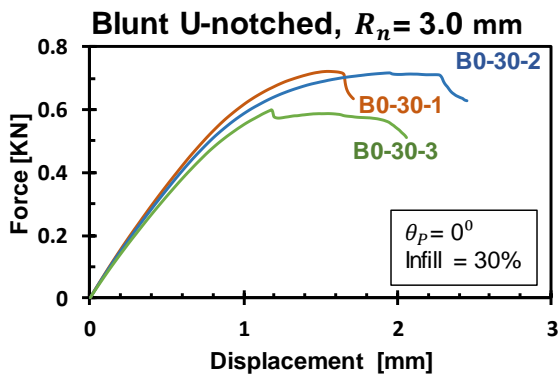
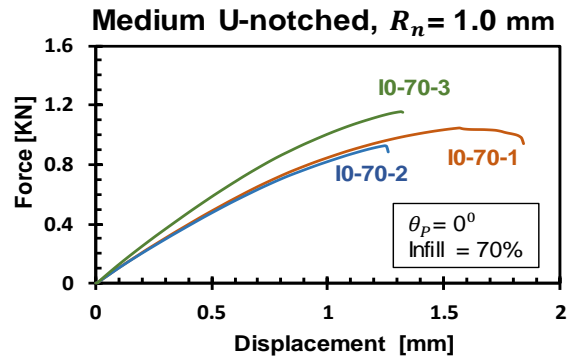
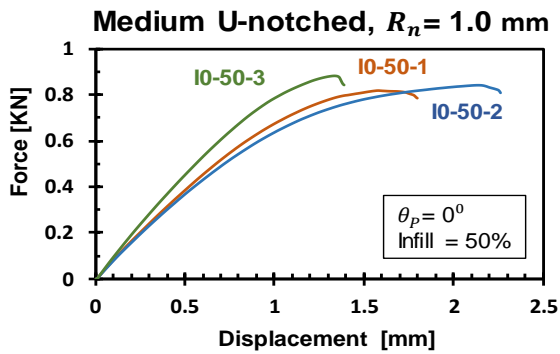
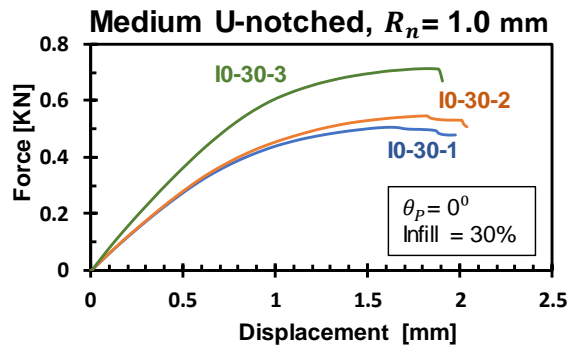
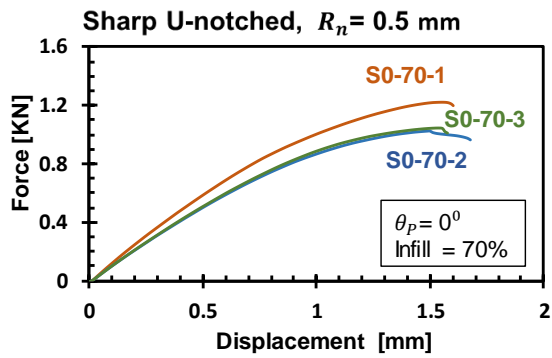
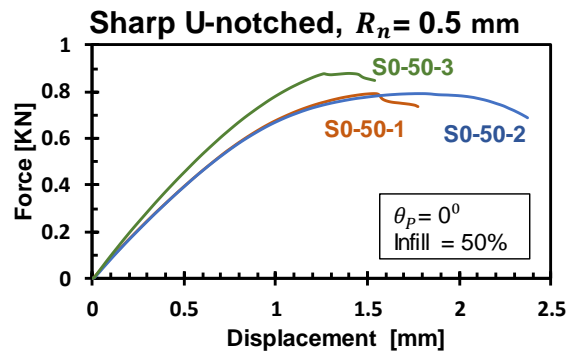
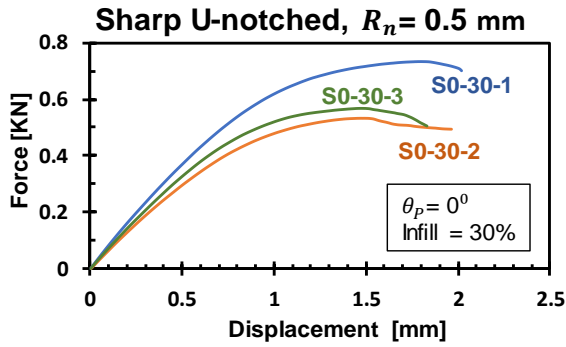
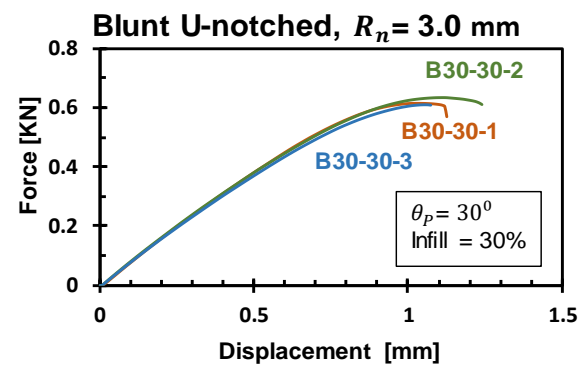
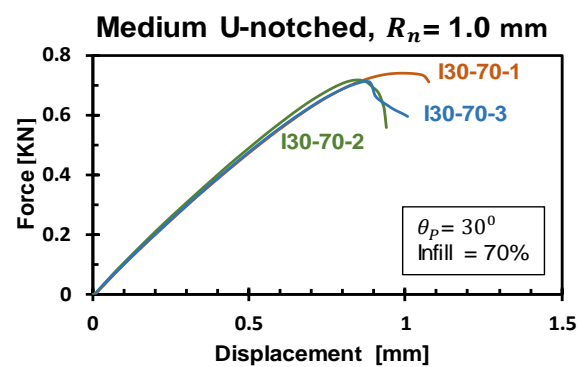
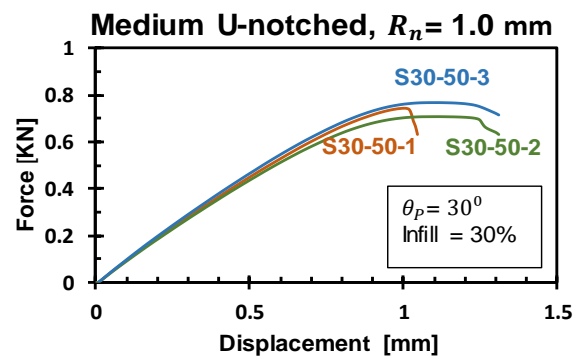
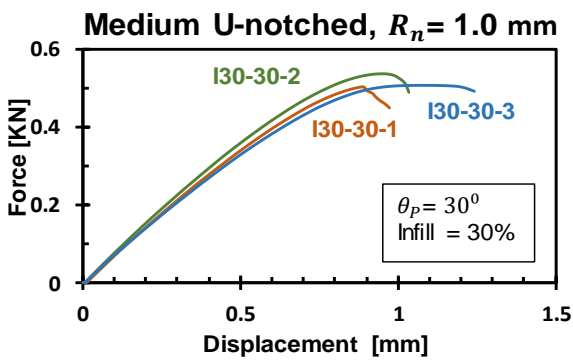
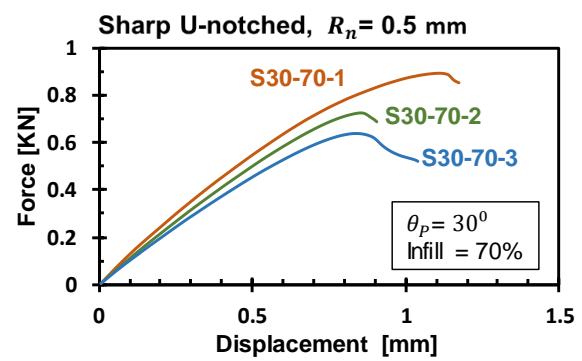
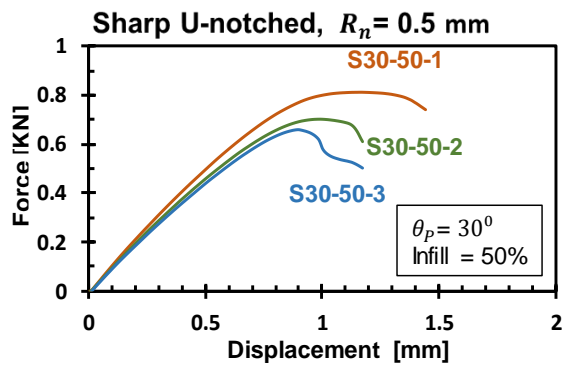
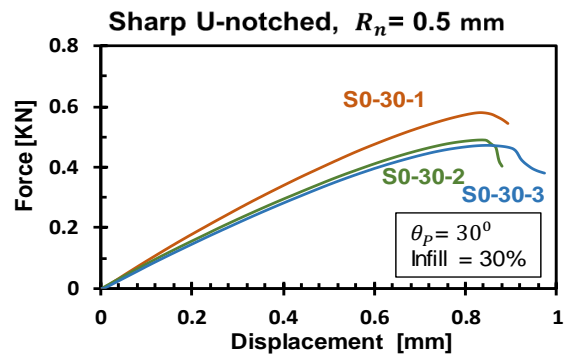
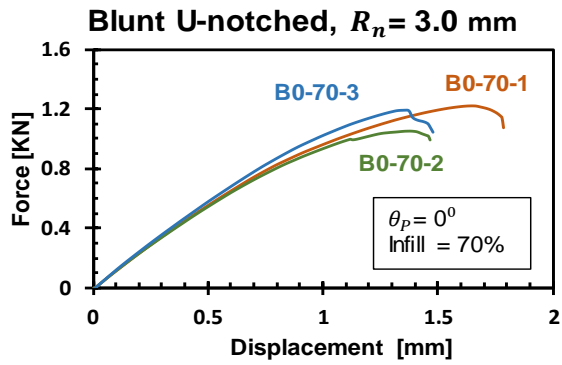
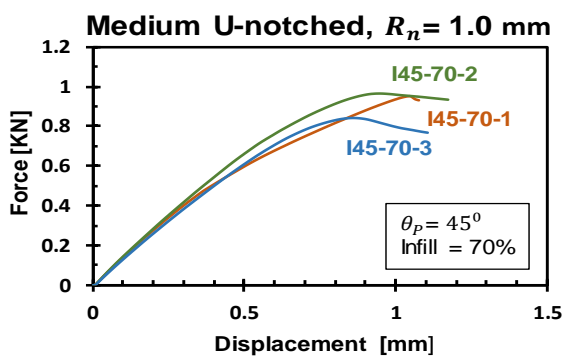
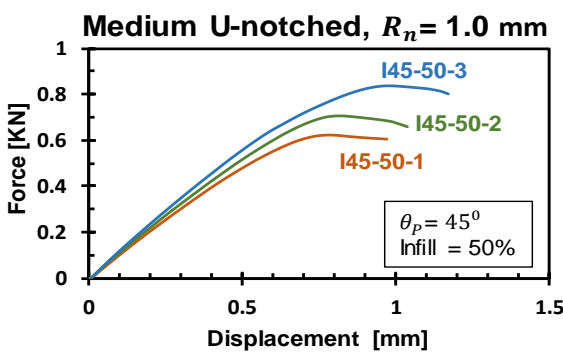
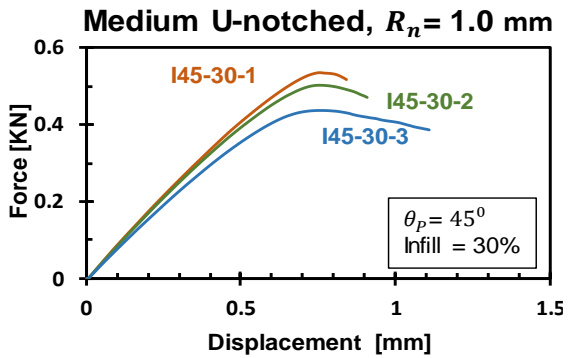
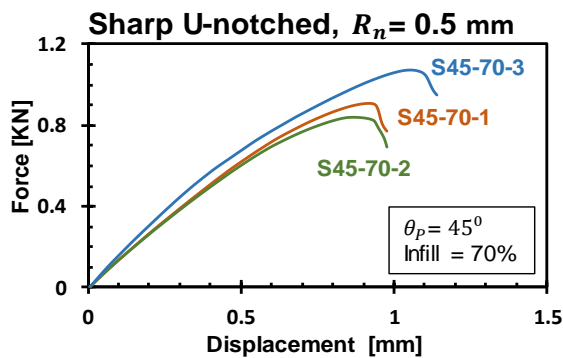
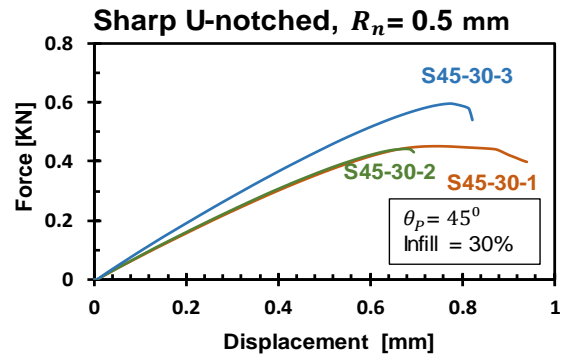
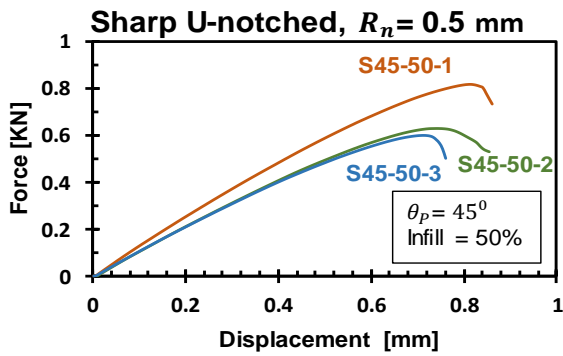
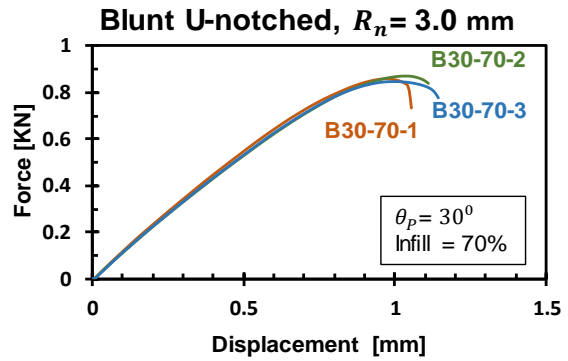
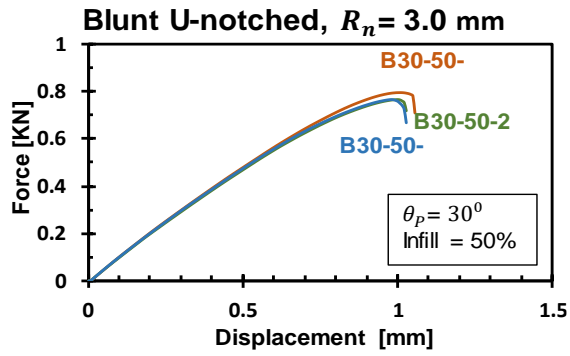


Figure B.3.1 Fictitious stress vs. strain for plain porous PLA samples







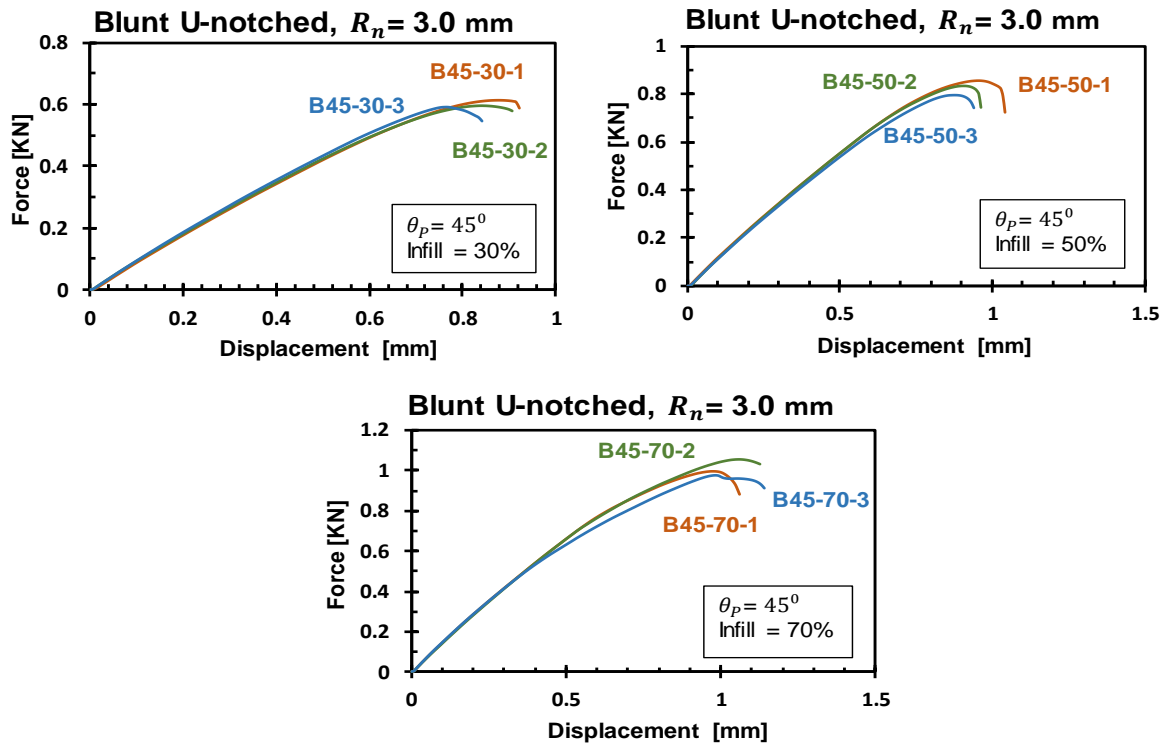
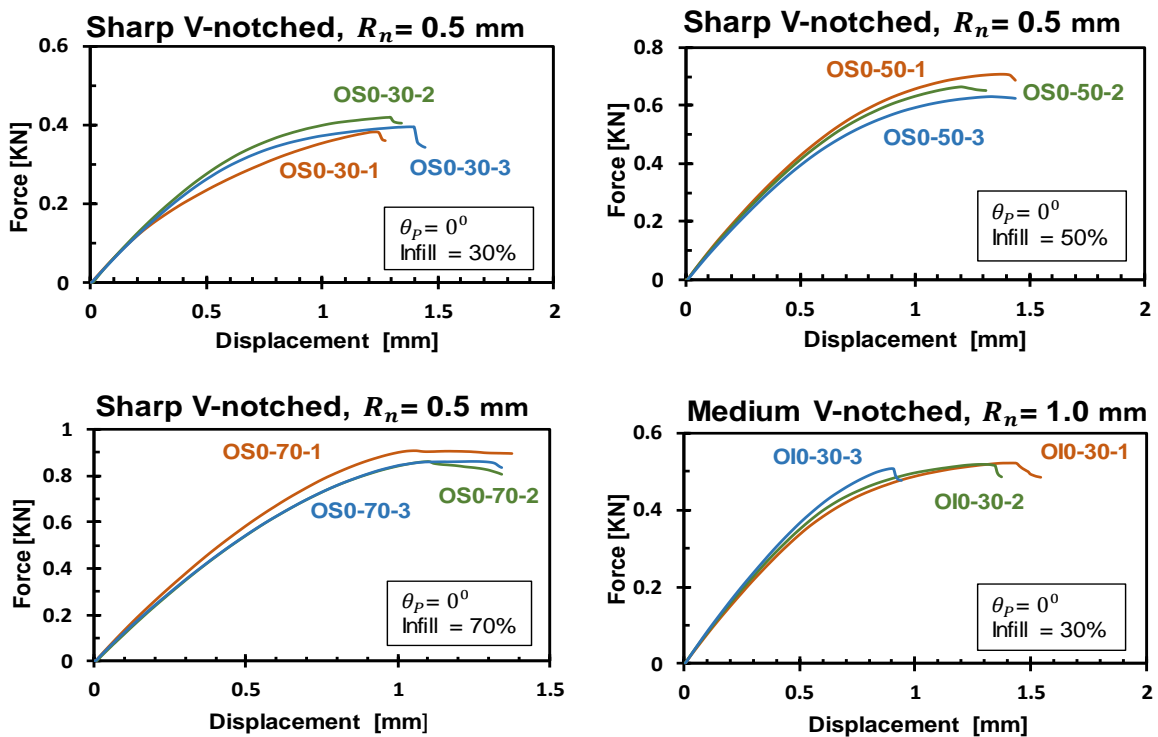
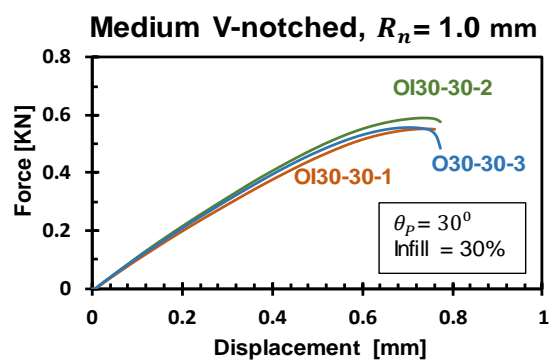
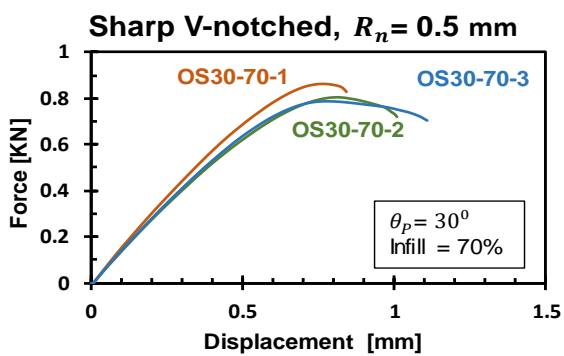
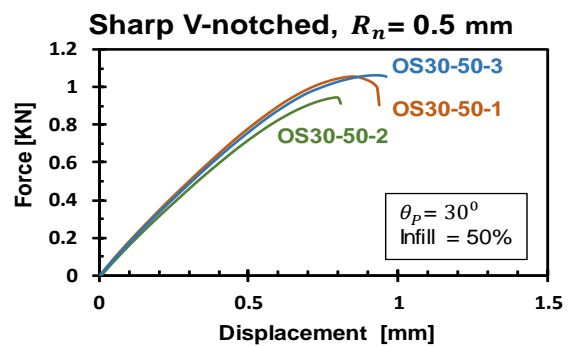
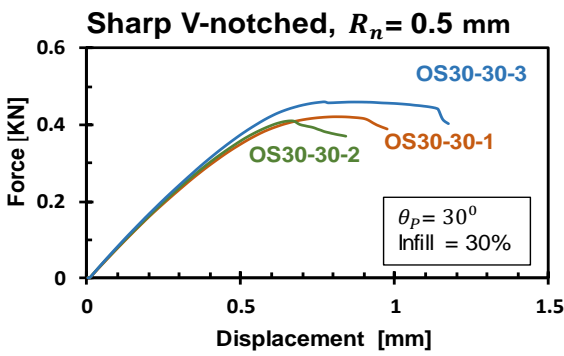
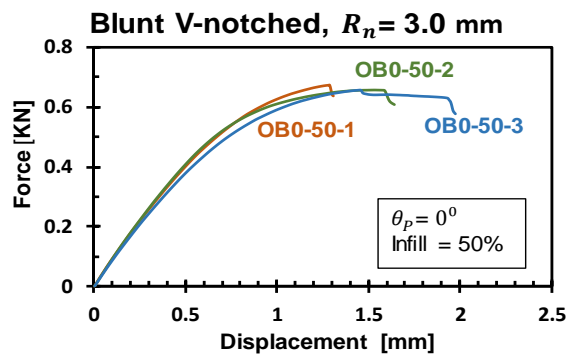
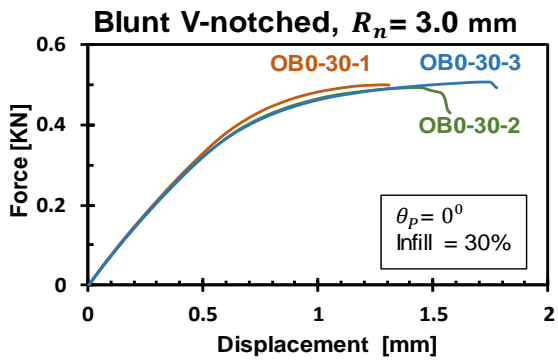
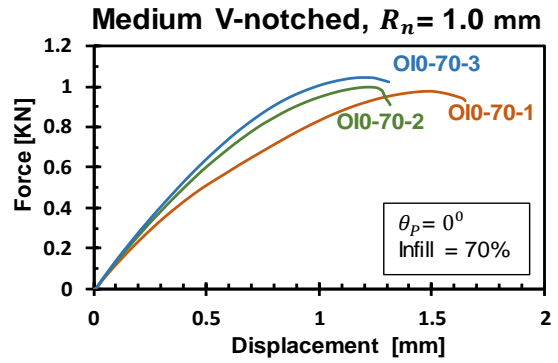
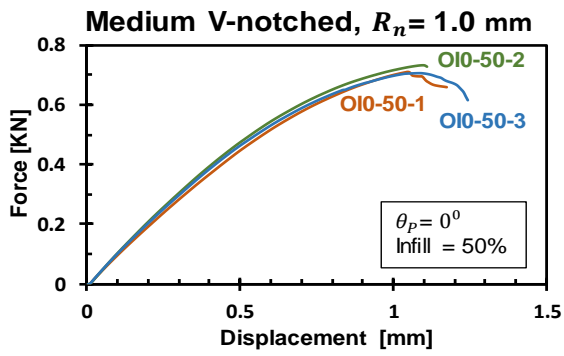
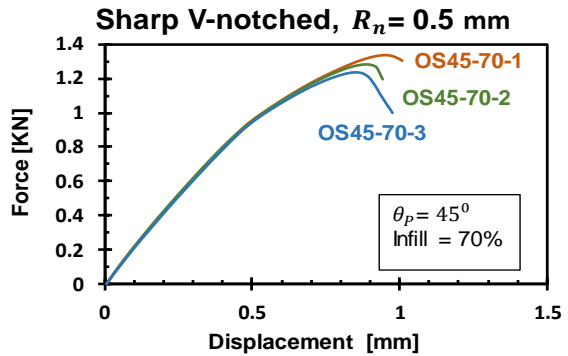
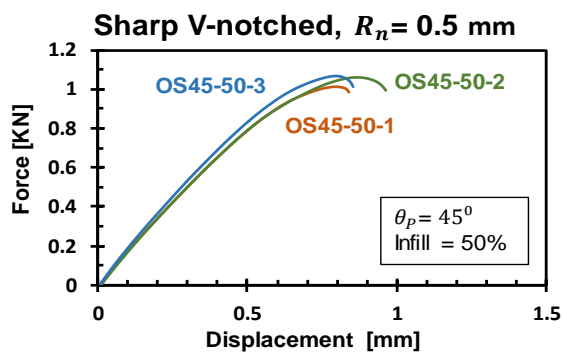
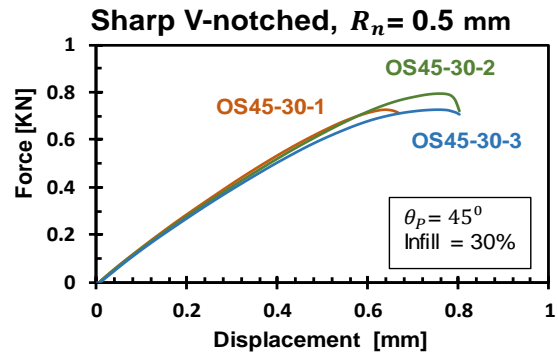
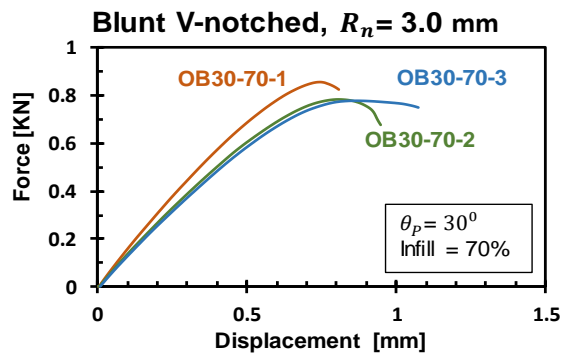
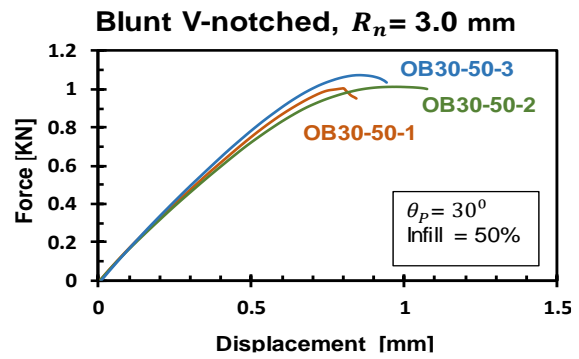
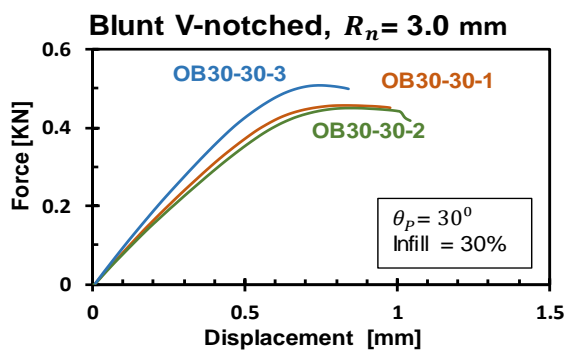
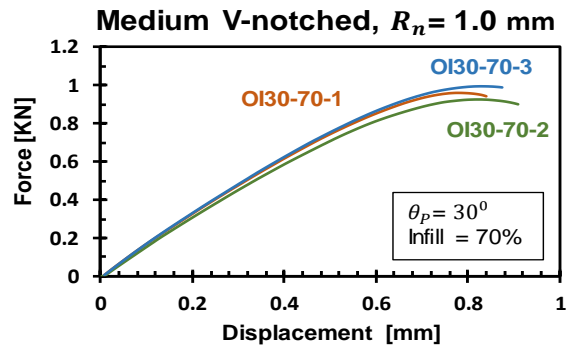
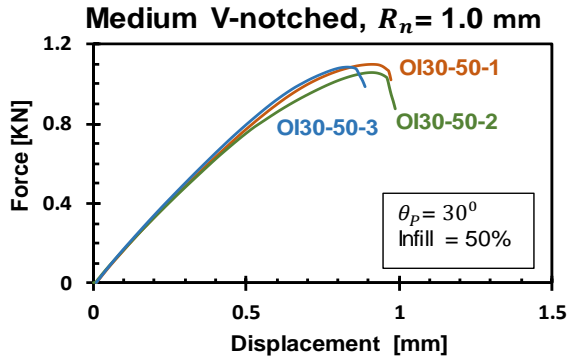


Figure B.3.2 Load vs displacement for U-notched porous samples







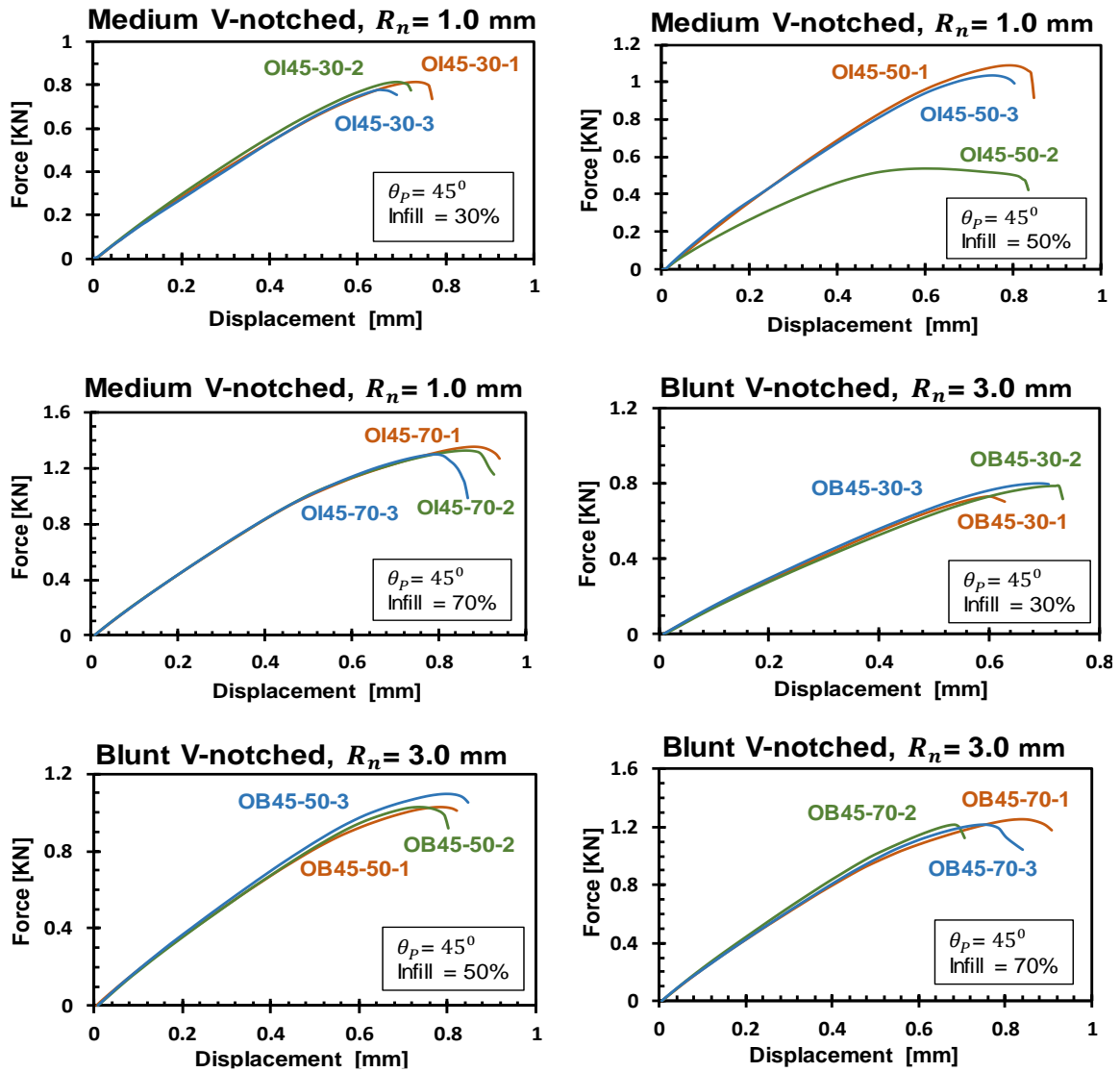
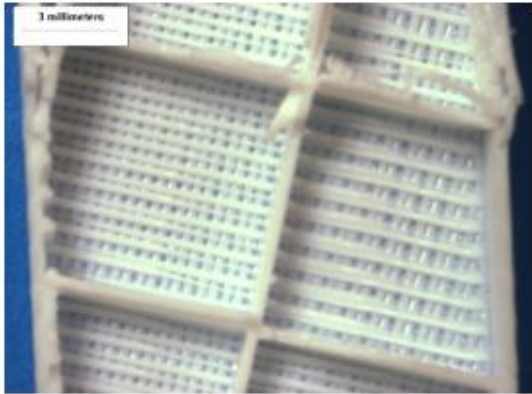


Figure B.3.3 Load vs displacement for V-notched porous samples

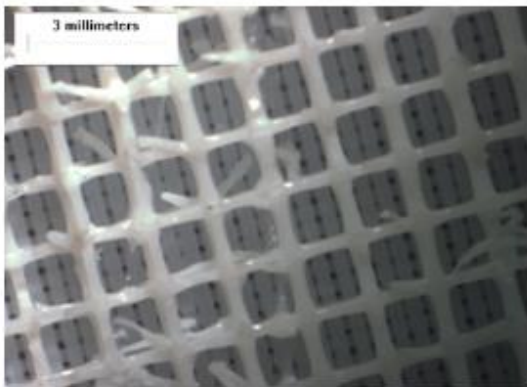
B.4 Microscopic pictures of porous plain PLA samples



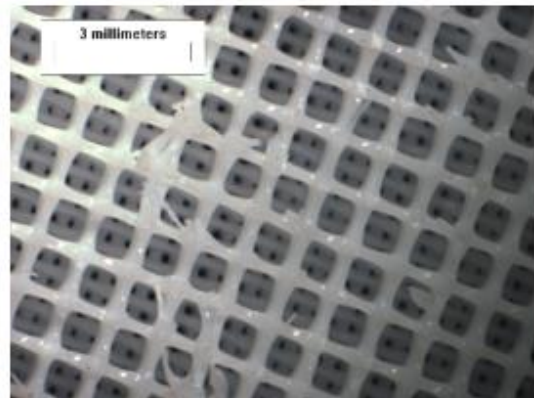
P30-10



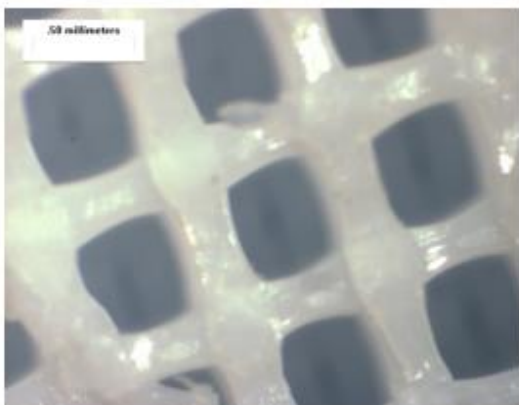
P30-20



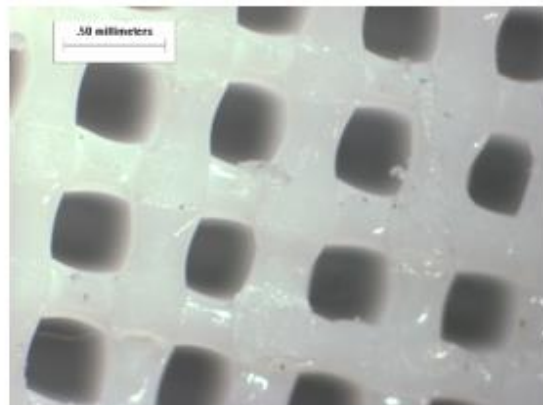
P 30-30



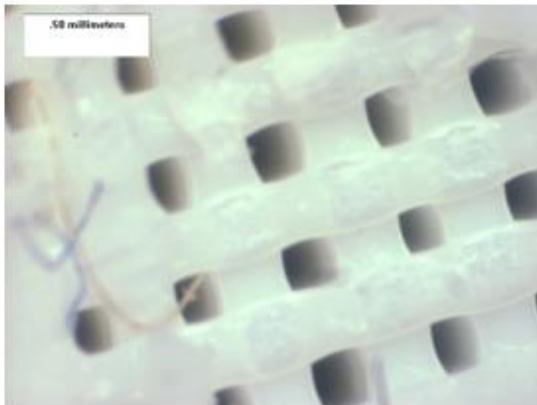
P 30-40



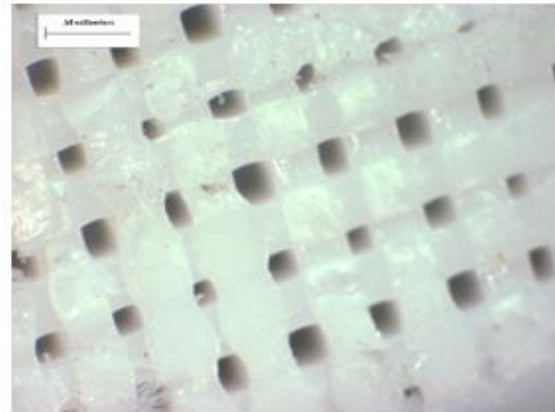
P 30-50



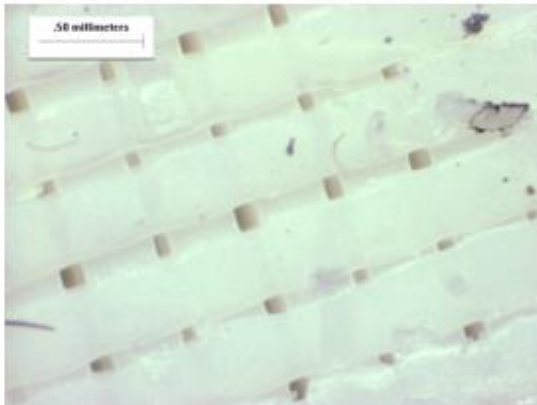
P 30-60



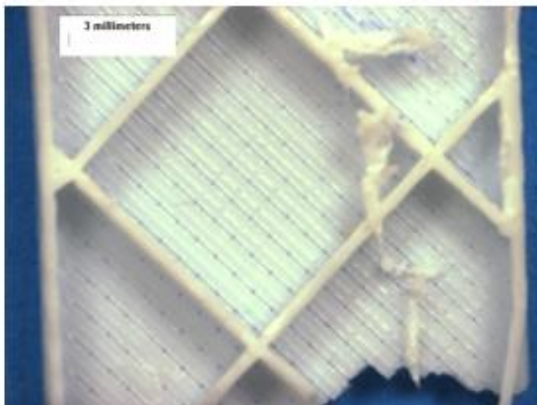
P30-70



P30-80



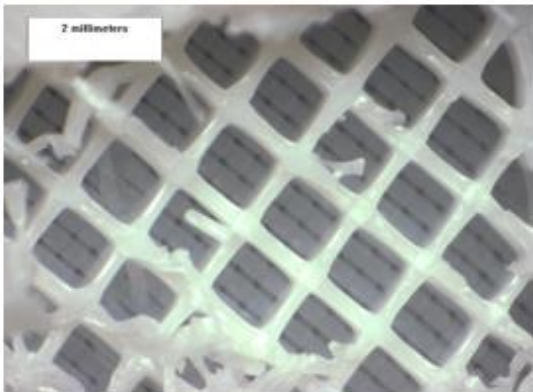
P30-90



PO-10



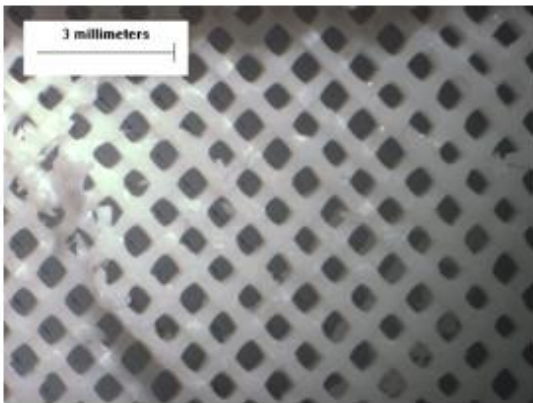
PO-20



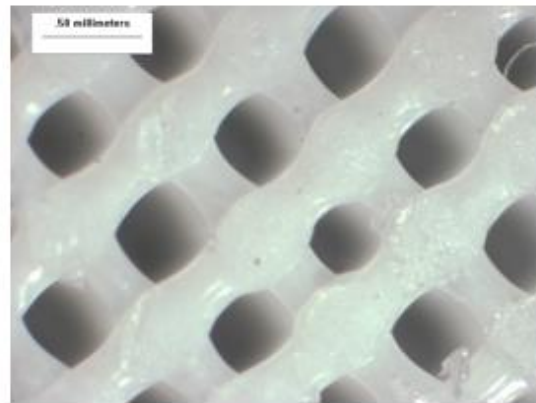
PO-30



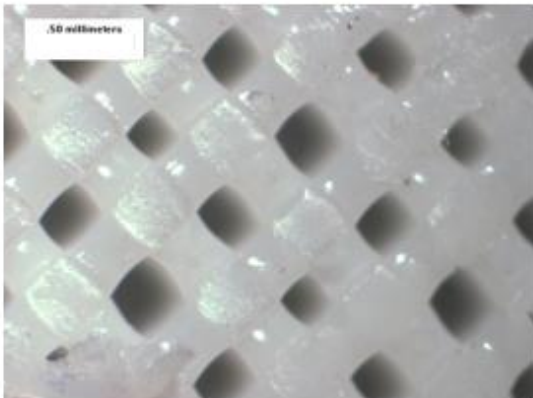
PO-40



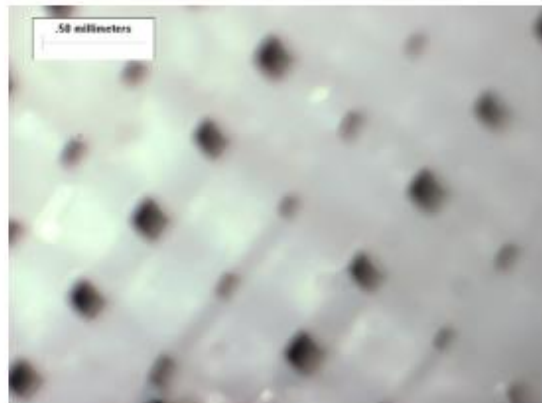
PO-50



PO-60



PO-70



PO-80



P0-90



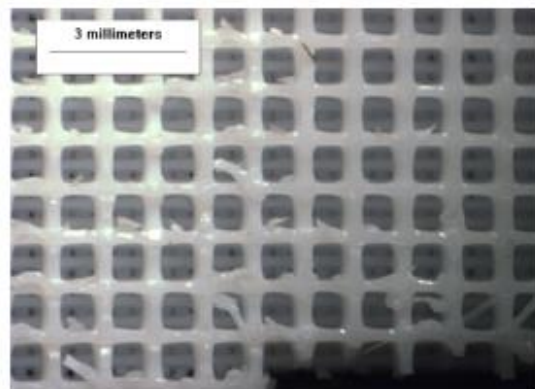
P45-10



P45-20



P45-30



P45-40

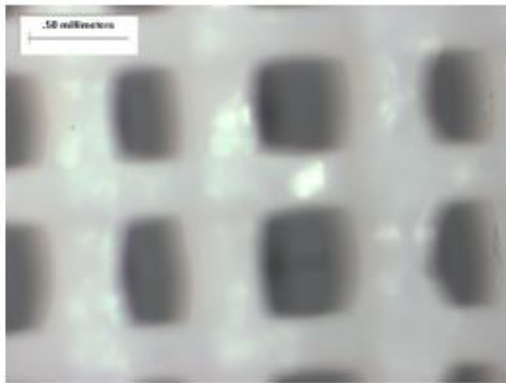
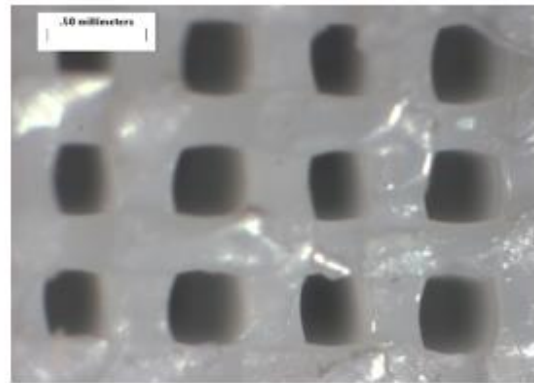
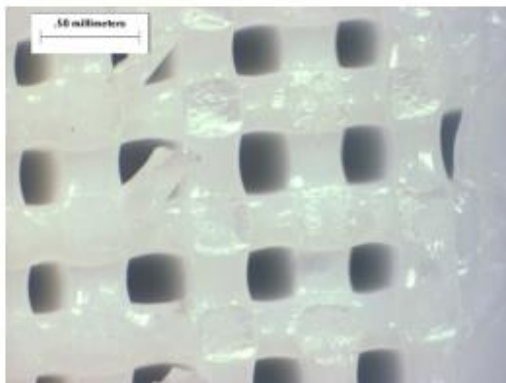
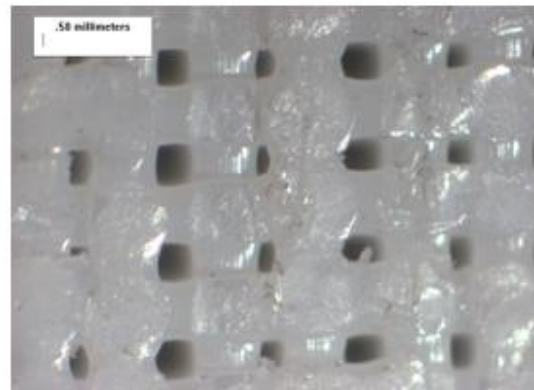
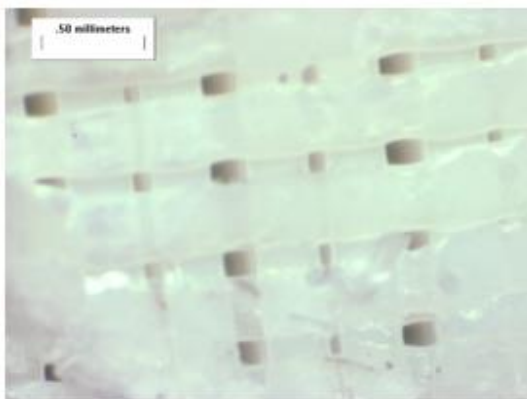
**P45-50****P45-60****P45-70****P45-80****P 45-90**

Figure B.4.1 Microscopic images for plain porous samples

B.5 Tables of the strength prediction for porous PLA samples

Table B.5.1 Strength prediction for plain porous samples, $\theta_p = 0^\circ$

P-0				PM	LM	LEFM
Code	a	α_{eq}	σ_{f-av}	σ_{fp}	σ_{fl}	σ_f
	[mm]	[mm]	[MPa]	[MPa]	[MPa]	[MPa]
P_10-1	10.46	351.9	8.4	3.5	3.5	3.5
P_20_1	4.85	163.0	9.2	5.2	5.2	5.2
P_30_1	1.30	43.7	10.4	9.8	9.8	10.0
P_40_1	0.89	29.8	11.9	11.8	11.7	12.1
P_50_3	0.62	20.7	13.6	14.0	13.8	14.5
P_60_1	0.44	14.8	16.4	16.3	16.0	17.2
P_70_1	0.32	10.8	19.8	18.7	18.3	20.1
P_80_1	0.20	6.7	22.5	22.7	22.0	25.5
P_90_1	0.13	4.2	25.8	27.0	25.9	32.2

Table B.5.2 Strength prediction for plain porous samples, $\theta_p = 30^\circ$

P-30				PM	LM	LEFM
Code	a	α_{eq}	σ_{f-av}	σ_{fp}	σ_{fl}	σ_f
	[mm]	[mm]	[MPa]	[MPa]	[MPa]	[MPa]
P_10-1	10.46	351.7	8.7	3.5	3.5	3.5
P_20_1	4.95	166.5	7.9	5.1	5.1	5.1
P_30_1	1.38	46.4	9.8	9.6	9.5	9.7
P_40_1	0.94	31.6	10.1	11.5	11.4	11.7
P_50_3	0.69	23.0	14.0	13.3	13.2	13.8
P_60_1	0.41	13.8	15.9	16.8	16.5	17.8
P_70_1	0.26	8.6	18.5	20.6	20.1	22.5
P_80_1	0.25	8.4	19.3	20.8	20.2	22.8
P_90_1	0.11	3.7	23.4	28.1	26.9	34.3

Table B.5.3 Strength prediction for plain porous samples, $\theta_p = 45^\circ$

P-45				PM	LM	LEFM
Code	a	a_{eq}	σ_{f-av}	σ_{fp}	σ_{fl}	σ_f
	[mm]	[mm]	[MPa]	[MPa]	[MPa]	[MPa]
P_10-1	10.65	358.3	8.3	3.5	3.5	3.5
P_20_1	4.97	167.0	9.5	5.1	5.1	5.1
P_30_1	1.37	45.9	10.8	9.6	9.6	9.7
P_40_1	0.89	29.8	12.4	11.8	11.7	12.1
P_50_3	0.64	21.5	14.1	13.8	13.6	14.2
P_60_1	0.44	14.6	15.9	16.4	16.1	17.3
P_70_1	0.31	10.3	18.1	19.1	18.7	20.6
P_80_1	0.14	4.8	20.6	25.7	24.7	30.0
P_90_1	0.08	2.6	22.8	31.3	29.8	41.0

Table B.5.4 Strength prediction for U-notched porous samples, $\theta_p = 0^\circ$

			PM	LM	PM	LM	AM	PM	LM	AM
Code	a	a_{eq}	σ_f	σ_f	σ_{eff}	σ_{eff}	σ_{eff}	Error	Error	Error
	[mm]	[mm]	[MPa]	[MPa]	[MPa]	[MPa]	[MPa]	[%]	[%]	[%]
S0_30_1	1.42	44.5	9.8	9.7	11.4	11.2	11.0	16.7	15.4	12.8
S0_50_1	0.70	21.8	13.7	13.5	15.5	15.2	14.9	13.3	12.4	8.9
S0_70_1	0.34	10.6	18.8	18.4	20.3	20.0	19.6	7.8	8.6	4.3
I0_30_1	1.45	45.3	9.7	9.6	11.6	10.1	10.9	19.8	5.0	12.6
I0_50_1	0.66	20.7	14.0	13.8	16.7	15.7	15.6	19.3	13.6	11.5
I0_70_1	0.35	10.9	18.6	18.2	20.4	19.3	19.2	9.7	6.1	3.2
B0_30_1	1.35	42.2	10.0	10.0	14.0	12.3	12.9	39.7	23.6	28.7
B0_50_1	0.67	20.9	13.9	13.8	18.6	16.3	17.0	33.5	18.5	22.0
B0_70_1	0.33	10.3	19.1	18.6	23.8	21.0	12.7	24.8	12.7	-33.4

Table B.5.5 Strength prediction for U-notched porous samples, $\theta_p = 30^\circ$

			PM	LM	PM	LM	AM	PM	LM	AM
Code	a [mm]	a_{eq} [mm]	σ_f [MPa]	σ_f [MPa]	σ_{eff} [MPa]	σ_{eff} [MPa]	σ_{eff} [MPa]	Error [%]	Error [%]	Error [%]
S30_30_1	1.23	38.44	10.5	10.4	9.7	9.5	9.3	-7.4	-8.7	-11.2
S30_50_1	0.68	21.25	13.8	13.7	13.6	13.4	12.9	-1.7	-2.0	-6.5
S30_70_1	0.43	13.54	17.0	16.6	14.5	14.2	13.7	-14.5	-14.7	-19.2
I30_30_1	1.44	45.00	9.7	9.7	10.4	9.8	9.7	7.1	1.5	-0.1
I30_50_1	0.69	21.46	13.8	13.6	14.9	13.9	13.8	8.2	2.2	0.2
I30_70_1	0.39	12.19	17.8	17.4	14.7	13.7	13.6	-17.2	-21.3	-23.4
B30_30_1	1.43	44.58	9.8	9.7	13.0	11.5	11.7	33.2	18.6	19.9
B30_50_1	0.72	22.50	13.5	13.3	16.2	14.3	14.8	20.2	7.4	9.8
B30_70_1	0.44	13.75	16.8	16.5	18.0	15.8	16.3	6.9	-4.5	-3.2

Table B.5.6 Strength prediction for U-notched porous samples, $\theta_p = 45^\circ$

			PM	LM	PM	LM	AM	PM	LM	AM
Code	a [mm]	a_{eq} [mm]	σ_f [MPa]	σ_f [MPa]	σ_{eff} [MPa]	σ_{eff} [MPa]	σ_{eff} [MPa]	Error [%]	Error [%]	Error [%]
S45_30_1	1.19	37.19	10.6	10.6	9.6	9.4	9.2	-9.8	-11.0	-13.6
S45_50_1	0.60	18.85	14.6	14.4	13.1	12.9	12.5	-10.4	-10.5	-14.5
S45_70_1	0.36	11.25	18.4	18.0	18.0	17.6	17.1	-2.3	-2.2	-6.8
I45_30_1	1.42	44.27	9.8	9.7	10.1	9.4	9.9	3.2	-3.1	1.5
I45_50_1	0.69	21.56	13.7	13.6	14.7	13.8	13.6	6.9	1.6	-1.1
I45_70_1	0.38	11.87	18.0	17.6	18.7	17.5	17.3	4.2	-0.5	-3.6
B45_30_1	1.45	45.41	9.7	9.6	12.7	11.2	11.5	31.3	16.5	18.9
B45_50_1	0.69	21.56	13.7	13.6	17.4	15.3	15.7	26.6	12.7	14.5
B45_70_1	0.38	11.77	18.0	17.7	21.1	18.6	19.1	17.1	5.4	6.0

Table B.5.7 Strength prediction for V-notched porous samples, $\theta_p = 0^\circ$

			PM	LM	PM	LM	AM	PM	LM	AM
Code	a [mm]	a_{eq} [mm]	σ_f [MPa]	σ_f [MPa]	σ_{eff} [MPa]	σ_{eff} [MPa]	σ_{eff} [MPa]	Error [%]	Error [%]	Error [%]
OS0_30_1	1.59	49.58	9.3	9.2	7.8	7.4	7.4	-15.9	-19.4	-20.2
OS0_50_1	0.68	21.35	13.8	13.6	12.9	12.3	12.2	-6.6	-9.8	-11.6
OS0_70_1	0.32	10.10	19.2	18.8	17.0	16.2	16.1	-11.6	-13.8	-16.3
OI0_30_1	1.49	46.56	9.6	9.5	11.5	10.3	10.8	20.3	8.4	13.0
OI0_50_1	0.67	21.04	13.9	13.7	15.7	14.0	14.7	12.9	2.0	5.7
OI0_70_1	0.34	10.73	18.8	18.3	22.2	19.8	20.8	18.4	7.9	10.9
OB0_30_1	1.51	47.08	9.5	9.4	11.3	9.8	10.5	18.9	3.7	10.7
OB0_50_1	0.68	21.35	13.8	13.6	15.1	13.1	14.1	9.4	-3.9	2.1
OB0_70_1	0.37	11.46	18.2	17.9	20.7	17.8	19.2	13.5	-0.3	5.4

Table B.5.8 Strength prediction for V-notched porous samples, $\theta_p = 30^\circ$

			PM	LM	PM	LM	AM	PM	LM	AM
Code	a [mm]	a_{eq} [mm]	σ_f [MPa]	σ_f [MPa]	σ_{eff} [MPa]	σ_{eff} [MPa]	σ_{eff} [MPa]	Error [%]	Error [%]	Error [%]
OS30_30_1	1.57	49.16	9.3	9.3	8.0	8.0	7.9	-14.6	-13.6	-15.1
OS30_50_1	0.65	20.31	14.1	13.9	19.7	19.7	18.3	39.4	41.3	29.5
OS30_70_1	0.39	12.08	17.8	17.5	16.2	16.2	15.0	-9.1	-7.2	-15.6
OI30_30_1	1.53	47.81	9.4	9.4	12.5	11.2	11.7	32.5	19.4	24.3
OI30_50_1	0.63	19.79	14.3	14.1	23.4	20.9	21.9	63.7	48.1	53.5
OI30_70_1	0.38	11.77	18.0	17.7	21.2	18.9	19.9	17.6	7.0	10.2
OB30_30_1	1.53	47.71	9.4	9.4	10.6	9.2	9.7	12.5	-2.0	2.9
OB30_50_1	0.64	19.89	14.3	14.1	23.0	19.8	21.0	61.3	40.7	47.3
OB30_70_1	0.35	10.94	18.6	18.2	18.1	15.6	16.5	-2.7	-14.3	-11.1

Table B.5.9 Strength prediction for V-notched porous samples, $\theta_p = 45^\circ$

			PM	LM	PM	LM	AM	PM	LM	AM
Code	a [mm]	a_{eq} [mm]	σ_f [MPa]	σ_f [MPa]	σ_{eff} [MPa]	σ_{eff} [MPa]	σ_{eff} [MPa]	Error [%]	Error [%]	Error [%]
OS45_30_1	1.51	47.29	9.5	9.4	14.3	13.6	13.5	50.8	44.2	42.8
OS45_50_1	0.69	21.56	13.7	13.6	22.9	20.6	19.1	66.6	51.7	39.0
OS45_70_1	0.32	10.10	19.2	18.8	27.8	24.8	23.2	44.5	31.9	20.4
OI45_30_1	1.42	44.48	9.8	9.7	17.6	15.7	16.5	80.2	61.7	68.4
OI45_50_1	0.66	20.62	14.0	13.9	19.4	17.3	18.2	38.3	24.9	29.7
OI45_70_1	0.31	9.79	19.5	19.0	28.6	25.4	26.9	46.7	33.4	37.7
OB45_30_1	1.48	46.25	9.6	9.5	15.4	14.0	14.3	60.6	46.9	49.6
OB45_50_1	0.68	21.14	13.9	13.7	23.5	20.3	19.6	69.4	48.2	41.5
OB45_70_1	0.31	9.69	19.6	19.1	27.5	23.8	23.0	40.5	24.5	17.7